



British  
Geological Survey

# Environmental Monitoring - Phase 4 Final Report (April 2018 - March 2019)

Groundwater Science Programme

Open Report OR/19/044



# Environmental Monitoring - Phase 4 Final Report (April 2018 - March 2019)

The National Grid and other  
Ordnance Survey data © Crown  
Copyright and database rights  
2019. Ordnance Survey Licence  
No. 100021290 EUL.

## Keywords

Monitoring, groundwater,  
seismicity, ground motion,  
greenhouse gases, atmospheric  
composition, air quality, radon,  
soil gas, water quality, shale gas.

## Bibliographical reference

R.S. WARD, P.L. SMEDLEY, G.  
ALLEN, B.J. BAPTIE, A.K.A.P.  
BARKWITH, L. BATESON, R.A.  
BELL, M. BOWES, M. COLEMAN,  
G. CREMEN, Z. DARAKTCHIEVA,  
M GONG, C.H. HOWARTH, R.  
FISHER, D. HAWTHORN, D.G.  
JONES, C. JORDAN, M.  
LANOISELLÉ, A.C. LEWIS, T.R.  
LISTER, D. LOWRY, R. LUCKETT,  
D. MALLIN-MARTIN, B.P.  
MARCHANT, C.J. MILNE, A.  
NOVELLINO, J. PITT, R.M.  
PURVIS, M.O. RIVETT, J. SHAW,  
H. TAYLOR-CURRAN, J.M.  
WASIKIEWICZ, M. WERNER AND  
S. WILDE. 2019. *British  
Geological Survey Open Report,  
OR/19/044*. 225 pp.

Copyright in materials derived  
from the British Geological  
Survey's work is owned by  
UK Research and Innovation  
(UKRI) and/or the authority that  
commissioned the work. You  
may not copy or adapt this  
publication without first  
obtaining permission. Contact the  
BGS Intellectual Property Rights  
Section, British Geological  
Survey, Keyworth,  
e-mail [ipr@bgs.ac.uk](mailto:ipr@bgs.ac.uk). You may  
quote extracts of a reasonable  
length without prior permission,  
provided a full acknowledgement  
is given of the source of the  
extract.

Maps and diagrams in this book  
use topography based on  
Ordnance Survey mapping.

© UKRI 2019. All rights reserved

R.S. Ward (1), P.L. Smedley (1), G. Allen (2), B.J. Baptie (1),  
A.K.A.P. Barkwith (1), L. Bateson (1), R.A. Bell (1), M. Bowes (1),  
M. Coleman (5), G. Cremen (6), Z. Daraktchieva (3), M Gong,  
Mengyi (1), C.H. Howarth (3), R. Fisher (5), D. Hawthorn (1), D.G.  
Jones (1), C. Jordan (1), M. Lanoisellé (5), A.C. Lewis (4), T.R.  
Lister (1), D. Lowry (5), R. Lockett (1), D. Mallin-Martin (1), B.P.  
Marchant (1), C.A. Miller (3), C.J. Milne (1), A. Novellino (1), J. Pitt  
(2), R.M. Purvis (4), M.O. Rivett (7), J. Shaw (2), H. Taylor-Curran  
(1), J.M. Wasikiewicz (3), M. Werner (6) and S Wilde (4)

- (1): British Geological Survey
- (2): University of Manchester
- (3): Public Health England
- (4): University of York (National Centres for Atmospheric Science)
- (5): Royal Holloway University of London
- (6): University of Bristol
- (7): GroundH20 plus Ltd

## BRITISH GEOLOGICAL SURVEY

The full range of our publications is available from BGS shops at Nottingham, Edinburgh, London and Cardiff (Welsh publications only) see contact details below or shop online at [www.geologyshop.com](http://www.geologyshop.com)

The London Information Office also maintains a reference collection of BGS publications, including maps, for consultation.

We publish an annual catalogue of our maps and other publications; this catalogue is available online or from any of the BGS shops.

*The British Geological Survey carries out the geological survey of Great Britain and Northern Ireland (the latter as an agency service for the government of Northern Ireland), and of the surrounding continental shelf, as well as basic research projects. It also undertakes programmes of technical aid in geology in developing countries.*

*The British Geological Survey is a component body of UK Research and Innovation.*

*British Geological Survey offices*

**Environmental Science Centre, Keyworth, Nottingham  
NG12 5GG**

Tel 0115 936 3100

**BGS Central Enquiries Desk**

Tel 0115 936 3143

email [enquiries@bgs.ac.uk](mailto:enquiries@bgs.ac.uk)

**BGS Sales**

Tel 0115 936 3241

email [sales@bgs.ac.uk](mailto:sales@bgs.ac.uk)

**The Lyell Centre, Research Avenue South, Edinburgh  
EH14 4AP**

Tel 0131 667 1000

email [scotsales@bgs.ac.uk](mailto:scotsales@bgs.ac.uk)

**Natural History Museum, Cromwell Road, London SW7 5BD**

Tel 020 7589 4090

Tel 020 7942 5344/45 email [bgs-london@bgs.ac.uk](mailto:bgs-london@bgs.ac.uk)

**Cardiff University, Main Building, Park Place, Cardiff  
CF10 3AT**

Tel 029 2167 4280

**Maclean Building, Crowmarsh Gifford, Wallingford  
OX10 8BB**

Tel 01491 838800

**Geological Survey of Northern Ireland, Department of  
Enterprise, Trade & Investment, Dundonald House, Upper  
Newtownards Road, Ballymiscaw, Belfast, BT4 3SB**

Tel 01232 666595

[www.bgs.ac.uk/gsni/](http://www.bgs.ac.uk/gsni/)

**Natural Environment Research Council, Polaris House,  
North Star Avenue, Swindon SN2 1EU**

Tel 01793 411500

Fax 01793 411501

[www.nerc.ac.uk](http://www.nerc.ac.uk)

**UK Research and Innovation, Polaris House, Swindon  
SN2 1FL**

Tel 01793 444000

[www.ukri.org](http://www.ukri.org)

Website [www.bgs.ac.uk](http://www.bgs.ac.uk)

Shop online at [www.geologyshop.com](http://www.geologyshop.com)

# Foreword

This report presents the results and interpretation for Phase 4 of an integrated environmental monitoring programme that is being undertaken around two proposed shale gas sites in England – Preston New Road, Lancashire and Kirby Misperton, North Yorkshire. The report should be read in conjunction with previous reports freely available through the project website<sup>1</sup>. These provide additional background to the project, presentation of earlier results and the rationale for establishment of the different elements of the monitoring programme.

# Acknowledgements

The work reported here has been enabled through a combination of BGS National Capability funding and a grant awarded by the UK Government's Department for Business, Energy & Industrial Strategy (BEIS). Additional benefit-in-kind contributions have also been provided by the project partners.

The authors would like to acknowledge the support provided by a wide range of organisations, community groups and individuals that have allowed the sampling teams to continue to undertake their work in the Fylde and the Vale of Pickering.

---

<sup>1</sup> [www.bgs.ac.uk/research/groundwater/shaleGas/monitoring/home.html](http://www.bgs.ac.uk/research/groundwater/shaleGas/monitoring/home.html)

# Contents

<b>Foreword.....</b>	<b>v</b>
<b>Acknowledgements .....</b>	<b>v</b>
<b>Contents .....</b>	<b>vi</b>
<b>Summary.....</b>	<b>20</b>
<b>1 Seismicity .....</b>	<b>24</b>
1.1 Introduction .....	24
1.2 Background.....	25
1.3 Network Performance .....	25
1.4 Station Noise and Performance .....	26
1.5 Data Processing and Analysis.....	29
1.6 Seismicity induced by hydraulic fracturing operations at Preston New Road, Lancashire, 2018 .....	31
1.7 Summary of operations .....	31
1.8 Event Detection and Location .....	32
1.9 Magnitude Uncertainty.....	34
1.10 Activity rates and magnitude of completeness .....	35
1.11 Evaluation of ground motions for induced seismicity .....	35
1.12 Better discrimination of man-made events .....	36
1.13 Data Availability.....	37
1.14 Conclusions .....	38
1.15 References .....	39
<b>2 Water quality monitoring .....</b>	<b>41</b>
2.1 Introduction and Summary .....	41
2.2 Water quality monitoring in the Vale of Pickering.....	41
2.3 Groundwater monitoring at KMA .....	43
2.4 Groundwater monitoring at Preston New Road, Lancashire.....	50
2.5 Multilevel samplers.....	53
2.6 Real-time monitoring .....	54
2.7 Statistical modelling of groundwater and surface water measurements .....	55
2.8 Summary of baseline: Vale of Pickering and The Fylde .....	67
2.9 References .....	69
<b>3 Ground Motion .....</b>	<b>71</b>
3.1 Introduction .....	71
3.2 Vale of Pickering SAR dataset .....	73
3.3 Lancashire SAR dataset .....	74
3.4 Vale of Pickering Ground Motion Baseline .....	74
3.5 Lancashire Ground Motion Baseline .....	83

3.6	Discussion.....	108
3.7	Lancashire Baseline .....	108
3.8	Conclusions .....	109
3.9	Acknowledgements.....	110
3.10	References .....	110
<b>4</b>	<b>Atmospheric composition.....</b>	<b>112</b>
4.1	Introduction .....	112
4.2	Summary of monitoring activities .....	112
4.3	Analysis and discussion .....	114
4.4	Mobile Methane Measurement Surveys.....	125
4.5	Summary of Mobile Surveys Since 2016.....	138
4.6	References .....	140
<b>5</b>	<b>Air Quality.....</b>	<b>141</b>
5.1	Introduction .....	141
5.2	The baseline dataset .....	141
5.3	Results and discussion.....	141
5.4	Methane event at LP .....	161
5.5	Mobile Surveys .....	162
5.6	Conclusions .....	166
5.7	References .....	167
<b>6</b>	<b>Radon.....</b>	<b>168</b>
6.1	Introduction .....	168
6.2	Indoor radon monitoring .....	169
6.3	Outdoor radon monitoring.....	170
6.4	Monitoring at the KMA enclosure.....	174
6.5	Comparison of Year 1, Year 2 and Year 3 results .....	175
6.6	Conclusions .....	176
6.7	References .....	177
<b>7</b>	<b>Soil gas .....</b>	<b>178</b>
7.1	Introduction .....	178
7.2	Site selection.....	178
7.3	Monitoring activities .....	178
7.4	Results and discussion.....	179
7.5	Geostatistical analysis of sampling requirements for soil gas survey measurements.....	196
7.6	summary and Conclusions (soil gas) .....	200
7.7	References .....	205
	<b>Appendix A.....</b>	<b>207</b>
	Abstract to Shaw et al. (2019): .....	207
	Abstract to Lowry et al. (submitted): .....	207

Abstract to Allen et al. (2019): .....	208
Abstract to Purvis et al. (2019): .....	208
<b>Appendix B .....</b>	<b>209</b>
Baseline statistics for PNR and KM.....	209
GHG change detection algorithm .....	210
7.8 Summary of greenhouse gases .....	210
<b>Appendix C .....</b>	<b>220</b>
Water quality baseline statistics.....	220

## FIGURES

Figure 1. Seismic monitoring network in the Vale of Pickering (a) and of the Fylde peninsula (b). In (a), red squares are surface sensors and orange squares borehole sensors. There are also surface sensors co-located with some of the borehole sensors. In (b), red squares are BGS sensors and blue squares are Liverpool University operated sensors. The yellow stars shows the surface positions of the KM8 and PNR-1Z wells. ....	25
Figure 2. Data completeness for the period 1/4/2018 to 31 /3/2019 for monitoring stations in the Vale of Pickering (AU07-AU20) and Blackpool (AQ02-AQ12).....	26
Figure 3. Median noise levels at three selected stations in the Vale of Pickering network as a function of frequency for 2016, 2017 and 2018. All thee sensors are at the surface. ....	27
Figure 4. Observed RMS noise levels determined from power spectral density estimates for each day over the time period 01/04/2016 to 31/03/2017.....	27
Figure 5. Modelled detection capability using observed noise levels for each station in (a) uniform, (b) low, (c) median and (d) high noise conditions. A signal in excess of three times the noise level is required at five or more stations for an earthquake to be detected. ....	28
Figure 6. Natural and anthropogenic seismic activity in 100 km squares centred on Kirby Misperton (a) and Preston New Road (b). Earthquakes in the time period from 1/4/2018 to 31/3/2019 are marked by yellow circles. Circles are scaled by magnitude. The locations of the shale gas wells are marked by green stars.....	29
Figure 7. Seismic events in the Vale of Pickering region. Yellow stars show events detected between 1/4/2017 and 31/3/2018. Red and orange squares show the positions of surface and borehole sensors, respectively. Nearly all detected events are of a suspected explosive origin, i.e. quarry blasts.....	30
Figure 8. Histograms showing the hour, (a), and the day, (b), of occurrence for all seismic events detected in the Vale of Pickering since the start of the project in 2015.....	31
Figure 9. (a) Map of events detected by the surface monitoring network during operations. Events are coloured by time and scaled by magnitude. The yellow star shows the surface position of the PNR-1z well. Map inset shows the location of the site. (b) Depth cross-section showing event depths along an east-west profile from A to A'. ....	32
Figure 10. Seismicity as a function of time during operations (red circles). Circles are scaled by magnitude. Blue lines show the cumulative volume of injected fluid during hydraulic fracturing operations. The magenta line shows the cumulative flow-back volume. No	

hydraulic fracturing was carried out between 3 November and 4 December as flow-back from the well took place. ....	33
Figure 11. Histograms showing the results of bootstrap resampling of the measured local magnitudes at each station for events with magnitudes greater than 0 ML. Red vertical lines show 95% confidence intervals and the median for each event. ....	34
Figure 12. Observed frequency magnitude distributions for the Preston New Road events (blue squares) and instrumentally recorded tectonic earthquakes across the British Isles from 1970 to present. The tectonic activity data are scaled to a time period of 57 days and for an area of 10 km by 10 km. The blue and red dashed lines show maximum likelihood estimates of the b-value and activity rate for each. ....	35
Figure 13. Schematic illustration of the evidence strength ratio (ESR) for an example with a relatively strong ESR. Gray shaded arrows show the maximum points available for each question given the best possible quality evidence. A total of 83 from 96 points could be scored, so the ESR is 87%. This figure is based on our scoring for the Newdigate sequence relative to the Horse Hill well as assessed after a full study of the sequence..	37
Figure 14. Schematic illustration of the induced assessment ratio (IAR). A total of 36 negative points and two positive points are scored, giving an IAR of $-34/43 = -79\%$ . Such a strongly negative indicates that the evidence points strongly toward these events not being induced by the industrial activity being examined. This figure is based on our scoring for the Newdigate sequence relative to the Horse Hill well as assessed after a full study of the sequence. ....	38
Figure 15. Temporal variation in concentrations of calcium, sodium, chloride and methane in groundwater from sites in the Superficial aquifer .....	42
Figure 16. Temporal variation in concentrations of calcium, sodium, chloride and methane in groundwater from sites in the Corallian aquifer.....	42
Figure 17. Temporal variation in concentrations of calcium, sodium and chloride in streamwater sites .....	43
Figure 18. Variations in concentrations of nitrate in streams (above) with regional rainfall for NE England and Vale of Pickering stream flows (Nb: Normanby; Ns: Ness; LM: Low Marishes; IB: Ings Bridge; CB: Costa Beck (Environment Agency) (below).....	44
Figure 19. Variations in calcium and chloride concentration in streamwater from Sites 10 and 30 with proximal stations in the Environment Agency's stream monitoring network (Pickering Beck in blue; Costa Beck in red) (rainfall also shown in green).....	44
Figure 20. Indicative monitoring data for redox potential, specific electrical conductance, iron, manganese, methane and methane/ethane ratio (C1/C2) in groundwater from KMA, analysed by BGS .....	45
Figure 21. Indicative monitoring data for pH, dissolved aluminium, potassium and methane in groundwater from KMA, analysis by BGS and Third Energy (Envireau Water, EW) 46	46
Figure 22. Monitoring data for calcium, magnesium, sulphate and manganese in groundwater from the five boreholes at KMA, analysis by BGS and Third Energy (Envireau Water, EW).....	48
Figure 23. Temporal variation in calcium and alkalinity in groundwater from the monitoring boreholes at PNR. Circles are BGS data, triangles Cuadrilla. The period of test hydraulic fracturing at borehole PNR-1z is also indicated.....	51

Figure 24. Temporal variation in arsenic and barium in groundwater from the monitoring boreholes at PNR. Circles are BGS data; triangles Cuadrilla .....	51
Figure 25. Temporal variation in methane and lithium in groundwater from the monitoring boreholes at PNR. Circles are BGS data; triangles Cuadrilla .....	52
Figure 26. Temporal variation in copper and lead in groundwater from the monitoring boreholes at PNR. Circles are BGS data; triangles Cuadrilla .....	53
Figure 27. Variations in dissolved methane concentration with depth and time in multilevel samplers installed in the Superficial/Kimmeridge formations in proximity to KMA (port depths given in metres in time-series plots).....	54
Figure 28. Real-time data for pH, SEC, temperature and water level in groundwater from five monitoring boreholes in the Vale of Pickering (2017-2019) .....	55
Figure 29. Boxplots of log transformed CH <sub>4</sub> (top left), log transformed Cl (top right), log transformed Na (bottom left) and NH <sub>4</sub> (bottom right) from 20 API sites investigated in this section (units: mg/L; µg/L for CH <sub>4</sub> ).....	58
Figure 30. (left): histogram of the standardised log(CH <sub>4</sub> ) data. (middle) Empirical spatial variogram (cut off at 2000 m); and (right) empirical temporal variogram (cut off at 6 sampling rounds) of the standardised data.....	60
Figure 31. The mean standardised time series and the adjusted 95% confidence band .....	61
Figure 32. (left) Histogram of the standardised log (Cl) data. (middle) Empirical spatial variogram (cut off at 2000m) and (right) empirical temporal variogram (cut off at 6 sampling rounds) of the standardised data.....	62
Figure 33. The averaged (over sites) time series and the adjusted 95% confidence band .....	62
Figure 34. (left) Histogram of the standardised log (Na) data. (middle) Empirical spatial variogram (cut off at 2000m) and (right) empirical temporal variogram (cut off at 6 sampling rounds) of the standardised data.....	63
Figure 35. The averaged (over sites) time series and the adjusted 95% confidence band .....	64
Figure 36. (left) Histogram of the standardised NH <sub>4</sub> data. (middle) Empirical spatial variogram (cut off at 2000m) and (right) empirical temporal variogram (cut off at 6 sampling rounds) of the standardised data.....	65
Figure 37. The averaged (over sites) time series and the adjusted 95% confidence band .....	65
Figure 38. Time series plots of the mean standardised log(CH <sub>4</sub> ) (top left), log(Cl) (top right), log(Na) (bottom left) and NH <sub>4</sub> (bottom right), along with the adjusted 95% (orange) and 99.7% (red) confidence bands from baseline models fitted to data up to July 2017.....	66
Figure 39. Geological map of the Vale of Pickering showing sampling locations used in this report. Insets shows boreholes close to Kirby Misperton and the shale gas well site (KM A). .....	68
Figure 40. Geological map of The Fylde showing sampling locations used in this report. Inset shows boreholes close to the shale gas well site (PNR). .....	68
Figure 41. ERS SBAS (a), ERS ISBAS (b) ENVISAT SBAS (c), ENVISAT ISBAS (d), Sentinel-1A SBAS (e) and Sentinel-1A ISBAS (f) results for the Vale of Pickering area, showing average rates of ground motion. Location of GNSS stations and InSAR reference point are indicated with a triangle and star, respectively. From Ward et al. (2017).....	76

Figure 42. InSAR SBAS (top) and ISBAS (bottom) analysis of ERS-1/2 satellite imagery (1992-2000) for the Vale of Pickering. Radar data supplied to BGS by ESA under grant id.31573. From Ward et al. (2017). .....	77
Figure 43. InSAR SBAS (top) and ISBAS (bottom) analysis of ENVISAT satellite imagery (2002-2009) for the Vale of Pickering. From Ward et al. (2017). .....	78
Figure 44. Average SBAS and ISBAS densities obtained for each land cover type from ERS, ENVISAT and Sentinel-1 results (CLC2012). From Ward et al. (2017). .....	79
Figure 45. Non-linear time series for selected ISBAS points. The solid lines represent the ISBAS non-linear vertical displacements for the different acquisitions and the dotted lines represent the GNSS linear and vertical displacements which were derived separately. It is worth noting that the InSAR time series reported were generated considering a linear displacement velocity in the temporal gaps between the ENVISAT and Sentinel-1A datasets. From Ward et al. (2017). .....	80
Figure 46. ISBAS InSAR results for the Pickering area of the Vale of York. Blue areas are undergoing uplift while green / yellow areas are stable. Dashed lines are geological faults. Solid black line is the trace of the section in Figure 47. Contains Ordnance Data © Crown Copyright and database rights 2017. ....	80
Figure 47. ISBAS InSAR results for the Pickering are of the Vale of York across the section identified in Figure 46. From Ward et al. (2017). .....	81
Figure 48. Bedrock geology and faults for the Pickering area of the Vale of York. Brown areas are clays from the quaternary glacial lake, green represents Chalk whilst the yellows and pinks to the North and South are the Coralline limestones and Calcareous Grits. From Ward et al. (2017). .....	82
Figure 49. ISBAS InSAR Time series for the Pickering (green) and Malton (blue) areas. From Ward et al. (2017). .....	82
Figure 50. InSAR processing using SBAS technique of ERS-1/2 data from 1992 to 2000. The red box outlines the extents of the Fylde study area. From Ward et al. (2018). .....	83
Figure 51. InSAR processing using ISBAS technique of ERS-1/2 data from 1992 to 2000. The red box outlines the extents of the Fylde study area. From Ward et al. (2018). .....	84
Figure 52. Areas of subsidence identified (in red) on the InSAR data in Leigh (outside of the Fylde study area) between 1992 and 2000. Black circle outlines the detailed time series results in Figure 53. From Ward et al. (2018). .....	85
Figure 53. Time series profiles of motion for 1996 to 2000. From Ward et al. (2018). .....	85
Figure 54. Areas of subsidence identified (in red) on the InSAR data in Blackpool between 1992 and 2000. Black circle indicates the location of boreholes in Figure 55. From Ward et al. (2018). .....	86
Figure 55. Scan of eight boreholes indicating the presence of ‘sand and peat’ at the top of the stratigraphy. For their location refer to Figure 54. ....	87
Figure 56. Sentinel 1 ascending average velocity (mm per year) ground motion results for May 2015 to February 2019; RapidSAR rural results .....	87
Figure 57. Sentinel 1 descending average velocity (mm per year) ground motion results for May 2015 to February 2019; RapidSAR rural results. ....	88
Figure 58. RapidSAR Sentinel-1 Ascending rural data showing uplift in Leigh to the west of Manchester. ....	89

Figure 59. RapidSAR Sentinel 1 Ascending rural data of the Ribble Estuary – at 1:150, 000 scale the subsidence seen in Figure 58 is not as apparent.....	90
Figure 60. RapidSAR Sentinel Sentinel-1 Ascending high-resolution data for the PNR site. [1] denotes the location of an underground reservoir.....	92
Figure 61. RapidSAR Sentinel Sentinel-1 Ascending high-resolution data for the PNR site. [1] denotes the location of an underground reservoir.....	92
Figure 62. RapidSAR Sentinel 1 Ascending high-resolution data for the metal covered underground water reservoir. ....	93
Figure 63. Ascending time series for points in the centre of the reservoir shown in Figure 62. ....	93
Figure 64. Descending time series for points in the centre of the reservoir shown in Figure 62. ....	94
Figure 65. Environment Agency groundwater monitoring sites in relation to PNR. ....	95
Figure 66. Ascending ground motion time series compared to groundwater levels for Crow Lady Farm. © Environment Agency and database right 2019.....	95
Figure 67. Ascending ground motion time series compared to groundwater levels for ‘BNFL’. © Environment Agency and database right 2019.....	96
Figure 68. Ascending ground motion time series for points in the centre of Manchester. ....	97
Figure 69. The original time series from the RapidSAR ascending data and the observed signal after the removal of the main cyclical components.....	97
Figure 70. Re-referenced ascending time series for points in the centre of the reservoir shown in Figure 62. ....	98
Figure 71. ISBAS Sentinel 1 descending average velocities for the Flyde (projected to the vertical). ....	99
Figure 72. ISBAS Sentinel 1 descending time series for points on the golf course the south of Blackpool (northern most circle in Figure 71). ....	99
Figure 73. Ascending ground motion time series for the region around the PNR site, showing locations of time series shown in Figure 74.....	100
Figure 74. High resolution ascending time series for points highlighted in Figure 73, the top plot shows the entire Sentinel 1 time series, the lower plot shows more detail for the red box including the time series for the period of hydraulic fracturing activity (highlighted by the green box). ....	101
Figure 75. Ground motion average velocity points closest to the PNR site as derived from ERS data, 1992 – 2000. Circle highlights points for which time series are shown in Figure 76. ....	102
Figure 76. Ground motion time series for the points closest to the PNR site as derived from ERS data, 1992 – 2000. ....	102
Figure 77. RapidSAR InSAR points displayed according to average velocity and seismic events in the PNR vicinity in October – December 2018.....	103
Figure 78. RapidSAR InSAR time series for the points highlighted by red circle in Figure 77. The top plot shows the full raw time series and the bottom plot shows the raw time series	

for the period of activity. On both plots the black line indicates the date of the closest recorded seismic event (25/10/2018).....	104
Figure 79. RapidSAR InSAR time series for the points highlighted by yellow circle in Figure 77. The black line indicates the date of the seismic events closest to these points (18/10/2018-23/10/2018). .....	104
Figure 80. Top: strength of seismic events denoted by size of circle; bottom: InSAR time series for the points highlighted by red circle. Black line on graph indicates date of seismicity. ....	105
Figure 81. ISBAS Sentinel-1 descending time series for points on the PNR site (points highlighted by black rectangle). .....	106
Figure 82. ISBAS Sentinel-1 descending points and magnitude of seismic events. ....	107
Figure 83. ISBAS Sentinel 1 descending time series at the location of strongest seismic event (yellow arrow in Figure 80). ....	107
Figure 84. Map showing the location of the measurement station at PNR relative to the Cuadrilla operated unconventional shale gas extraction facility. Other notable infrastructure is also shown.....	113
Figure 85. Map showing the location of the measurement station on the KM8 shale gas site relative to the locality and other gas production infrastructure.....	114
Figure 86. Wind rose plots for the Preston New Road site showing wind speed and direction statistics. Data from three 12-month periods defined in Table 15 are shown. The radii of the paddles illustrate the percentage of total sampling time in each of the 12 wind direction cones (30 degree increments relative to true North) and the colour of the paddle shows the wind speed (see colour legend). ....	115
Figure 87. Wind rose plots for the Kirby Misperton site showing wind speed and direction statistics. Data from three 12-month periods defined in Table 15 are shown. The radii of the paddles illustrate the percentage of total sampling time in each of the 12 wind direction cones (30 degree increments relative to true North) and the colour of the paddle shows the wind speed (see colour legend). ....	116
Figure 88. Time series of one-hour averaged CH <sub>4</sub> mixing ratios measured at PNR for the three 12-month periods between 1 <sup>st</sup> February 2016 and 31 <sup>st</sup> January 2019.....	117
Figure 89. Time series plots of one-hour averaged CO <sub>2</sub> mixing ratios measured at PNR for three 12-month periods between 1 <sup>st</sup> February 2016 and 31 <sup>st</sup> January 2019.....	118
Figure 90. CH <sub>4</sub> concentration-frequency and wind rose plots showing CH <sub>4</sub> mixing ratios as a function of wind direction for the three 12-month periods. The radii of the paddles illustrates the percentage of total time in each of the 12 wind direction cones (30 degree sections relative to true North) and the colour of the paddle shows the CH <sub>4</sub> mixing ratio (see colour legend).....	119
Figure 91. CO <sub>2</sub> pollution rose plots showing CO <sub>2</sub> mixing ratios as a function of wind direction for three 12-month periods. The radii of the paddles illustrates the percentage of total time in each of the 12 wind direction cones (30 degree sections relative to true North) and the colour of the paddle shows the CO <sub>2</sub> mixing ratio (see colour legend)... ..	120
Figure 92. Monthly CH <sub>4</sub> percentile rose plots showing percentile ranges in CH <sub>4</sub> mixing ratios as a function of wind direction for 36 monthly-averaged periods between 1 <sup>st</sup> February 2016 and 31 <sup>st</sup> January 2019. The radii of the paddles show the percentile ranges of	

absolute CH <sub>4</sub> concentrations (see coloured scale) in each of the 36 wind direction cones (10 degree sections). .....	120
Figure 93. Monthly median (solid line) percentile mixing ratios of CH <sub>4</sub> and CO <sub>2</sub> at PNR over the three year measurement period. 5 <sup>th</sup> , 25 <sup>th</sup> , 75 <sup>th</sup> and 95 <sup>th</sup> percentile values are indicated by the transparent boxes and whiskers. ....	122
Figure 94. Time series plots of one-hour averaged CH <sub>4</sub> mixing ratios measured at KM for three 12-month periods between 1 <sup>st</sup> February 2016 and 31 <sup>st</sup> January 2019.....	123
Figure 95. Time series plots of one-hour averaged CO <sub>2</sub> mixing ratios measured at KM for three 12-month periods between 1 <sup>st</sup> February 2016 and 31 <sup>st</sup> January 2019.....	124
Figure 96. Monthly median percentile mixing ratios of CH <sub>4</sub> and CO <sub>2</sub> at KM over the three year measurement period. 5 <sup>th</sup> , 25 <sup>th</sup> , 75 <sup>th</sup> and 95 <sup>th</sup> percentile values are indicated by the transparent boxes. ....	125
Figure 97. Left: Very close up view of multiple survey passes, each point represents a single data point of CH <sub>4</sub> . Right: Downscaled data to give 10 m <sup>2</sup> averages from the point data depicting the average methane above background measured on the circuit around the shale gas site, darker colours represent higher average mixing ratios of CH <sub>4</sub> .....	127
Figure 98. Isotopic signatures and averaged enhanced methane mole fraction map in the area around the shale gas extraction site. Labels represent known sources and associated $\delta^{13}\text{C}_{\text{CH}_4}$ source signature determined from Miller-Tans analysis.....	128
Figure 99. Regional isotopic and averaged enhanced methane mole fraction map in the Fylde region. Labels represent known sources and associated $\delta^{13}\text{C}_{\text{CH}_4}$ source signature determined from Miller-Tans analysis.....	130
Figure 100. Overview map of ethane:methane ratios superimposed on the average enhanced methane mole fraction for the Fylde region. Labels represent known sources as examples. Light colours represent biogenic sources and darker colours more thermogenic sources of methane. ....	130
Figure 101. Overview map of ethane:methane ratios superimposed on the 10m <sup>2</sup> average enhanced methane mixing ratios for the local area around the shale gas extraction site. Labels show known sources of methane. Light colours represent biogenic sources and darker colours more thermogenic sources of methane. ....	131
Figure 102. Demonstrating the value of mobile continuous ethane and methane ratios, here we can see the sudden change in ratio as the vehicle goes through what may have been otherwise considered a continuous plume, but is in fact a change from a gas leak source to a landfill source in the centre of the map. ....	131
Figure 103. Ethane and methane ratios near the Treales gas offtake station and the nearby plume of methane from the local farm. The plume sources are easily distinguished using the ethane:methane ratios from the mobile measurements. ....	132
Figure 104. Ethane vs Methane for data collected across FY4 to FY9 using the Los Gatos UMEA instrument. Data is filtered to only include points where either CH <sub>4</sub> > 200ppb or C <sub>2</sub> H <sub>6</sub> > 50ppb. ....	133
Figure 105. Methane elevations above baseline measured in the Fylde during FY10, 15 <sup>th</sup> and 16 <sup>th</sup> January 2019.....	133
Figure 106. Methane elevations above baseline measured in the Fylde during FY11, 6 <sup>th</sup> and 7 <sup>th</sup> March 2019. The large peak observed on 6 March 2019 is the Midgeland closed landfill site, 2.8 km west of the PNR site. ....	134

Figure 107. Methane elevations above baseline measured in the Vale of Pickering on 18 <sup>th</sup> July 2018. Methane $\delta^{13}\text{C}$ measured in the bags collected is also shown. ....	135
Figure 108. Methane elevations above baseline measured in the Vale of Pickering on 5 <sup>th</sup> March 2019. ....	136
Figure 109. Ethane vs Methane for data collected across KM4 to KM9 using the Los Gatos UMEA instrument. Data is filtered to only include points where either $\text{CH}_4 > 200\text{ppb}$ or $\text{C}_2\text{H}_6 > 50\text{ppb}$ . ....	137
Figure 110. A rare southerly wind on 6 March 2019, allowed two separate peaks to be identified at the western and eastern sides of the Pickering gas offtake station when surveying outside of the perimeter fence. At further distances the plumes merge together and the availability of downwind roads meant that the plume could be traced 800-900m north of the site with more than 100 ppb $\text{CH}_4$ excess. ....	139
Figure 111. Phase 4 daily time series at the KM site for (a) $\text{O}_3$ , (b) $\text{NO}$ , $\text{NO}_2$ , $\text{NO}_x$ (c) $\text{PM}_{10}$ , $\text{PM}_{2.5}$ , $\text{PM}_4$ , $\text{PM}_{10}$ and $\text{PM}_{\text{Total}}$ .....	145
Figure 112. Phase 4 daily time series at the LP site for (a) $\text{O}_3$ , (b) $\text{NO}$ , $\text{NO}_2$ , $\text{NO}_x$ (c) $\text{PM}_{10}$ , $\text{PM}_{2.5}$ , $\text{PM}_4$ , $\text{PM}_{10}$ and $\text{PM}_{\text{Total}}$ .....	146
Figure 113. Diurnal variations at KM for (a) $\text{NO}_x$ and (b) $\text{PM}$ .....	148
Figure 114. Hebdomadal Cycles at KM for (a) $\text{NO}_x$ and (b) $\text{PM}$ .....	149
Figure 115. Annual cycles at KM for (a) $\text{NO}_x$ and (b) $\text{PM}$ .....	149
Figure 116. Polar plots for LP (a) $\text{NO}$ (b) $\text{NO}_2$ , (c) $\text{NO}_x$ , (d) $\text{PM}_{2.5}$ , (e) $\text{PM}_{10}$ .....	150
Figure 117. Diurnal variations at LP for (a) $\text{O}_3$ (b) $\text{NO}_x$ and (c) $\text{PM}$ .....	152
Figure 118. Hebdomadal Cycles at LP for (a) $\text{O}_3$ (b) $\text{NO}_x$ and (c) $\text{PM}$ .....	153
Figure 119. Annual cycles at KM for (a) $\text{O}_3$ , (b) $\text{NO}_x$ and (c) $\text{PM}$ .....	153
Figure 120. Polar plots for LP (a) $\text{O}_3$ , (b) $\text{NO}$ (c) $\text{NO}_2$ , (d) $\text{NO}_x$ , (e) $\text{PM}_{2.5}$ , (f) $\text{PM}_{10}$ .....	155
Figure 121. Polar plot for $\text{H}_2\text{S}$ in LP.....	155
Figure 122. Selected hydrocarbon boxplot of annual hydrocarbon mixing ratios measured at KM and LP during phase 4 (2018). Vertical bars are median values. The left and right edges of the box correspond to the 25 <sup>th</sup> and 75 <sup>th</sup> percentiles respectively. The horizontal whiskers show the largest or smallest values no further than 1.5 times the interquartile range respectively. Data beyond the end of the whiskers are not included here.....	157
Figure 123. Monthly variation in selected hydrocarbons at KM for 2018.....	158
Figure 124. Monthly variation in selected hydrocarbons at LP for 2018. ....	159
Figure 125. Baseline concentrations compared against four distinct operational phases (a) period mean values (Table 26) over each period and (b) hourly maximum peak values during each period. ....	159
Figure 126. Two LP operational phases compared to the corresponding baseline period from the previous year (a) period-averaged values and (b) hourly-maximum concentrations.....	160
Figure 127. A comparison of previous baseline values (2017), drill and frack phases filtered for air masses from NW, W and SW that passed over the well-site before arriving at the monitors. (a) average values for representative baseline period and each phase and (b) maximum 1-hour values for baseline and each phase. ....	161

Figure 128. NO and NO <sub>2</sub> from the 11 – 15 <sup>th</sup> January 2019 methane enhancement was observed at the LP monitoring station. ....	162
Figure 129. H <sub>2</sub> S measurements during the LP event .....	162
Figure 130. WACL Air Sampling Platform at the KMA Monitoring Site .....	163
Figure 131. Instrument layout in the van .....	164
Figure 132. Drive track coloured by CH <sub>4</sub> on 17/10/18. The red circle designates the position of the hydraulic fracturing site. ....	165
Figure 133. Drive track coloured by CH <sub>4</sub> on 18/10/18. ....	165
Figure 134. Measured mixing ratios of pollutants throughout the survey of the hydraulic fracturing site on 17/10/18 .....	166
Figure 135. Seasonal variation of average indoor radon concentrations in the area of Kirby Misperton and Little Barugh (KM_LB), Yedingham, Pickering and Malton .....	170
Figure 136. Outdoor radon sampling points in the Vale of Pickering .....	171
Figure 137. Average radon concentrations at the sampling points around Kirby Misperton. ....	172
Figure 138. Average radon concentrations at the sampling points around Yedingham. ....	172
Figure 139. Average radon concentrations at the sampling points around Pickering. ....	173
Figure 140. Average radon concentrations at the sampling points around Malton .....	173
Figure 141. Average radon concentrations at the sampling points in Oxfordshire.....	174
Figure 142. Time series of radon concentrations recorded by AlphaGUARD between April 2017 and April 2019 .....	175
Figure 143. Continuous time series plot of CO <sub>2</sub> flux from chambers 1, 2, 3 and 4, along with ground and chamber temperature, and 10 day period in March 2017 showing flux changes in response to diurnal cycles and weather events (inset).....	181
Figure 144. Individual time series plot of KM8 CO <sub>2</sub> flux from Chamber 1, along with ground temperature.....	182
Figure 145. Individual time series plot of KM8 CO <sub>2</sub> flux from Chamber 2, along with ground temperature.....	182
Figure 146. Individual time series plot of KM8 CO <sub>2</sub> flux from Chamber 3, along with ground temperature.....	182
Figure 147. Individual time series plot of KM8 CO <sub>2</sub> flux from Chamber 4, along with ground temperature.....	183
Figure 148. Summary of long term CO <sub>2</sub> flux at KM8, October 2016 to May 2018.....	183
Figure 149. Soil gas monitoring station appearance (left) and layout in 2017-18 (right).....	184
Figure 150. Summary of all continuous soil gas data from the monitoring station east of Kirby Misperton, August 2016 to January 2019. ....	185
Figure 151. Illustration of broad agreement between KM8 CO <sub>2</sub> flux and Kirby Misperton soil gas station CO <sub>2</sub> in soil gas from June 2017. ....	185
Figure 152. Geospatial distribution of CO <sub>2</sub> flux measured over three 2016 field surveys at Kirby Misperton. Top to bottom: June 2016, August 2016, October 2016.....	187

Figure 153 Compiled Vale of Pickering soil gas CO <sub>2</sub> (%), O <sub>2</sub> (%) and CH <sub>4</sub> (ppm) data, separated by site .....	188
Figure 154 Compiled Vale of Pickering soil gas data, all sites .....	189
Figure 155 Binary plot of soil gas compositions, Vale of Pickering, by survey .....	189
Figure 156. Geospatial distribution of CO <sub>2</sub> flux measured over two 2016 field surveys at Roseacre, dashed line denotes location of linear fault.....	190
7.4.8 Figure 157. Geospatial distribution of CO <sub>2</sub> flux measured over three field surveys at Preston New Road. Top to bottom: August 2015, September 2016, September 2018Lancashire: Soil gas .....	192
Figure 158. Compiled Lancashire soil gas CO <sub>2</sub> (%), O <sub>2</sub> (%) and CH <sub>4</sub> (ppm) data, separated by site. No CH <sub>4</sub> data are available for Site B.....	193
Figure 159. Compiled Lancashire soil gas data, all sites combined .....	193
Figure 160. Binary plot of soil gas compositions, Lancashire, by survey .....	194
Figure 161. Mobile laser CO <sub>2</sub> , September 2018 (upper panel) and December 2018 (lower panel). CO <sub>2</sub> values are concentration in ppm.....	195
Figure 162. Preliminary: Geospatial distribution of CO <sub>2</sub> flux measured at Preston New Road, April 2019 .....	196
Figure 163. Geostatistical prediction of log (CO <sub>2</sub> flux +0.2) with measurement locations denoted by black dots (left) and associated standard errors (right). Units are log(g m <sup>-2</sup> d <sup>-1</sup> ). .....	197
Figure 164. Maximum likelihood estimates of variograms for of log (CO <sub>2</sub> flux +0.2).....	197
Figure 165. Standard errors for spatial log (CO <sub>2</sub> flux +0.2) predictions at the centre of 81-point regular square grids of different sizes.....	198
Figure 166. Standard errors for spatial log (CO <sub>2</sub> conc +0.2) predictions at the centre of 81-point regular square grids of different sizes. Units are log (%). .....	199
Figure 167. Standard errors for temporal log (CO <sub>2</sub> flux +0.2) predictions at the time midway between two measurements as a function of time between measurements. ....	199
Figure 168. Standard errors for temporal log (CO <sub>2</sub> concentration +0.2) predictions at the time midway between two measurements as a function of time between measurements. ....	200
Figure 169. Example geospatial distribution of CO <sub>2</sub> flux at Kirby Misperton, from field survey June 2016. ....	202
Figure 170 Compiled 2015-2018 survey soil gas data for Vale of Pickering sites .....	202
Figure 171. Example geospatial distribution of CO <sub>2</sub> flux at Preston New Road, from field survey August 2015 .....	203
Figure 172. Compiled 2015-2018 survey soil gas data for Vale of Pickering sites .....	203
Figure 173. Summary of all continuous soil gas data from the monitoring station east of Kirby Misperton, August 2016 to January 2019. ....	204
Figure 174. Continuous time series plot of CO <sub>2</sub> flux from chambers 1, 2, 3 and 4, along with ground and chamber temperature, and 10 day period in March 2017 showing flux changes in response to diurnal cycles and weather events (inset).....	204

## TABLES

Table 1. Statistical summary data for the water monitoring boreholes at KMA (TE 51 data 2018 only). .....	<b>Error! Bookmark not defined.</b>
Table 2. Details of groundwater monitoring points at Preston New Road, Lancashire.....	50
Table 3. Means and standard deviations of log(CH <sub>4</sub> ) .....	60
Table 4. The fitted temporal random effect model .....	61
Table 5. Means and standard deviations of log(Cl) .....	61
Table 6. The fitted temporal random effect model .....	62
Table 7. Means and standard deviations of log(Na) .....	63
Table 8. The fitted temporal random effect model .....	64
Table 9. Means and standard deviations of NH <sub>4</sub> .....	64
Table 10. The fitted temporal random effect model .....	65
Table 11 Comparison of remote and in situ ground surface motion monitoring systems .....	72
Table 12. Analyses of InSAR processing for the Vale of Pickering. ....	73
Table 13. ERS-1/2 image metadata .....	74
Table 14. Sentinel-1 image metadata (Lancashire).....	75
Table 15. Details of the three 12-month measurement periods. ....	115
Table 16. Literature values for ethane:methane ratios. In Summary: <0.01 Probably Biogenic, >0.03 Probably Thermogenic. ....	129
Table 17. Isotopic signatures of the main methane sources seen on each campaign in the Fylde identified from Keeling plot analysis. On some campaigns different signatures were identified for cows in barns <sup>(a)</sup> and cows in fields <sup>(b)</sup> .....	134
Table 18. Isotopic signatures of the main methane sources seen on each campaign in the Vale of Pickering identified from Keeling plot analysis.....	137
Table 19. UK National air quality objectives .....	142
Table 20. Summary of annual statistics for KM and LP locations for various air pollutants and comparison against annual mean limit values * Ozone annual mean appears low due to missing summer data. ....	142
Table 21. Exceedance of UK air quality standards.....	143
Table 22. Phase IV wind sector averages at KM.....	147
Table 23. Phase IV wind sector averages at LP.....	151
Table 24. Summary of NMHC measurements for 2018 at KM, N = 36. All NMHC have an uncertainty of < 10% .....	156
Table 25. Summary of NMHC measurements for 2018 at LP, N = 37. All NMHC have an uncertainty of < 10%. ....	156
Table 26. Breakdown of the recent operation cycles at PNR..	<b>Error! Bookmark not defined.</b>
Table 27. Breakdown of time periods of different phases used to compare Drilling and Hydraulic fracturing against baseline conditions from similar periods in a previous year at LP.....	160

Table 28. WASP instrumentation .....	163
Table 29. Range and distribution of estimated annual average indoor radon measurements from December 2017 to December 2018.....	169
Table 30. Range and distribution of radon measurements made with AlphaGUARD and passive detectors in the KMA enclosure.....	175
Table 31. Overview of soil gas monitoring 2015-2019. *post-hydraulic fracturing, †data acquisition from the Kirby Misperton soil gas station is ongoing but can no longer be accessed remotely and requires manual download; March 2019 data will be reported in Phase 5. ....	179
Table 32. Summary of CO <sub>2</sub> flux data from soil gas surveys in Kirby Misperton. *negative value suggests soil acting as CO <sub>2</sub> sink.....	186
Table 33. Summary of CO <sub>2</sub> flux data from soil gas surveys in Lancashire. *negative value suggests soil acting as CO <sub>2</sub> sink.....	191
Table 34. Overview of soil gas monitoring 2015-2019. ....	201
Table 35. Summary of baseline CO <sub>2</sub> flux data from soil gas surveys in Kirby Misperton. *negative value suggests soil acting as CO <sub>2</sub> sink.....	201
Table 36. Summary of baseline CO <sub>2</sub> flux data from soil gas surveys in Lancashire. *negative value suggests soil acting as CO <sub>2</sub> sink.....	201
Table 37. Summary statistics for groundwater chemistry from the Third Energy monitoring boreholes at KMA (SEC µS/cm; Ba,Li: µg/L, all others: mg/L) .....	220
Table 38. Summary statistics for groundwater chemistry from the Superficial aquifer of the Vale of Pickering (n=25; units as for Table 1).....	221
Table 39. Summary statistics for groundwater chemistry from the Corallian aquifer around the margins of the Vale of Pickering (n=10; units as for Table 1).....	221
Table 40. Summary statistics for streamwater chemistry from the Vale of Pickering (n=12; units as for Table 1) .....	222
Table 41. Summary statistics for groundwater chemistry from the Cuadrilla monitoring boreholes at Preston New Road site (units as for Table 1) .....	222
Table 42. Summary statistics for groundwater chemistry from the Quaternary aquifer of the Fylde, Lancashire (n=30; units as for Table 1) .....	224
Table 43. Summary statistics for groundwater from the Sherwood Sandstone aquifer east of Woodsfold Fault (n=8; units as for Table 1).....	225
Table 44. Summary statics for streamwater chemistry from the Fylde, Lancashire (n=14; units as for Table 1) .....	225

# Summary

This report describes the results of activities carried out as part of the Environmental Monitoring Project (EMP) led by the British Geological Survey (BGS) in areas around two shale gas sites in England – Kirby Misperton (Vale of Pickering, North Yorkshire) and Preston New Road (Fylde, Lancashire). It focuses on the monitoring undertaken during the period April 2018–March 2019 but also considers this in the context of earlier monitoring results that have been covered in reports for earlier phases of the project (Phases I–IV)<sup>2</sup>.

The EMP project is a multi-partner project involving BGS together with Public Health England (PHE), University of Birmingham, University of Bristol, University of Manchester, Royal Holloway University of London (RHUL) and University of York. The work has been enabled by funding from a combination of the BGS National Capability programme, a grant awarded by the UK Government’s Department for Business Energy & Industrial Strategy (BEIS) and additional benefit-in-kind contributions from all partners.

The project comprises the comprehensive monitoring of different environment compartments and properties at and around the two shale-gas sites. The component parts of the EMP are all of significance when considering environmental and human health risks associated with shale gas development. Included are seismicity, ground motion, water (groundwater and surface water), soil gas, greenhouse gases, air quality, and radon.

The monitoring started before hydraulic fracturing had taken place at the two locations, and so the results obtained before the initiation of operations at the shale-gas sites represent baseline conditions. It is important to characterise adequately the baseline conditions so that any future changes caused by shale gas operations, including hydraulic fracturing, can be identified. This is also the case for any other new activities that may impact those compartments of the environment being monitored as part of the project.

In the period October 2018–December 2018, an initial phase of hydraulic fracturing took place at the Preston New Road (PNR) shale-gas site (shale gas well PNR1-z) in Lancashire. This was followed by a period of flow testing of the well to assess its performance (to end of January 2019). The project team continued monitoring during these various activities and several environmental effects were observed. These are summarised below and described in more detail within the report. The initiation of operations at the shale-gas site signified the end of baseline monitoring. At the Kirby Misperton site (KMA), approval has not yet been granted for hydraulic fracturing of the shale gas well (KM8), and so no associated operations have taken place during the period covered by this report. The effects on air quality arising from the mobilisation of equipment in anticipation of hydraulic fracturing operations starting was reported in the Phase III report, and in a recently published paper<sup>3</sup>. Following demobilisation

---

<sup>2</sup> Ward, R.S., Allen, G.; Baptie, B.J., Daraktchieva, Z., Jones, D.G., Jordan, C.J., Purvis, R.M., Smedley, P.L. 2016. *Environmental baseline monitoring - Vale of Pickering: Phase I - Final Report (2015/16)*. BGS Report, OR/16/002.

Ward, R.S., Smedley, P.L., Allen, G., Baptie, B.J., Daraktchieva, Z., Horleston, A., Jones, D.G., Jordan, C.J., Lewis, A., Lowry, D., Purvis, R.M., Rivett, M.O. 2017. *Environmental Baseline Monitoring Project. Phase II, Final Report*. BGS Report, OR/17/049.

Ward, R.S., Smedley, P.L., Allen, G., Baptie, B.J., Cave, M.R., Daraktchieva, Z., Fisher, R., Hawthorn, D., Jones, D.G., Lewis, A., Lowry, C., Luckett, R., Marchant, B.P., Miller, C.A., Purvis, R. and Wilde, S. 2018. *Environmental Baseline Monitoring: Phase III Final Report (2017-2018)*. BGS Report, OR/18/026.

<sup>3</sup> Purvis, R.M., Lewis, A.C., Hopkins, J.R., Wilde, S.E.; Dunmore, R. E.; Allen, G.; Pitt, J.; Ward, R. S 2019 Effects of ‘pre-fracking’ operations on ambient air quality at a shale gas exploration site in rural North Yorkshire, England. *Science of The Total Environment*, 673. 445-454.

of the equipment and its removal from the site, conditions returned to baseline and the on-going monitoring (reported in this report) is effectively a continuation of baseline monitoring.

**Atmospheric composition** (greenhouse gas and air-quality indicator composition) has continued to be monitored near the PNR and KMA shale gas sites. The initiation of operational activities at the PNR site has led to a shift in analytical focus from baseline monitoring to operational-phase monitoring. An algorithmic method has been developed<sup>4</sup> for the identification of periods with elevated concentrations above the typical statistical range of baseline conditions. This facilitates an automated detection of periods/data of interest that may be related to greenhouse gas emissions events from the shale gas extraction facilities. The algorithm was used to determine that a period of enhanced CH<sub>4</sub> detected at the PNR monitoring site in January 2019 was related to emissions from the Cuadrilla shale gas extraction facility<sup>5</sup>. Slightly increased NO<sub>x</sub> concentrations were also observed at the same time but there was no increase in H<sub>2</sub>S concentrations. However, there were no exceedances of any national air quality limits recorded during the period of hydraulic fracturing and associated activities.

Mobile surveys continue to detect fugitive emissions from a variety of sources in the Fylde and Vale of Pickering areas. Many of these have persisted over the last three years. They include gas mains network leakages, landfills and farms. The larger gas mains leaks can be detected, along with landfills up to 1 km downwind and farms up to 500 m downwind. Each has a distinctive isotopic signature that is expected to be different to a shale gas source, allowing a differentiation to be made should a release occur and be detected. None was detected during any of the mobile survey campaigns. A notable change occurred in the characteristics of two landfills (one in the Fylde and the other in the Vale of Pickering) which have recently closed. Emissions have reduced due to capping and the isotopic signatures have changed, reflecting increased methane oxidation<sup>6</sup>.

Measurement of **radon in air** continues at about 110 homes in the Vale of Pickering with results indicating distributions of indoor radon concentrations consistent with the usual log-normal distribution for indoor radon in the UK. The results for Kirby Misperton and Little Barugh area are consistent with their status as not being radon Affected Areas. In Yedingham, also an area with low radon potential, all measurements are below the Action Level (200 Bq m<sup>-3</sup>) except for one house which had results that were above the Action Level on more than one occasion.

The results for Pickering and Malton confirmed their status as a radon Affected Areas with radon concentrations up to 350 Bq m<sup>-3</sup> measured in Pickering. Several homes were found to have results exceeding the Action Level. All householders were given standard advice on any action required; those with high radon levels were given additional information on reducing their radon concentrations. Results indicated that there is little seasonal variation in measurements made in homes in the areas of Kirby Misperton and Little Barugh, and also in Yedingham. The seasonal variation observed in Pickering was higher. All areas follow the

---

<sup>4</sup> Shaw, J., Allen, G., Pitt, J., Mead, M.I., Purvis, R.M., Dunmore, R., Wilde, S.E., Shah, A., Barker, P., Bateson, P., Bacak, A., Lewis, A.C., Lowry, D., Fisher, R.L., Lanoiselle, M., Ward, R. S. 2019. A baseline of atmospheric greenhouse gases around prospective UK shale gas sites. *Science of The Total Environment*, 684. 1-13.

<sup>5</sup> Allen, G., Shaw, J., Shah, A., Pitt, J., Ricketts, H., Williams, P., Ward, R.S 2019. Environmental baseline monitoring project: Methane enhancements detected at Little Plumpton air monitoring site. Nottingham, UK, British Geological Survey. <https://www.bgs.ac.uk/news/item.cfm?id=9410>.

<sup>6</sup> Lowry, D., Fisher, R.E., France, J.L., Coleman, M., Lanoisellé, M., Zazzer, G., Nisbet, E., Shaw, J.T., Allen, G., Pitt, J., Ward, R.S. 2019. Environmental baseline monitoring for shale gas development: Identification and geochemical characterisation of local source emissions of methane to atmosphere. *Science of The Total Environment*. In review.

normal seasonal pattern in the UK with the highest radon concentrations in winter and lowest radon concentrations in summer.

For outdoor radon, measurements indicate that radon concentrations in the Vale of Pickering have varied over time, reaching up to 1.5 times those observed from previous studies in the area. There is no indication of elevated outdoor radon concentrations in the Pickering or Malton radon Affected Areas, relative to those that are not radon affected. The analysis of results for the control site in Oxfordshire also showed no significant increases. Results from an active monitor and passive detectors, placed at the KMA site are in good agreement with the average outdoor radon concentrations within the area of Kirby Misperton village.

Over the baseline monitoring period, a range of techniques has been used to measure *soil gas* and characterise baseline conditions around the PNR and KMA sites. Gas composition analysis indicates that baseline CO<sub>2</sub> primarily originates from biological processes in the shallow subsurface, with a smaller contribution from the oxidation of CH<sub>4</sub>, depending on the time of year. An initial estimate of the baseline CO<sub>2</sub> flux and soil gas has been developed.

The challenge with soil gas measurement in survey mode is weather dependency. The pragmatic optimum season for UK soil gas surveys has been found from the long-term monitoring to be autumn; winter campaigns in the UK typically yield limited useful data because moisture conditions mean that soil gas becomes trapped and flux to atmosphere is impeded. Statistical analysis of Vale of Pickering data suggests autumn campaigns are least sensitive to changes in grid spacing. Early summer is also favourable statistically; while variation in parameter values is higher overall (because of the growing season).

A rapidly-mobilised field campaign to identify any impact from the shale gas operational activities on soil gas close to PNR was a qualified success. While no discrete signature was detected that might be related to the shale gas activities, the diffuse spatial distribution of CO<sub>2</sub> across the survey area appeared to be constrained by field boundaries and was therefore more likely to be related to surface agricultural activities.

**Water-quality** monitoring under baseline conditions has continued during the Phase IV period in the Fylde area and Vale of Pickering. Spatial variability in chemical composition continues to be large; temporal variability is also large for streamwater, but compositions are more consistent for groundwater.

High baseline concentrations of methane are a consistent feature in the Vale of Pickering, with maxima of 78 mg/L observed in the shallow groundwater. The monitoring is now revealing some notable seasonal variations in groundwater chemistry in the shallow aquifers and this highlights the need for baseline monitoring to be undertaken for a sufficiently long period of time to capture this temporal variability in baseline conditions. For the deeper groundwater, seasonal variability is not apparent, but concentrations of several analytes have decreased consistently over the period of monitoring, taking some two years to reach a steady-state composition. This is believed to be due to the challenges of purging and sampling deep boreholes. This indicates a need for time-series data of greater than 12 months to assess the baseline condition adequately in such circumstances.

A statistical approach predicting the distribution of the standardised space-time mean of analytes for the baseline condition has been proposed for distinguishing baseline from operational effects. From the limitations of the approach described, and as a cautionary principle, we recommend that apparently significant deviations from the baseline model be viewed as a recommendation for further investigation rather than as a definitive indicator of impact from hydrocarbon exploration activities.

Analysis of the water quality monitoring results for the Fylde area, including the PNR shale gas site, indicates that there was no change detected in water quality during the period of hydraulic fracturing and up to three months afterwards. However, any impacts on groundwater from sub-surface releases of pollutants/contaminants, if there have been any, are likely to take a considerable time until they are observed, and so long-term monitoring is necessary.

The networks of sensors measuring *seismicity* in both the Vale of Pickering and the Fylde have continued to operate with levels of data completeness of over 95%. Event detection capability is 0.5 ML or less.

A number of small local ( $\leq 100$  km away) seismic events have been detected in the Vale of Pickering which relate to quarry blasting. All of these events are in the daytime and have ranged from 1.0 ML to 2.3 ML.

At Preston New Road a combination of conventional, energy-transient detection algorithms along with template matching have been able to detect seismic events with magnitudes as low as -1.8 ML during the hydraulic fracturing operations using only surface sensors. The detected seismicity was strongly clustered in space and time, and closely associated with periods of fluid injection during hydraulic fracturing operations. Only a small number of “trailing” events were observed. Using a bootstrap approach to quantify magnitude uncertainty showed that the 95% confidence limits in the mean magnitudes for each event are at least  $\pm 0.1$  ML. The analysis found that the magnitude of completeness for events detected in near real-time without template matching is close to the 0.0 ML amber light threshold of the Traffic Light System, which further highlights the problem of reliable characterisation of induced seismicity during operations using surface monitoring networks alone.

A number of Ground Motion Prediction Equations (GMPs) have been tested to determine the most suitable. The Douglas et al. (2013) equation was found to be the most suitable, although it can over-estimate ground motion variability. Shale-gas-related ground motion intensities were also found to be consistently higher than those from a sequence of natural earthquakes and are similar to or lower than those from a sequence of mining induced events.

Previous reports have presented an analysis of baseline *ground motion* across the Fylde and the Vale of Pickering. This analysis has shown that overall the areas have been stable. In each area, natural and man-made ground motion is observed which is linked to compressible ground, groundwater level changes and underground mining activities.

During the Phase IV reporting period, further analysis has been carried out using satellite based InSAR for the period during and after hydraulic fracturing at the PNR site. A comparison of the time series in the Fylde for the period when hydraulic fracturing took place with the established baseline indicates that ground motion does not differ from that observed in the baseline. Examination of the ground motion time series for points closest to seismic events also shows no significant motion at the time of the events.

The InSAR data therefore indicates that to date the hydraulic fracturing and associated activities at the PNR site have not produced measurable ground motion that can be attributed to the shale gas activities within the time period of the monitoring. Also, there is no measurable ground motion linked to the specific seismic events which occurred in October, November and December 2018.

# 1 Seismicity

## 1.1 INTRODUCTION

The network of seismometers installed to monitor background seismicity in the Vale of Pickering, Yorkshire, and the Fylde Peninsula, Lancashire have continued to operate throughout the reporting period. All but three of the twenty stations show levels of data completeness that are over 95%. There was no significant change in recorded noise levels at any of the stations and the networks remained capable of events with magnitudes of 0.5 ML or less.

The monitoring networks successfully detected a number of small local seismic events at distances of 100 km away or greater. The proximity of many of the events in the Vale of Pickering to quarries where blasting is known to take place, along with recorded waveforms that are characteristic of a shallow source, suggests that all these events are quarry blasts. All the suspected blasts occurred during the daytime, which adds further evidence to an anthropogenic origin. The magnitudes of these events range from 1.0 ML to 2.3 ML.

We used the dense array of surface seismometers on the Fylde Peninsula to study the seismicity associated with hydraulic fracturing of the Carboniferous Bowland Shale at the Preston New Road site in late 2018. We used a combination of algorithms to detect seismic events with magnitudes as low as -1.8 ML during operations. The detected seismicity is strongly clustered in space and time, and is closely associated with periods of fluid injection. A small number of events were detected after injection was stopped (trailing events), but these ultimately decayed quickly to background levels. We quantified the uncertainty in the mean magnitudes for each event using a bootstrap approach and found 95% confidence limits of at least  $\pm 0.1$  ML. We also found that the magnitude of completeness for events detected in near real-time is close to the 0.0 ML amber light threshold, which highlights the problem of reliable characterisation of induced seismicity in real-time during operations using surface monitoring networks.

We tested the suitability of a number of existing ground motion prediction equations (GMPEs) for modelling the ground motions from seismic events induced by hydraulic fracturing of unconventional shale reservoirs. We find that the Douglas et al. (2013) equation is the most suitable, at least for the considered ground motion intensity measures, although it can over-estimate ground motion variability. We also found that the shale gas-related ground motion intensities are consistently higher than those from a sequence of natural earthquakes and are similar to, or lower than, those from a sequence of mining induced events.

While it was clear that the seismicity observed at Preston New Road was related to hydraulic fracturing operations, in other cases it might not be so clear. With this in mind, we have developed a new framework for assessing whether earthquakes occurring near to subsurface industrial activity have a natural cause or are induced. The new approach was applied to a sequence of earthquakes in the southeast of England not far from conventional hydrocarbon exploration and production operations. The conclusion was that the earthquakes were natural rather than induced. The criteria could also be applied retrospectively to historic baseline data to identify any induced events.

Processed event data (automatically determined and manually revised event parameters) are available from the BGS FTP site at <ftp://seiswav.bgs.ac.uk/events/>.

## 1.2 BACKGROUND

The primary aim of the seismicity work package is to deploy a network of seismic sensors to monitor background seismic activity in the vicinity of proposed shale gas exploration and production near Kirby Misperton, Yorkshire and Preston New Road, Lancashire. The data collected will allow reliable characterisation of baseline levels of natural seismic activity in the region. This will facilitate discrimination between any natural seismicity and induced seismicity related to future shale gas exploration and production. A further aim is to make recommendations for a suitable traffic-light system to mitigate earthquake risk. The initial design requirement for the seismic monitoring network was reliable detection and location of earthquakes with magnitudes of 0.5 and above within a 20 km by 20 km area around the shale gas sites.

## 1.3 NETWORK PERFORMANCE

The seismic monitoring network around Kirby Misperton consists of seven near-surface sensors (red squares in Figure 1(a)) and four sensors installed in boreholes (orange squares in Figure 1(a)). The latter comprise of three down-hole geophones and a down-hole broadband seismometer. The borehole sensors are situated at a depth of approximately 30 m below the surface and are all close to the Kirby Misperton drill site. Installing instruments in boreholes is intended to improve the signal-to-noise ratio of the recorded data and allow smaller events to be detected and located.

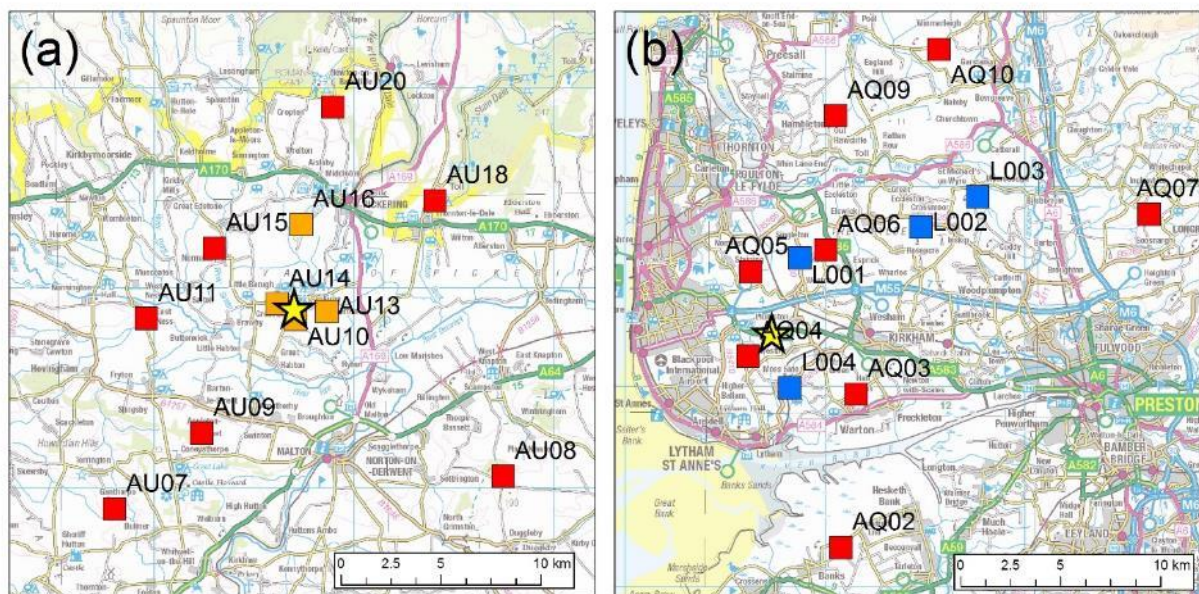


**Figure 1. Seismic monitoring network in the Vale of Pickering (a) and of the Fylde peninsula (b). In (a), red squares are surface sensors and orange squares borehole sensors. There are also surface sensors co-located with some of the borehole sensors. In (b), red squares are BGS sensors and blue squares are Liverpool University operated sensors. The yellow stars shows the surface positions of the KM8 and PNR-1Z wells.**

The seismic monitoring network around Preston New Road consists of eight near-surface sensors (red squares in squares in Figure 1(b)). Stations AQ05 and AQ06 were installed in March 2018 and September 2017, respectively. We also receive real-time data from four stations installed and operated by Liverpool University. The latter were installed independent of this project and data from these is not guaranteed.

Continuous data from all stations are transmitted in near real-time to the BGS office in Edinburgh, where the data are processed and archived. The completeness of these data can be easily checked to gain an accurate picture of network performance. The completeness levels are shown in Figure 2. All stations in the Vale of Pickering show high levels of data completeness for the time period 1/4/2018 to 31 /3/2019, with over 95% available from all stations except AU10 and AU16, which were 94% and 89% complete, respectively. Only one station in Lancashire had data completeness of less than 95%, AQ10, which was 94% complete.

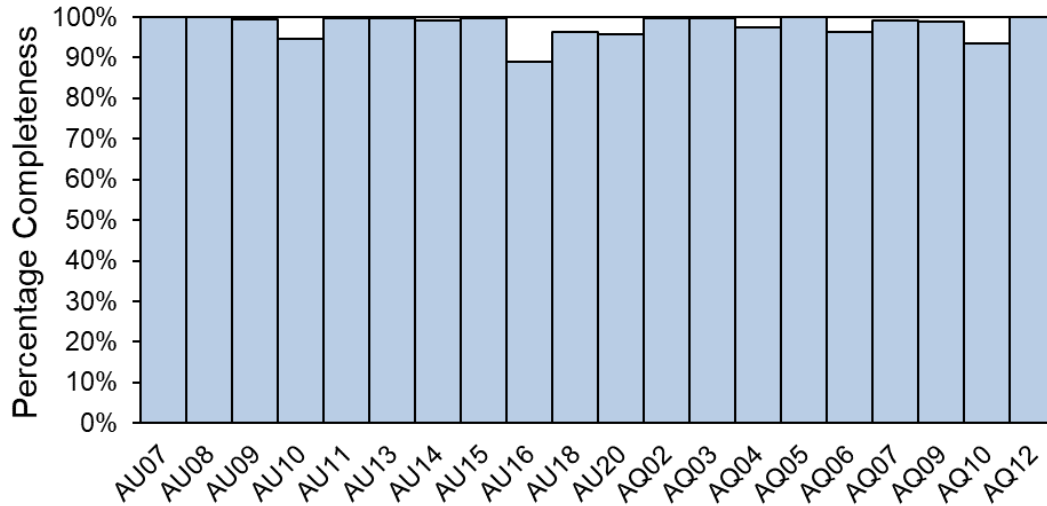


**Figure 2. Data completeness for the period 1/4/2018 to 31 /3/2019 for monitoring stations in the Vale of Pickering (AU07-AU20) and Blackpool (AQ02-AQ12).**

This means that the detection capability of both networks was good over this time period and loss of data was minimal. The level of data completeness is a similar to the values for previous years. A value of over 95% is extremely good for data transmitted in near real-time using mobile phone networks and is better than many of the BGS permanent monitoring stations that use similar technology. Data losses result from failure of outstation hardware, communications problems, or failure of central data processing. The data acquisition is able to recover from short breaks in communications links to outstations by re-requesting missing packets of data from local data buffers, but failure of outstation hardware requires intervention by local operators or maintenance visits.

#### 1.4 STATION NOISE AND PERFORMANCE

We use power spectral density (PSD), calculated from one-hour segments of continuous data, to characterize noise levels at a range of frequencies or periods at each of the installed stations.

A statistical analysis of the PSDs yields probability density functions (PDFs) of the noise power for each of the frequency bands at each station and component. Figure 4 compares the median noise levels calculated at three stations in the Vale of Pickering network (AU08, AU13 and AU15) in three different time periods, 1/4/2016 to 31/3/2017 (solid lines), 1/4/2017 to 31/03/2018 (dashed lines) and 1/4/2018 to 31/03/2019 (dotted lines). Although there are clear differences in noise levels at different stations, the noise levels at each station do not change significantly in different time periods, demonstrating that there is no significant degradation in stations performance. This is also the case for the other stations in the network.

Comparing the median noise levels at the selected stations in the Vale of Pickering and Blackpool networks shows that the Blackpool stations are noisier than those in the Vale of

Pickering and most other stations in the BGS permanent network. This is because the Fylde Peninsula is densely populated, with many sources of cultural noise.

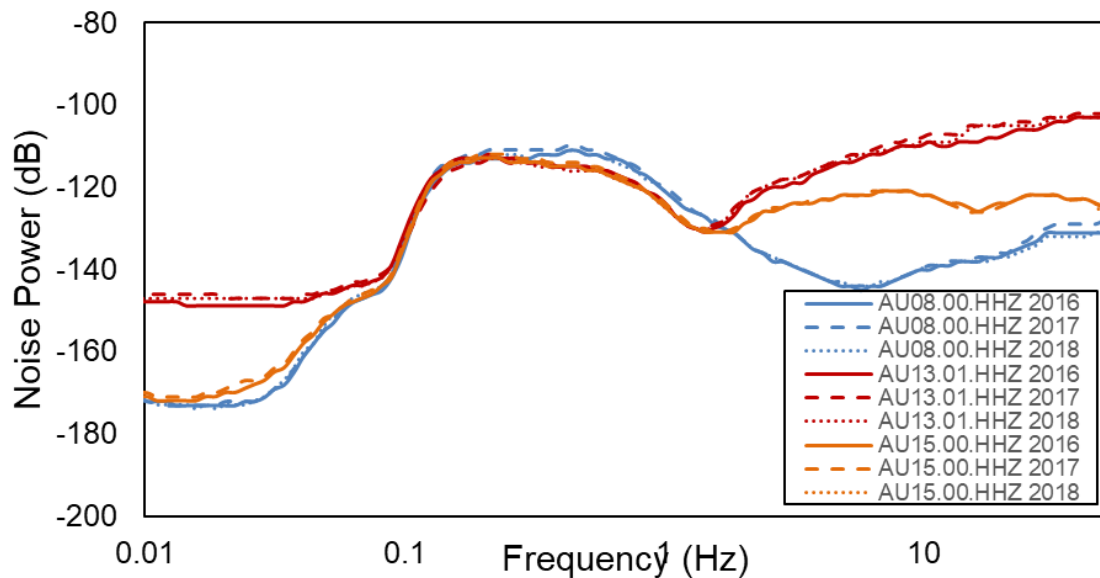


**Figure 4. Median noise levels at three selected stations in the Vale of Pickering network as a function of frequency for 2016, 2017 and 2018. All three sensors are at the surface.**

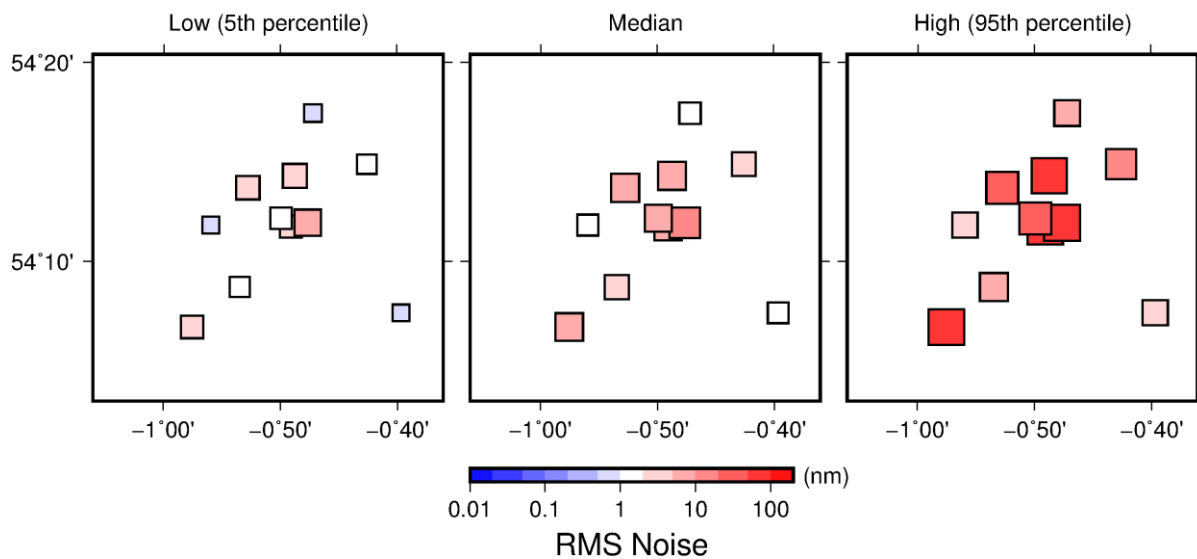


**Figure 3. Observed RMS noise levels determined from power spectral density estimates for each day over the time period 01/04/2016 to 31/03/2017.**

We use the median, 5th and 95th percentiles of the observed noise at each station to test the variation in the detection capability of the Vale of Pickering network in different noise conditions. First, we calculate the RMS amplitudes of ground displacement in a constant relative bandwidth of one decade for each station. The resulting RMS amplitudes for each station and for each percentile are shown in Figure 3. As before, we find that noise can vary significantly even for stations that are close together, with variations in RMS displacement

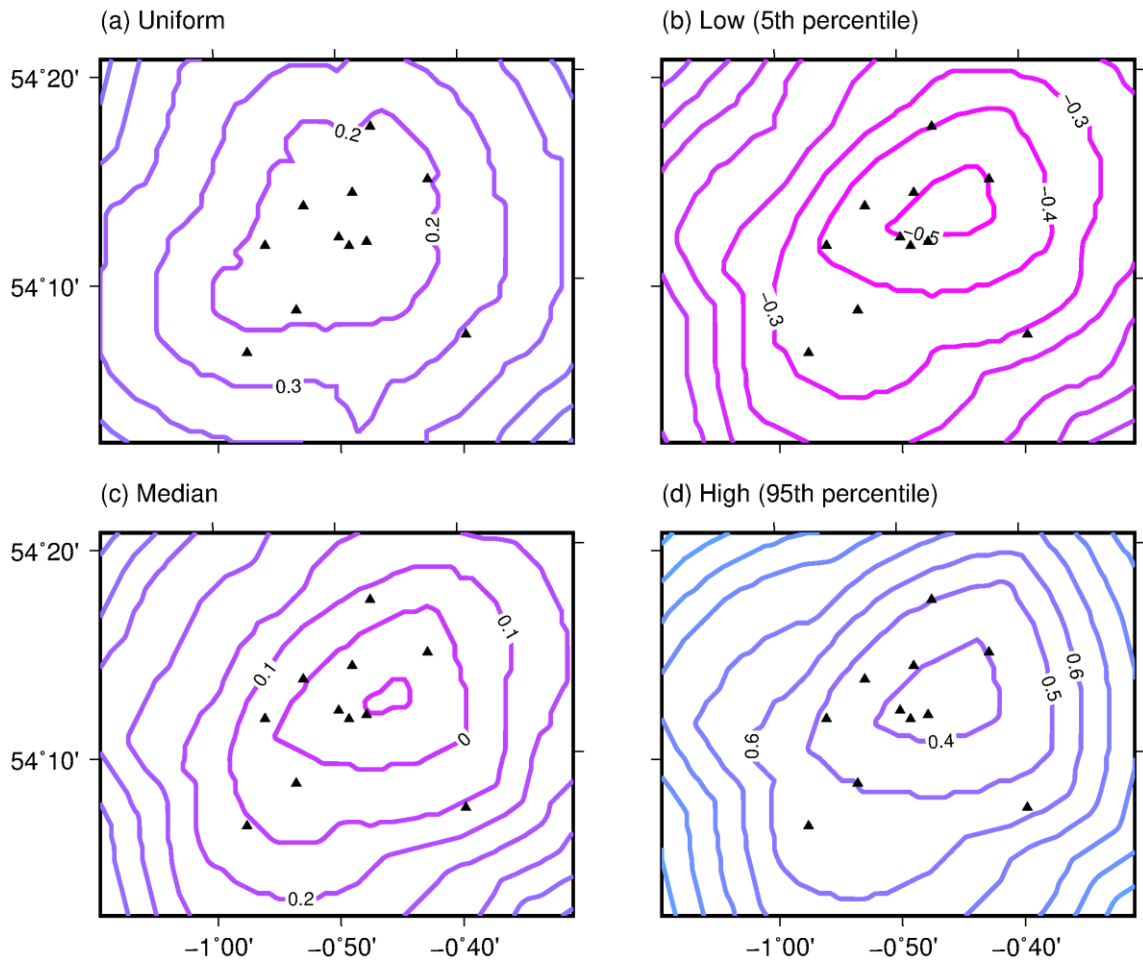


**Figure 5. Modelled detection capability using observed noise levels for each station in (a) uniform, (b) low, (c) median and (d) high noise conditions. A signal in excess of three times the noise level is required at five or more stations for an earthquake to be detected.**

amplitudes exceeding two orders of magnitude even in quiet conditions. We also find significant variation between low (5<sup>th</sup> percentile) and high (95<sup>th</sup> percentile) noise conditions, which suggests that detection capability will vary strongly with time.

We model the detection capability of the network in different noise conditions as follows:

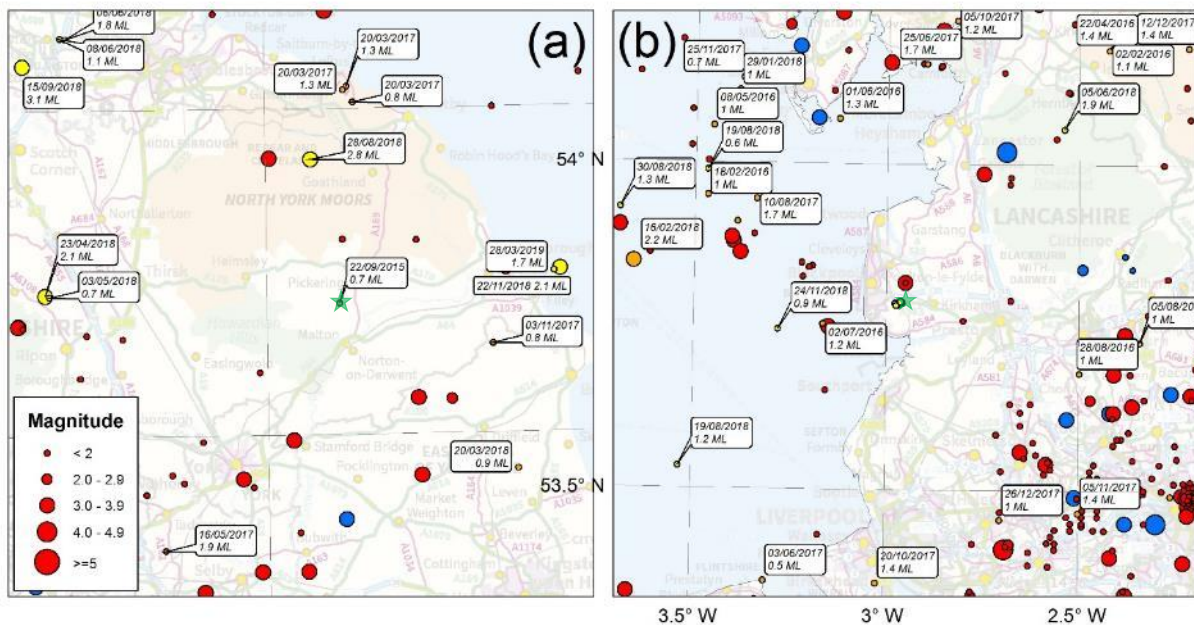
1. Divide the region into a regular grid of points.
2. For each grid point calculate the distances between the grid point and each station.
3. For each station calculate ground displacement amplitudes for different magnitudes.
4. Find the smallest magnitude value for which the signal amplitude exceeds the noise amplitude by a factor of three at five or more stations.

Figure 5 shows the variation in the magnitude of earthquakes that would be detected by the network in different noise conditions. In the quietest conditions (Figure 5b), the network is capable of detecting events with magnitudes as low as -0.5 ML, however, this is only the case 5% of the time. The lowest detectable magnitude increases to just under 0.0 ML in median noise conditions (Figure 5c). For the high noise model (Figure 5d), the network is still able to detect event with a magnitude of 0.5 ML close to the centre of the network.

## 1.5 DATA PROCESSING AND ANALYSIS

Continuous data from all installed stations are transmitted in real-time to the BGS offices in Edinburgh and have been incorporated in the data acquisition and processing work-flows used for the permanent UK network of real-time seismic stations operated by BGS. A simple detection algorithm is applied to the data from the Vale of Pickering and the Fylde peninsula, including data from permanent BGS monitoring stations in the region, to detect possible events. An experienced analyst has reviewed all detections.

Earthquake activity from the BGS earthquake catalogue in 100 km squares centred on the Kirby Misperton and Preston New Road sites is shown in Figure 6. Yellow circles show earthquakes in the time period from 1/4/2018 to 31/3/2019. Apart from a magnitude 0.7 ML earthquake close to Kirby Misperton on 22 September 2015 at the very start of the monitoring project, no other earthquakes have been detected in the immediate locality of the Vale of Pickering, however, a number of other earthquakes from the surrounding region, along with quarry blasts have been detected.



In the time period from 1/4/2018 to 31/3/2019, the closest earthquake to the network was a

**Figure 6. Natural and anthropogenic seismic activity in 100 km squares centred on Kirby Misperton (a) and Preston New Road (b). Earthquakes in the time period from 1/4/2018 to 31/3/2019 are marked by yellow circles. Circles are scaled by magnitude. The locations of the shale gas wells are marked by green stars.**

magnitude 2.8 ML earthquake near Fryup in North Yorkshire on 28 August 2018. The epicentre was approximately 25 km north of Kirby Misperton. A magnitude 2.1 earthquake was detected just off the coast of Scarborough on 22 November 2018, approximately 40 km west. This was followed by a magnitude 1.7 ML event on 28 March 2019, approximately 28 km east of Kirby Misperton. A magnitude 2.1 ML earthquakes was detected near Masham in North Yorkshire on 23 April 2018, approximately 50 km to the west.

A magnitude 3.1 ML earthquake near Newton Aycliffe was recorded on 15 September 2018, approximately 70 km northwest of Kirby Misperton. This earthquake occurred in an area where there has been little other recorded seismicity and it is the largest earthquake in this part of the UK since a magnitude 3.6 ML earthquake near Ripon in 2011. BGS received no reports of the earthquake being felt, perhaps because of the relatively deep focus of 24 km, which was well

constrained by the recent deployment of UKArray stations. A well constrained focal mechanism shows strike slip faulting on fault planes that strike either NNE-SSW or ESE-WNW.

Apart from the seismicity associated with hydraulic fracturing operations at Preston New Road, a number of earthquakes were detected in the Fylde Peninsula region in the period from 1/3/2018 to 31/3/2019. The closest of these to Preston New Road was a 0.9 ML earthquake in the Irish Sea on 24 November 2018, approximately 20 km west of the Preston New Road site. Three other events were detected offshore in the Irish Sea, the largest of which was a magnitude 1.3 ML event on 30 August 2018, 50 km west-northwest of Preston New Road the other detected earthquakes were at greater distances either to the north or south. Onshore, the largest event detected close to the network was a magnitude 1.9 ML event on 5 June 2018, approximately 40 km northeast of Preston New Road.

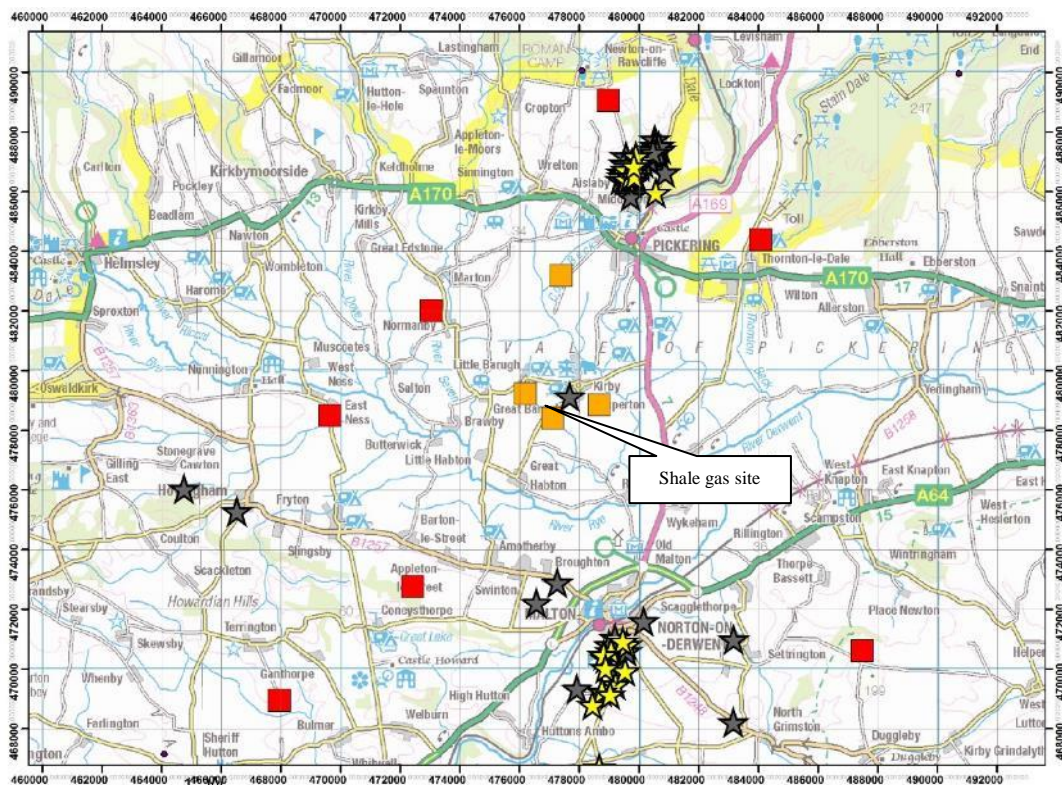


**Figure 7. Seismic events in the Vale of Pickering region. Yellow stars show events detected between 1/4/2017 and 31/3/2018. Red and orange squares show the positions of surface and borehole sensors, respectively. Nearly all detected events are of a suspected explosive origin, i.e. quarry blasts.**

A number of other events were detected in the Vale of Pickering. These are shown in Figure 7. The proximity of the calculated locations to quarries where blasting is known to take place, along with the recorded waveforms that are characteristic of a shallow source, suggests that all these events are of an explosive origin, i.e. quarry blasts. Fourteen events were detected in the time period from 1/4/2018 to 31/3/2019 that were located just north of Pickering in close proximity to the Newbridge quarry, where a number of other quarry blasts have been detected in the past three years. The magnitudes of these events range from 1.0 ML to 1.7 ML. Eleven blasts were detected close to a quarry south of Malton. The magnitudes for these events ranged from 1.5 to 2.3 ML.

All of the suspected blasts occurred during the working week during the day. Histograms showing the hour, (a), and the day, (b), of occurrence for all seismic events detected in the Vale of Pickering since the start of the project in 2015. Seventy-three of the ninety-two detected events occurred between 10am and 2pm. Similarly, eighty-seven of the ninety-two detected events occurred during the working week, with most of the events occurring on Tuesday, Wednesday and Thursday. The strong clustering of the events around the middle of the day provides further evidence of the man-made origin of these events, since we might expect natural seismicity to be more evenly distributed throughout the day.

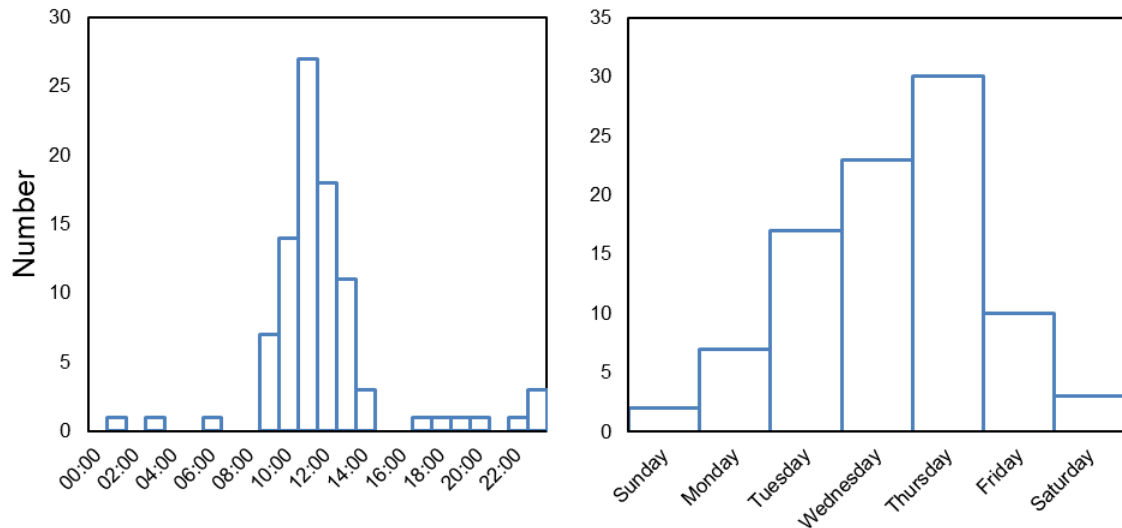


**Figure 8. Histograms showing the hour, (a), and the day, (b), of occurrence for all seismic events detected in the Vale of Pickering since the start of the project in 2015.**

## 1.6 SEISMICITY INDUCED BY HYDRAULIC FRACTURING OPERATIONS AT PRESTON NEW ROAD, LANCASHIRE, 2018

In late 2018, hydraulic fracturing of the of the Carboniferous Bowland Shale was carried out at the Preston New Road 1z (PNR-1z), approximately 4 km south of Preese Hall. Operations were accompanied by microseismicity, and despite the relatively modest injected volumes a number of events during operations exceeded the magnitude limit of 0.5 ML that requires operators to stop hydraulic fracturing. We used the dense array of surface seismic stations installed by BGS for baseline monitoring as well as stations installed by the operator, Cuadrilla Resources, to determine locations and magnitudes for the detected microseismicity. We find that the microseismicity is strongly clustered in space and time and is closely associated with periods of injection, with only a small numbers of “trailing” events. We used a bootstrap approach to quantify magnitude uncertainty and define confidence intervals for local magnitude estimates. We also estimated the magnitude of completeness for our catalogue and use this, along with the location and magnitude uncertainties to assess the suitability of the surface monitoring network for reliable characterization of the microseismicity. Finally, we calculated activity rates and recurrence parameters for the frequency-magnitude distribution and compared these to the background activity rates. This work will be published in Baptie and Luckett (2019).

## 1.7 SUMMARY OF OPERATIONS

The PNR-1 well targets the Bowland shale at a depth of approximately 2,300 m, and has a horizontal lateral section of 782 m extending in a westerly direction from the well pad. A

sliding-sleeve completion method was used, with 41 individual sleeves spaced at intervals of 17.5 m along the well. The hydraulic fracture plan allowed for up to 765 m<sup>3</sup> of fluid per sleeve. A “mini-frac” consisting of a few 10s of m<sup>3</sup> of fluid was pumped prior to each main stage. The sleeves were numbered from 1 to 41 proceeding from the toe (west) to the heel (east) of the well. A total of 15 sleeves were hydraulically fractured with an additional 18 mini-fracs between 16 October 2018 and 17 December 2018. The sleeves were used in the following order: 1, 2, 3, 12, 13, 14, 22, 30, 31, 32, 37, 38, 39, 40 and 41. The average injected volume for each fracture was 234 m<sup>3</sup> and the maximum injected volume was 431 m<sup>3</sup>. No hydraulic fracturing was carried out between 3 November and 4 December as flow-back from the well took place. Further information on the hydraulic fracturing operations for PNR-1z can be found on the OGA website<sup>7</sup>.

### 1.8 EVENT DETECTION AND LOCATION

Events were initially detected using the Carltrig STA/LTA algorithm (Johnson et al., 1995). To detect further low-magnitude seismicity, we selected a number of templates from the previously detected events then applied a cross-correlation template-matching algorithm (e.g. Schaff and Richards, 2004) to the continuous data from all stations. For this, we used template waveforms that incorporated both P- and S-waves from the events in the catalogue and cross-correlated these continuous data filtered at 2–20 Hz. Detections were made when the network-stacked cross-correlation sum exceeds nine times the median absolute deviation. We then manually re-picked and relocated positive detections.

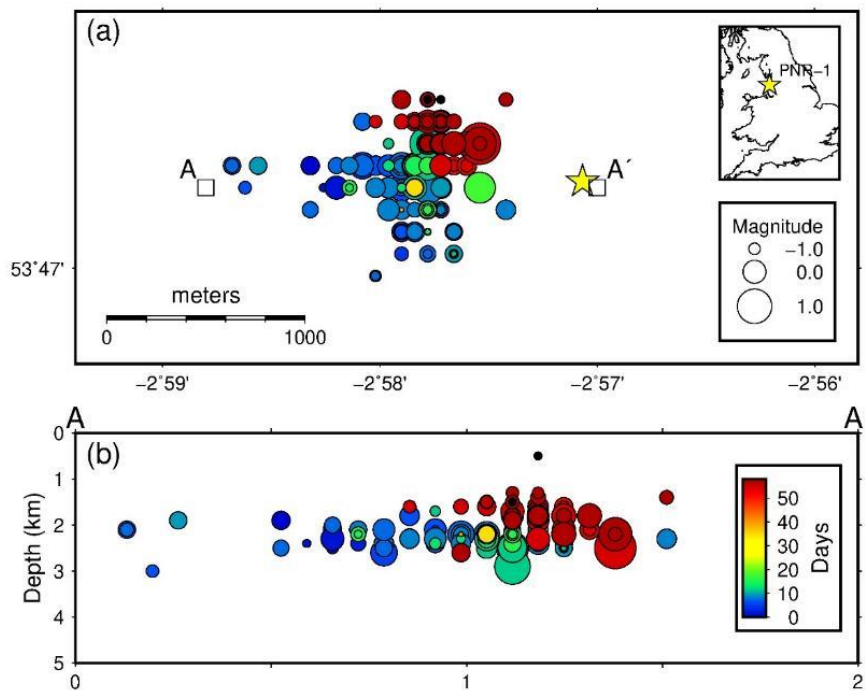


**Figure 9. (a) Map of events detected by the surface monitoring network during operations. Events are coloured by time and scaled by magnitude. The yellow star shows the surface position of the PNR-1z well. Map inset shows the location of the site. (b) Depth cross-section showing event depths along an east-west profile from A to A’.**

<sup>7</sup>[www.ogaauthority.co.uk/onshore/onshore-reports-and-data/preston-new-road-pnr-1z-hydraulic-fracturing-operations-data/](http://www.ogaauthority.co.uk/onshore/onshore-reports-and-data/preston-new-road-pnr-1z-hydraulic-fracturing-operations-data/)

We used the NonLinLoc (NLLoc) non-linear earthquake location algorithm (Lomax et al., 2009) to calculate hypocenters for the detected events. This algorithm provides robust constraints on location uncertainties compared with traditional single-event location codes.

A total of 57 microseismic events were detected in near real-time using the Carltrig STA/LTA algorithm. 22 of these had magnitudes greater than 0.0 ML, the amber TLS threshold and 7 had magnitudes greater than the TLS limit of 0.5 ML. The largest event had a magnitude of 1.6 ML and was felt by a few people close to the site. The smallest event detected in near real-time had a magnitude of -0.9 ML and was a “trailing” event, i.e. it occurred after operations had stopped, in this case at night time, when background noise levels were lower than during the working day. The cross-correlation template-matching algorithm identified a further 115 events related to hydraulic fracturing operations, all with magnitudes of less than 0.0 ML.

Locations for all detected events and calculated using NLLoc are shown in Figure 9. Events are coloured by time and move from west to east corresponding to different stages of hydraulic fracturing in the horizontal well PNR-1. Event depths are around 2 km, but decrease slightly from around 2.3 km at the toe of the well to approximately 1.8 km closer to the heel. Horizontal errors varied from around 400 to 750 m, with events better constrained in latitude than longitude. Depth errors varied from 500 m to 1 km. Note that the operator derived a new velocity model during operations in an effort to improve location estimates. This model is used for all locations shown in this report.

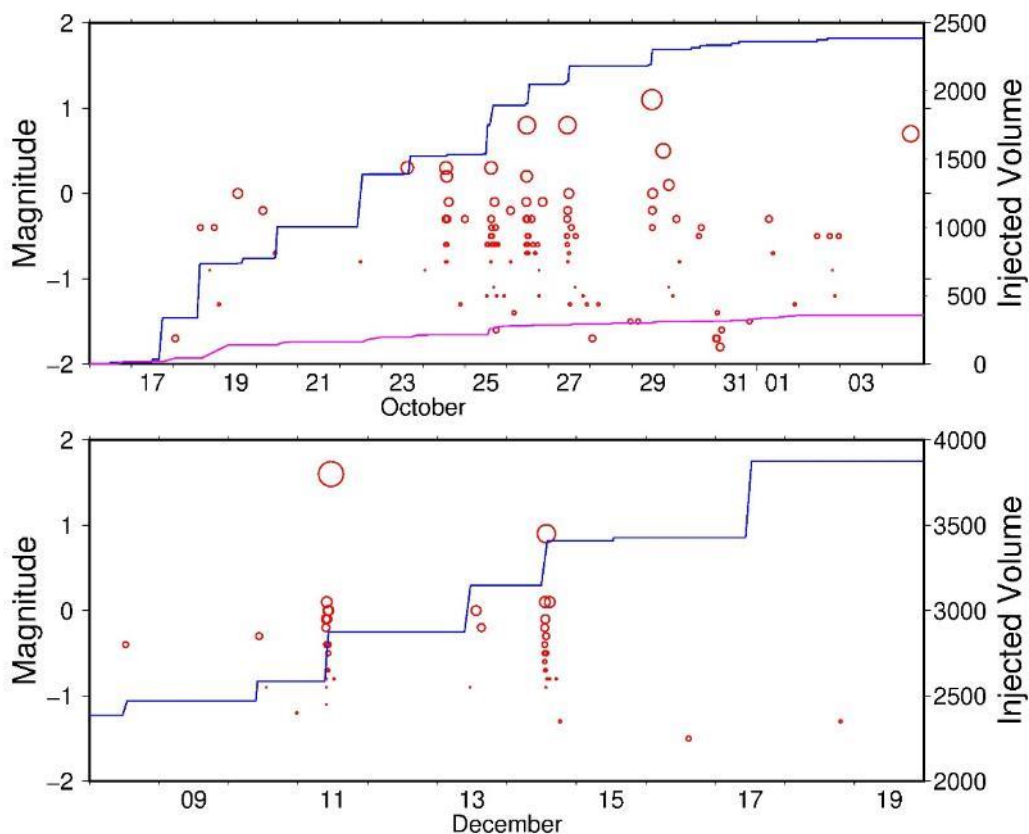
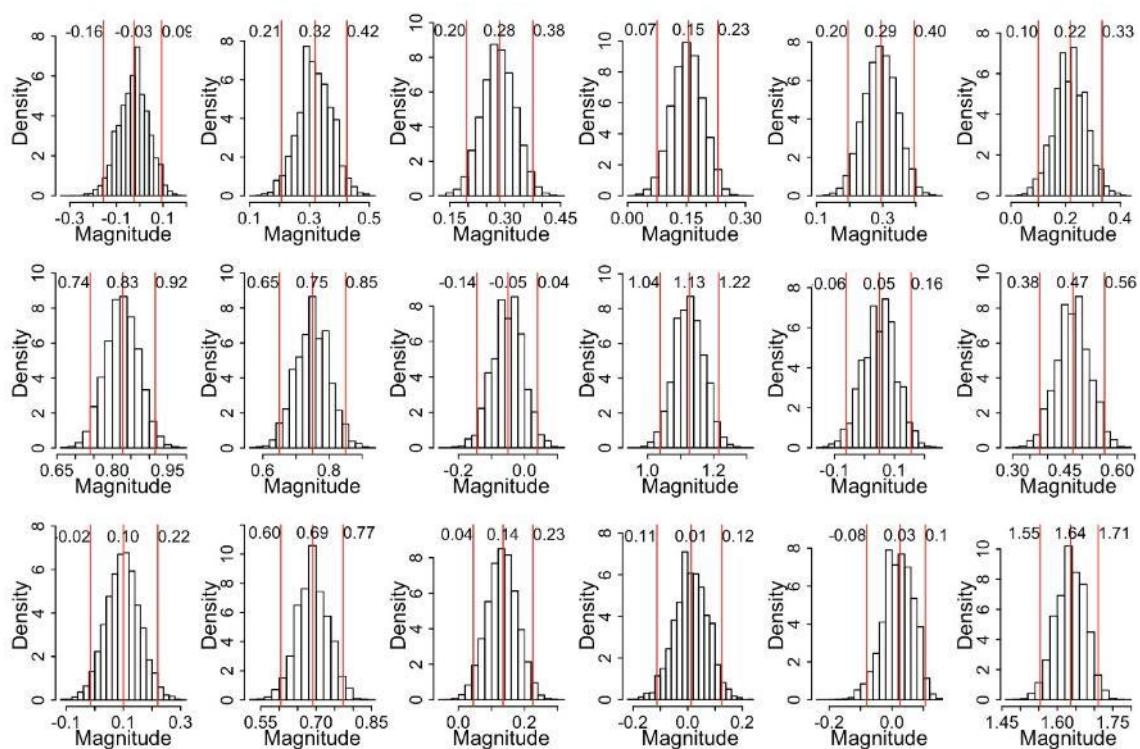


**Figure 10. Seismicity as a function of time during operations (red circles). Circles are scaled by magnitude. Blue lines show the cumulative volume of injected fluid during hydraulic fracturing operations. The magenta line shows the cumulative flow-back volume. No hydraulic fracturing was carried out between 3 November and 4 December as flow-back from the well took place.**

Figure 10 shows detected seismicity as a function of time during operations (red circles) along with the cumulative volume of injected fluid during hydraulic fracturing (blue line) and the cumulative flow-back volume (magenta line). Events are clustered during periods of injection with relatively few events outside these periods, suggesting that activity decays rapidly with time after injection stops. It is clear that most of the seismicity is associated with certain stages or sleeves. For example, sleeves 22, 30, 31 and 32 on 25, 26, 27 and 29 October, all had relatively high levels of detected seismicity. Similarly, sleeves 38, 39 and 40 on 11, 13 and 14 December also have relatively high levels of detected seismicity. These sleeves are all at or closer to the heel (east) end of the horizontal part of the well and all the events with magnitudes greater than 0.5 ML occurred during these hydraulic fracture stages. Conversely, sleeves 1, 2 and 3 on 16, 17 and 18 October at the toe (west) end of the well all have relatively low levels of seismicity, despite similar injected volumes.

## 1.9 MAGNITUDE UNCERTAINTY

Figure 11 shows histograms of the mean local magnitudes for each event with a magnitude greater than 0 ML, calculated using 10,000 bootstrap resampling replicates. The resulting distributions are approximately normal for most events. The non-parametric 95% confidence limits (red vertical lines in Figure 11) in the mean magnitude for each event are typically  $\pm 0.1$  ML. However, standard deviations in the observed station magnitudes are significantly greater,



varying from approximately 0.2 to 0.25 ML, while the overall spread in the magnitude measurements is typically one magnitude unit. Also the distributions of station magnitudes for each event are often skewed suggesting that magnitudes may be strongly influenced by individual station measurements.

**Figure 11. Histograms showing the results of bootstrap resampling of the measured local magnitudes at each station for events with magnitudes greater than 0 ML. Red vertical lines show 95% confidence intervals and the median for each event.**

## 1.10 ACTIVITY RATES AND MAGNITUDE OF COMPLETENESS

To assess the completeness of the catalogue we calculated magnitude of completeness,  $M_c$ , using two different methods: maximum curvature (Wiemer and Wyss, 2000), which computes the maximum value of the first derivative of frequency magnitude distribution (FMD); and, the Goodness-of-Fit test (GFT) (Wiemer and Wyss, 2000), which calculates  $M_c$  by comparing the observed FMD with synthetic ones. We then calculate the  $b$ -value for the catalogue using maximum likelihood method (e.g. Aki, 1965). We find a magnitude of completeness of  $-0.6 \pm 0.2$  ML using both methods. Errors were calculated using bootstrapping. The maximum likelihood estimate of the  $b$ -value is  $1.029 \pm 0.118$ , with an activity rate,  $a$ , of 1.360.

To assess how seismicity rates increase during operations, we compare the frequency magnitude distribution calculated for the Preston New Road events with a frequency magnitude distribution calculated for instrumentally recorded tectonic earthquake activity across the British Isles from 1970 to present (Figure 12). The numbers of tectonic events are scaled for the time period of operations, 57 days, and for the approximate area of operations (10 km by 10 km). A  $b$ -value of close to 1 was calculated for the tectonic event catalogue using a magnitude of completeness of 3.5 ML. This suggests that activity rates increase during the period of operations by a factor of around 100 against the average background activity rate for the UK. The activity will decay to background after the operation stop.

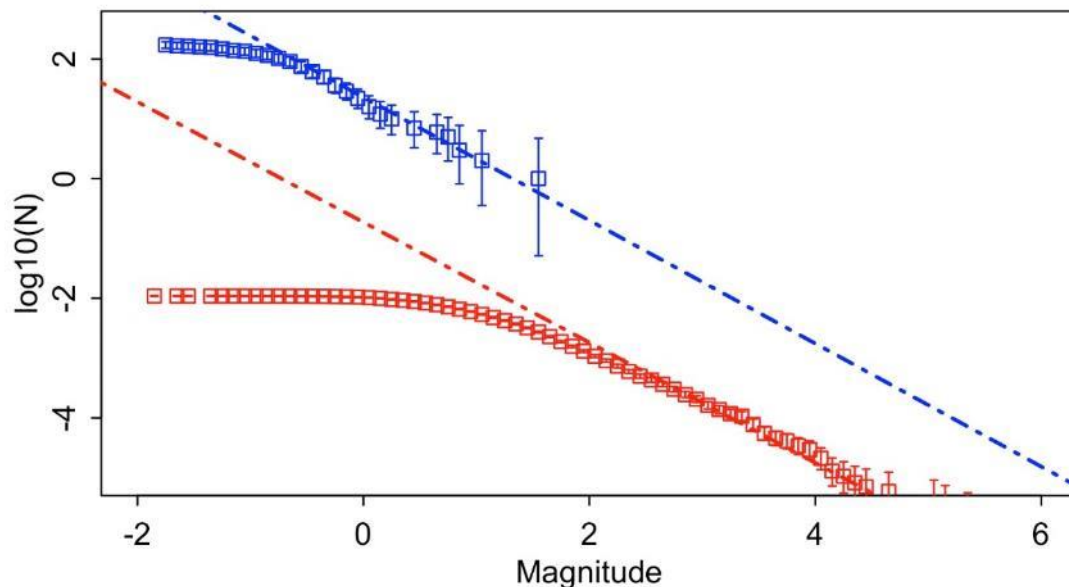


**Figure 12.** Observed frequency magnitude distributions for the Preston New Road events (blue squares) and instrumentally recorded tectonic earthquakes across the British Isles from 1970 to present. The tectonic activity data are scaled to a time period of 57 days and for an area of 10 km by 10 km. The blue and red dashed lines show maximum likelihood estimates of the  $b$ -value and activity rate for each.

## 1.11 EVALUATION OF GROUND MOTIONS FOR INDUCED SEISMICITY

An essential component of understanding seismic hazard in a region is the ability to predict the level of ground shaking (and its associated uncertainty) at a given distance from a particular

magnitude event, using ground motion prediction equations (GMPEs). While the magnitudes of the microseismic events at Preston New Road (PNR) are significantly lower than those considered in typical seismic hazard analyses, GMPEs are still useful for assessing whether the associated shaking has the potential to be felt. We use the PNR data to test a number of pre-existing GMPEs for suitability to modelling the ground motions induced by UK shale gas exploration: (1) the Akkar et al. (2014a) equations, developed for European seismicity, (2) the Douglas et al. (2013) equation, developed for induced seismicity in geothermal areas, and (3) the Atkinson (2015) equation, developed for induced seismicity in eastern North America. This work will be published in Cremen et al (2019). Evaluation of the GMPEs is specifically carried out for peak ground velocity (PGV), peak ground acceleration (PGA), and 5% damped spectral accelerations at periods of 0.05s, 0.1s, and 0.2s (SA0.05, SA0.1, and SA0.2 respectively).

It is also important to understand whether the seismic hazard associated with UK shale gas exploration differs relative to that associated with other types of UK seismicity. To achieve this, we compare the ground motions produced by PNR earthquakes to ground motions produced by similar magnitude events at similar depths in the 2018-2019 sequence of earthquakes near Newdigate, Surrey, which is believed to be naturally occurring (Verdon et al. 2019), and the 2013- 2014 sequence of events near New Ollerton, Nottinghamshire, which was induced by coal-mining at the Thoresby Colliery (Verdon et al, 2017).

We find that the Douglas et al. (2013) equation is the most suitable, at least for the considered ground motion intensity measures, although it can over-estimate ground motion variability. We find that the shale gas-related intensities are consistently higher than those of the Newdigate sequence and - depending on the intensity measure- are similar to or lower than those of the New Ollerton sequence.

## **1.12 BETTER DISCRIMINATION OF MAN-MADE EVENTS**

Robust methods are needed to assess whether detected earthquakes near industrial sites are natural or induced by the industrial activity. However, the most commonly used approach, the question based scheme suggested by Davis and Frohlich (1993) has a number of shortcomings that became apparent in the assessment of whether or not the Newdigate earthquake sequence in 2018/2019 (Baptie and Luckett, 2018) had been induced by nearby hydrocarbon exploration and production. For example: not specifically addressing the question of whether available evidence supports the case against induced seismicity; giving all questions equal weighting regardless of the relative influence of the different factors in determining whether or not seismicity is induced; producing final outcomes that may be difficult to interpret.

Verdon et al (2019) propose a new question-based framework that addresses these shortcomings by assigning numerical scores to each question, with positive values for answers that support induced seismicity and negative values for responses favouring natural seismicity.

The scores available for each question reflect the relative importance of the different questions, and for each question the absolute value of the score is modulated according to the degree of uncertainty.

When applying the framework, the first step is to assess how much information is available for each question. This then defines the first outcome, which we call the Evidence Strength Ratio (ESR), which is the ratio of the maximum score that can be assigned with the available data to the maximum score that would be available in an ideal case with all desirable data fully available.

$$ESR = \frac{(|-ve\ points| + |+ve\ points|)}{Absolute\ number\ of\ points}$$

A schematic illustration of this is shown in Figure 13. A low ESR suggests that relatively little information is available for the assessment, while a high ESR suggests that much more data is available.

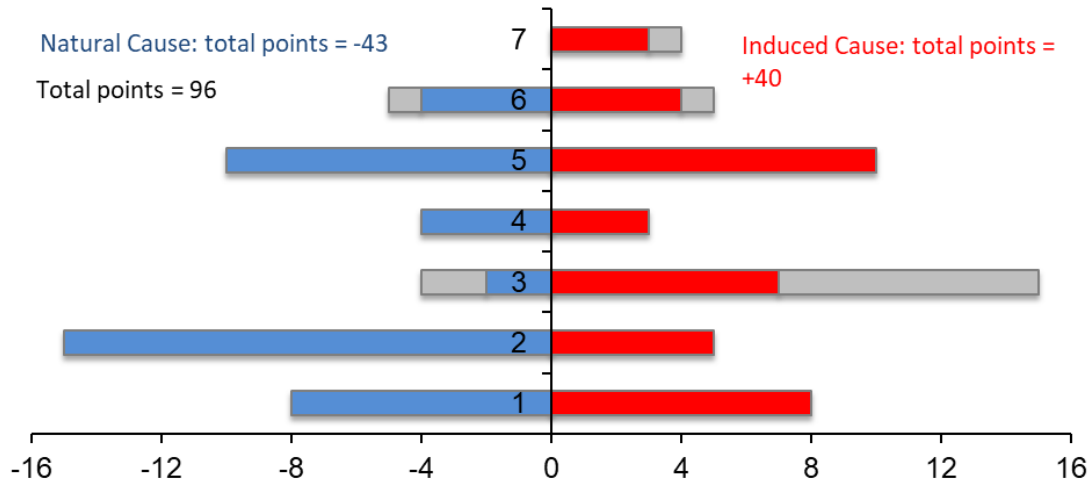


**Figure 13. Schematic illustration of the evidence strength ratio (ESR) for an example with a relatively strong ESR. Gray shaded arrows show the maximum points available for each question given the best possible quality evidence. A total of 83 from 96 points could be scored, so the ESR is 87%. This figure is based on our scoring for the Newdigate sequence relative to the Horse Hill well as assessed after a full study of the sequence.**

The second outcome is the Induced Assessment Ratio (IAR), which quantifies whether the overall assessment indicates a natural or an induced cause. The total number of points scored across each criterion, combining both positive and negative values, is expressed as a ratio of the maximum points that could have been scored if all answers were positive (if the summed score is positive) or negative (if the summed score is negative).

$$IAR = \frac{Summed\ Score}{Maximum\ points\ available}$$

A schematic illustration of this is shown in Figure 14. A positive IAR value indicates an induced cause, while a negative IAR indicates a natural cause. However, low values should be interpreted as an ambiguous assessment, based on insufficient data (low ESR).

### 1.13 DATA AVAILABILITY

Helicorder plots showing 24 hours of data from each station are available online and can be found on our web site and at: <http://www.earthquakes.bgs.ac.uk/research/BaselineMonitoring.html>. The web pages also contain background information on the baseline monitoring project as well as educational material to explain the scientific context. Processed event data (automatically determined and manually revised event parameters) are also available from our FTP site at <ftp://seiswav.bgs.ac.uk/events/>. Continuous recordings of ground motions from all stations are stored in a public open-data archive. These data are available in the standard data format developed in the international seismological community for data exchange.

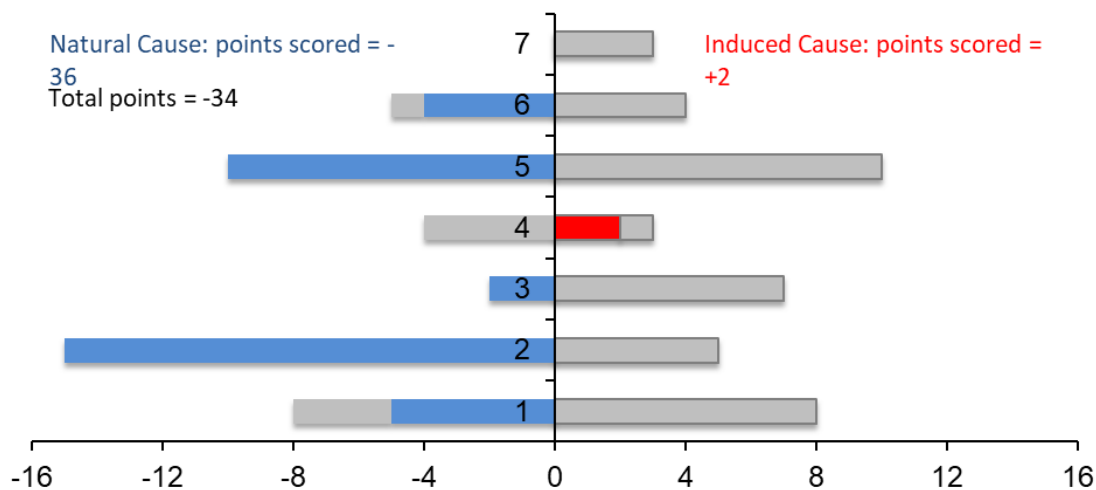


**Figure 14. Schematic illustration of the induced assessment ratio (IAR). A total of 36 negative points and two positive points are scored, giving an IAR of  $-34/43 = -79\%$ . Such a strongly negative indicates that the evidence points strongly toward these events not being induced by the industrial activity being examined. This figure is based on our scoring for the Newdigate sequence relative to the Horse Hill well as assessed after a full study of the sequence.**

## 1.14 CONCLUSIONS

The networks of seismometers installed to monitor background seismicity in both the Vale of Pickering and the Blackpool areas have been successfully operated throughout the reporting period and all phases of the project. All but three of the twenty stations show levels of data completeness that are over 95%. There has been no significant change in recorded noise levels at any of the stations in the network.

PDFs of the observed noise at each station have been used to estimate the detection capability of the Vale of Pickering network in low, median and high noise conditions. Although detection capability varies significantly, the network is capable of detecting events with magnitudes of 0.5 ML or less around Kirby Misperton.

The monitoring networks have successfully detected a number of small local seismic events at distances of 100 km away or greater. The proximity of a many of the events in the Vale of Pickering to quarries where blasting is known to take place, along with recorded waveforms that are characteristic of a shallow source, suggests that all these events are quarry blasts. All the suspected blasts occurred during the daytime, which adds further evidence to an anthropogenic origin. The magnitudes of these events range from 1.0 ML to 2.3 ML.

A combination of conventional, energy transient detection algorithms along with template matching has been used to detect seismic events with magnitudes as low as -1.8 ML during the hydraulic fracturing operations at Preston New Road between October and December 2018 using only surface sensors. The results also show that the detected seismicity is strongly clustered in space and time, and is closely associated with periods of injection, with only small numbers of “trailing” events. We have used a bootstrap approach to better quantify magnitude uncertainty, finding that the 95% confidence limits in the mean magnitudes for each event are at least  $\pm 0.1$  ML. We have also found that the magnitude of completeness for events detected in near real-time without template matching is close to the 0.0 ML amber light threshold, which

further highlights the problem of reliable characterisation of induced seismicity during operations using only surface monitoring networks.

We have tested the suitability of a number of existing GMPEs for modelling the ground motions from seismic events induced by hydraulic fracturing of unconventional shale reservoirs. We found that the Douglas et al. (2013) equation is the most suitable, at least for the considered ground motion intensity measures, although it can over-estimate ground motion variability. We also found that the shale gas-related ground motion intensities are consistently higher than those from a sequence of natural earthquakes (Figure 12) and are similar to or lower than those from a sequence of mining induced events.

We have developed a new framework for identifying whether earthquakes occurring near to subsurface industrial activity have a natural cause or are induced. The new approach was applied to the Newdigate sequence of events that occurred in 2018 with the conclusion that the earthquakes here were natural rather than induced. This work has now been published in *Seismological Research Letters* (Verdon et al, 2019).

## 1.15 REFERENCES

Akkar S, Sandikkaya MA and JJ Bommer (2014), Empirical ground-motion models for point- and extended-source crustal earthquake scenarios in Europe and the Middle East, *Bulletin of Earthquake Engineering*, 12: 359-387

Aki K (1965), Maximum Likelihood Estimate of  $b$  in the Formula  $\log N = a - bM$  and its confidence limits, *Bulletin of the Earthquake Research Institute*, 43: 237-239.

Atkinson GM (2015), Ground-motion prediction equation for small-to-moderate events at short hypocentral distances, with application to induced-seismicity hazards, *Bulletin of the Seismological Society of America*, 105(2A): 981-992

Baptie, B and R Lockett (2018), The Newdigate earthquake sequence 2018. British Geological Survey Open Report, OR/18/059.

Baptie, B and R Lockett (2018), Seismicity induced by hydraulic fracturing operations at Preston New Road, Lancashire, 2018, Proceedings of the Society for Earthquake and Civil Engineering Dynamics Conference 2019.

Clarke H, Eisner L, Styles P and P Turner (2014), Felt seismicity associated with shale gas hydraulic fracturing: The first documented example in Europe. *Geophysical Research Letters*, 41, 23, 8308–8314.

Cremen G, Werner MJ and B Baptie (2019), Understanding induced seismicity hazard related to shale gas exploration in the UK, Proceedings of the Society for Earthquake and Civil Engineering Dynamics Conference 2019.

Davis SD and C Frohlich (1993), Did (or will) fluid injection cause earthquakes? Criteria for a rational assessment, *Seismological Research Letters* 64, 207–224.

Douglas J, Edwards B, Convertito V, Sharma N, Tramelli A, Kraaijpoel D, Cabrera BM, Maercklin N, and C Troise (2013), Predicting ground motions from induced earthquakes in geothermal areas, *Bulletin of the Seismological Society of America*, 103(3): 1875-1897

Johnson C, Bittenbinder A, Bogaert B, Dietz L and W Kohler (1995), Earthworm: A Flexible Approach to Seismic Network Processing, *IRIS Newsletter*, 14(2): 1-4

Lomax A, Michelini A and A Curtis (2009), Earthquake Location, Direct, Global-Search Methods, in Complexity In Encyclopedia of Complexity and System Science, Part 5, Springer, New York, 2449-2473

Schaff, DP and PG Richards (2004), Repeating seismic events in China, Science, 303: 1176–1178

Peterson J (1993), Observation and modelling of seismic background noise, U.S. Geol. Surv. Tech. Rept., 93-322, 1-95.

Verdon JP, Kendall J-M, Butcher A, Luckett R and B Baptie (2017), Seismicity induced by longwall coal mining at the Thoresby Colliery, Nottinghamshire, U.K., Geophysical Journal International, 212 (2).

Verdon JP, Baptie BJ and JJ Bommer (2019), An improved framework for discriminating seismicity induced by industrial activities from natural earthquakes, Seismological Research Letters, doi: <https://doi.org/10.1785/0220190030>

Wiemer S and Wyss M (2000), Minimum magnitude of complete reporting in earthquake catalogs: examples from Alaska, the western United States, and Japan, Bull. Seismol. Soc. Am., 90: 859-869.

## 2 Water quality monitoring

### 2.1 INTRODUCTION AND SUMMARY

Water-quality monitoring under baseline conditions has continued during the Phase 4 period of investigation at a quarterly frequency. Spatial variability in chemical composition is large; temporal variability is also large for streamwater, but compositions are more consistent for most groundwater samples in the monitoring network.

High baseline concentrations of methane are a consistent feature of some of the groundwaters in the Vale of Pickering, with extremes up to 78 mg/L observed in groundwater from the Superficial aquifer and up to 60 mg/L in the deep confined section of the Corallian aquifer. Discrepancies in measurements of dissolved CH<sub>4</sub> in groundwater from both the KMA and PNR boreholes between BGS' and site operators' data merit further detailed scrutiny of sampling and analytical protocols for CH<sub>4</sub>; this will be addressed in the next phase.

Monitoring of groundwater quality in the Third Energy shallow water boreholes at KMA (Superficial aquifer) showed some notable seasonal variations in chemical composition (e.g. calcium, magnesium, sulphate and manganese) and highlights the need for monitoring to capture the temporal variation in baseline conditions. For the deep borehole penetrating the Corallian aquifer at KMA, while seasonal variability was not apparent, concentrations of several analytes (e.g. aluminium and potassium) have decreased consistently over the period of monitoring, taking some two years to reach a steady-state composition. This is likely due to a low-flow sampling regime and the difficulty of purging with such constraints. This further reiterates the need for time-series data greater than 12 months to assess the baseline condition adequately in such circumstances.

A statistical approach predicting the distribution of the standardised space-time mean of analytes for the baseline condition has been proposed for distinguishing baseline from operational effects. From the limitations of the approach described and as a cautionary principle, we recommend that apparently significant deviations from the baseline model be viewed as a recommendation for further investigation rather than as a definitive indicator of impact from hydrocarbon exploration activities.

### 2.2 WATER QUALITY MONITORING IN THE VALE OF PICKERING

Monitoring of water quality at sites from the Vale of Pickering water monitoring network (streams and groundwater) has continued at approximately quarterly intervals over the year of investigation. As no subsurface exploration activities have been carried out by the operator during this time, baseline conditions have continued with respect to water quality.

Results for groundwater samples from the Superficial and Corallian aquifers (shallow aquifer in central part of the vale and along the periphery respectively) have continued to show consistencies in chemical compositions over time, with often high concentrations of methane in the former (Figure 15, Figure 16). Site 15 from the Superficial aquifer continues to show the largest variability in dissolved methane concentrations, with the lowest observation in the most recent round of sampling. The reason for this variability remains unclear although the suggestion is that it is related to hydrogeological conditions. Analytical issues have been ruled as has sampling approach, particular as other sites sampled at the same time, and using the same methods for sampling and analysis, show consistency over time. The observed behaviour will continue to be investigated.

Spatial variability between sites is large, and this reflects the natural spatial variability in hydrogeochemical conditions.

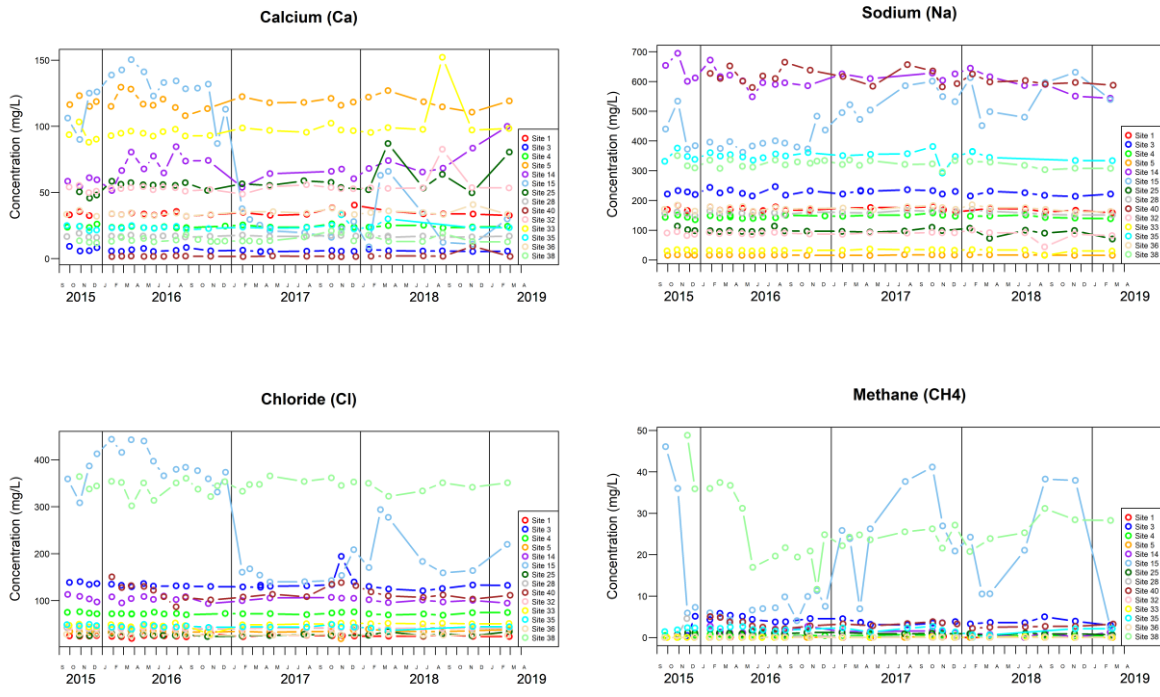


**Figure 15. Temporal variation in concentrations of calcium, sodium, chloride and methane in groundwater from sites in the Superficial aquifer**

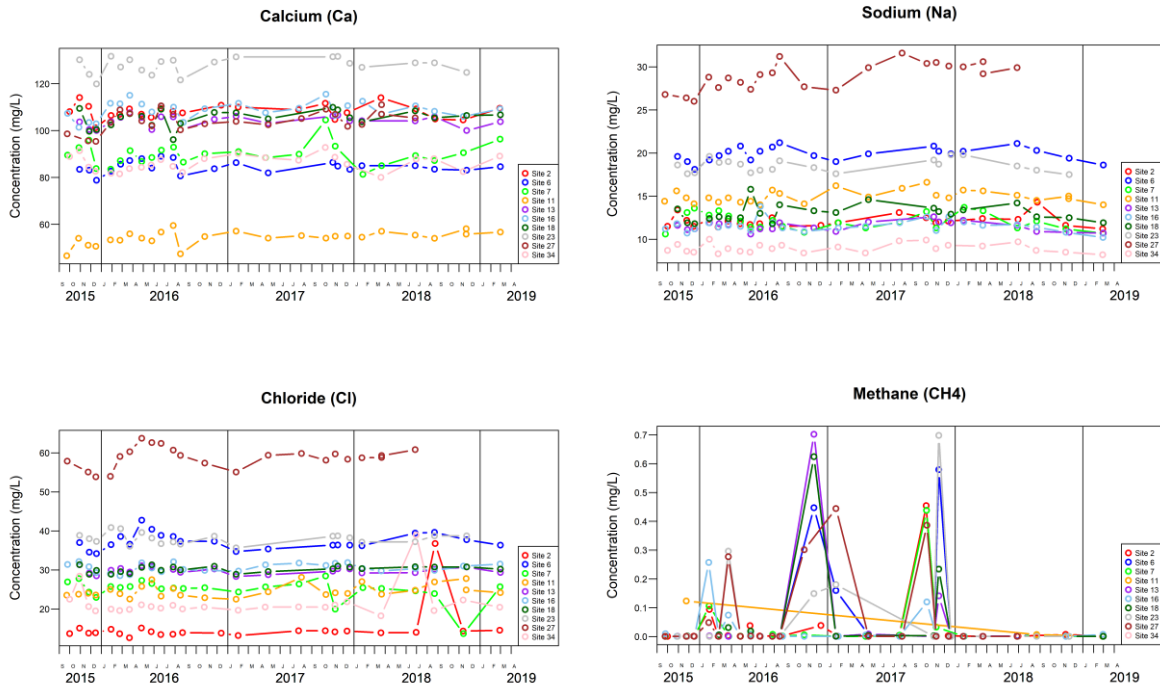


**Figure 16. Temporal variation in concentrations of calcium, sodium, chloride and methane in groundwater from sites in the Corallian aquifer**

Water quality has continued to show the largest temporal variability in the streams compared to the groundwater samples, as demonstrated by calcium, sodium and chloride in Figure 17. Such large variations in dissolved solids are likely in large part related to variations in rainfall, although variable inputs of pollutants with time could also have had an impact.

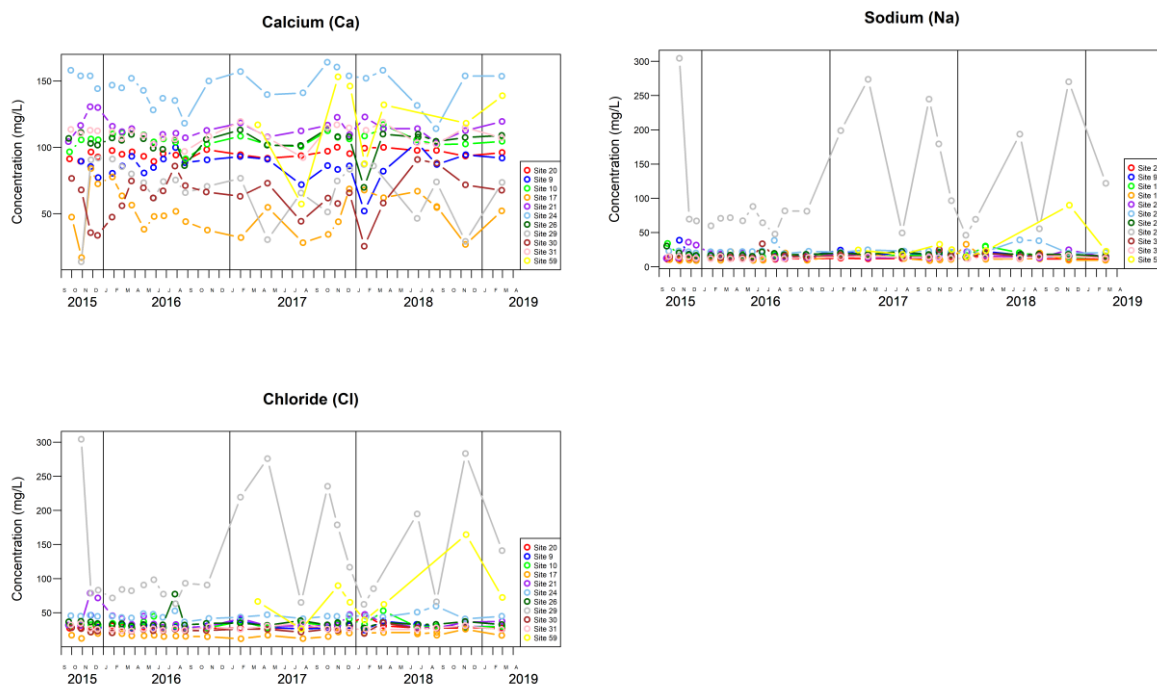


**Figure 17. Temporal variation in concentrations of calcium, sodium and chloride in streamwater sites.**

Concentrations of calcium in streams from the monitoring network are shown again in Figure 18 alongside variations in rainfall amounts and stream flow discharges in the Vale of Pickering (rainfall data from Meteorological Office: <https://www.metoffice.gov.uk/hadobs/hadukp/data/download.html>; stream flow data from the Environment Agency: <http://environment.data.gov.uk/hydrology/>). As expected, the larger streams show the greatest fluctuations in flow discharge. The stream flow and chemical data are difficult to compare directly as, in most cases, they are not monitored at corresponding sites. However, the variability in stream discharge over time can explain as least partly the greater variability seen in streamwater chemistry relative to that observed in groundwater.

For two sites in the streamwater quality monitoring network, stream flow *is* also gauged in the corresponding streams, these are: Sites 10 and 30 (Costa Beck and Pickering Beck respectively). Streamwater-quality data in relation to flow discharge for flow gauging stations proximal to individual sites are shown for calcium and chloride (as examples) in Figure 19. Some hint of reduced calcium concentration (and possibly also chloride) is shown for Pickering Beck (blue) during periods of increased stream flow. Trends for Costa Beck (red) are less clear, although variation in stream discharge is also much less pronounced for that stream.

### 2.3 GROUNDWATER MONITORING AT KMA

Investigation of the water monitoring boreholes at the KMA (shale gas) site has been conducted using BGS monitoring data together with those from Third Energy's contractors (<https://consult.environment-agency.gov.uk/onshore-oil-and-gas/third-energy-kirby->

[misperton-information-page/](#)). Contractors' data for October 2018 onwards were not available at the time of writing.

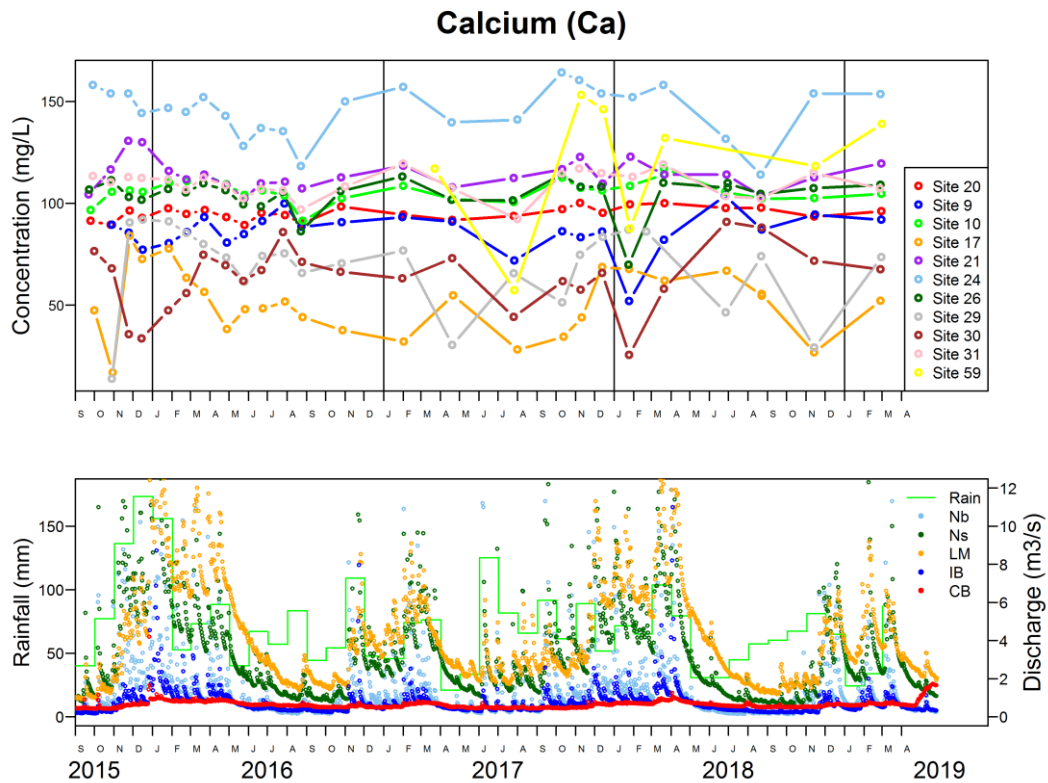


**Figure 18. Variations in concentrations of nitrate in streams (above) with regional rainfall for NE England and Vale of Pickering stream flows (Nb: Normanby; Ns: Ness; LM: Low Marishes; IB: Ings Bridge; CB: Costa Beck (Environment Agency) (below)**

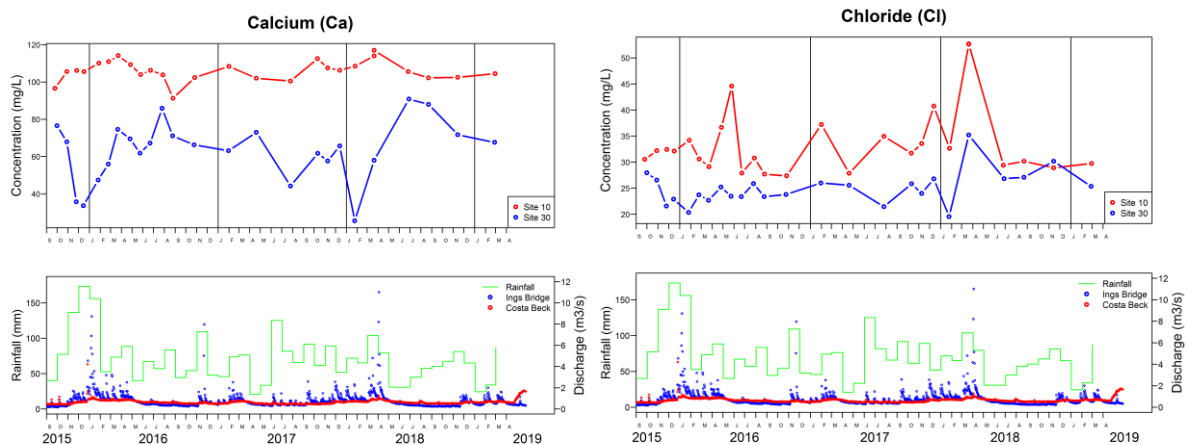


**Figure 19. Variations in calcium and chloride concentration in streamwater from Sites 10 and 30 with proximal stations in the Environment Agency's stream monitoring network (Pickering Beck in blue; Costa Beck in red) (rainfall also shown in green)**

The five groundwater monitoring boreholes at KMA were installed by Third Energy in Nov–December 2015 (Envireau Water, 2017; Third Energy, 2015). These consist of three shallow boreholes (11.5 m depth: BHA, BHB, BHC) to target the superficial deposits and shallowest parts of the weathered Kimmeridge Clay, one intermediate (38 m depth: BHD) to target deeper

sections of the Kimmeridge Clay, and one deep (ca. 220 m: BHE) to target upper sections of limestone of the Corallian Group. Full details of borehole construction are given by Envireau Water (2017). Boreholes are each located around the periphery of the KMA site.

The lithological sequence proved by the boreholes consists of soil/Quaternary deposits to ca. 4 m depth (0.3–5.5 m), mudrocks of the Kimmeridge Clay (Ancholme Group) to ca. 177 m (bgl), and Corallian Group limestone below. The junction between the Ancholme and Corallian groups is gradational and is proven over the depth interval 177 m to 190 m (Envireau Water, 2017). Sampling of the boreholes has been by low-flow pumping using bladder pumps (<1 L/min), permanently installed by Third Energy.



**Figure 20. Indicative monitoring data for redox potential, specific electrical conductance, iron, manganese, methane and methane/ethane ratio (C1/C2) in groundwater from KMA, analysed by BGS**

Selected results for baseline monitoring conducted at KMA for 2016–2018 are shown in Figure 20 and Figure 21. Figure 20 shows the redox potential (Eh) for groundwater in the five boreholes. Results indicate that all five boreholes have reducing groundwater, the values

becoming more strongly reducing with increasing borehole depth. Groundwater from the Corallian borehole has consistently negative Eh.

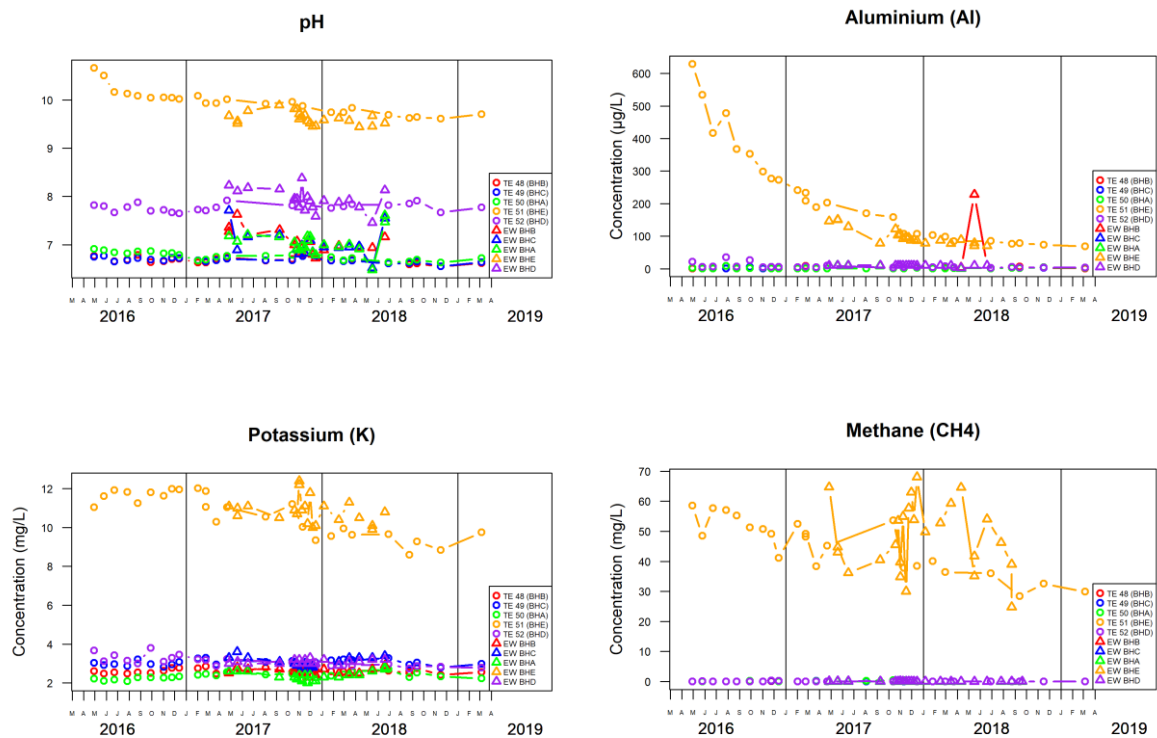


**Figure 21. Indicative monitoring data for pH, dissolved aluminium, potassium and methane in groundwater from KMA, analysis by BGS and Third Energy (Envireau Water, EW)**

Values for SEC show the large range of mineralisation of groundwater from the different boreholes, the highest solute concentrations being in the Corallian groundwater. Some temporal variation is seen in the shallowest boreholes.

Values for Fe and Mn show a large range but typically high values for the shallow and intermediate (Kimmeridge) boreholes. The compositions indicate that these groundwaters are Fe- and Mn-reducing. Values are much lower in the Corallian borehole, corroborating the Eh evidence that they are much more strongly reducing.

Figure 20 also shows the consistently high values of dissolved methane in the deep Corallian groundwater. From BGS data, this was typically around 60 mg/L at the start of monitoring, but has been declining over the period, with more recent values typically around 30 mg/L. Methane at the other sites is much lower but still measurable, see **Error! Reference source not found..** Alkalinity shows a corresponding increase over the period. The figure also shows the time variation in molar C1/C2 ratios, which although variable, have been consistently greater than 10,000. This range of high values is strongly indicative of a biogenic origin for the methane, and is consistent with negative  $\delta^{13}\text{C-CH}_4$  values (around -80 ‰) reported earlier (Ward et al., 2017) for groundwater from this site. The presence of methane is also consistent with the very low Eh values, and lower Fe and Mn concentrations described above.

Results in Figure 21 show the variations in compositions of selected solutes in groundwater at KMA from BGS analyses, together with 2017–2018 analyses from the same boreholes by Third Energy (EW). Monitoring of pH shows typically neutral values for the shallow boreholes

(BHA, BHB, BHC) and slightly alkaline pH for the intermediate borehole (BHD, pH 8). The Corallian borehole has strongly alkaline groundwater. At the start of monitoring following borehole installation, pH was ca. 10–11, but values have fallen over the period to closer to ca. 9.8. EW analyses for the boreholes are broadly consistent over the equivalent periods.

Figure 21 also shows a notable reduction over time in concentrations of dissolved (<0.2  $\mu\text{m}$  filtered) aluminium and potassium in BHE. Corresponding decreases (not shown) are observed in concentrations of a number of other elements including phosphorus, rubidium, silicon, titanium and tungsten. These trends are not observed in groundwater from the shallower boreholes. The initial high values in BHE are inferred to be due to the remnant influence of cement grout, bentonite and possibly steel casing in the early stages of well pumping, suggesting incomplete development and purging of this deep well before sampling commenced. Aluminium concentrations may also have decreased in response to the pH dependence of Al hydroxide solubility. Since commissioning, the deep borehole has been pumped under low-flow conditions, with care taken to minimise groundwater discharge at the site. This has resulted in an apparently longer time to reach steady state than for the shallower boreholes. For most solutes with observed decreasing trends in BHE, steady-state conditions were achieved in the winter 2017–2018 period, some two years after the start of monitoring. This is an important finding from this study.

More recent monitoring data for BHE (pH 9.8, Na-HCO<sub>3</sub> compositions) are consistent with a groundwater that has evolved from the Ca-HCO<sub>3</sub> typical of Corallian groundwater at outcrop. Inverse modelling (NETPATH, PHREEQC) suggests the composition has evolved via dissolution of carbonate (calcite) together with cation exchange (especially Ca-Na). Water chemistry and isotopic compositions suggest that the confined Corallian groundwater from BHE has also been impacted by numerous redox reactions, including denitrification, sulphate reduction and methanogenesis. The groundwater is old with little modern radiocarbon. A tentative conservative model age of around 18,000 years, i.e. Pleistocene, has been derived for the groundwater from BHE. Large uncertainties on the derivation of the model age arise from the numerous geochemical reactions involving carbon mass transfer that are implicated in the evolution of the Corallian groundwater. Nonetheless, enriched <sup>13</sup>C (similar to that expected for the limestone, Bishop and Lloyd, 1991) and depleted  $\delta^{18}\text{O}$  and  $\delta^2\text{H}$  values (ca. -8.9 and -58.5 respectively) support the inference that the groundwater is old. The presence of palaeowater in the Corallian aquifer, albeit from only a single location, suggests that flow has been slow in the deep confined conditions. The piezometric surface of groundwater at BHE (Envireau Water, 2017) is typically at least 3 m higher than observed from the Kimmeridge boreholes, indicating an upward flow direction.

Monitoring data for methane is repeated in Figure 21 to show the corresponding values obtained from EW over the 2017–2018 period. Unlike the BGS analyses, there is less evidence of decreasing concentrations and the absolute concentrations appear to be commonly higher than detected by BGS. The reason for this is unclear. BGS samples were taken inline at pump pressure from the borehole headworks into doubled-valved steel bombs, with headspace analysis by GC-FID (Bell et al., 2017). Differences in sampling and analytical techniques are likely contributory, including differences in sample containers. Further work is being undertaken on this.

Figure 22 shows the variations in concentrations of calcium, magnesium, sulphate and manganese in groundwater from the KMA water monitoring boreholes from both BGS and EW data. The data reveal some notable temporal variation, especially in the shallowest boreholes (BHA, BHB, BHC). Variations in groundwater level over the period 2017–2018 are relatively minor (Envireau Water, 2017) with responses to variations in rainfall dampened. Nonetheless,

the variations in chemistry appear seasonal with maxima in late Spring in the shallow boreholes. A possible inverse link may exist with seasonal recharge, with dilution of shallow groundwater during recharge periods in winter. Seasonal influence of groundwater derived from the Quaternary deposits above the Kimmeridge Clay could also result in some temporal variation.

Figure 22 shows uniformly low concentrations of sulphate in BHE. This is consistent with the low observed Eh values, supporting the inference that they have undergone sulphate reduction. This is also associated with the low Fe and Mn concentrations in BHE and is due to the low solubility of Fe and Mn sulphide minerals.

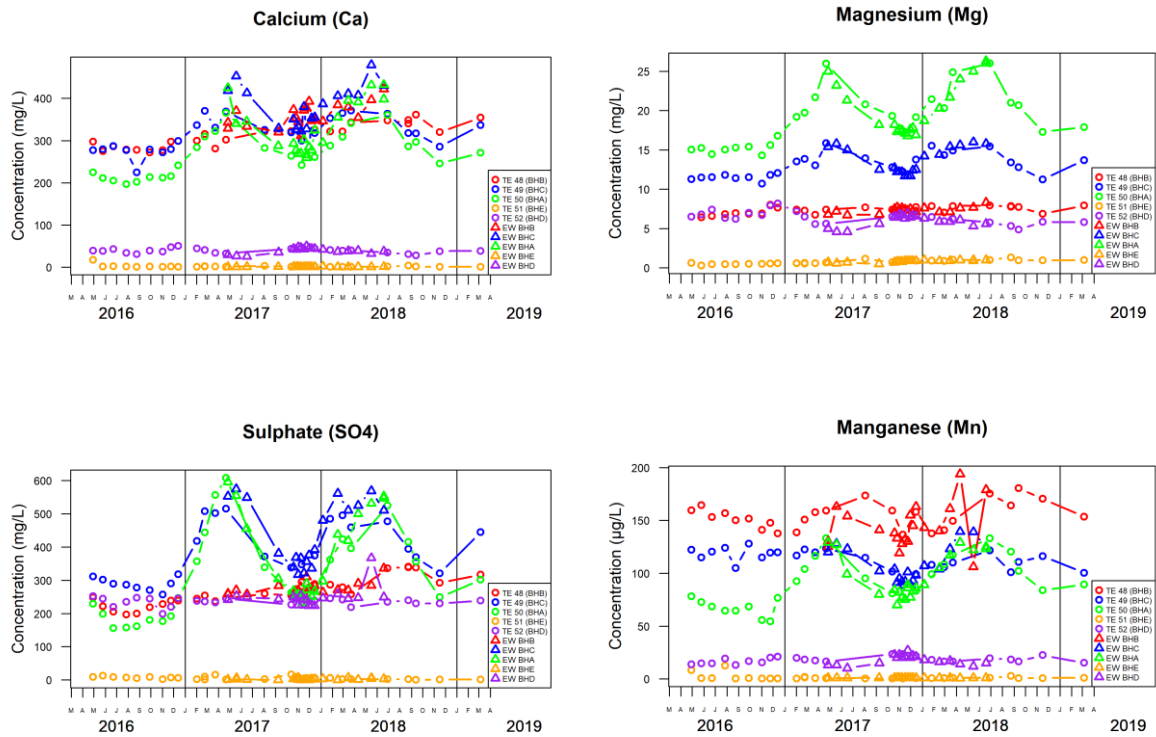


**Figure 22. Monitoring data for calcium, magnesium, sulphate and manganese in groundwater from the five boreholes at KMA, analysis by BGS and Third Energy (Envireau Water, EW)**

Interim summary statistical data for key analytes in groundwater samples taken from the KMA water monitoring boreholes (BGS data only) are given in **Error! Reference source not found.** Monitoring site locations relative to the KM8 shale ags well are shown in Figure 39. The P95 value can be considered the upper baseline concentration and therefore a potential change indicator threshold value. The summary statistical data for groundwater and streams in the wider area around the KMA site are presented in Appendix C.

**Table 1. Statistical summary data for the monitoring boreholes at KMA.**

Site	Analyte	n	ncens	min	mean	max	median	95%ile
TE 48	SEC	26	0	1399	1560	1730	1540	1720
(BH B)	Alk HCO <sub>3</sub>	26	0	496.7425	524	566	516	555
	NH <sub>4</sub>	26	0	0.084	0.134	0.321	0.103	0.298
	Ca	26	0	272.2	312	361	315	354
	Mg	26	0	6.43	7.34	8.03	7.4	7.94
	Na	26	0	30.5	34.5	40.5	34.2	40.2
	K	26	0	2.41	2.6	2.85	2.58	2.77
	Cl	26	0	96.3324	116	137	118	137
	SO <sub>4</sub>	26	0	196.8073	264	341	254	339
	Ba	26	0	68.6	91.4	146	88.1	108
	Li	26	0	44	53.3	61	53	59
	CH <sub>4</sub>	26	3	<0.0005	0.0249	0.326	0.0043	0.071
TE 49	SEC	25	0	1220	1530	1780	1530	1760
(BH C)	Alk HCO <sub>3</sub>	25	0	498	523	552	523	550
	NH <sub>4</sub>	25	0	0.149	0.208	0.433	0.189	0.31
	Ca	25	0	224	314	371	318	370
	Mg	25	0	10.7	13	15.9	12.8	15.5
	Na	25	0	28.2	33.5	49.4	31.9	42
	K	25	0	2.78	3.05	3.29	3.05	3.28
	Cl	25	0	51.3	54.6	59.2	54.4	58.3
	SO <sub>4</sub>	25	0	256	377	515	369	508
	Ba	25	0	17.9	26.5	48.1	25.3	33.3
	Li	25	0	56	67.2	79	67	75
	CH <sub>4</sub>	25	6	<0.0004	0.0321	0.246	.0037	0.232
TE 50	SEC	25	0	1080	1350	1770	1320	1700
(BH A)	Alk HCO <sub>3</sub>	25	0	465	503	564	504	538
	NH <sub>4</sub>	25	0	0.174	0.383	0.892	0.357	0.759
	Ca	25	0	196	266	366	264	360
	Mg	25	0	14.3	18.8	26	19.2	26
	Na	25	0	21.8	24.9	33.7	24.1	29.4
	K	25	0	2.08	2.34	2.7	2.32	2.56
	Cl	25	0	30.7	34.5	40.9	33.9	37.8
	SO <sub>4</sub>	25	0	155	313	608	273	556
	Ba	25	0	68.7	138	206	126	203
	Li	25	0	32	37.4	43	38	42.8
	CH <sub>4</sub>	25	1	<0.0005	0.0688	0.482	0.0055	0.377
TE 51	SEC	26	0	3020	3170	3220	3180	3220
(BH E)	Alk HCO <sub>3</sub>	25	0	422	643	678	649	675
	NH <sub>4</sub>	26	0	0.579	0.974	1.21	0.954	1.17
	Ca	26	0	0.7	2.01	17.3	1.2	3.9
	Mg	26	0	0.3	0.737	1.34	0.64	1.14
	Na	26	0	625	690	747	693	738
	K	26	0	8.59	10.7	12	11	12
	Cl	26	0	610	669	725	670	699
	SO <sub>4</sub>	26	12	<0.5	5.86	16.4	2.65	15.7
	Ba	26	0	29.4	45.9	58.6	45.2	55.1
	Li	26	0	118	146	175	147	162
	CH <sub>4</sub>	23	0	28.4	45.0	58.6	48.2	57.7
TE 52	SEC	24	0	1650	1740	1780	1740	1780
(BH D)	Alk HCO <sub>3</sub>	24	0	737	770	794	764	793
	NH <sub>4</sub>	24	0	1.3	1.81	2.08	1.76	2.06
	Ca	24	0	28	38.9	50.5	38.7	47
	Mg	24	0	4.88	6.43	8.17	6.45	7.95
	Na	24	0	351	384	416	379	409
	K	24	0	2.74	3.09	3.8	3	3.66
	Cl	24	0	39.4	46.1	64.1	42.3	61.7
	SO <sub>4</sub>	24	0	199	235	252	236	248
	Ba	24	0	12.9	17.7	23.2	17.8	23
	Li	24	0	38	46.6	57	46	56.2
	CH <sub>4</sub>	24	4	<0.0005	0.0472	0.356	0.0176	0.181

nits: mg/L (Ba, Li: in µg/L; SEC in µS/cm). HCO<sub>3</sub>: bicarbonate alkalinity as HCO<sub>3</sub>. ncens: number of censored values; P: percentile values; statistics computed by Kaplan-Meier method

## 2.4 GROUNDWATER MONITORING AT PRESTON NEW ROAD, LANCASHIRE

### 2.4.1 Infrastructure

Comparable programmes of groundwater monitoring have also been carried out by the site operator and independently by BGS (also independently funded) at the Preston New Road (PNR) shale gas site in Lancashire. Groundwater quality has been monitored there from eight boreholes/sampling ports since the PNR monitoring infrastructure was set up in 2016. The sampling sites consist of three nested boreholes with two boreholes in each nest, plus a Solinst CMT multilevel sampling system equipped to sample two further sampling ports. Details of the boreholes are given in Table 2.

All screened sections abstract from Quaternary superficial deposits at depths less than 30 m below ground level. Groundwater levels are shallow: typically within 2 m of the ground surface; borehole 2 is artesian. Boreholes 1, 2 and 4 have bladder pumps permanently installed for sampling while borehole 3 ports are sampled (both Cuadrilla consultants and BGS) using a portable peristaltic pump. Extra ports in the CMT are not accessible for sampling due to clogging and turbidity problems; records indicate that port 7 in glacial till has been plugged permanently due to artesian flow (Cuadrilla, 2016). Boreholes 1–4 are sited to the S, W, N and E edges of the PNR compound respectively [337 433].

Consultants for Cuadrilla have been monitoring water quality from the boreholes since July 2016 and BGS has been monitoring the same sites since May 2017. Water-quality data for the boreholes produced by Cuadrilla’s consultants were all downloaded from the Environment Agency website: <https://consult.environment-agency.gov.uk/onshore-oil-and-gas/information-on-cuadrillas-preston-new-road-site/>.

Cuadrilla carried out a programme of hydraulic fracturing of its PNR-1z borehole at PNR during the interval October–December 2018.

**Table 2. Details of groundwater monitoring points at Preston New Road, Lancashire**

Borehole/port	Total depth (mbgl)	Slotted screen depth (mbgl)	Elevation (mOD)	Lithology
BH01A	33.0	9–12	13.64	Glacial sand
BH01B		27–30	13.64	Sand
BH02A	30.0	9–11	11.35	Glacial sand
BH02B		21–26	11.35	Sand
BH03CMT1	26.6	12.6	13.12	Glacial sandy clay, gravel
BH03CMT5	26.6	20.3	13.12	Sand
BH04A	25.8	16.5–19.5	13.50	Glacial sand
BH04B		22–24.8	13.50	Sand

### 2.4.2 PNR groundwater quality

Results for selected parameters analysed independently by Cuadrilla’s consultants and BGS are shown graphically in Figure 23, Figure 24 and Figure 25. Data for sampling carried out by BGS are depicted using circles; those analysed from Cuadrilla sampling by triangles; colours reflect the corresponding boreholes/ports and should be comparable directly. The period of test hydraulic fracturing of borehole PNR-1z (late 2018) at the site is also indicated. The parameters depicted represent features of the analytical data from which some general observations can be drawn.

Data from Cuadrilla represent monitoring of much longer duration and greater frequency than that achieved by BGS. Cuadrilla sampling has typically been monthly and BGS quarterly, albeit with some variations.

The principal ions in the PNR groundwater are Ca and HCO<sub>3</sub> and trends in each are depicted in Figure 23. The concentrations show comparable ranges with corresponding values for individual sites (e.g. borehole 01B has the lowest Ca and highest HCO<sub>3</sub> values of the suite in both datasets). Data for Ca show some temporal variability in both datasets but Cuadrilla trends for both Ca and HCO<sub>3</sub> are relatively noisy. This may be partly reflected by the frequency of sampling but is more likely an artefact of differences in sampling and analytical protocols between the two monitoring organisations.

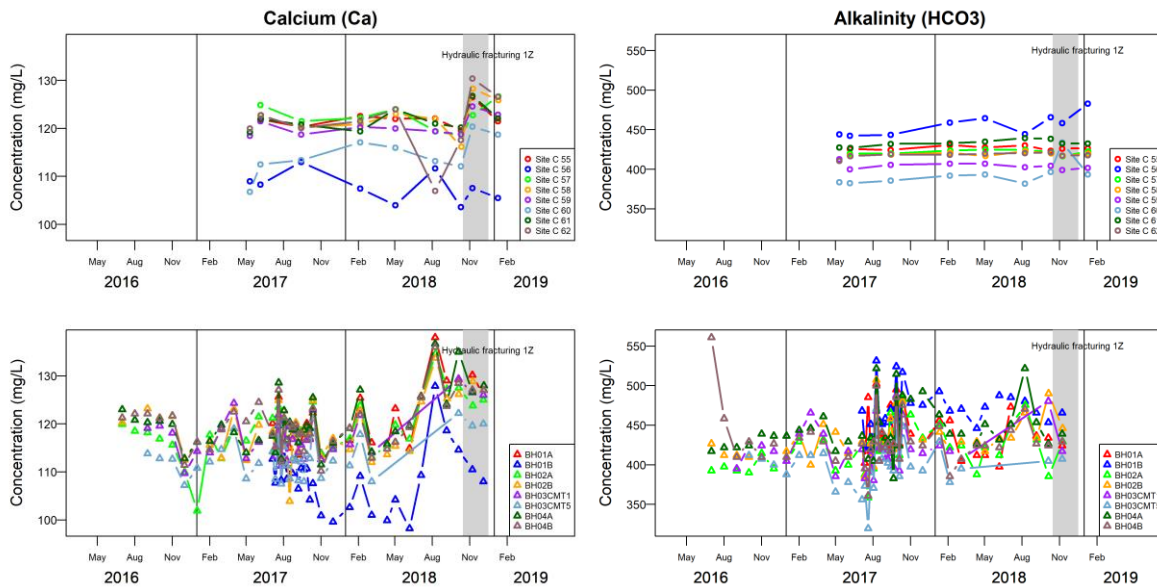


**Figure 23. Temporal variation in calcium and alkalinity in groundwater from the monitoring boreholes at PNR. Circles are BGS data, triangles Cuadrilla. The period of test hydraulic fracturing at borehole PNR-1z is also indicated**

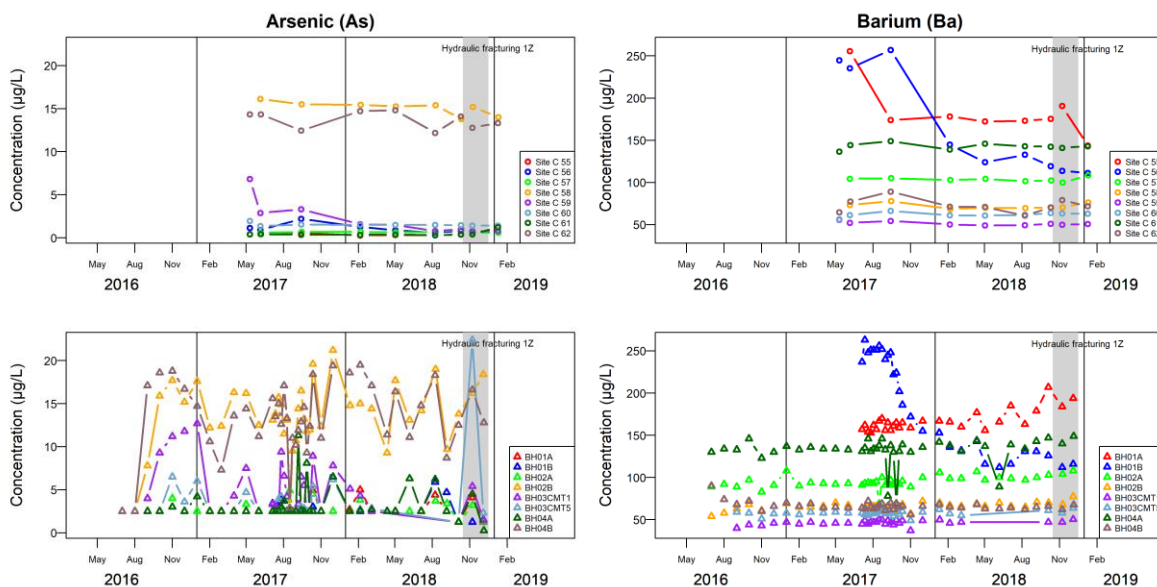


**Figure 24. Temporal variation in arsenic and barium in groundwater from the monitoring boreholes at PNR. Circles are BGS data; triangles Cuadrilla**

Data for arsenic (As) (Figure 24) also largely show consistency in absolute concentrations between different boreholes/sampling ports but again with greater variation in the Cuadrilla dataset. An anomalous peak in As concentration observed in the Cuadrilla data during one sampling event in November 2018 was not reproduced in the BGS dataset. The possible

differences may be due to different sampling methodology (e.g. filtration pore sizes, sampling receptacles) between sampling organisations or analytical problems. We do not have information on the analytical QA procedures used by Cuadrilla, and therefore cannot interpret further with confidence. However, it is unlikely to be due to temporal differences since BGS and Cuadrilla sampled on the same day and therefore on the basis of available evidence, the anomalous As result in the Cuadrilla dataset is indicative of a sampling/analytical error. Future measurement results will assist in further interpretation. Time-series data for Ba are much less noisy and largely consistent between datasets. Borehole 01A in particular shows initial higher concentrations in 2017 in both, with comparable concentration ranges. The reason for the initial high values is unclear but may link to a presence of residual clay in the borehole before removal by purging under the low-flow conditions operated to sample the boreholes.

Values for CH<sub>4</sub> (Figure 25) show consistently the highest values in borehole 01B. Both datasets have variable concentrations for CH<sub>4</sub> in this borehole (typically 1–7 mg/L). Maxima are higher in the Cuadrilla dataset than that from BGS although absolute differences are small. Concentrations in the other boreholes are universally low ( $\leq 1$  mg/L). The lower CH<sub>4</sub> concentrations measured by BGS are consistent with the discrepancies observed between sampling organisations at KMA and merit further scrutiny.

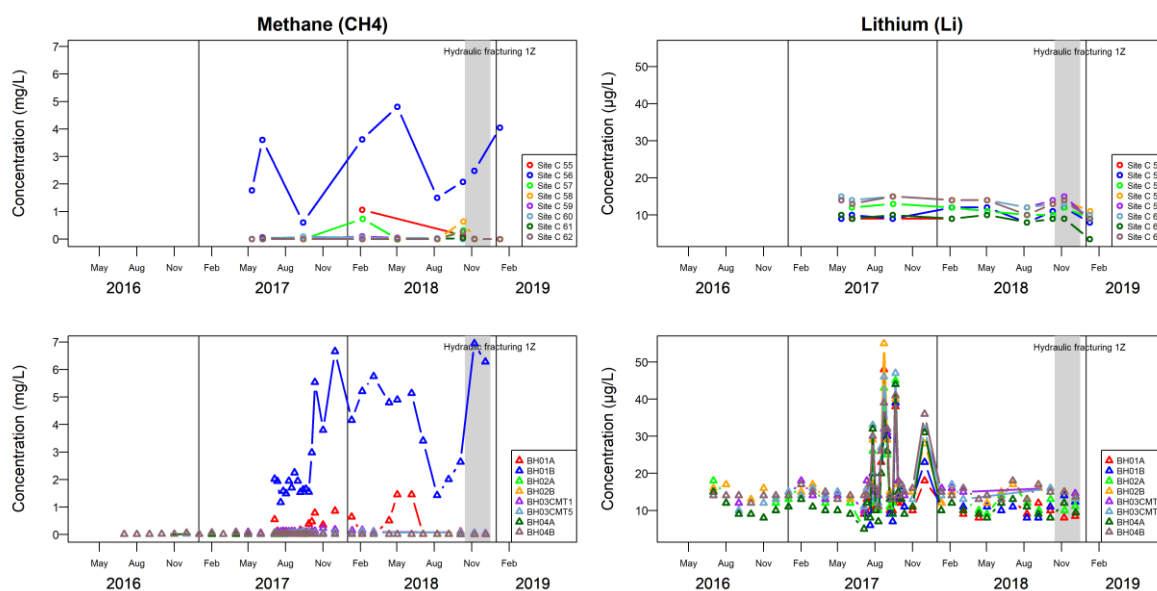


**Figure 25. Temporal variation in methane and lithium in groundwater from the monitoring boreholes at PNR. Circles are BGS data; triangles Cuadrilla**

Data for Li in the groundwater samples show usually low and consistent concentrations between sampling points (Figure 25), albeit with some significantly higher concentrations in the Cuadrilla dataset at intervals in mid–late 2017. Sampling during this period was conducted less frequently by BGS but samples collected in September 2017 did not display similarly anomalous values for Li. Differences in sampling protocol including filtration between organisations could have been responsible.

Data for Cu and Pb (Figure 26) show some notable discrepancies between BGS and Cuadrilla datasets. Concentrations of Cu up to 12 µg/L were found in BGS samples, although most were <5 µg/L. BGS data for Pb show consistently <0.5 µg/L at all PNR sites. The figure for Cu and Pb shows a feature common to many of the trace elements in the Cuadrilla analytical suite. Up until October 2018, not only were the detection limits for some trace elements much higher than those in the BGS dataset (by 1 or 2 orders of magnitude) but all values at the detection limit (e.g. 7 µg/L for Cu, 5 µg/L for Pb) were reported as detects. This was rectified from

October 2018 by distinguishing detects from non-detects (for convenience, non-detects are reported as half detection-limit values in Figure 26 for October–November 2018 analyses), and by improved detection limits from December 2018. The pre-October 2018 Cuadrilla data for a number of trace elements are therefore very difficult to interpret. Certainly, care should be taken with data handling and interpreting results close to the recorded detection limits.

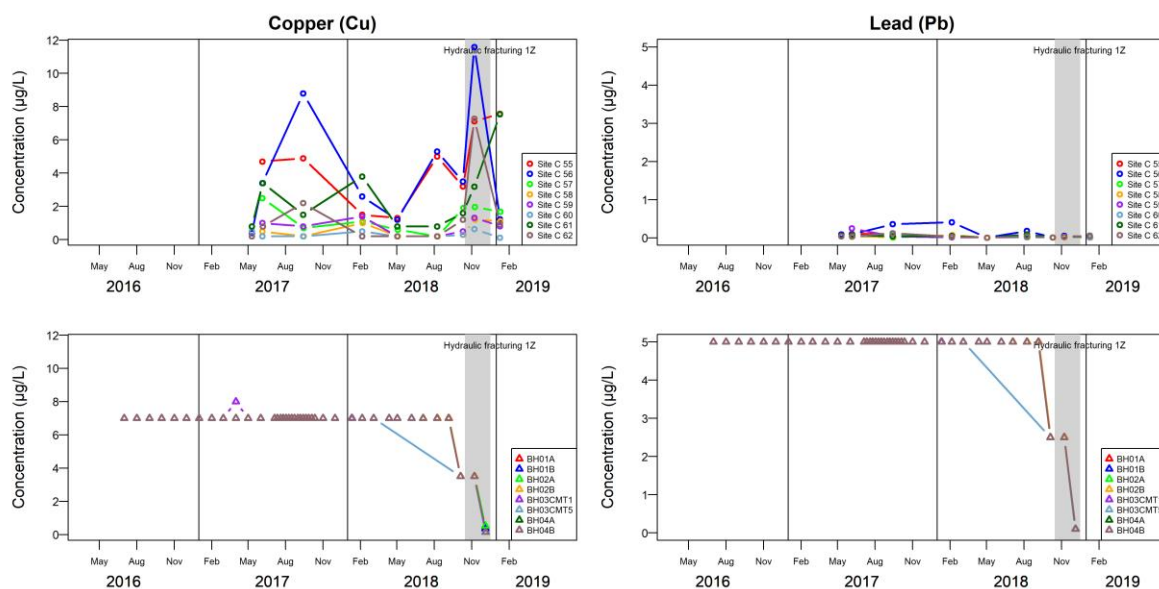


**Figure 26. Temporal variation in copper and lead in groundwater from the monitoring boreholes at PNR. Circles are BGS data; triangles Cuadrilla**

Cuadrilla detection limits for some organic compounds are also relatively high (e.g. acrylamide: 50 µg/L); again all compounds were reported as detects pre-October 2018.

Despite the temporal variability displayed by several analytes for the PNR boreholes, preliminary investigation shows no clear evidence of impact on groundwater quality from hydraulic fracturing of PNR borehole PNR-1z during late 2018. For key water-quality indicator parameters in the analytical suite (e.g. Na, CH<sub>4</sub>), variations appear to have been within the range of baseline concentrations at any given sampling site.

From the timescale of monitoring of the PNR boreholes, it is as yet unclear whether groundwater has any systematic seasonal variation in chemical composition, as observed in boreholes at KMA. There is a hint of seasonality in the groundwater in BH01B (Site C 56), though for the other boreholes/ports, any trends are masked by noise (Cuadrilla) or infrequent sampling (BGS).

## 2.5 MULTILEVEL SAMPLERS

Groundwater from the BGS multilevel array (CMT<sup>8</sup>/Waterloo system<sup>9</sup>) installed close to KMA has been sampled up to nine times since 2017 (Figure 27). Dissolved CH<sub>4</sub> concentrations show a large range over the depth intervals of the sampling ports, with consistent maxima (up to 78 µg/L) observed in the range 50–70 mbgl. Highest concentrations occur in less weathered portions of the Kimmeridge Formation, although a comparatively low concentration occurs in groundwater from the lowest port at 75 m depth. Temporal variations in CH<sub>4</sub> concentration (Figure 27) show either no discernible trend or an indication of a decrease over the period of

<sup>8</sup> Solinst Model 401 CMT Multilevel sampling system

<sup>9</sup> Solinst Model 403 Waterloo Multilevel sampling system

monitoring. Further research to better understand the controls on methane production and behaviour is being carried out as part of the NERC-ESRC funded Equipt4Risk project.

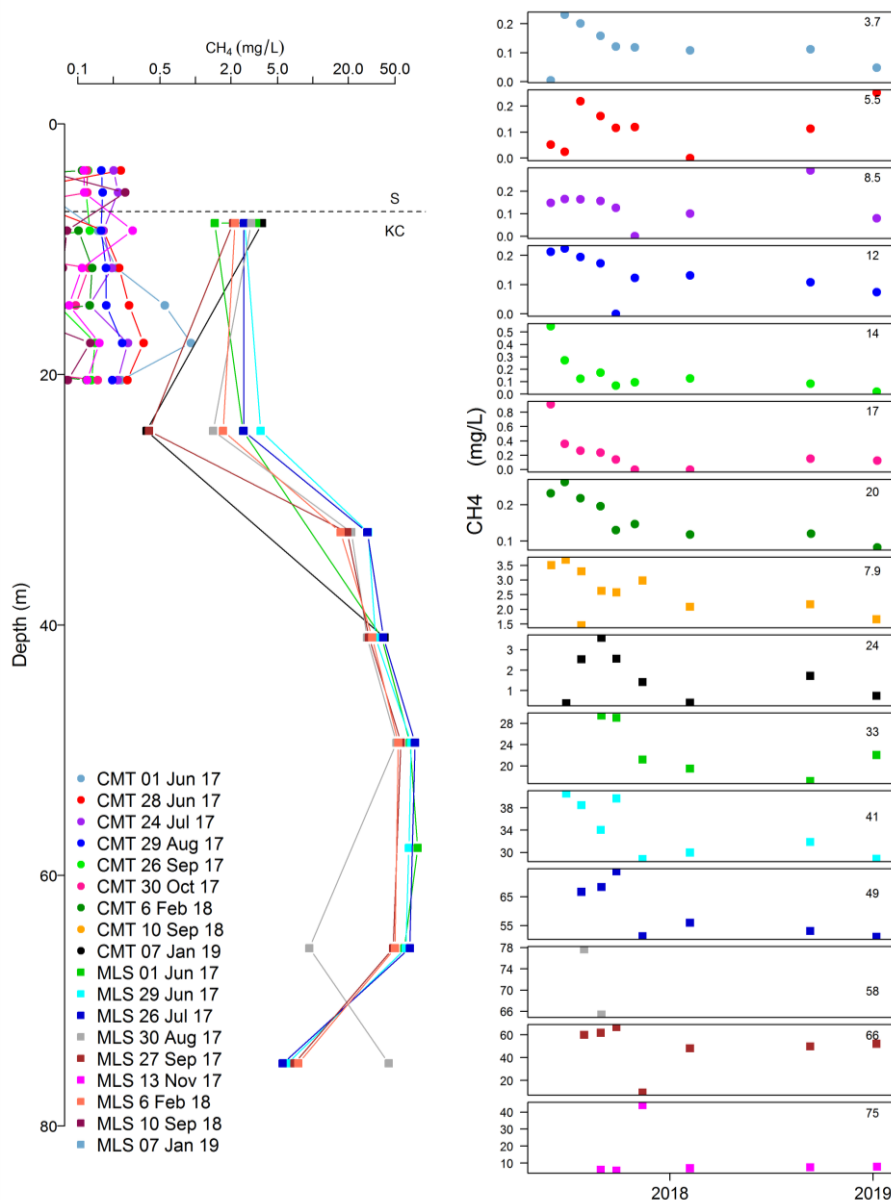


**Figure 27. Variations in dissolved methane concentration with depth and time in multilevel samplers installed in the Superficial/Kimmeridge formations in proximity to KMA (port depths given in metres in time-series plots)**

## 2.6 REAL-TIME MONITORING

Real-time monitoring of groundwater quality and level has continued in five boreholes within the Superficial aquifer over the year of investigation. Data are shown for pH, SEC, water temperature and groundwater level for the five boreholes in Figure 28. Obviously-spurious data due to sensor malfunction have been omitted but data recording periods of recalibration (depicted by vertical traces) remain as an indication of recalibration frequency and impact.

The time-series data record limitations due to instrument drift in some pH and SEC measurements (Figure 28). However, the largest variation observed, in excess of some 1000  $\mu\text{S}/\text{cm}$  for SEC in EBM8, is believed to record a real temporal variation. The two years' worth

of real-time data provide a further record of baseline groundwater chemical and physical conditions beyond the spot sampling described above, against which any changes can be compared in the event of exploration activity taking place.

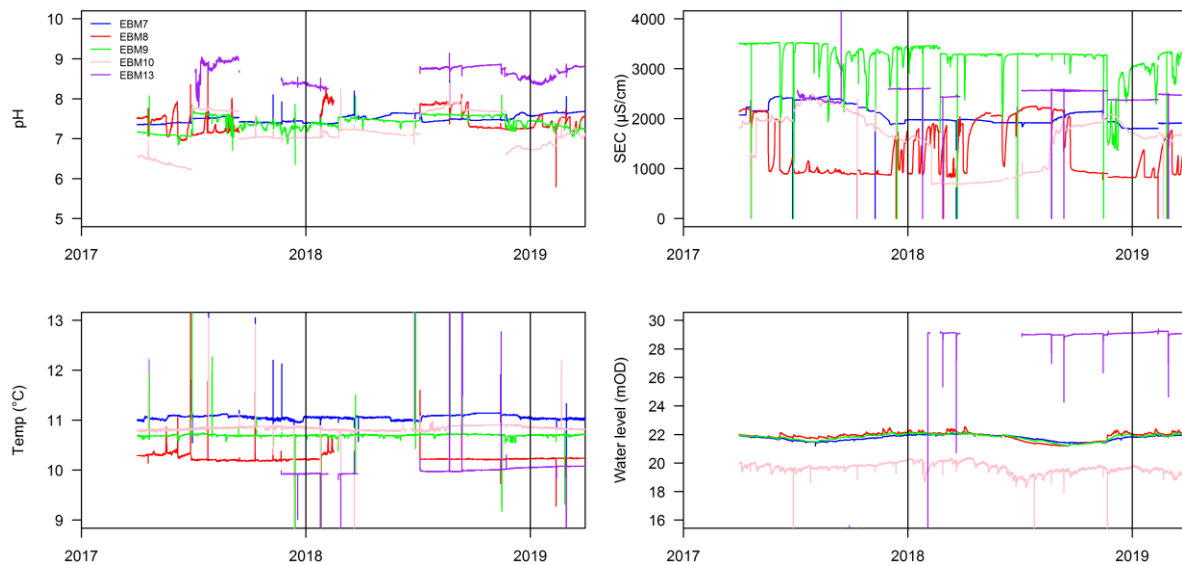


**Figure 28. Real-time data for pH, SEC, temperature and water level in groundwater from five monitoring boreholes in the Vale of Pickering (2017-2019)**

## 2.7 STATISTICAL MODELLING OF GROUNDWATER AND SURFACE WATER MEASUREMENTS

### 2.7.1 Rationale

In the event of hydrocarbon operations beginning in Kirby Misperton, our measurements of water-quality parameters made during the baseline phase will be compared to measurements during the operational phase to determine whether any detectable changes have occurred. Robust and objective protocols are required to determine whether any differences observed between measurements from each phase are larger than those that could have resulted wholly due to the underlying variability of the measurements.

However, as demonstrated, the baseline measurements indicate complex patterns of variation for each analyte:

- the mean and standard deviation for a given parameter vary greatly from site to site.;
- the time series from individual sites include large fluctuations and spikes where single large values occur during a period of generally small measurements;
- the large measurement fluctuations that are evident do not appear to follow regular seasonal or temporal trends nor do they occur at the same time at different sites.

Such behaviour is inconsistent with many statistical tests of differences between sets of measurements.

Previous statistical analyses of baseline datasets have centred upon the methods presented in a report by the Environment Agency (EA, 2019) which suggests that:

1. graphical summaries (time series and box-whisker plots) of a subset of key analytes be produced for each site and inspected;
2. outliers amongst these data be identified;

3. summary statistics of the central tendency and spread of the measurements be produced for each site and for each analyte, both including and omitting outliers;
4. tests be conducted to determine whether the measurements of each analyte at each site are consistent with data drawn independently from a Normal distribution with a constant mean;
5. change indicator values (CIVs) be established for each analyte at each site. These values are defined as the sum of the mean of the data with outliers omitted plus the magnitude of the detectable change, the detectable change being the degree of change that would be expected (with a probability of 80%) to be recognised as significant at the  $p=0.05$  level. These CIVs should prompt further investigation rather than being seen as strict thresholds or limits.

A number of questions remain regarding the precise manner in which the CIVs will be applied. First, over what time period will measurements from the operational phase be compared to the CIVs? The method used for deriving them appears to imply that the comparison will be made once the number of sampling rounds in the operational phase matches the number of rounds in the baseline phase. If this were the case, changes in the analytes on the commencement of hydraulic fracturing activities will remain uninvestigated for months or years.

The handling of outliers amongst the data is also of concern. Since outliers are omitted from the mean values used in the derivation of the CIVs, they would presumably be omitted from the operational phase data which are compared to the CIVs to ensure a fair comparison. However, in the event that activities did lead to large measurement values during the operational phase, these could be dismissed as outliers and not considered.

The approach outlined in a recent Environment Agency report (EA, 2019) indicates that where the baseline data are inconsistent with independent samples from a Normal distribution, the comparisons to the CIV should be treated with caution. It is not clear what this would mean in practice.

In addition, conducting comparisons to the CIVs on a site-by-site basis could lead to a rather confused picture if measurements exceed the CIV at a subset of locations.

Early plans for our statistical evaluation of the baseline and operational water-quality data concerned use of an approach based on the calculation of the space-time mean of each analyte according to the method of Brus (2014). The space-time mean is the average of the analyte value across a specified window in space and time as predicted by a statistical model. The model used by Brus (2014) assumes much more regular variation of the analytes than was observed during the baseline period.

We propose to modify the model of Brus (2014) so that it is consistent with the baseline data and then use it to predict the space-time mean across portions or windows of the operational phase. We define the spatial extent of the window of interest to be the set of API (Area of Potential Impact; Ward et al., 2017) measurement locations<sup>10</sup>. The temporal extent is flexible but in this report we consider it to be each individual round of sampling. We determine the space-time mean for each round of sampling during the operational phase and test whether this quantity is consistent with the baseline data. Thus, this approach could reveal a change in the

---

<sup>10</sup> Whilst API – Area of Potential Interest – suggest as an area, it should be recognised that for groundwater monitoring sites within the API area are monitoring a three-dimensional system or volume, i.e. part of an aquifer. The selection of monitoring sites to be included in the API (or control area) should be informed by the conceptual model and be monitoring at locations with the same hydrogeological characteristics. Therefore they are necessarily aquifer- and, by association, depth-specific.

analytes from just one round of sampling. It does not automatically omit outliers from the analysis and does not require the assumption of the measurements being consistent with an independently sampled Normal distribution. Also, it reduces the statistical analyses to a single test or each analyte.

### **2.7.2 Overview of the approach**

We require a statistical model of the baseline variation of each analyte. We will then use this model to determine the degree of variation that could be expected in the data from the operational period if no underlying change has occurred. Finally, we will compare the actual variation in the operational phase to this expected variation to determine if they are consistent. The baseline model must account for any patterns in the model due to spatial or temporal correlation amongst the data or a tendency for measurements from the same round of sampling to be similar.

Before estimating a statistical model, we standardise the data so that the measurements from each site are comparable. The majority of the analytes have a highly skewed (i.e. asymmetric) distribution. Where this is the case we apply a log-transform to reduce this skew so that the data are more consistent with a Normal distribution. We then standardise the data from each site by subtracting the mean for that site and then dividing by the standard distribution.

Our most basic model assumes that the standardised data are drawn from a Normal distribution with mean of zero and unit variance. We calculate and inspect variograms of the standardised data to see if any spatial and/or temporal correlation is evident. Where it is, an appropriate correlation term is added to the model. Similarly, we explore whether the mean of the baseline data varies with time and again add an appropriate term to the model if required. A statistical test is used to confirm that any additional term does improve the model before it is finally accepted.

We use our baseline model to determine the expected mean standardised measurement value across the API for a future round of sampling and the specified confidence limits for this mean. The model can account for sites being missed in a future sampling round. If the observed mean of the standardised measurements falls outside the confidence limits then this is seen as an indication that further investigation is required.

One concern about the approach is whether sufficient baseline data exist to estimate such a model accurately. We test this by using the models to simulate long time series of data that could be expected for each analyte. We then follow the above procedure, estimating models for baselines of different length and treating the remaining simulated data as the operational phase. In these simulated examples there is no underlying difference between the baseline and operational phases. Therefore, a substantial number of cases where further investigation is required will be an indication that more baseline data are required.

### **2.7.3 Technical details of the modelling methodology**

Statistical analysis of Vale of Pickering data is presented of data of four analytes (CH<sub>4</sub>, Cl, Na and NH<sub>4</sub>) from 20 API Superficial groundwater sites (Figure 29). The approach can be applied to any analyte, but only four are presented here to demonstrate the development/application of the statistical methodology. However, the four were selected as being representative change indicators. For example, demonstrating variations in salinity (Na, Cl), the hydrocarbon source gas (CH<sub>4</sub>) and a redox indicator (NH<sub>4</sub>). The selection of analytes also considered the frequency of measurement quantification (LOQ). Automation of the process and production of a 'plug-in' programme for rapid analysis of data will be produced in a further phase of the project.

The data considered were collected irregularly from September 2015 to August 2018. The intervals between two adjacent sampling rounds range from 1 month to 3 months.

For the purpose of modelling, the sampling dates are rearranged into 29 ‘representative’ sampling dates, by shifting the actual dates to their nearest ‘representative’ sampling dates.

Log transformation was applied to the CH<sub>4</sub>, Cl and Na data as the distributions for these variables are severely right skewed. No transformation was applied to the NH<sub>4</sub> data. The (transformed) data were first standardised site by site, as:

$$Y_{tj} = \frac{Y_{tj}^* - \hat{\mu}_j}{\hat{\sigma}_j}, \quad j = 1, \dots, J; t = 1, \dots, T,$$

where  $Y_{tj}^*$  is the observation taken at site  $j$  time  $t$ ,  $\hat{\mu}_j$  and  $\hat{\sigma}_j$  are the sample mean and standard deviation of the data at site  $j$ . Then spatial/temporal correlation in the data were investigated through empirical spatial and temporal variograms, computed as:

$$\gamma(h) = \frac{1}{2|N(h)|} \sum_{i,j \in N(h)} (Y_i - Y_j)^2,$$

where  $N(h)$  is the collection of pairs of standardised observations  $Y_i, Y_j$  that are distance  $h$  apart (distance can be in space or in time) and  $|N(h)|$  is the number of such pairs in the collection. The empirical variograms can be computed using the ‘gstat’ package in R (Gräler et al., 2016). Provided that there are no evident spatial or temporal correlations, the baseline distribution can be established by the sample means and standard deviations.

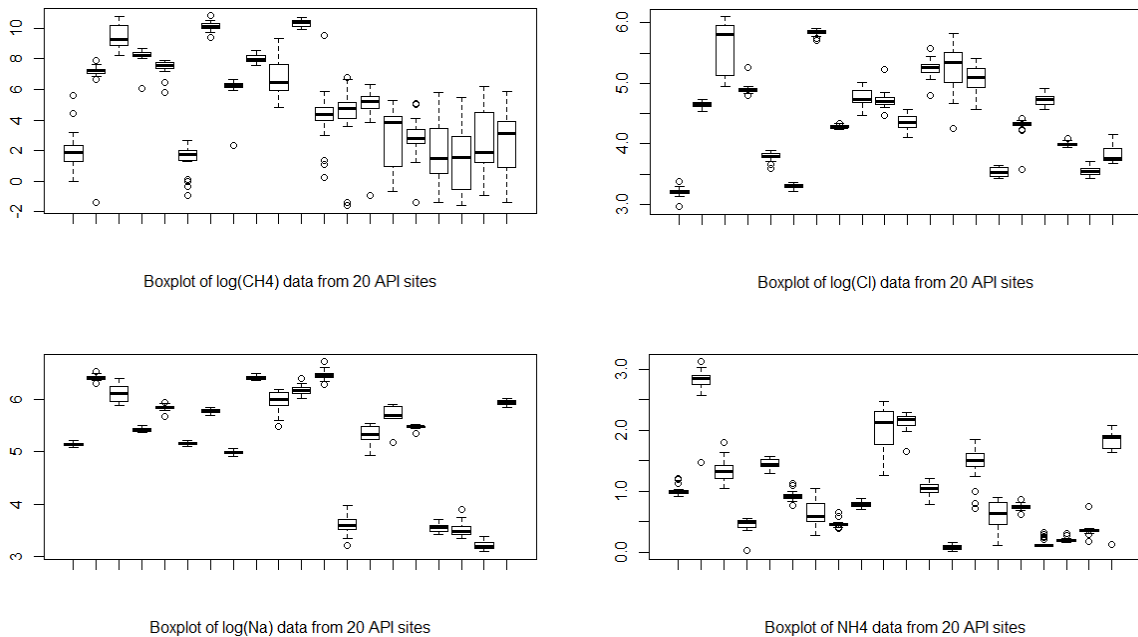


**Figure 29.** Boxplots of log transformed CH<sub>4</sub> (top left), log transformed Cl (top right), log transformed Na (bottom left) and NH<sub>4</sub> (bottom right) from 20 API sites investigated in this section (units: mg/L; µg/L for CH<sub>4</sub>)

In the presence of spatial/temporal correlations, they will need to be appropriately accounted for in the model to quantify better the uncertainty of the space-time mean. Different models with residual correlation structure reflecting the spatial/temporal correlations may be considered, such as:

$$Y = X\beta + \varepsilon, \quad \varepsilon \sim N(0, \sigma_\varepsilon^2 V),$$

where  $V$  is a valid correlation matrix describing the spatial/temporal structure in the data. Furthermore, a random effect component may be introduced to account for additional unexplained variations, e.g. temporal random variation not explained by the covariates in the design matrix  $X$ . This can be modelled as:

$$Y = X\beta + Z\eta + \varepsilon, \quad \eta \sim N(0, \sigma_\eta^2 I), \quad \varepsilon \sim N(0, \sigma_\varepsilon^2 V)$$

where  $Z$  is the temporal random effect design matrix,  $\eta$  is the corresponding random effect coefficient vector and  $I$  is the identity matrix. Parameters in the above models can be estimated by maximizing the (residual) log-likelihood, using package ‘nlme’ in R (Pinheiro et al., 2018).

The sample standard deviations may be adjusted using the estimated covariance matrix and/or the random effect variance. Confidence interval of the mean standardised observations (i.e. standardised observations averaged over sites) at time point  $t$  can be obtained from the estimated model, as:

$$\pm z_\alpha \sqrt{\hat{\sigma}_\eta^2 + \frac{\hat{\sigma}_\varepsilon^2}{n_t}},$$

where  $z_\alpha$  is the upper  $\alpha$  quantile of the standard Normal distribution (e.g. 1.96 for the 95% confidence interval) and  $n_t$  is the number of observations recorded at the sampling round  $t$ . The pointwise confidence intervals form a confidence band, which can be extended to future time points to decide if the measurements taken at a future date should raise any concern.

The above approach is applied to the observed data to establish the baseline model. When new data are acquired, they are first standardised using the empirical site means and standard deviations from the baseline model. Then the mean of these standardised data across the API are calculated for each round of sampling. The corresponding confidence bands are constructed using the estimated baseline model parameters (including the parameters associated with the random effect or the correlation matrix). Finally, the observed standardised mean is compared to these confidence limits to assess whether this should trigger further investigation, i.e. if it was outside the confidence limit range.

The resulting baseline models for the CH<sub>4</sub>, Cl, Na and NH<sub>4</sub> data from the 20 API sites are presented in Table 3 - Table 10.

There appear to be no distinctive spatial or temporal correlation in the data for any of the four analytes. However, there are random temporal fluctuations in the standardised data that cannot be explained fully by a simple intercept model. Therefore, models with temporal random effect were fitted.

(1) Baseline model for the log-transformed CH<sub>4</sub> data

**Table 3. Means and standard deviations of log(CH<sub>4</sub>)**

<i>log(CH<sub>4</sub>)</i>	<i>mean</i>	<i>std.dev</i>
Site 1	2.1313	1.3495
Site 14	6.7410	2.1199
Site 15	9.4393	0.7974
Site 3	8.2055	0.5189
Site 35	7.4375	0.5034
Site 36	1.4336	0.9981
Site 38	10.1261	0.2998
Site 4	6.0893	0.8776
Site 40	8.0146	0.2636
Site BGS 41	6.6386	1.2599
Site BGS 42	10.3406	0.2239
Site BGS 43	4.2012	1.8683
Site BGS 44	4.2803	2.0305
Site BGS 45	4.9707	1.4722
Site BGS 46	2.9145	2.2709
Site BGS 54	2.8170	1.3402
Site TE 48	1.7266	1.9625
Site TE 49	1.6137	2.2599
Site TE 50	2.4442	2.2160
Site TE 52	2.4195	2.2945

Table 3 shows the sample mean, standard deviation of the 20 API sites. A histogram of the standardised data is shown in the left panel of Figure 30.

The empirical spatial and temporal variograms (middle/right panel of Figure 30) show no distinctive patterns and hence no distinctive correlations.

A linear mixed effect model with temporal random effect was fitted. The model was tested against a simple intercept model and the likelihood ratio test suggests that the temporal random effect is significant (Table 3). The mean standardised time series and the adjusted confidence bands are shown in Figure 31.

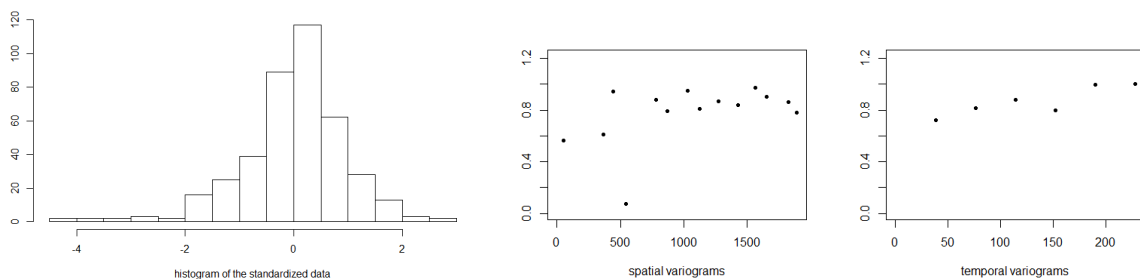


**Figure 30. (left): histogram of the standardised log(CH<sub>4</sub>) data. (middle) Empirical spatial variogram (cut off at 2000 m); and (right) empirical temporal variogram (cut off at 6 sampling rounds) of the standardised data**

**Table 4. The fitted temporal random effect model**

<i>The estimated linear mixed effect model</i>				
	<b>Value</b>	<b>95% interval</b>		
<b>Random std</b>	0.3065	(0.1929, 0.4871)		
<b>Residual std</b>	0.9304	(0.8664, 0.9992)		
<i>Likelihood ratio (LR) test</i>				
	<b>DF</b>	<b>LogLik</b>	<b>LR</b>	<b>p-value</b>
<b>Simple</b>	2	-566.52		
<b>Mixed</b>	3	-559.53	13.97	0.0002

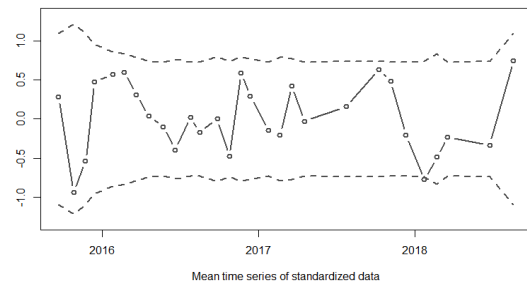


**Figure 31. The mean standardised time series and the adjusted 95% confidence band**

(2) *Baseline model for the log transformed Cl data*

**Table 5. Means and standard deviations of log(Cl)**

<i>log(Cl)</i>	<i>mean</i>	<i>std.dev</i>
Site 1	3.1958	0.0793
Site 14	4.6386	0.0510
Site 15	5.5996	0.4334
Site 3	4.8976	0.0879
Site 35	3.7910	0.0757
Site 36	3.3019	0.0400
Site 38	5.8389	0.0472
Site 4	4.2831	0.0261
Site 40	4.7641	0.1321
Site BGS 41	4.7254	0.1401
Site BGS 42	4.3543	0.1340
Site BGS 43	5.2502	0.1564
Site BGS 44	5.2573	0.3975
Site BGS 45	5.0552	0.2302
Site BGS 46	3.5344	0.0845
Site BGS 54	4.2917	0.1682
Site TE 48	4.7244	0.0922
Site TE 49	3.9930	0.0375
Site TE 50	3.5437	0.0655
Site TE 52	3.8327	0.1604

Table 5 shows the sample mean, standard deviation of 20 API sites. A histogram of the standardised data is shown in the left panel of Figure 32.

The empirical variograms (middle/right panel of Figure 32) show no distinctive spatial or temporal correlation.

A linear mixed effect model with temporal random effect was fitted. The model was tested against a simple intercept model and the likelihood ratio test suggests that the temporal random effect is significant (Table 5). The mean standardised time series and the adjusted confidence bands are shown in Figure 33.

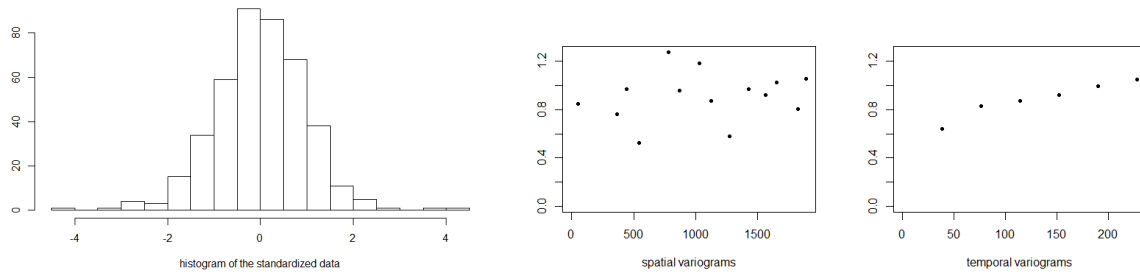


**Figure 32. (left) Histogram of the standardised log (CI) data. (middle) Empirical spatial variogram (cut off at 2000m) and (right) empirical temporal variogram (cut off at 6 sampling rounds) of the standardised data**

**Table 6. The fitted temporal random effect model**

<i>The estimated linear mixed effect model</i>				
	Value	95% interval		
<b>Random std</b>	0.3134	(0.2020, 0.4860)		
<b>Residual std</b>	0.9280	(0.8651, 0.9954)		
<i>Likelihood ratio (LR) test</i>				
	DF	LogLik	LR	p-value
<b>Simple</b>	2	-586.41		
<b>Mixed</b>	3	-578.18	16.46	<.0001

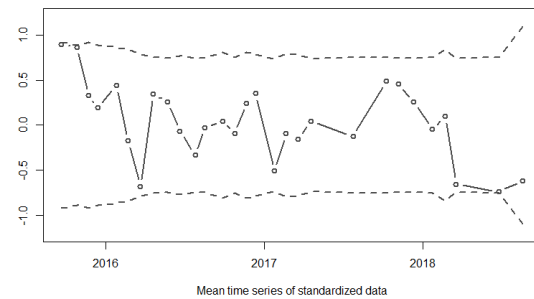


**Figure 33. The averaged (over sites) time series and the adjusted 95% confidence band**

(3) Baseline model for the log transformed Na data

**Table 7. Means and standard deviations of log(Na)**

<i>log(Na)</i>	<i>mean</i>	<i>std.dev</i>
Site 1	5.1414	0.0354
Site 14	6.4211	0.0512
Site 15	6.1216	0.1692
Site 3	5.4266	0.0374
Site 35	5.8552	0.0530
Site 36	5.1615	0.0354
Site 38	5.7823	0.0369
Site 4	4.9864	0.0349
Site 40	6.4208	0.0413
Site BGS 41	5.9700	0.1994
Site BGS 42	6.1841	0.0839
Site BGS 43	6.4713	0.0883
Site BGS 44	3.6084	0.1827
Site BGS 45	5.3307	0.1744
Site BGS 46	5.6686	0.2642
Site BGS 54	5.4771	0.0311
Site TE 48	3.5399	0.0858
Site TE 49	3.5100	0.1309
Site TE 50	3.1995	0.0815
Site TE 52	5.9516	0.0452

Table 7 shows the sample mean and standard deviation of 20 API sites for Na. A histogram of the standardised data is shown in the left panel of Figure 34.

The empirical variograms (middle/right panel of Figure 34) show no distinctive spatial or temporal correlation.

A linear mixed-effect model with temporal random effect was fitted. The model was tested against a simple intercept model and the likelihood ratio test suggests that the temporal random effect is significant (Table 8). The mean standardised time series and the adjusted confidence bands are shown in Figure 35.

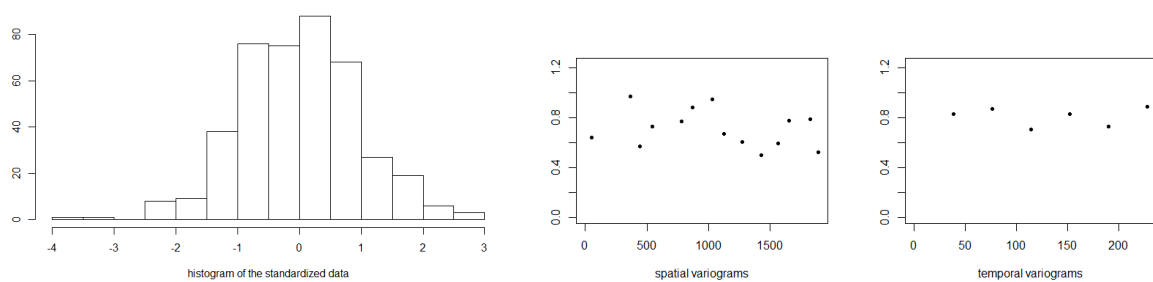


**Figure 34. (left) Histogram of the standardised log (Na) data. (middle) Empirical spatial variogram (cut off at 2000m) and (right) empirical temporal variogram (cut off at 6 sampling rounds) of the standardised data**

**Table 8. The fitted temporal random effect model**

<i>The estimated linear mixed effect model</i>				
	<b>Value</b>	<b>95% interval</b>		
<b>Random std</b>	0.5432	(0.3938, 0.7492)		
<b>Residual std</b>	0.8434	(0.7861, 0.9048)		
<i>Likelihood ratio (LR) test</i>				
	<b>DF</b>	<b>LogLik</b>	<b>LR</b>	<b>p-value</b>
<b>Simple</b>	2	-586.41		
<b>Mixed</b>	3	-551.46	69.89	<.0001

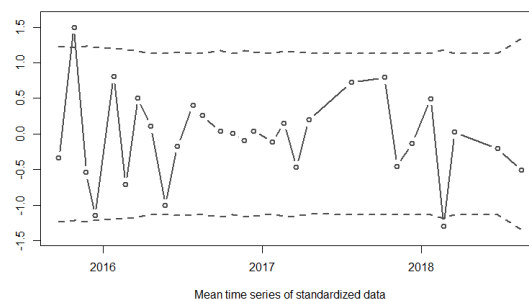


**Figure 35. The averaged (over sites) time series and the adjusted 95% confidence band**

(4) *Baseline model for the NH<sub>4</sub> data*

**Table 9. Means and standard deviations of NH<sub>4</sub>**

<i>NH<sub>4</sub></i>	<i>mean</i>	<i>std.dev</i>
<i>Site 1</i>	1.0068	0.0789
<i>Site 14</i>	2.7772	0.3352
<i>Site 15</i>	1.3326	0.1671
<i>Site 3</i>	0.4540	0.1121
<i>Site 35</i>	1.4509	0.0794
<i>Site 36</i>	0.9227	0.0832
<i>Site 38</i>	0.6324	0.2112
<i>Site 4</i>	0.4646	0.0591
<i>Site 40</i>	0.7912	0.0441
<i>Site BGS 41</i>	2.0101	0.3747
<i>Site BGS 42</i>	2.1443	0.1438
<i>Site BGS 43</i>	1.0454	0.1074
<i>Site BGS 44</i>	0.0783	0.0434
<i>Site BGS 45</i>	1.4473	0.3012
<i>Site BGS 46</i>	0.5918	0.3020
<i>Site BGS 54</i>	0.7407	0.0540
<i>Site TE 48</i>	0.1434	0.0736
<i>Site TE 49</i>	0.2034	0.0414
<i>Site TE 50</i>	0.3635	0.1013
<i>Site TE 52</i>	1.7615	0.4066

Table 9 shows the sample mean, standard deviation of 20 API sites. A histogram of the standardised data is shown in the left panel of Figure 36.

The empirical variograms (middle/right panel of Figure 36) show no distinctive spatial or temporal correlation.

A linear mixed effect model with temporal random effect was fitted. The model was tested against a simple intercept model and the likelihood ratio test suggests that the temporal random effect is significant at the level of 0.05 (Table 10). The mean standardised time series and the adjusted confidence bands are shown in Figure 37.

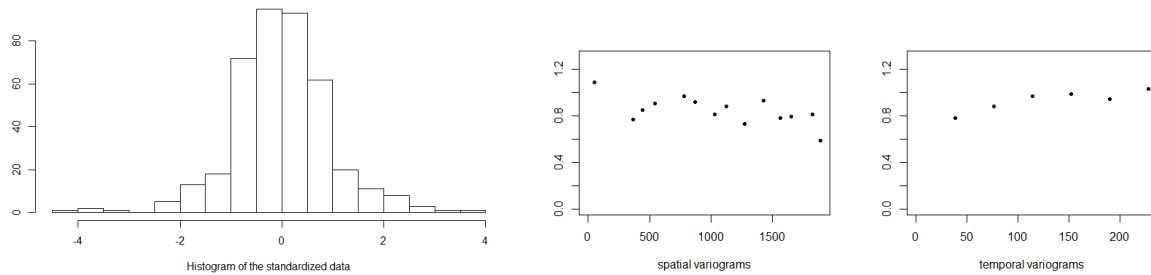


**Figure 36. (left) Histogram of the standardised NH4 data. (middle) Empirical spatial variogram (cut off at 2000m) and (right) empirical temporal variogram (cut off at 6 sampling rounds) of the standardised data**

**Table 10. The fitted temporal random effect model**

<i>The estimated linear mixed effect model</i>				
	Value	95% interval		
<b>Random std</b>	0.2244	(0.1182, 0.4261)		
<b>Residual std</b>	0.9519	(0.8865, 1.0221)		
<i>Likelihood ratio (LR) test</i>				
	DF	LogLik	LR	p-value
<b>Simple</b>	2	-567.94		

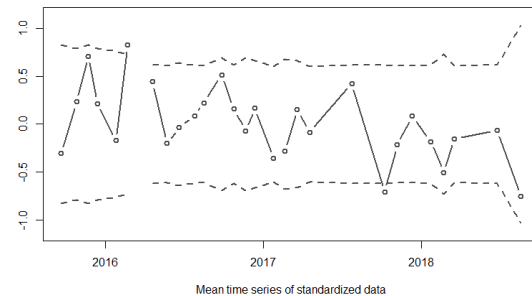


**Figure 37. The averaged (over sites) time series and the adjusted 95% confidence band**

## 2.7.4 Application of the modelling approach

The statistical approach assumes that the model reflects accurately the baseline variation and it does not account for any uncertainty in estimating this model. We therefore need to confirm that each model has been estimated sufficiently accurately such that this missing component of uncertainty does not lead to observations from the operational period being erroneously identified as inconsistent with the baseline period.

For demonstration purposes, we do this by splitting the available data into two parts. One, consisting of 21 rounds of sampling up to July 2017, is treated as the ‘baseline’ period, whereas the remaining eight rounds of sampling are treated as if they were the ‘operational’ phase. The modelling approach was applied to these ‘baseline’ data and then the observed means from the ‘operational’ phase were compared to the estimated baseline model. If the fitted baseline model is able to capture the expected variation (i.e. the natural, background variation) in the data appropriately, then the majority, if not all, of the standardised operational data should fall within the constructed confidence band. However, in our tests there are a number of cases where the mean standardised operational value falls outside the 95% and the 99.7% (3 times the standard deviations) confidence bands (see Figure 38).

A closer examination of the data suggests that this is due to the large fluctuations in the analyte measurements towards the end of the time series. Thus it appears that 20 rounds of sampling are not sufficient to estimate the baseline model accurately.

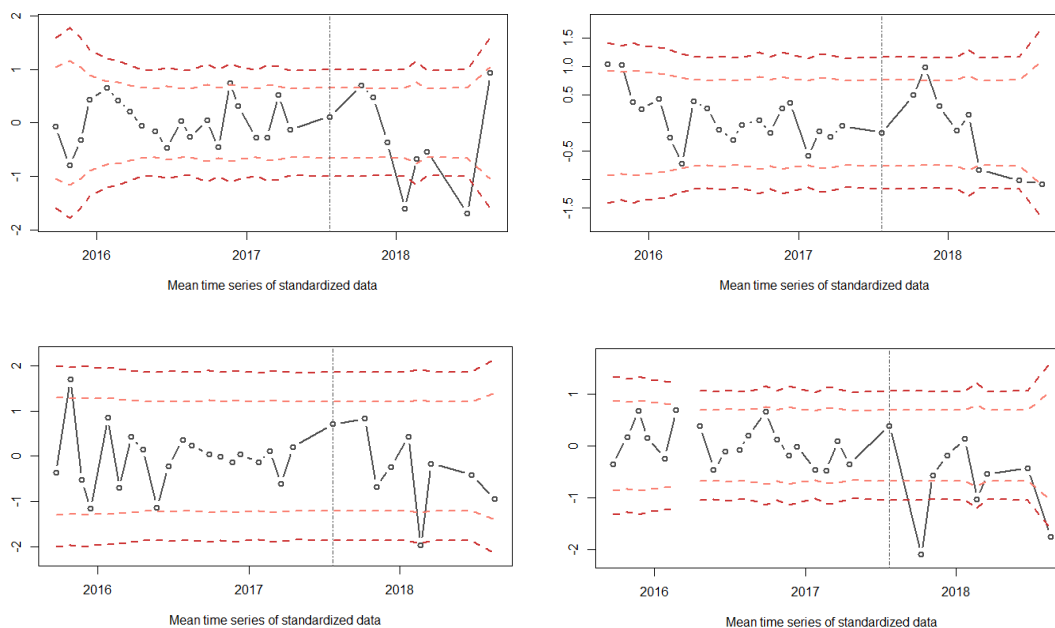


**Figure 38. Time series plots of the mean standardised  $\log(\text{CH}_4)$  (top left),  $\log(\text{Cl})$  (top right),  $\log(\text{Na})$  (bottom left) and  $\text{NH}_4$  (bottom right), along with the adjusted 95% (orange) and 99.7% (red) confidence bands from baseline models fitted to data up to July 2017**

To investigate further the number of observations required to capture the scale of variation in the observed data, a simulation study was carried out. Time series were generated for the 20 sites based on the empirical distributions of the observed data of the four analytes. Baseline models were built using the first 20, 30, 50 and 80 simulated observations and were tested on the next 100 simulated observations. The process was repeated 500 times. The results confirm that using only 20 rounds of sampling to characterise the baseline leads to a substantial number of false positive results. On average, almost 10% (rather than the expected 5%) of the simulated rounds of sampling have a standardised mean outside the 95% confidence interval. This decreases to an average of 8% when the baseline is characterised by 30 rounds of sampling, 6.5% for 50 rounds and 6% for 80 rounds. The number of locations at which the analytes were measured appeared to be less important than the number of rounds of sampling, with similar results being achieved based on data from only four sites.

### 2.7.5 Discussion

We have described an approach for predicting the distribution of the standardised space-time mean of analytes under baseline conditions. These predictions can be used to determine whether the measurements from future sampling rounds are significantly different than would be expected under the baseline conditions. Tests using data simulated from this model indicate that sufficient baseline data have been gathered for its estimation.

Some caution should be adopted when using this approach to determine the impact of hydraulic fracturing activities. The model assumes that the baseline data are representative of the long-term variation of each analyte. This might not be the case if the analytes naturally fluctuate over timescales that are longer than the baseline period captured or if long-term trends occur for reasons unrelated to the hydraulic fracturing activities. If these long-term trends apply over a sufficient spatial extent then they should also be evident in the measurements from the control (non-API) sites.

The analysis relies on a statistical model that greatly simplifies the variation of the analytes. Given the enormously heterogeneous variation that was observed over time and space and the logistic constraints that limit the frequency and density of sampling it is not possible to create a model that can replicate the full complexity of the analyte variation. These limitations of the model could lead to actual impacts being overlooked or behaviour being falsely flagged as inconsistent with the baseline.

Therefore, in common with the Environment Agency (EA, 2019) report we recommend that apparently significant deviations from the baseline model be viewed as an indication that further investigation is required and not as a definitive sign of the water quality being impacted by hydrocarbon exploration activities.

In studying the space-time mean across the API, this approach considers one potential signature of anthropogenic impact upon groundwater quality – namely a change in the average behaviour throughout the API. Impacts could potentially be more localised. If statistical tests were conducted for impacts over every plausible spatial scale then, even in the absence of impacts, some of these tests are likely to indicate significant change due to the problems of conducting multiple hypothesis tests (Miller, 1981).

An adjustment could be made to the tests to account for this false discovery rate (Yoav and Hochberg, 1995), but this would reduce the power of each individual test. Whilst we do not recommend a large number of formal tests on the data, it would be prudent to inspect the individual measurements from each round of sampling and flag any that exceed the maximum observed during the baseline period as being worthy of further investigation. Longer-term (e.g. across two or three sampling rounds) means of the analyte measurements at each site could also be inspected in a similar way.

Our simulation tests indicate that this approach to monitoring the standardised mean concentrations in the API does lead to a number of false positive results. For example, if the baseline is characterised by 30 rounds of sampling and the same models of variation apply in the operational period, then the standardised mean of 8% rather than the expected 5% of simulated rounds of sampling will lie outside the 95% confidence interval. This implies that a substantial amount of sampling effort is required to characterise the baseline. Further work will explore whether more pragmatic statistical approaches requiring fewer baseline data might be applied. These approaches could be tested on the statistical models that we have generated to determine the detection limits for any impact of hydraulic fracturing operations upon the concentrations of analytes and the expected proportion of false positive results.

## **2.8 SUMMARY OF BASELINE: VALE OF PICKERING AND THE FYLDE**

Water monitoring networks (groundwater and surface water) have been designed according to the underlying conceptual models and infrastructure installed where necessary to instigate monitoring programmes in the Vale of Pickering (Figure 39) and The Fylde (Figure 40). The monitoring networks comprise private boreholes where suitable, purpose-designed and drilled boreholes, multi-level samplers and surface water (streams and rivers) sampling sites. Sampling began at each location in 2015 and has continued thereafter, usually on a quarterly schedule, but increasing to monthly immediately before and during hydraulic fracturing (Fylde), or in anticipation of hydraulic fracturing (Vale of Pickering).

Monitoring has established temporal variability in water compositions at both groundwater and surface water monitoring sites. Variability is particularly large in streamwater samples at any given site but shallow groundwaters also display variations, including notable seasonal variation at some sites. In both the Vale of Pickering and The Fylde, the spatial variability is

observed to be much greater than temporal variability. The data emphasise the fact that baseline compositions vary over range which requires monitoring effort to capture. At each location, data for groundwater from aquifers that are below the shallowest aquifer and separated by low permeability rocks reveal that groundwater quality in these deeper aquifers is too poor for practical use, e.g. as a drinking water source, albeit with limited numbers of sampling points.

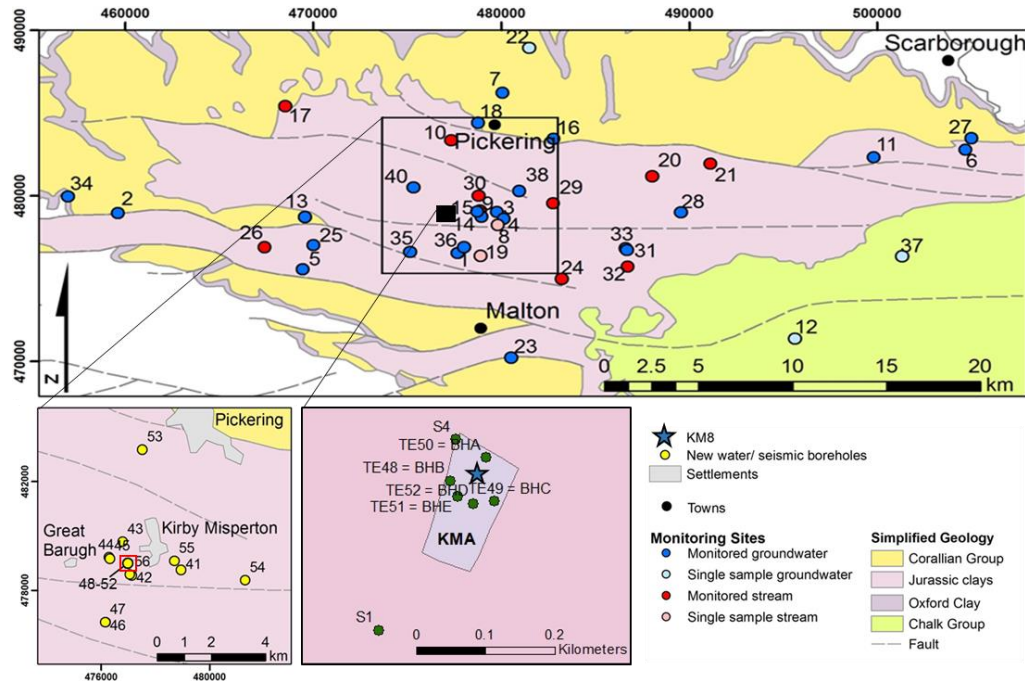


**Figure 39. Geological map of the Vale of Pickering showing sampling locations used in this report. Insets shows boreholes close to Kirby Misperton and the shale gas well site (KM A).**

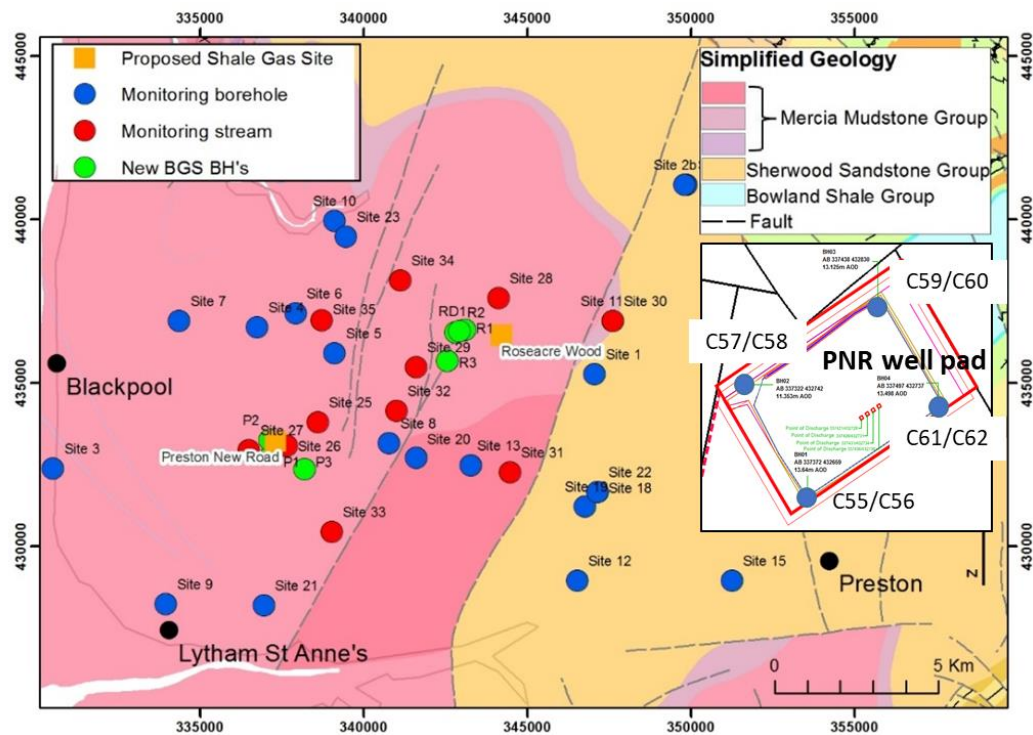


**Figure 40. Geological map of The Fylde showing sampling locations used in this report. Inset shows boreholes close to the shale gas well site (PNR).**

Tables in Annex 3 provide statistical summaries of water compositions in both locations under baseline conditions, i.e. up to February 2019 in the Vale of Pickering and early October 2018 in Fylde (end of baseline). The tables include summaries for individual boreholes on the well pads at the Preston New Road (PNR) and Kirby Misperton (KM8) shale gas exploration sites and summaries of spatial data for the main aquifers and streamwaters in the surrounding area at each location. In each case, the 95<sup>th</sup> percentile is given as a simple representation of the upper limit of baseline compositions. The summary tables include selected diagnostic analytes that summarise diverse characteristics of the water compositions (salinity, alkalinity, redox characteristics) and which are typically detectable. Organic compounds are not included as fully quantitative baseline analyses almost invariably have concentrations below detection limits. Analytes included in the local environmental permits for hydraulic fracturing fluid compositions (acrylamide) are also not detectable in baseline samples at either location.

Monitoring of water samples has been augmented with information provided from real-time monitoring (pH, temperature, SEC, total dissolved gases) at 5 locations close to PNR site, and 4 close to KM8 site. These records provide data for time periods between monitoring events. Data from these have been summarised periodically in project reports and are displayed on the BGS website ([www.bgs.ac.uk/lancashire](http://www.bgs.ac.uk/lancashire); [www.bgs.ac.uk/valeofpickering](http://www.bgs.ac.uk/valeofpickering)).

## 2.9 REFERENCES

- Bell, R A, Darling, W G, Ward, R S, Basava-Reddi, L, Halwa, L, Manamsa, K, and Dochartaigh, B E O. 2017. A baseline survey of dissolved methane in aquifers of Great Britain. *Science of the Total Environment*, Vol. 601, 1803-1813.
- Bishop, P K, and Lloyd, J W. 1991. Use of <sup>14</sup>C modelling to determine vulnerability and pollution of a carbonate aquifer: the Lincolnshire Limestone, eastern England. *Applied Geochemistry*, Vol. 6, 319-331.
- Brus, D.J. 2014. Statistical sampling approaches for soil monitoring. *European Journal of Soil Science*, 65, 779-791.
- Cuadrilla. 2016. PO7: Preston New Road groundwater monitoring borehole installation report. *Cuadrilla*, Hsse-Rpt-Site-001 (UK).
- Envireau Water. 2017. K8 Monitoring Boreholes as built construction report; KM8 Well, Kirby Misperton A Wellsite, North Yorkshire. *Envireau Water*.
- Gräler, B., Pebesma, E., and Heuvelink, G. 2016. Spatio-temporal interpolation using gstat. *The R Journal*, 8(1), 204-218.
- Miller, R.G. 1981. *Simultaneous Statistical Inference* 2nd Ed. Springer Verlag New York.
- Pinheiro, J., Bates, D., DebRoy, S., Sarkar, D., the R Core Team, 2018. nlme: Linear and Nonlinear Mixed Effects Model. R package version 3.1-137. <https://CRAN.R-project.org/package=nlme>.
- Environment Agency, 2019. Onshore Oil and Gas Monitoring: assessing the statistical significance of changes. Guidance Document. Ricardo Energy and the Environment Agency. Report No. SC160020.
- Third Energy. 2015. Kirby Misperton A Wellsite. KM8 Production Well, Water Monitoring Boreholes; Planning Statement. *Third Energy*.

Ward, R.S.; Smedley, P.L.; Allen, G.; Baptie, B.J.; Daraktchieva, Z.; Horleston, A.; Jones, D.G.; Jordan, C.J.; Lewis, A.; Lowry, D.; Purvis, R.M.; Rivett, M.O. 2017. Environmental Baseline Monitoring Project. Phase II, final report. British Geological Survey, OR/17/049, 163 pp.

Yoav, B, and Hochberg, Y. 1995. Controlling the false discovery rate: a practical and powerful approach to multiple testing. *Journal of the Royal Statistical Society, Series B.* 57, 289–300.

## 3 Ground Motion

### 3.1 INTRODUCTION

The Oil and Gas Authority (OGA) requires hydraulic fracturing operators to adhere to controls and protocols, including the levels of ground motion close to nearby dwellings and other structures (OGA, 2018).

There is speculation whether there is potential for shale gas operations at depth to cause surface ground deformation. Conventional oil and gas operations have on rare occasions been shown to result in subsidence above compacting oil and gas reserves (Geertsma 1973) and a recent study suggests that surface uplift in eastern Texas was due to fluid injection, which was distinguished using satellite remote sensing (Shirzaei et al., 2016). These studies do not imply that shale gas operations at depth will cause ground motion.

During this project, the authors have encountered public concern that induced seismicity may be accompanied by surface ground motion. It is therefore important to investigate impartially the possibility of induced surface motion. The shale gas operational activity at Preston New Road (PNR) in Lancashire along with the baseline monitoring offers an opportunity to determine anthropogenic surface ground motion at a hydraulic fracturing site in the UK.

An assessment of the environmental baseline in the Fylde was established prior to permitted hydraulic fracturing at PNR (Ward et al. 2018). This study assessed the baseline conditions for several environmental factors; ground motion for 1992 to 2000 was established. During this period, the PNR site was found to be stable and free from natural ground motion, other motion was observed within the broader area covered by the satellite image frame. Areas of subsidence and uplift associated with coal mining and related groundwater level changes are observed in Manchester and Leigh. Compressible ground in the west of the Fylde also resulted in subsidence in Blackpool (Ward et al 2018).

Undertaking objective and authoritative monitoring of the ground surface at operation sites and surrounding regions is advisable (a) to determine if there are any impacts on the ground surface and (b) to reassure the public that appropriate independent monitoring of all potential environmental impacts is being undertaken. Knowledge regarding the baseline ground motion conditions, compared with the current situation, would enable the provision of impartial and objective information on whether shale gas operations have affected the status of the landscape.

A key monitoring question is whether shale gas operations alter the earth surface processes that are operating at a site. We cannot assume that an area is stable prior to shale gas operations. When considering a monitoring system, it is important to account for the dynamic nature of the earth's surface i.e. there may be some pre-existing displacement due to either natural or induced factors. Therefore, a baseline survey is required to determine the pre-existing conditions of the site including displacement such as upwards motion (uplift), downwards motion (subsidence) or horizontal / lateral motion, and ongoing monitoring during any operations is required to characterise the current situation.

This investigation is designed to monitor the surface ground motion (subsidence, uplift or stability) of the target area using line of sight (LOS) Interferometric Synthetic Aperture Radar (InSAR) from orbiting satellites. They operate with ascending and descending looking angle geometries. In the former orbit the satellite travels from the south towards the north pole, and vice versa along the latter.

BGS has experience of applying InSAR techniques to several ground surface monitoring applications in the UK e.g. to investigate ground motion linked to ceased mining operations in

south Wales (Bateson et al 2015). InSAR is considered an appropriate technique for ground motion monitoring because

- a) archive radar data (acquired by satellites since 1992) are available and can be utilised to ascertain a baseline of motion (or lack of motion) prior to any permitted gas operations
- b) data from currently-orbiting satellites such as Sentinel-1A and Sentinel-1B can be freely downloaded and analysed to acquire information about the ongoing surface ground motion conditions in a region
- c) the analysis produces information over a wide region rather than at a point location, which other geodetic techniques such as GNSS or topographic levelling provide.

Table 11 provides a guide to the advantages and limitations of remote and in situ systems for ground motion monitoring.

**Table 11 Comparison of remote and in situ ground surface motion monitoring systems**

<b>Monitoring technique</b>	<b>Advantages</b>	<b>Limitations</b>
<b>InSAR</b>	<p>Measurements are made remotely (non-invasive)</p> <p>Retrospective measurements can be made using historic data to gain a baseline prior to operations.</p> <p>Imagery can cover a large area simultaneously.</p> <p>Entire deformation field can be imaged, rather than isolated points.</p>	<p>Conventional techniques have difficulty in vegetated areas.</p> <p>Rapid motion cannot be measured.</p> <p>Temporal and spatial resolution is limited by satellite set up and orbital parameters.</p> <p>Affected by steep topography (shown not be an issue in most of the UK).</p>
<b>GNSS</b>	<p>High precision.</p> <p>Does not require line of sight between benchmarks.</p> <p>Continuous site can operate without frequent human interaction.</p>	<p>Potentially difficult to installed in remote or difficult to access areas.</p> <p>Equipment can be stolen / vandalised / damaged.</p> <p>Sampling of deformation field is limited to individual points; several points are required.</p> <p>Requires at least 4 satellites in view simultaneously.</p>
<b>Tiltmeters</b>	<p>High precision.</p> <p>Does not require line of sight between benchmarks.</p> <p>Continuous site can operate without frequent human interaction.</p>	<p>Potentially difficult to installed in remote or difficult to access areas.</p> <p>Equipment can be stolen / vandalised / damaged.</p> <p>Sampling of deformation field is limited to individual points.</p> <p>Complex installation (e.g. in boreholes) – several tiltmeters are required.</p>
<b>Total Stations</b>	<p>High precision.</p> <p>Continuous sites can operate without frequent human interaction.</p>	<p>Potentially difficult to installed in remote or difficult to access areas.</p> <p>Requires line of sight between benchmarks.</p> <p>Generally they are operated manually, requiring repeat site visits to operate the system.</p>

InSAR techniques have been applied to the shale exploration sites in both the Vale of Pickering (Ward et al., 2016; 2017) and Preston New Road in Lancashire (Ward et al., 2018) to establish baselines of ground motion from 1992 onwards and, in the case of Lancashire only, to assess any impacts of the hydraulic fracturing process on the background ground motion.

After the planning permission for the development of an exploration wellsite for shale gas was granted by the Secretary of State for Communities and Local Government in October 2016 to Cuadrilla Bowland Ltd (Lancashire County Council, 2017), the construction of PNR wellsite commenced in January 2017 and then two horizontal wells were drilled: PNR-1z and PNR-2.

“PNR-1z was completed in April 2018 through the Lower Bowland shale rock at approximately 2,300m below surface and extends westwards for some 800m. PNR-2, drilled through the Upper Bowland shale at an approximate depth of 2,100m below the surface, extends westwards for some 750 metres through the shale gas reservoir and was completed in July 2018.” (from <https://cuadrillaresources.com/site/preston-new-road/>). Hydraulic fracturing of the shale surrounding one of the wells started in October 2018, this work was complete by mid-December, however it is understood that flow testing occurred during January 2019.

Two InSAR techniques have been utilised to detect and monitor ground motion, with interpretation of the result undertaken by BGS (i) RapidSAR (Spaans and Hooper, 2016) from SatSense Ltd and (ii) ISBAS (Sowter et al., 2013; Bateson et al., 2015) from BGS and Geomatic Ventures Ltd. The former provides a higher density coverage for urban areas, and less measurement points in rural areas but with more accurate measurements while the latter provides more measurement points over rural areas with a lower accuracy. Therefore, the combination of multiple methods can eliminate the inherent defects of a single method, play a complementary role, and greatly improve the capability to detect ground displacements.

Sections 3.2 and 3.2 provide the information on the satellite data selected during the four monitoring phases, with the corresponding results in Sections 3.4 and 3.5 where the interpretation of the hydraulic fracturing period at PNR is shown for the first time.

Discussion on the comparison between the hydraulic fracturing period and the baseline survey is covered in Section 3.7 and conclusion on the benefits of monitoring ground stability from space over the two shale gas sites are in the conclusions (Section 3.8).

**Table 12. Analyses of InSAR processing for the Vale of Pickering.**

Satellite	Time period	No. of scenes in the stack	Processing mode	Processed by	Max velocity (mm/yr)	Min velocity (mm/yr)
<b>ERS-1/2</b>	1992-2000	72	SBAS	BGS	+3.3	-3.1
<b>ERS-1/2</b>	1992-2000	72	ISBAS	BGS	+6.2	-4.4
<b>ENVISAT</b>	2002-2009	25	SBAS	BGS	+5.8	-4.4
<b>ENVISAT</b>	2002-2009	25	ISBAS	BGS	+9.3	-7.3
<b>SENTINEL-1</b>	2015-2016	36	ISBAS	GVL	+18.4	-11.8

### 3.2 VALE OF PICKERING SAR DATASET

Three sets (stacks) of satellite radar data were acquired for the Vale of Pickering (Table 12). Archive radar data were captured by the ERS-1/2 and ENVISAT satellites for the periods 27th May 1992 – 30th December 2000 and 13th July 2002 – 21st February 2009 respectively. Data were also acquired by the Sentinel-1 satellite covering the period 8th May 2015 to 30th August

2016. There is no satellite coverage in the region between 2009 and 2014 due to the orbital decay of ENVISAT. No alternative commercial data are available to this study due to lack of acquisition in this time period. Nonetheless, we consider the period 1992–2009 is sufficient to provide a meaningful baseline assessment of ground motion prior to unconventional gas operations. The three stacks of data were analysed using SBAS and ISBAS InSAR techniques, i.e. six sets of analysis were undertaken and completed within this ground motion work package.

### 3.3 LANCASHIRE SAR DATASET

#### 3.3.1 1992-2000 baseline

This BGS-funded research project utilised archive radar images from the ERS-1/2 satellite for the period 1992-2000 (Table 13). The stack of radar data consisted of 63 images that were analysed using ISBAS and SBAS InSAR techniques, i.e. two sets of analyses were undertaken and completed within this ground motion work package.

**Table 13. ERS-1/2 image metadata**

Satellite	Time period	No. of scenes in the stack	Processing mode	Processed by	Max velocity (mm/yr)	Min velocity (mm/yr)
ERS-1/2	1992-2000	63	SBAS	BGS	+13.93	-12.28
ERS-1/2	1992-2000	63	ISBAS	BGS	+15.75	-13.58

#### 3.3.2 2015-2019 baseline and hydraulic fracturing period

Following the decision to move BEIS funding from VoP to Lancashire in light of commencement of hydraulic fracturing activities in Lancashire, BGS commissioned two commercial InSAR results for the Lancashire area. It was necessary to wait until as late as possible in the fourth phase of the project in order to ensure we captured a consistent period whilst hydraulic fracturing was taking place. This restricted the interpretation time.

The radar imagery was acquired by Sentinel-1 satellites. InSAR processing data was undertaken by SatSense (using their RapidSAR technique), and GVL (using their ISBAS technique). Both techniques were applied to ascending and descending frames acquired between May 2015 and February 2019. RapidSAR provided both rural results and higher resolution urban results for the entire Sentinel-1 scene. High resolution, full time-series, results delivered approximately 4.4 million measurements points, whilst the rural results delivered approximately 750,000 points. The ISBAS results cover a subset of the Flyde region. Ascending and Descending Sentinel-1 datasets have been processed to produce Line Of Sight (LOS) and Vertical average velocity maps and time series.

### 3.4 VALE OF PICKERING GROUND MOTION BASELINE

Processing of the InSAR data has provided the first baseline assessment of land surface deformation covering a 25-year period in the Vale of Pickering, albeit with a gap in the coverage following the ENVISAT de-orbit and prior to Sentinel-1 launch. The results from the SBAS analysis comprises 47,930 ERS, 72,697 ENVISAT and 71,881 Sentinel-1A points which increase to 836,939 ERS, 234,793 ENVISAT and 637,753 Sentinel-1A points in the ISBAS results (Figure 41).

**Table 14. Sentinel-1 image metadata (Lancashire)**

Satellite	Time period	No. of scenes in the stack	Processing mode	Processed by	Max velocity (mm/yr)	Min velocity (mm/yr)
Sentinel-1 (Asc)	2015-2019		ISBAS	GVL	+5.6	-7.03
Sentinel-1 (Desc)	2015-2019	177	ISBAS	GVL	+3.54	-7.97
Sentinel-1 (Asc)	2015-2019	178	Urban	SatSense	+28.36	-50.75
Sentinel-1 (Asc)	2015-2019	178	Rural	SatSense	+6.83	-34.59
Sentinel-1 (Desc)	2015-2019	164	Urban	SatSense	+26.78	-54.56
Sentinel-1 (Desc)	2015-2019	164	Rural	SatSense	+18.59	-27.23

**3.4.1 1992-2000 Baseline**

75 ERS-1/2 SAR scenes for 1992-2000 are available along satellite track 366 in descending mode. Of the 75 ERS-1/2 scenes in the archive, three were not used due to missing lines within the data. The results of the ERS-1/2 InSAR analysis are shown in Figure 42. Green areas are considered stable, red are subsiding on average over the time period, and blue are undergoing uplift.

As expected, the SBAS results are primarily constrained to urban areas (including roads) as these provided coherence in all of the radar images in the stack. It is apparent that the area was predominantly stable between 1992 and 2000. There is a discrete zone of subsidence north of Whitby (in the Loftus area) but this is outside the Vale of Pickering monitoring area.

The ISBAS analysis of the ERS-1/2 radar data also indicates that the majority of the area was stable. There are three zones of ‘dispersed’ uplift in this analysis, to the west, southwest and south of Scarborough. We believe that these zones in the ISBAS analysis are not related to geological motion (in our experience geological motion is more discrete), but are most likely due to vegetation changes and agricultural practices.

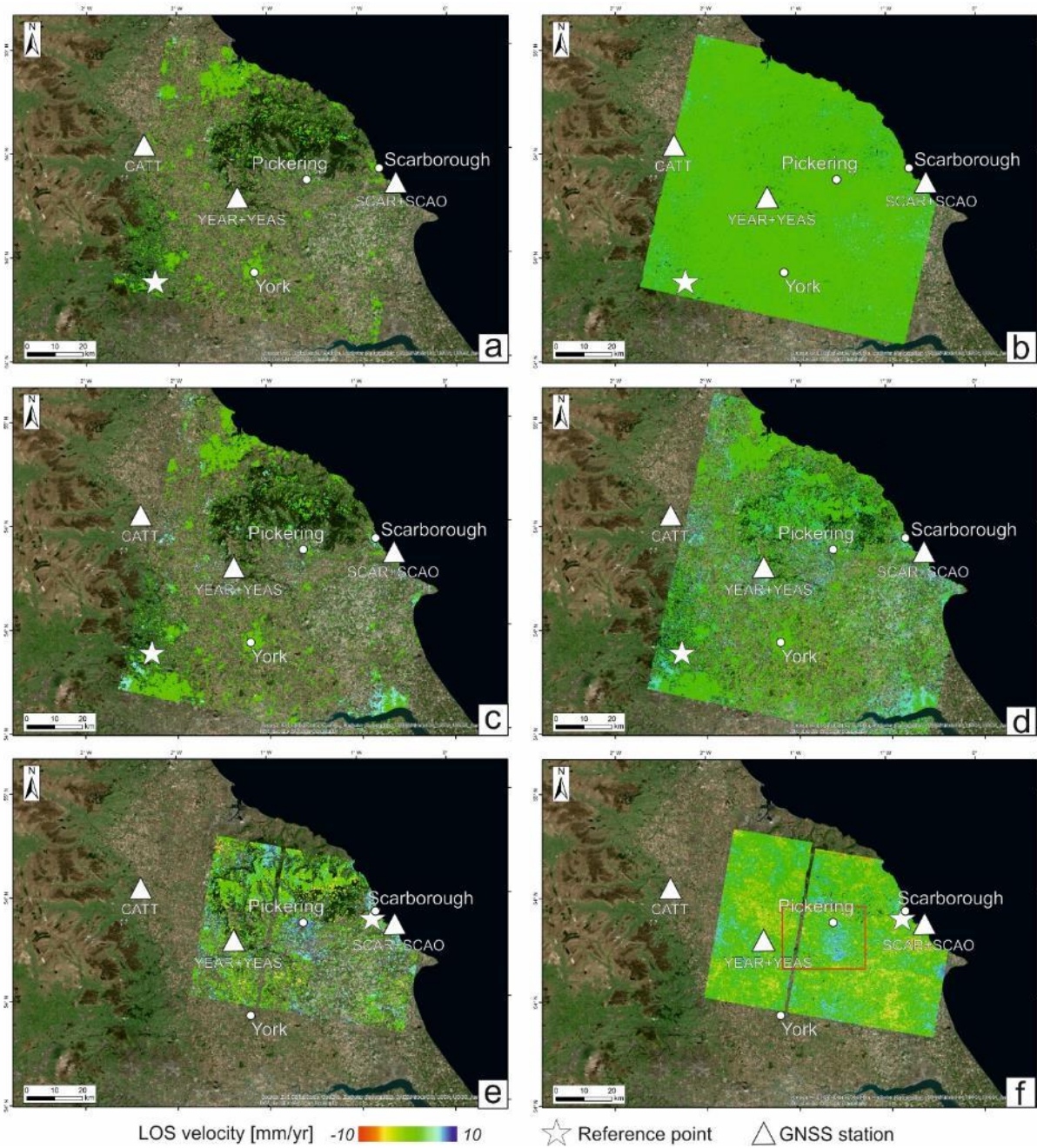


**Figure 41. ERS SBAS (a), ERS ISBAS (b) ENVISAT SBAS (c), ENVISAT ISBAS (d), Sentinel-1A SBAS (e) and Sentinel-1A ISBAS (f) results for the Vale of Pickering area, showing average rates of ground motion. Location of GNSS stations and InSAR reference point are indicated with a triangle and star, respectively. From Ward et al. (2017).**

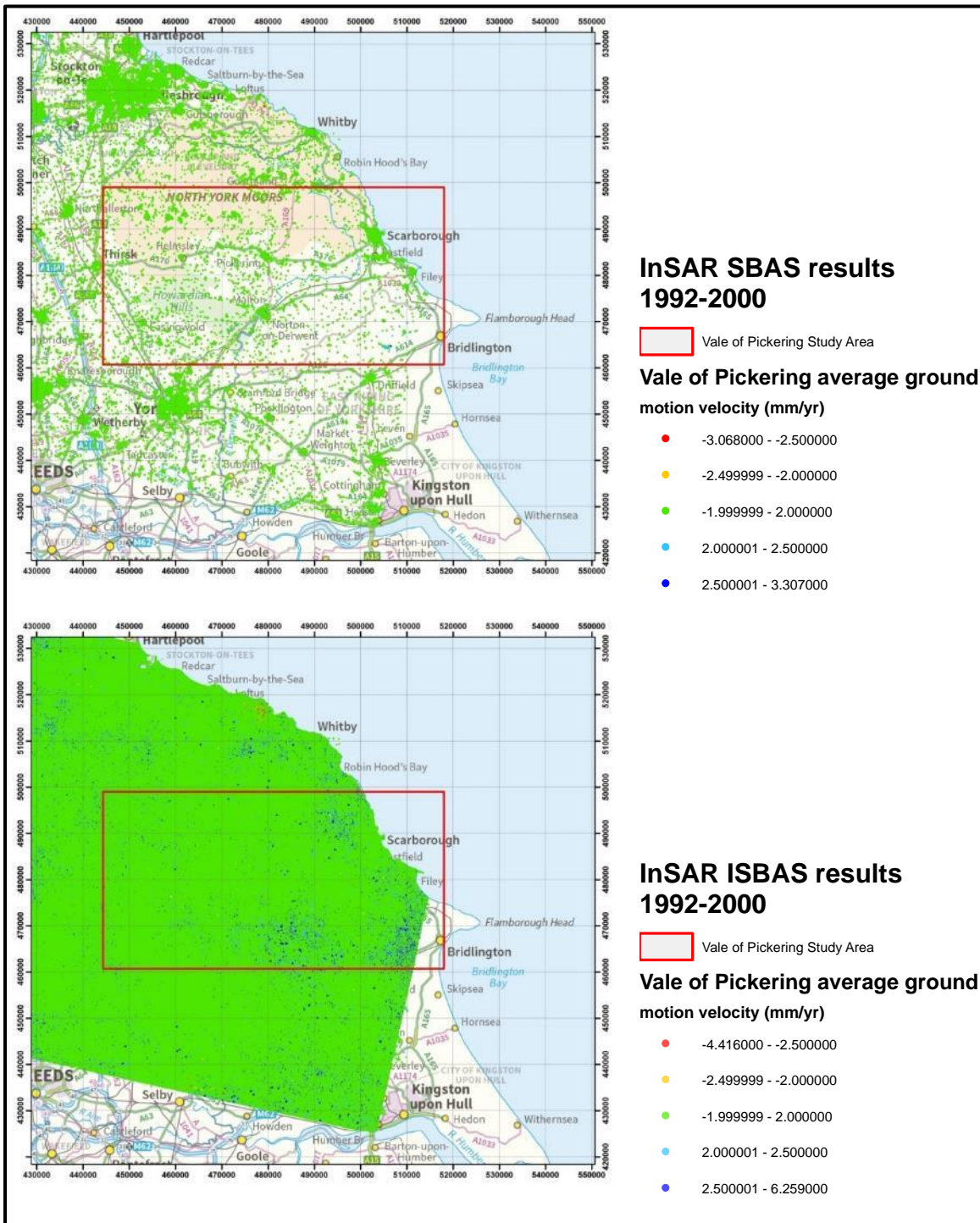
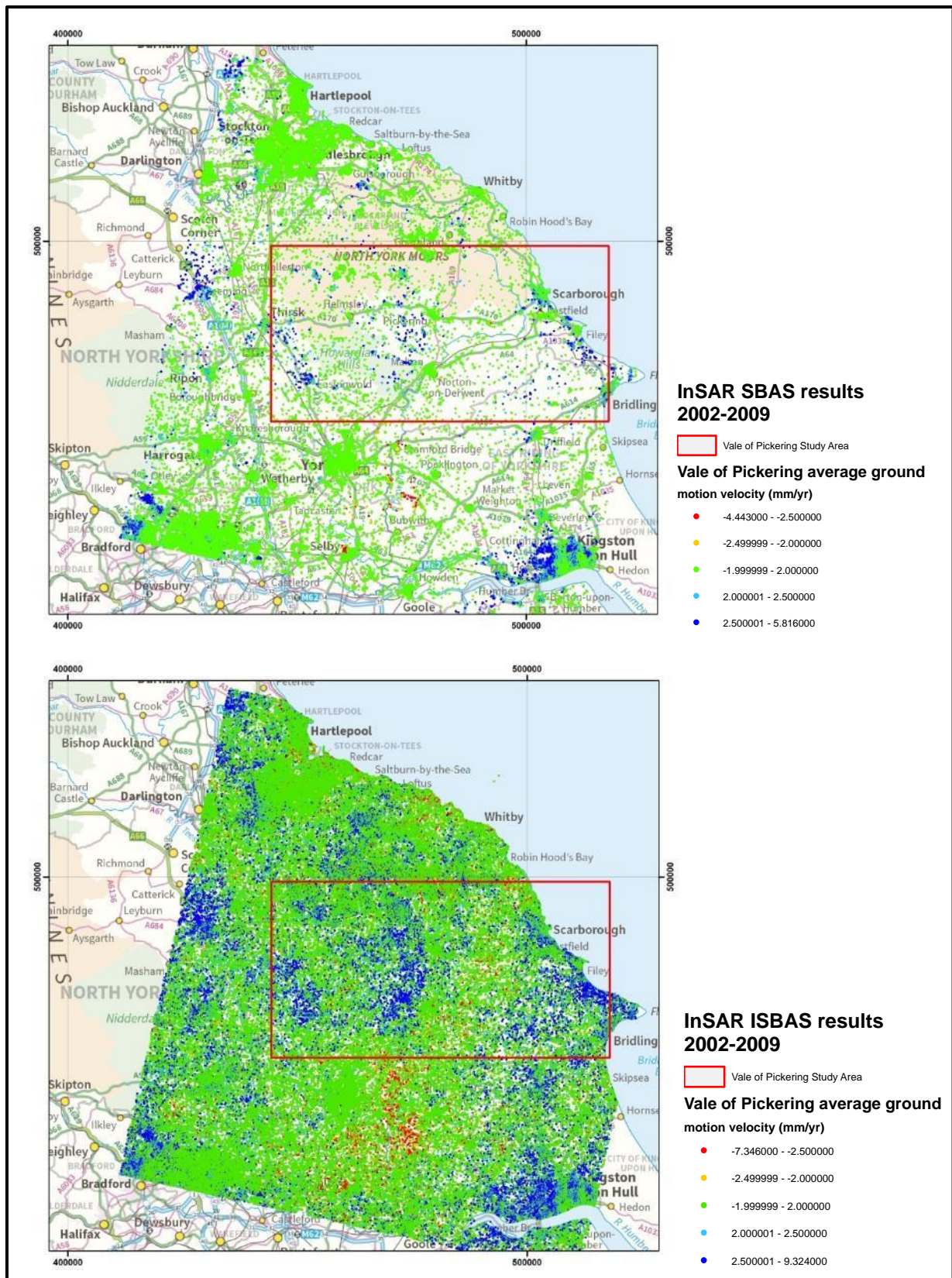


Figure 42. InSAR SBAS (top) and ISBAS (bottom) analysis of ERS-1/2 satellite imagery (1992-2000) for the Vale of Pickering. Radar data supplied to BGS by ESA under grant id.31573. From Ward et al. (2017).



**Figure 43. InSAR SBAS (top) and ISBAS (bottom) analysis of ENVISAT satellite imagery (2002-2009) for the Vale of Pickering. From Ward et al. (2017).**

### 3.4.2 2015-2016 Baseline

Imagery acquired by the Sentinel-1A between 8<sup>th</sup> May 2015 to 30<sup>th</sup> August 2016 was acquired and processed. The stack comprised 36 images. SBAS processing of the Sentinel-1A data resulted in an average point density of  $\sim 17$  SBAS points/km<sup>2</sup>. When the Sentinel-1A data was processed with ISBAS the number of points increased by a factor of  $\sim 8.3$ , providing a coverage of 89% (corresponding to  $\sim 141$  points/km<sup>2</sup>) with the highest increase in measurement density observed in areas of non-irrigated arable land, pastures and natural grasslands (Figure 44). The additional coverage has not come at the sacrifice of quality with an average standard error of 1.93 mm/year. As expected, the coherent targets concentrate over the urban areas of Scarborough, Pickering and Malton where the highest values of the interferometric coherence were observed.

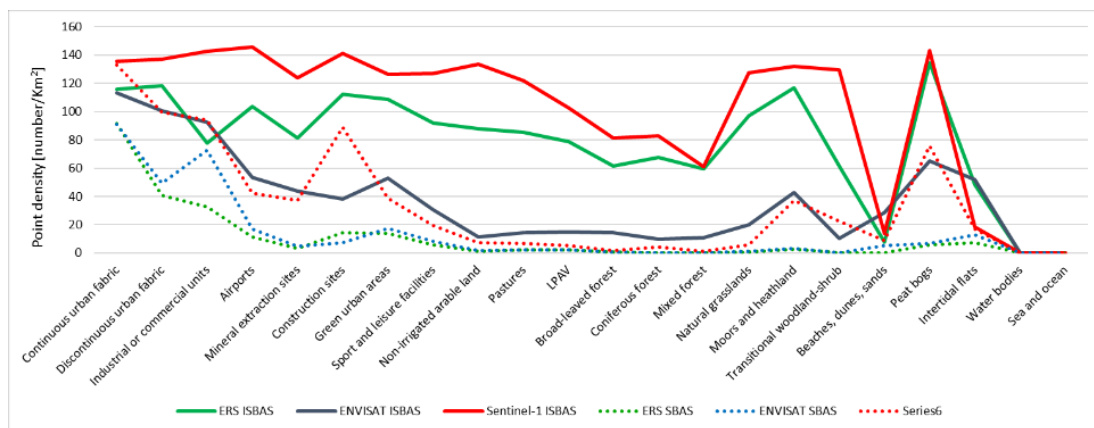


**Figure 44. Average SBAS and ISBAS densities obtained for each land cover type from ERS, ENVISAT and Sentinel-1 results (CLC2012). From Ward et al. (2017).**

The network of GNSS receiving stations from the NERC British Isles continuous GNSS facility (available at [www.bigf.ac.uk](http://www.bigf.ac.uk)) was used to validate the ISBAS time-series over two sites (Figure 45). The SCAR station (from 05/01/03 to 09/02/09) renamed to SCAO (from 20/02/09) and the YEAR station (from 24/05/04-22/01/09) then renamed to YEAS (from 16/04/09 to 10/03/16) time-series GNSS data were used to validate / constrain the magnitude and timing of ENVISAT and Sentinel-1A motion (Figure 46).

The displacements at the two GNSS stations, at rates of -0.54 mm/yr for SCAO-SCAR and -0.56 mm/yr for YEAR-YEAS, are in agreement with the subsidence observed at the closest ISBAS points for the equivalent time span, confirming the validity of the InSAR results.

Figure 45 illustrates the average annual ground motion derived from ISBAS results for the Pickering-Malton area. An area of uplift (of  $\sim 5$ mm/yr) is visible in the western sector of the valley, between Pickering and Malton, for the 2002-2009 time-span which almost doubles (to  $\sim 10$ mm/yr) for the 2014-2016 period and has been detected through intermittently coherent targets. The uplift is delimited both to the north and south to the presence of Quaternary lacustrine deposits of the Glacial Lake Pickering (Evans et al., 2016). There also appears some correspondence between uplift and east-west faults, identified as dashed lines in Figure 45.

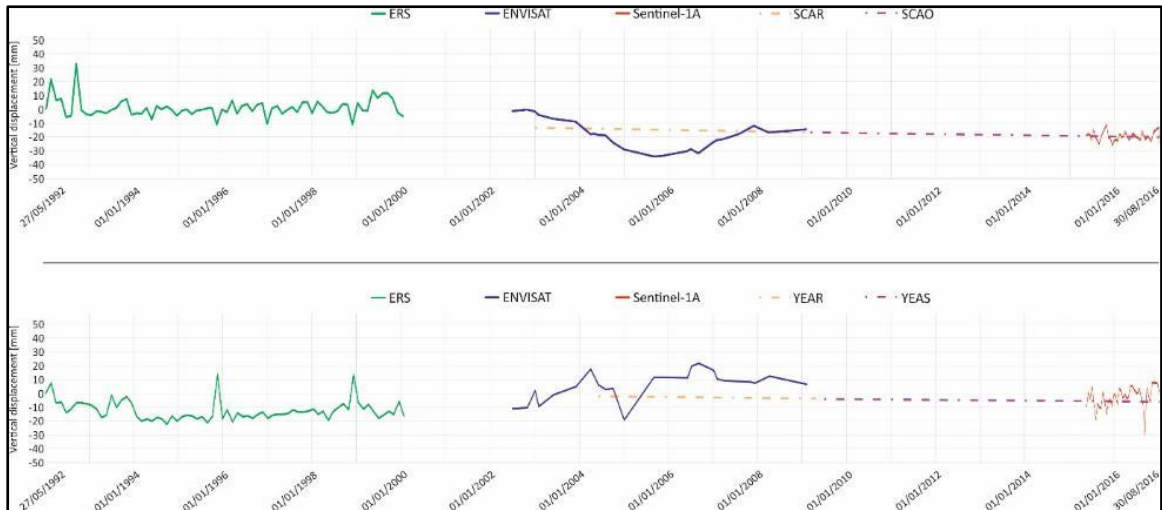


**Figure 45. Non-linear time series for selected ISBAS points. The solid lines represent the ISBAS non-linear vertical displacements for the different acquisitions and the dotted lines represent the GNSS linear and vertical displacements which were derived separately. It is worth noting that the InSAR time series reported were generated considering a linear displacement velocity in the temporal gaps between the ENVISAT and Sentinel-1A datasets. From Ward et al. (2017).**

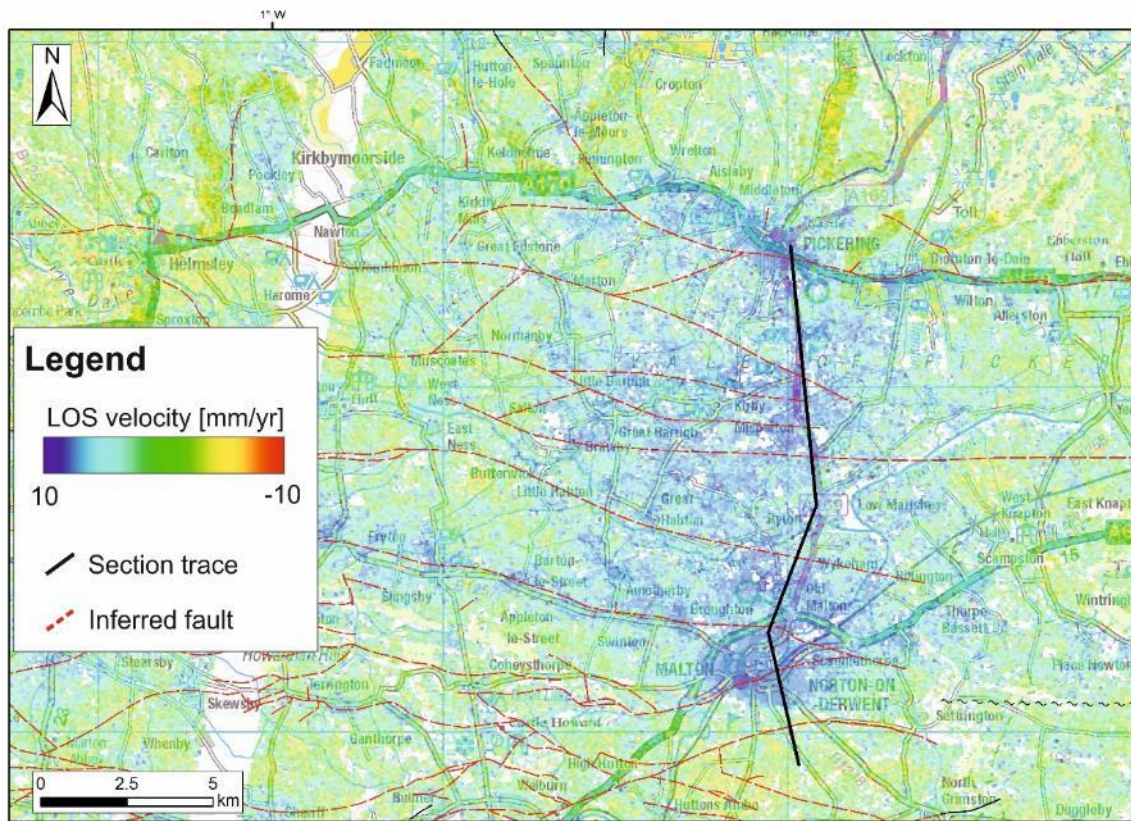


**Figure 46. ISBAS InSAR results for the Pickering area of the Vale of York. Blue areas are undergoing uplift while green / yellow areas are stable. Dashed lines are geological faults. Solid black line is the trace of the section in Figure 47. Contains Ordnance Data © Crown Copyright and database rights 2019.**

The spatial pattern of the Sentinel-1 ISBAS velocities reveals the occurrence of instability within the clay and silt sediments of the lacustrine deposit, which south of Kirby Misperton exceeds 20 m in thickness (Figure 47). Faults of the basement play a significant role in the heterogeneity of the uplift rates by identifying three main domains:

1. the northern area with average velocities  $\geq 6\text{mm/yr}$ ,
2. the central section with velocities  $\leq 3\text{mm/yr}$
3. southern portion with velocities  $\sim 5\text{mm/yr}$ .

Abrupt changes in the ground motion at the location of a fault (Figure 47) suggesting that the faults constrain the motion, possibly by their influence on the groundwater flow at depth.

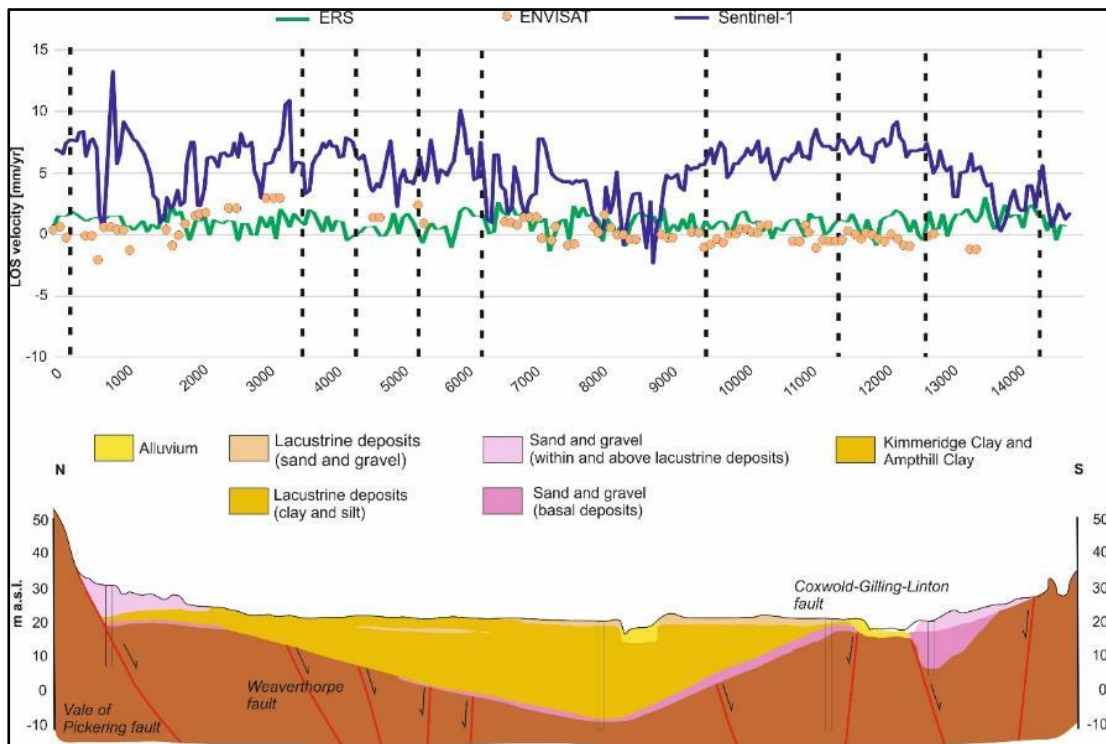


**Figure 47. ISBAS InSAR results for the Pickering area of the Vale of York across the section identified in Figure 46. From Ward et al. (2017).**

A possible explanation for the observed uplift relates to the wet winter of 2015-2016. The Coralline Limestone to the North and South of the Vale of Pickering (Figure 48) may allow a groundwater flow, which recharges the aquifer at depth, thereby increasing the pressure. Alternatively, the uplift may relate to shallower processes; the increase in surface water (many members of the public at the engagement events suggested there was a great deal of surface flooding during the winter of 2015-16) may have led to a swelling of the glaciolacustrine clays (Figure 48), which are responsible for the flat topography of the Vale. The InSAR time series supports the notion that the uplift relates to the timing of a wet winter as we see an increase in uplift rates following the winter of 2015-2016 (Figure 49).

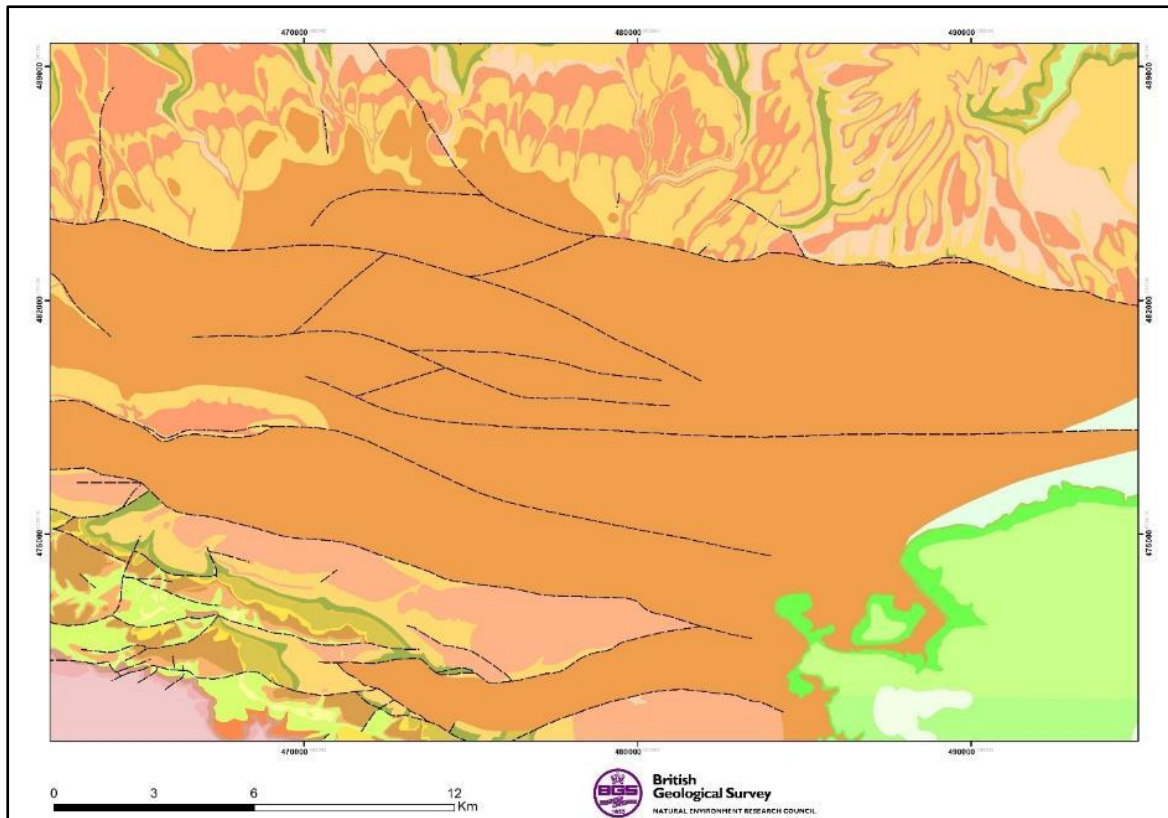


**Figure 48. Bedrock geology and faults for the Pickering area of the Vale of York. Brown areas are clays from the quaternary glacial lake, green represents Chalk whilst the yellows and pinks to the North and South are the Coralline limestones and Calcareous Grits. From Ward et al. (2017).**

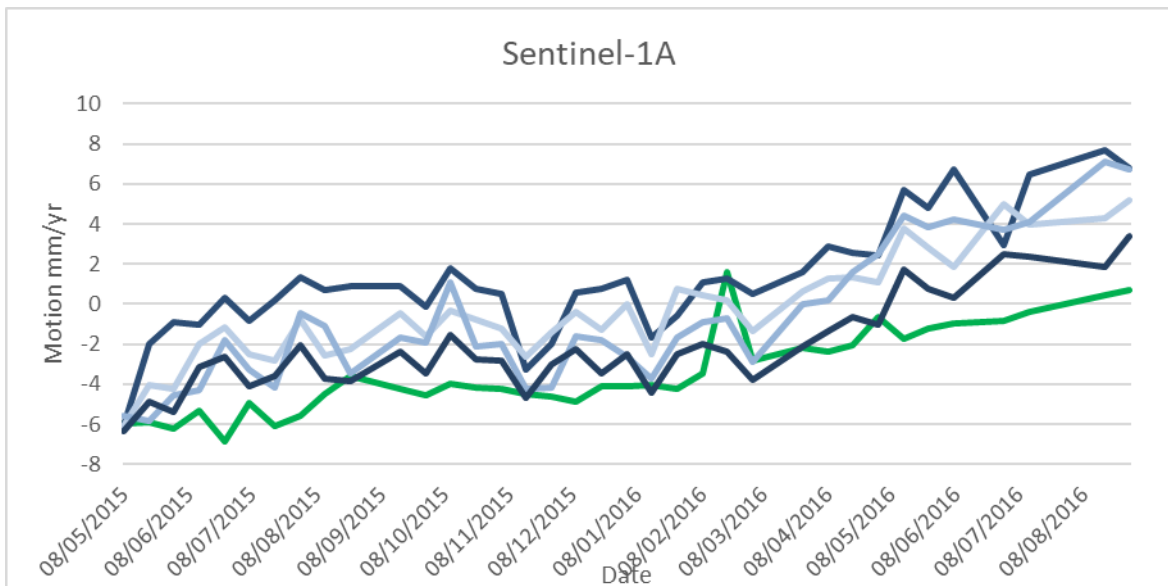


**Figure 49. ISBAS InSAR Time series for the Pickering (green) and Malton (blue) areas. From Ward et al. (2017).**

### 3.5 LANCASHIRE GROUND MOTION BASELINE

#### 3.5.1 1992-2000 Baseline

In the Fylde, the ERS-1/2 radar data have been analysed to produce InSAR results for urban and non-urban areas. The results indicate a maximum velocity of +15.8 mm/year and a minimum velocity of -13.6 mm/year. The SBAS InSAR analysis comprises 140k points while the ISBAS analysis comprises 890k points.

The results of the ERS-1/2 InSAR analysis for SBAS and ISBAS are shown for the regional area in Figure 50 and Figure 51 respectively. Green areas are considered stable, red are subsiding on average over the time period, and blue are undergoing uplift.

A larger area than the Fylde was processed; the results highlight the potential for InSAR to detect the range of motion in the region including discrete areas of subsidence and uplift, as well as confirming the stability of large areas (Figure 50 and Figure 51).

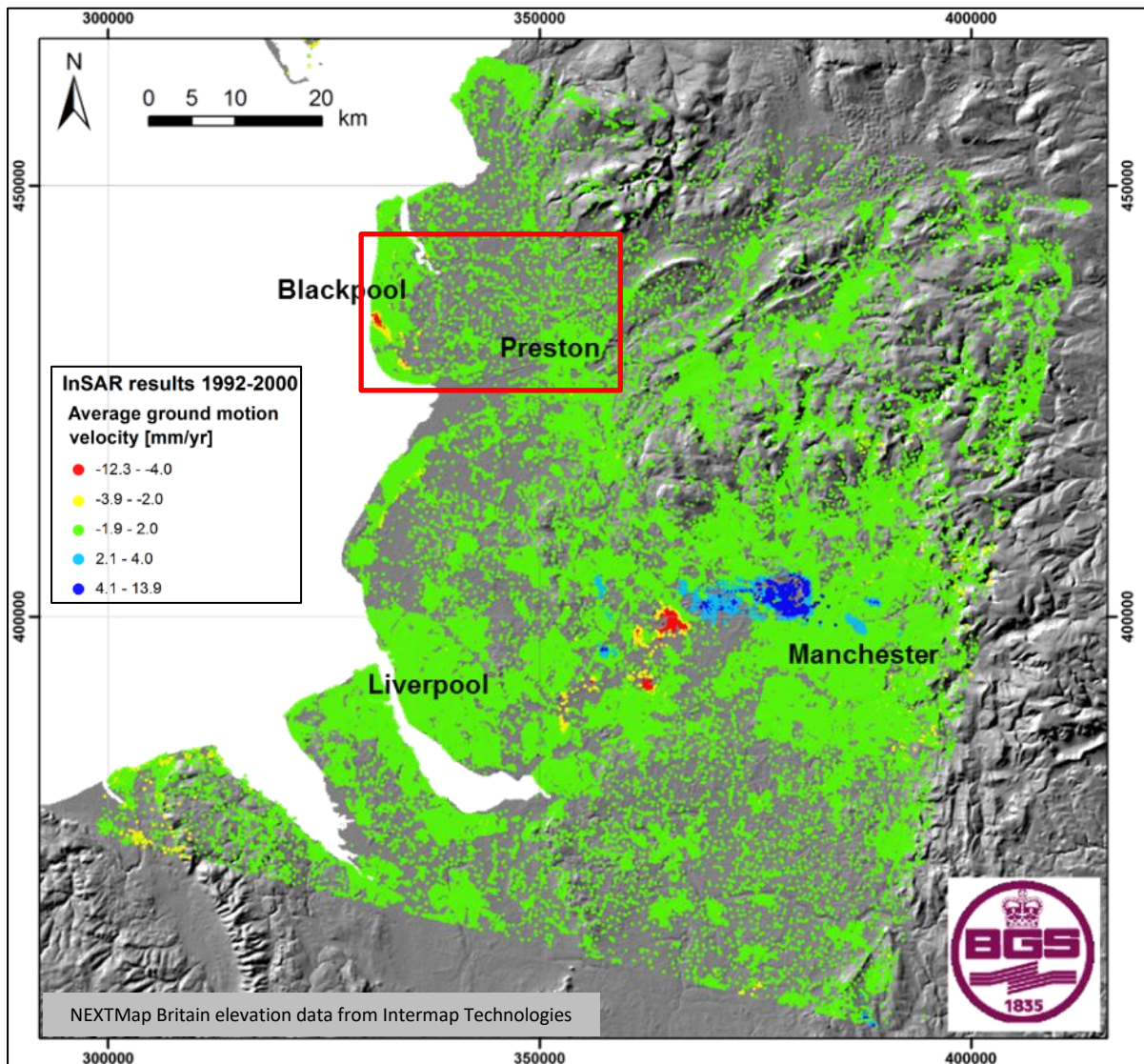


**Figure 50. InSAR processing using SBAS technique of ERS-1/2 data from 1992 to 2000. The red box outlines the extents of the Fylde study area. From Ward et al. (2018).**

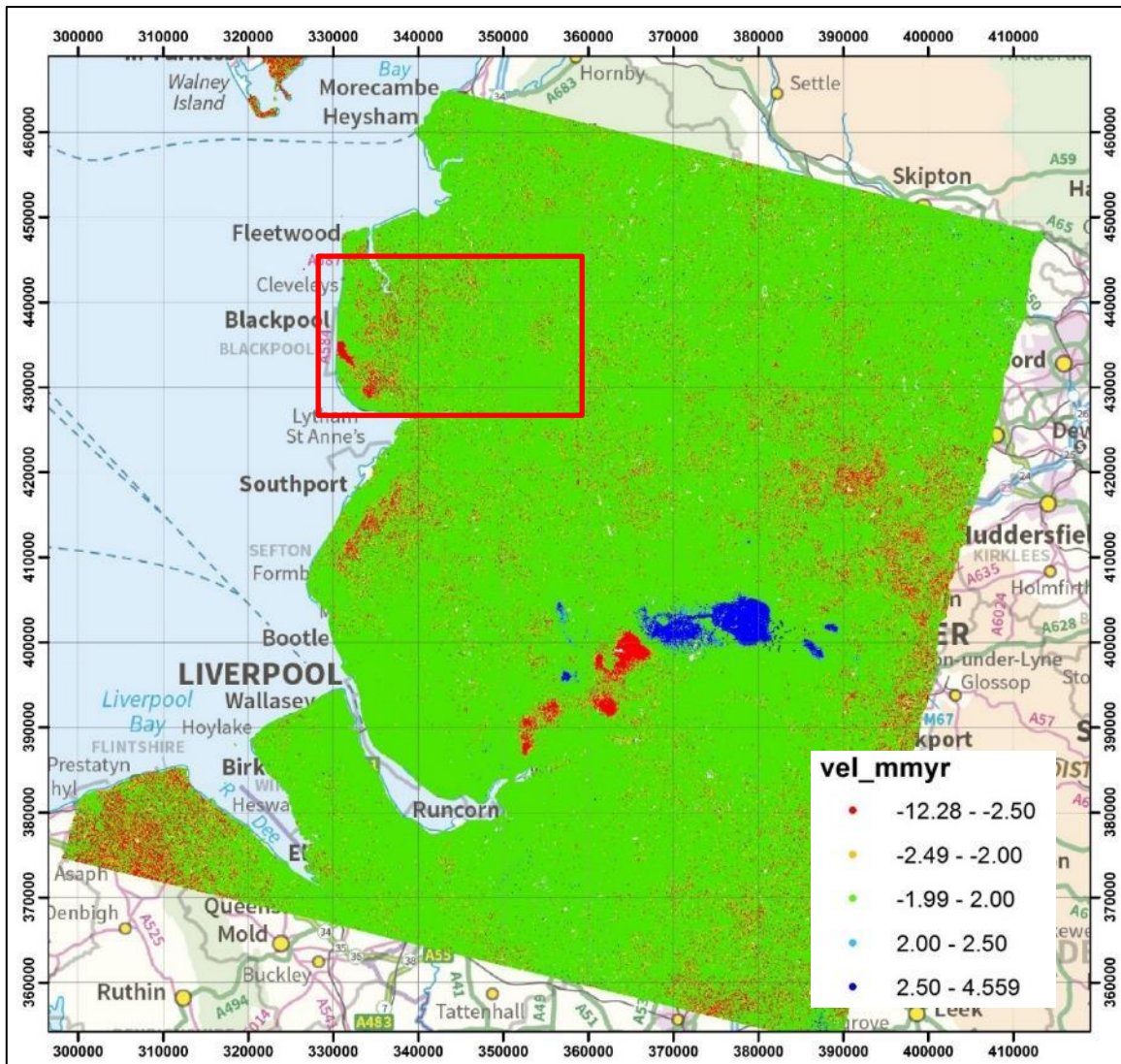


**Figure 51. InSAR processing using ISBAS technique of ERS-1/2 data from 1992 to 2000. The red box outlines the extents of the Fylde study area. From Ward et al. (2018).**

Outside the Fylde, the discrete area of uplift (blue points) north-west of Salford is likely due to the rise in groundwater levels following cessation of water pumping in abandoned coal mines. Minewater pumping data have not been evaluated to assess this hypothesis. There is an area of subsidence to the south-west of the uplift, in the Bickershaw-Goldborne-Leigh region. This is likely due to mining activity in the three collieries including water abstraction (Arrick, 1995), and formation of the Pennington Flash, illustrated in Figure 52.

A detailed view of the InSAR results for the Fylde area is presented in Figure 54. The results in this time period (1992-2000) contain discrete areas of subsidence indicating that the Fylde area is undergoing some ground motion. Sufficient resources were not available in this preliminary study to validate these with ground surveys.

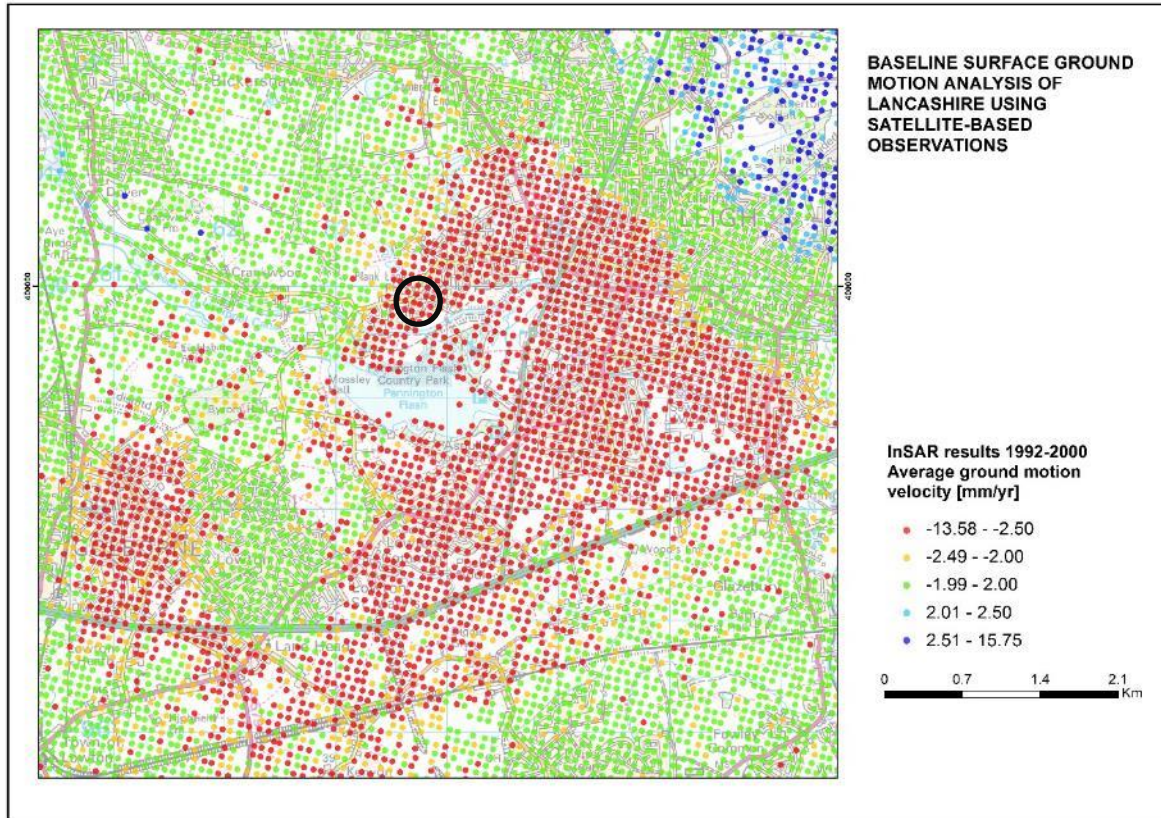


**Figure 52. Areas of subsidence identified (in red) on the InSAR data in Leigh (outside of the Fylde study area) between 1992 and 2000. Black circle outlines the detailed time series results in Figure 53. From Ward et al. (2018).**

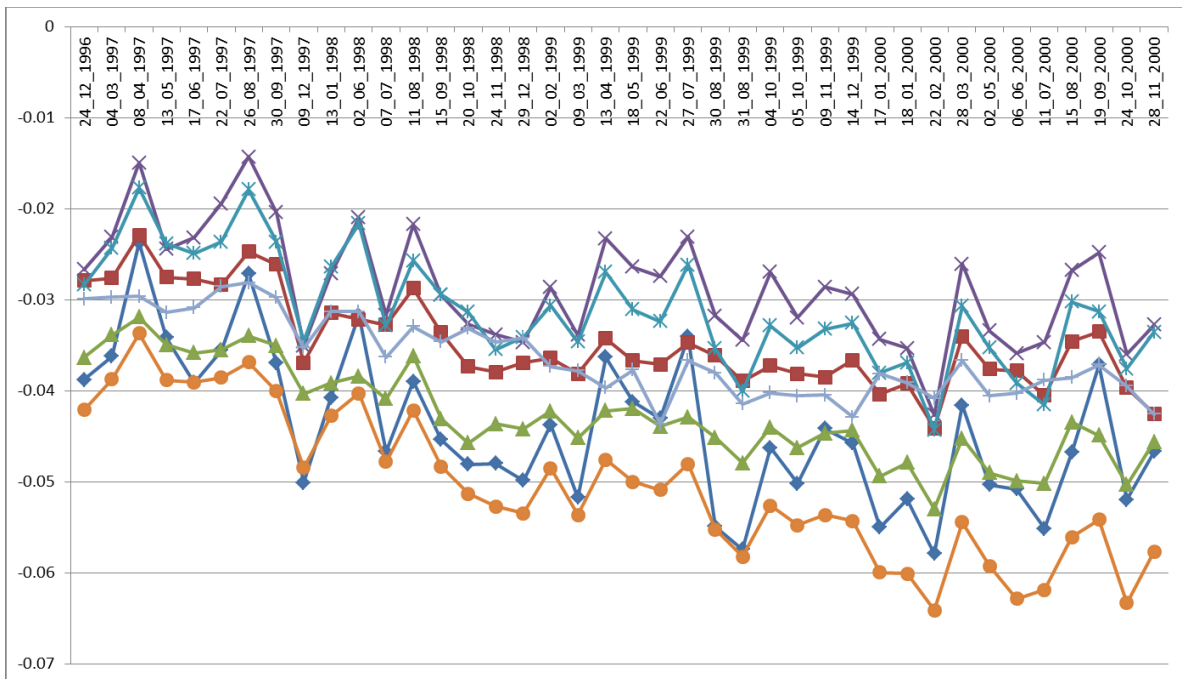


**Figure 53. Time series profiles of motion for 1996 to 2000. From Ward et al. (2018).**

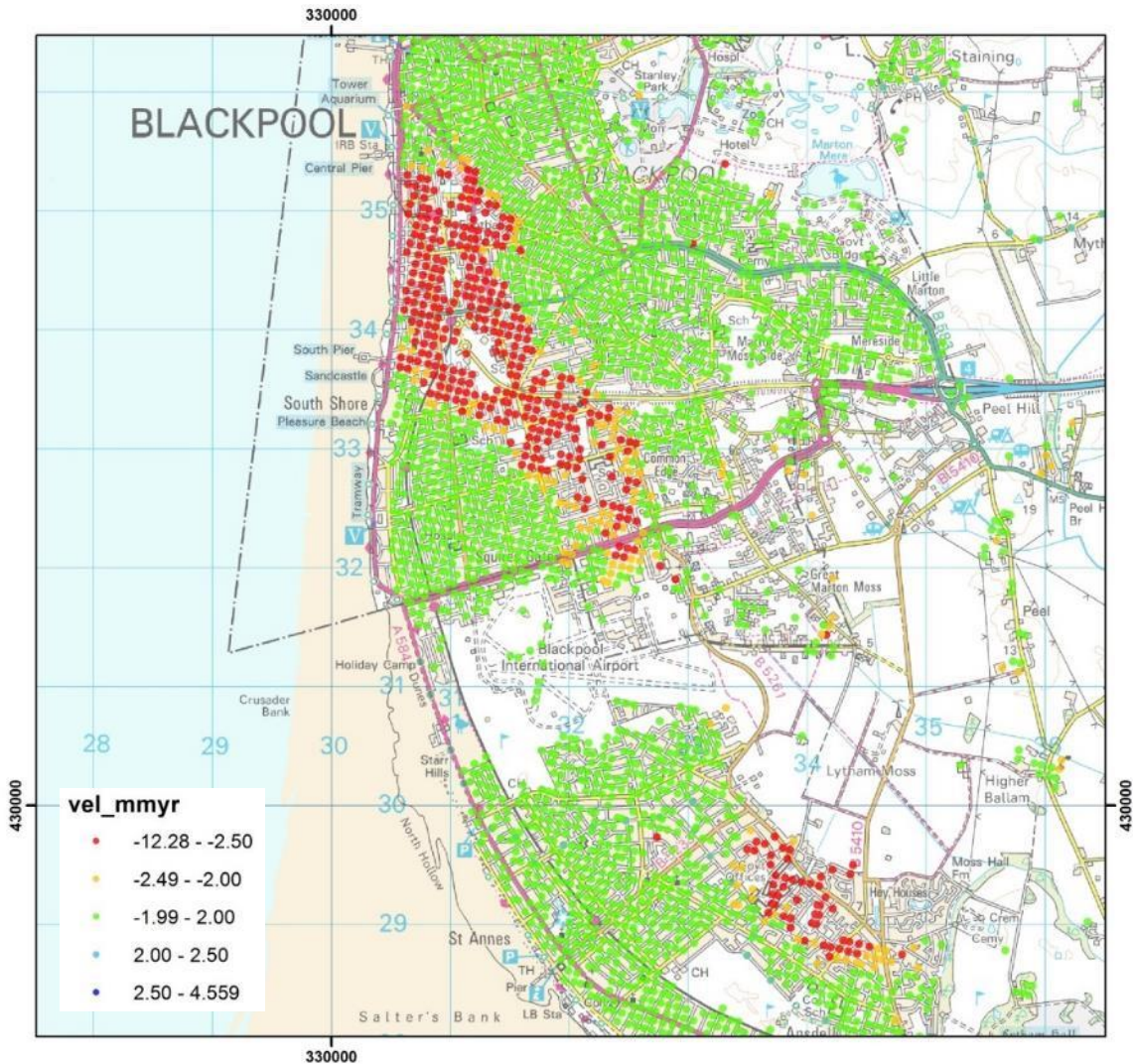


**Figure 54. Areas of subsidence identified (in red) on the InSAR data in Blackpool between 1992 and 2000. Black circle indicates the location of boreholes in Figure 55. From Ward et al. (2018).**

These areas of subsidence correspond to an area of ‘peat and blown sand’ on the published geological maps. Boreholes from the area indicate the presence of ‘sand and peat’ at the top of the stratigraphy (Figure 55) suggesting that the subsidence may therefore be caused by the existence of compressible ground.

### 3.5.2 2015-2018 Baseline

A baseline for 2015–2018 has been established with RapidSAR and ISBAS InSAR techniques. RapidSAR results have been provided with two different coverages for both the ascending and descending orbit: rural results (see Section 3.5.2.1) and urban results (see Section 3.5.2.2).

RapidSAR rural results have a lower density of point measurements than the urban routine as the detected motion is ‘averaged’ for each radar image resolution cell. This technique has the advantage that the effects of multiple weaker signals (which would not normally become a measurement point) add up to create sufficient signal to be considered as a measurement point. The outcome is measurements within rural areas, which do not exhibit measurement points in the RapidSAR urban result.

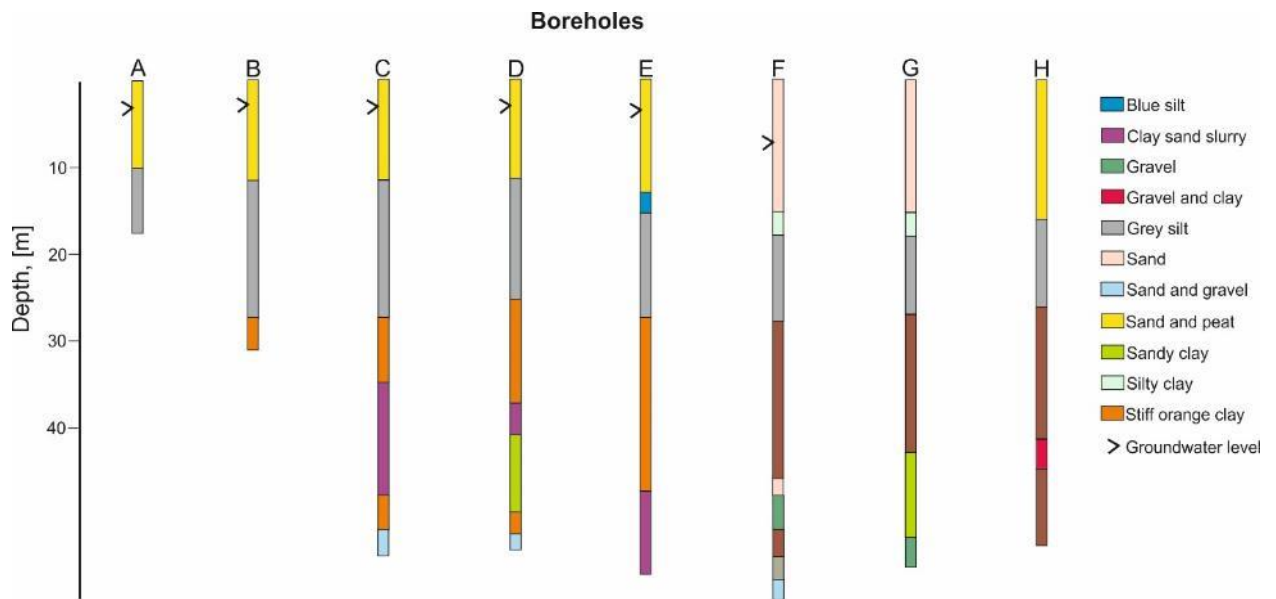


**Figure 55.** Scan of eight boreholes indicating the presence of ‘sand and peat’ at the top of the stratigraphy. For their location refer to Figure 54.

### 3.5.2.1 RAPIDSAR RURAL RESULTS

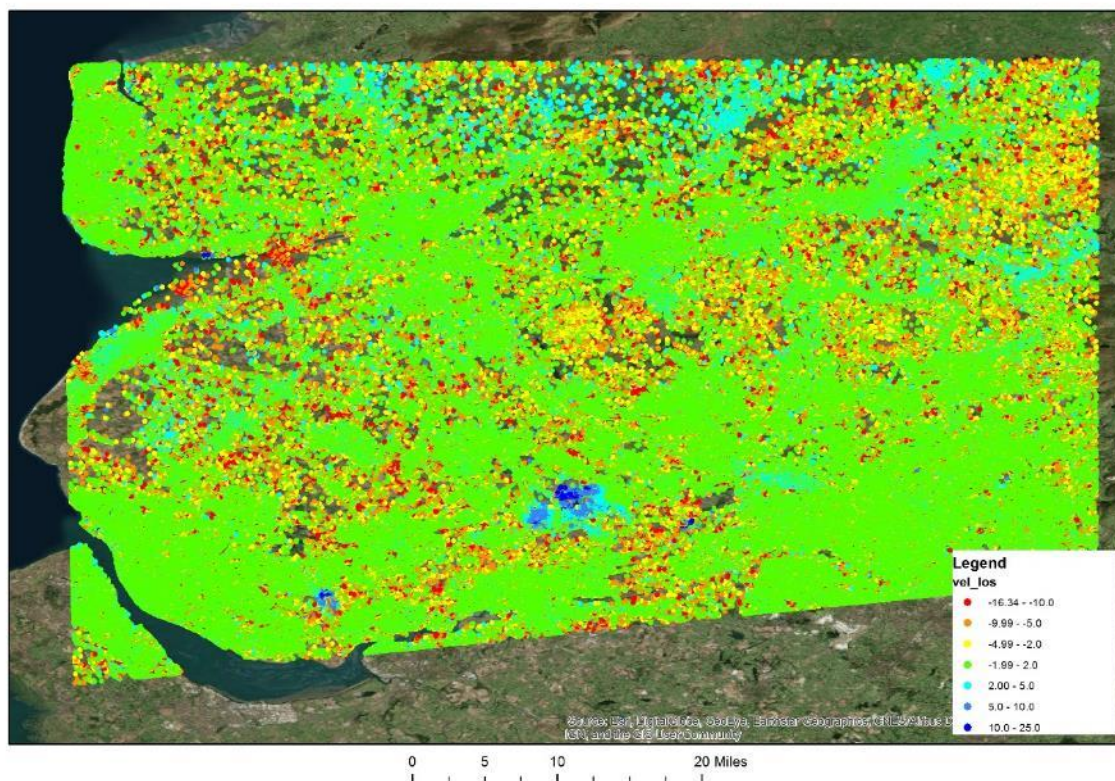


**Figure 56.** Sentinel 1 ascending average velocity (mm per year) ground motion results for May 2015 to February 2019; RapidSAR rural results

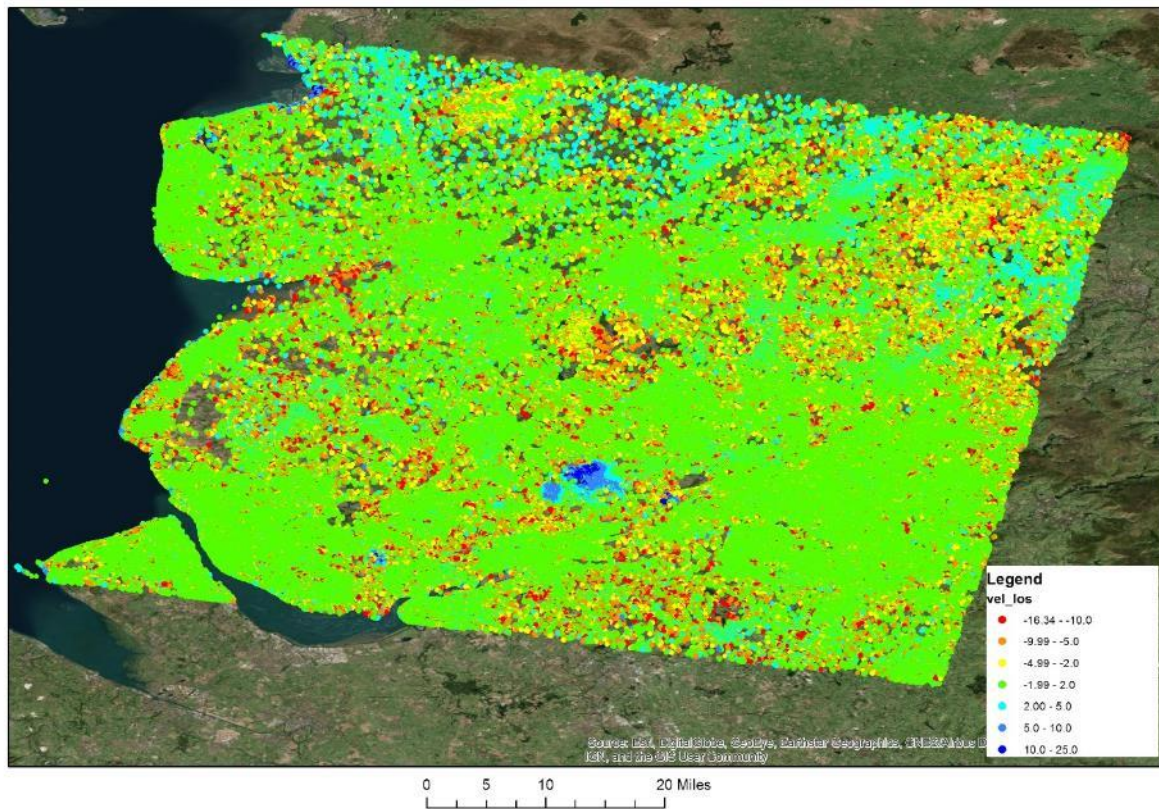


**Figure 57. Sentinel 1 descending average velocity (mm per year) ground motion results for May 2015 to February 2019; RapidSAR rural results.**

Both descending and ascending rural average velocity plots (Figure 56 and Figure 57) show the same patterns of motion; urban centres, where higher accuracy results are typically obtained, show a general pattern of stability (green points) over the four years processed. These areas of stability also extend to the lower elevation plains and valleys. When interpreting InSAR average velocities it is important to look for spatially coherent patterns of motion, i.e. discrete areas of uplift or subsidence. Within the rural data (Figure 58 and Figure 59) there are several such areas apparent when viewing at the scale shown in the figures (1:40,000). The most prominent is the area of uplift in Leigh to the west of Manchester, an area that was undergoing subsidence in the 1990's ERS data (Ward et al 2018). The observed patterns of ground motion relate to ground water level changes brought about by coal mining practices. During the 1990's this area was still being actively undermined hence the water level was depressed causing a drop in pore water pressure and hence subsidence. Mining has since ceased and the pumps turned off, water levels are allowed to recover hence pore pressure increases and uplift is observed (Figure 58). The same patterns of motion are seen in many former coal mining area of the UK (Bateson, et al 2015, Jordan et al, 2017 and Gee et al, 2017).

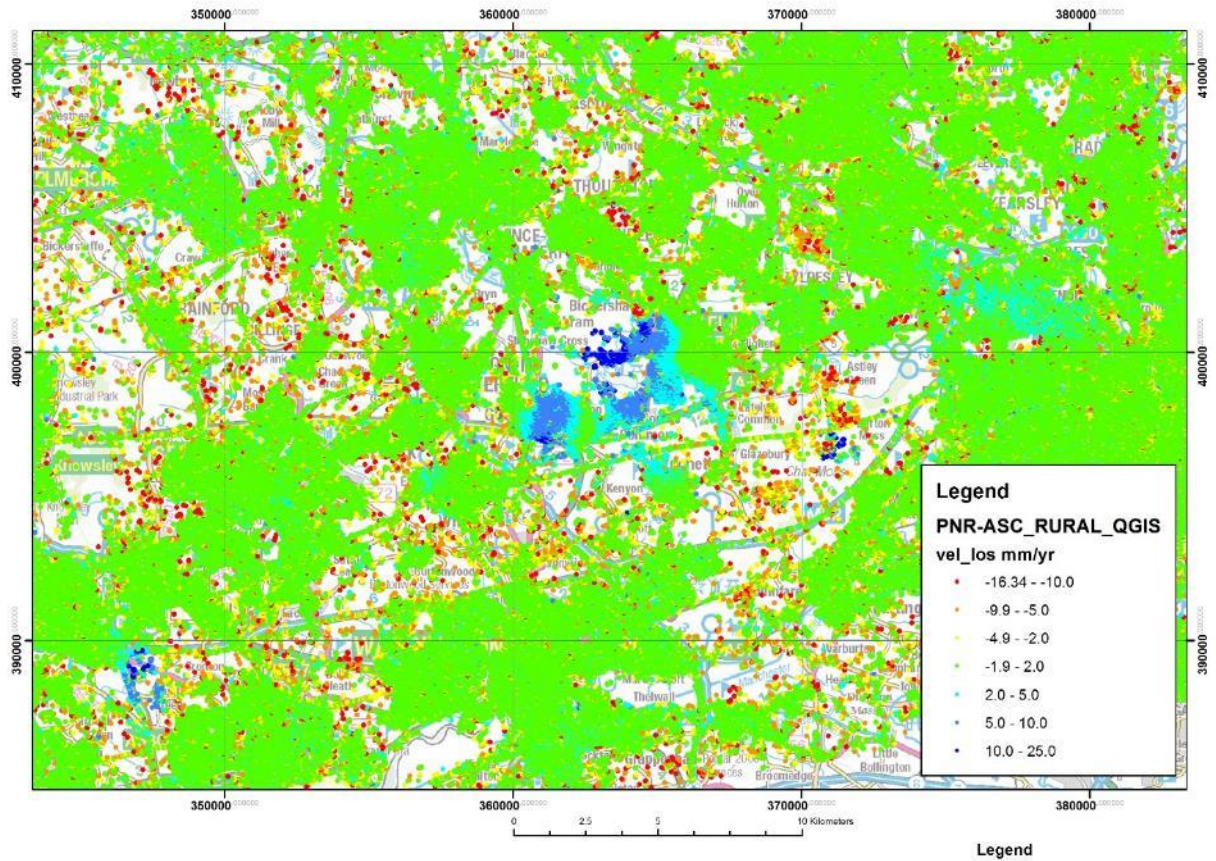


**Figure 58. RapidSAR Sentinel-1 Ascending rural data showing uplift in Leigh to the west of Manchester.**

The Ribble Estuary exhibits patterns of subsidence when the average velocity measurements are displayed at the scale shown in Figure 56, this is likely to be due to compressible poorly consolidated sediments along the estuary. However when viewed at 1:150,000 scale as in Figure 59, it is apparent that there are far fewer subsiding (red) points than there would appear to be when viewing at 1:400,000 scale as in Figure 56. This area (in Figure 59) is therefore a good example of the dangers of interpreting average annual motion when displayed at a large scale: these arise due to two reasons:

1. GIS point display characteristics: when zoomed out points are scaled to be larger so that the viewer can see the points, if there are many points in an area then they will sit on top of one another and the dominant colour come through (e.g. green). However, where there are few points they will not be overlaid each other and therefore the colour of those present will appear more dominant.
2. Noise in InSAR results: InSAR measurements are noisier where the point coverage is less dense; this is because the algorithms use adjacent points to help with phase unwrapping to derive the patterns of motion (Vajedian et al., 2015). The less dense the coverage the more likely noise will be present and the more likely these are to show larger motion which will then get disproportionately displayed as in point 1 above.

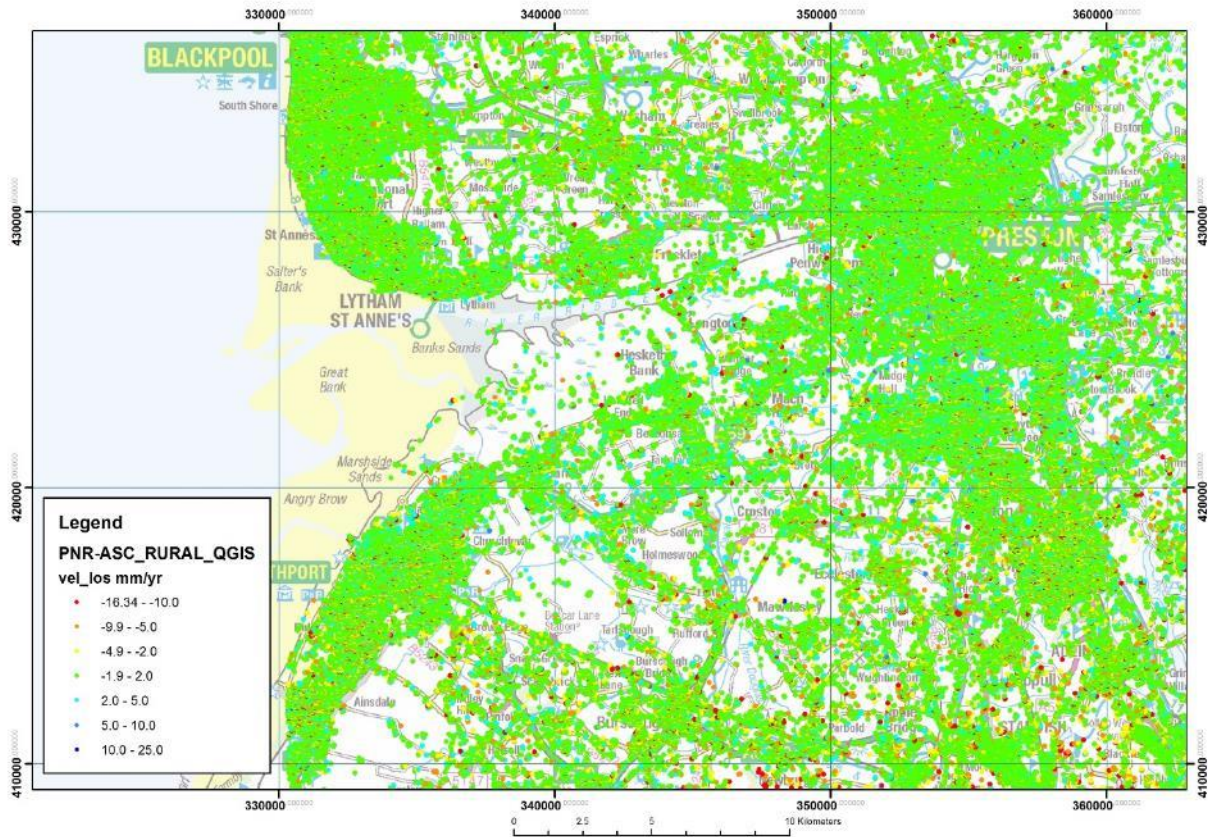


**Figure 59. RapidSAR Sentinel 1 Ascending rural data of the Ribble Estuary – at 1:150,000 scale the subsidence seen in Figure 58 is not as apparent.**

### 3.5.2.2 RAPIDSAR URBAN RESULTS

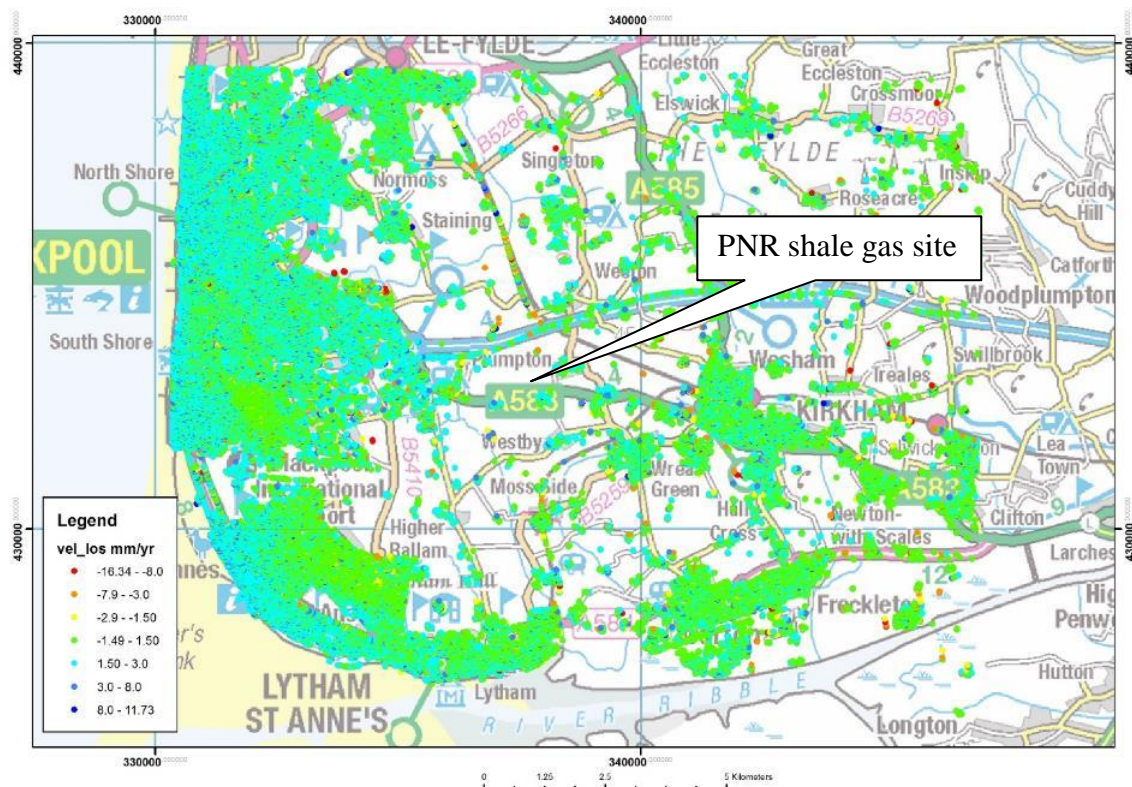
The urban results have been used to study the PNR site in detail. High-resolution results were provided for the entire radar frame, the data were composed of 4.4 million points, and this was cropped to the study area for ease of viewing and interrogation.

The average velocity for the ascending data show the Fylde to be stable over the four-year period examined (Figure 60). This Sentinel-1 time period prior to the shale gas activity is also an important baseline. Hydraulic fracturing activities took place during three to four months from October 2018 onwards, it is therefore necessary to examine the Sentinel-1 time series in the area of interest for the period prior to October 2018 to establish the baseline in the Sentinel-1 data.

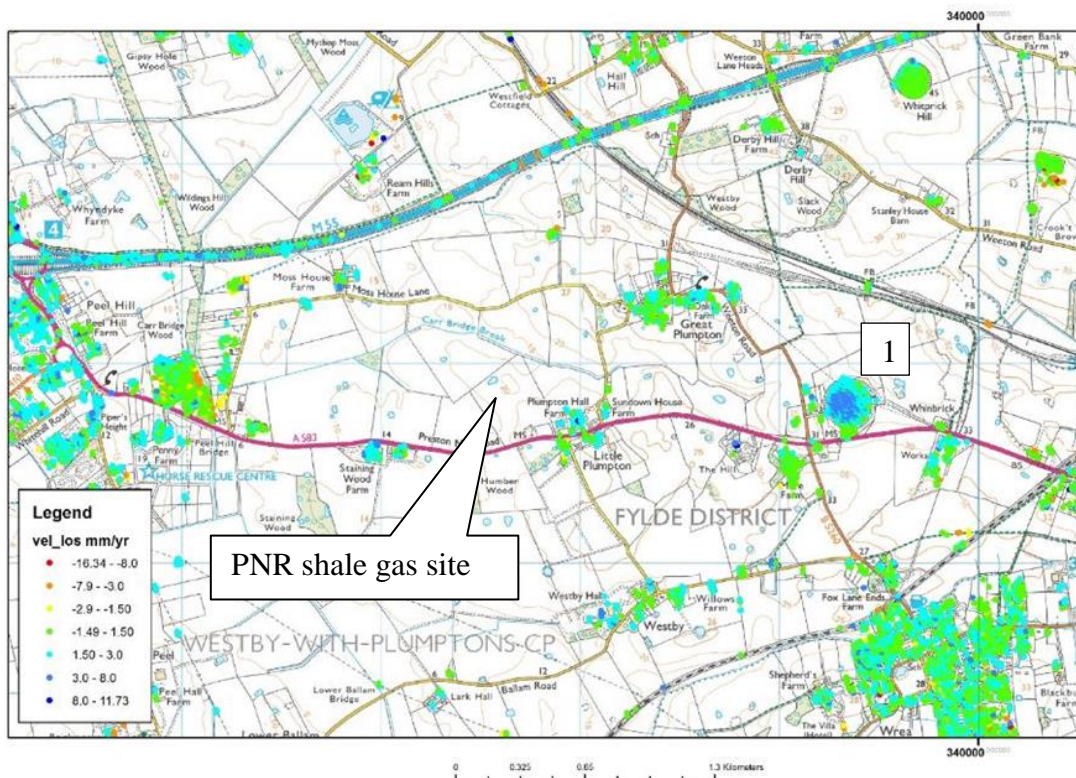
The average annual velocity for the PNR site (



Figure 61) reveals that there are areas displaying a small uplift (approximately 3 mm per year) and a small area showing rates of subsidence of up to 5 mm per year.



**Figure 60. RapidSAR Sentinel Sentinel-1 Ascending high-resolution data for the PNR site. [1] denotes the location of an underground reservoir**



**Figure 61. RapidSAR Sentinel Sentinel-1 Ascending high-resolution data for the PNR site. [1] denotes the location of an underground reservoir**

One area of uplift is an underground water reservoir (marked with a [1] on Figure 62), this reservoir has a metal structure over the top of it, which is a strong radar backscattering surface with a very high InSAR point density (Figure 62). InSAR points derived from this target should therefore exhibit a high signal to noise ratio. This is therefore a key target to understand the time series characteristics of the high resolution data.

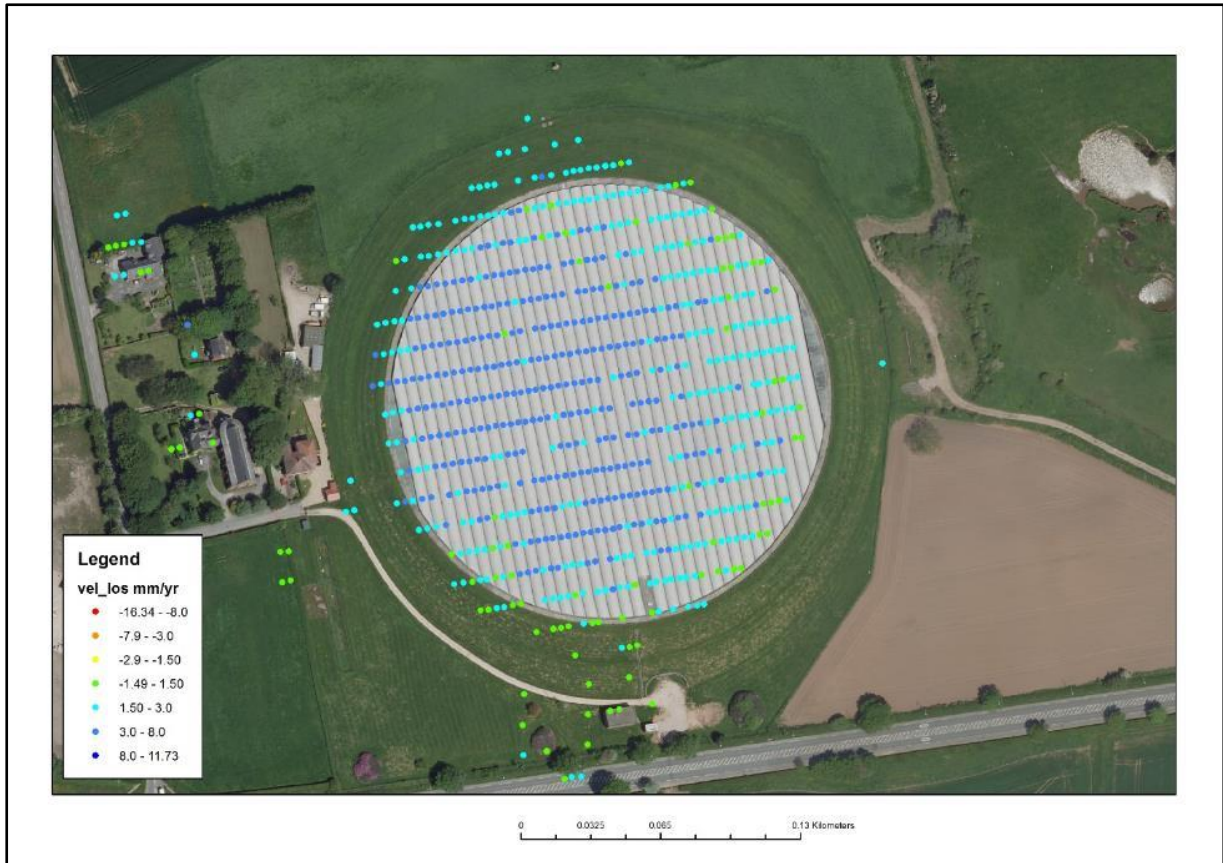


**Figure 62. RapidSAR Sentinel 1 Ascending high-resolution data for the metal covered underground water reservoir.**

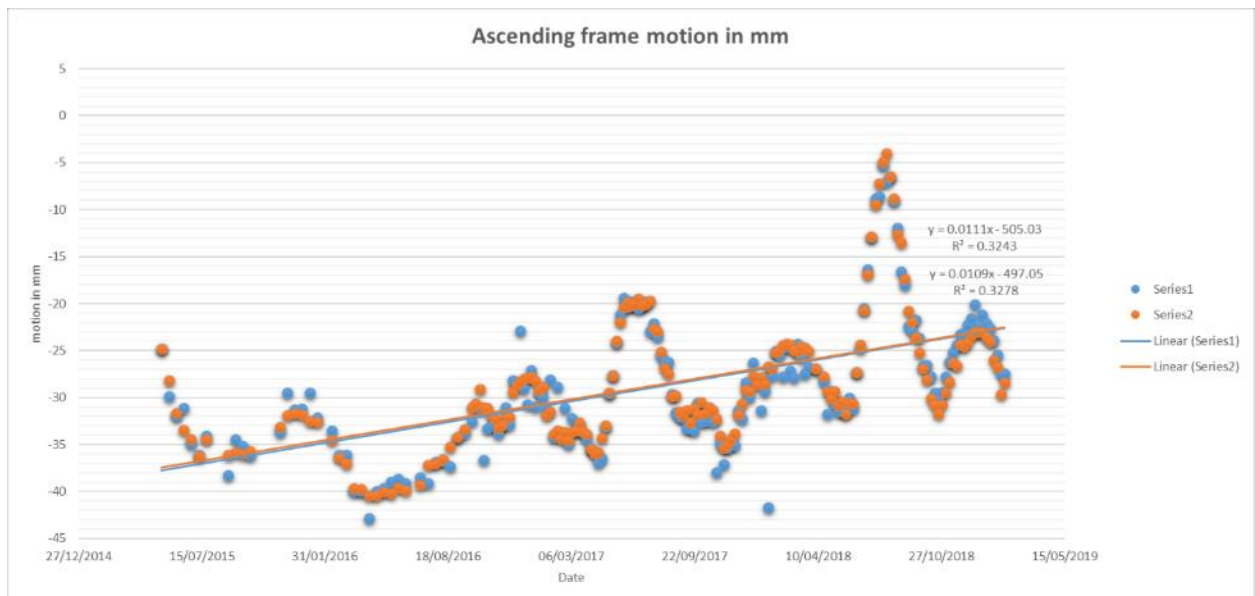


**Figure 63. Ascending time series for points in the centre of the reservoir shown in Figure 62.**

The time series in Figure 63 displays an overall signal of uplift, however there are also periodic signal events. The periodic signal occurs in all of the time series plots from the ascending high resolution data from the points surrounding the PNR site. The cyclicity is heterogeneous in amplitude and wavelength with peaks in December 2018, July 2018, March 2018, July 2017, December 2017, and December 2015. In order to determine if the cyclicity is the result of a

pattern of ground motion or an external factor such as atmospheric conditions, or the use of an unstable reference point, they have been investigated in five ways:

1. Comparison of ascending and descending time series for the same area;
2. Comparison of time series with changes in groundwater level;
3. Comparison of time series across the radar scene;
4. Removing the cyclic components with the Fast Fourier Transform (FFT);
5. Changing the reference point to be nearer the area of shale gas operations.

#### *Comparison of ascending and descending time series*

The ascending and descending time series show the same pattern of motion although the magnitudes are different. In the descending time series (Figure 64) the range of motion is smaller (-14 to +3 mm in comparison to -42 to +6 mm seen in the ascending data), but peaks are observed in the ascending and descending at the same dates.

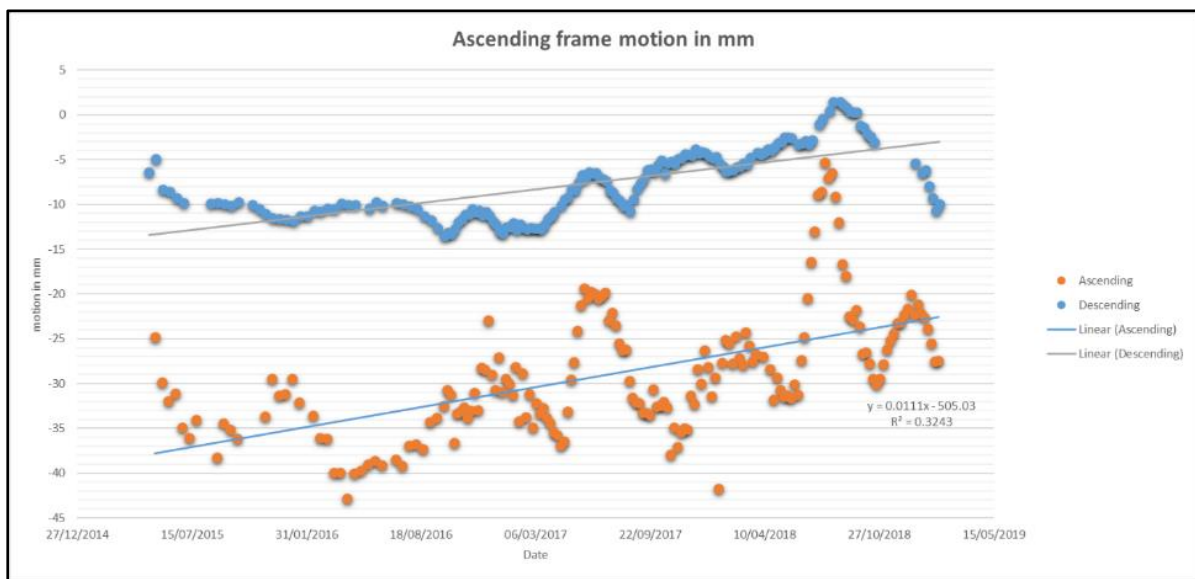


**Figure 64. Descending time series for points in the centre of the reservoir shown in Figure 62.**

#### *Comparison of time series with changes in groundwater level*

Environment Agency (EA) groundwater level data is available for two locations near to the PNR site. These are ‘Crow Lady Farm’ and ‘Bnfl’. Bnfl is just over 10km to the east of the PNR site and Crow Lady Farm just over 11km to the east (Figure 65).

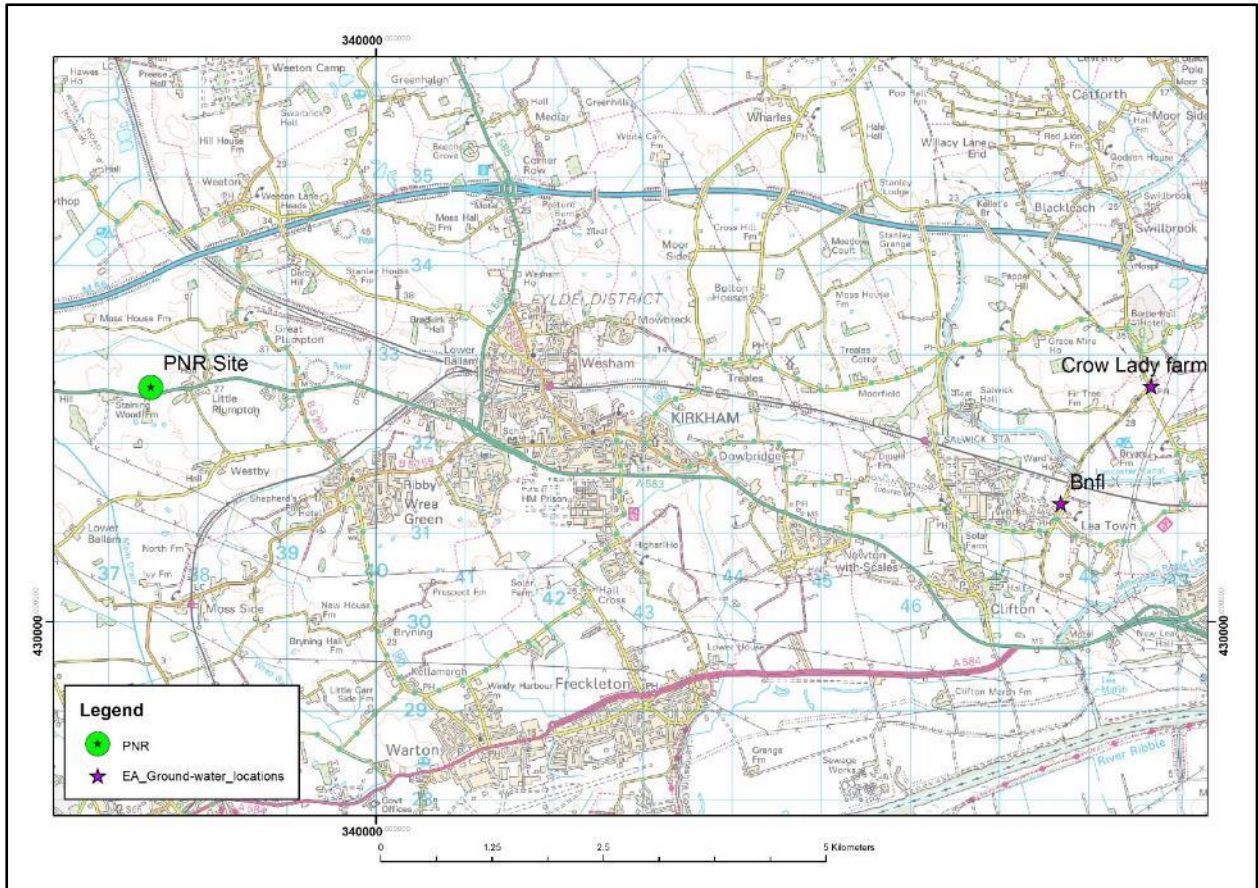


**Figure 65. Environment Agency groundwater monitoring sites in relation to PNR.**

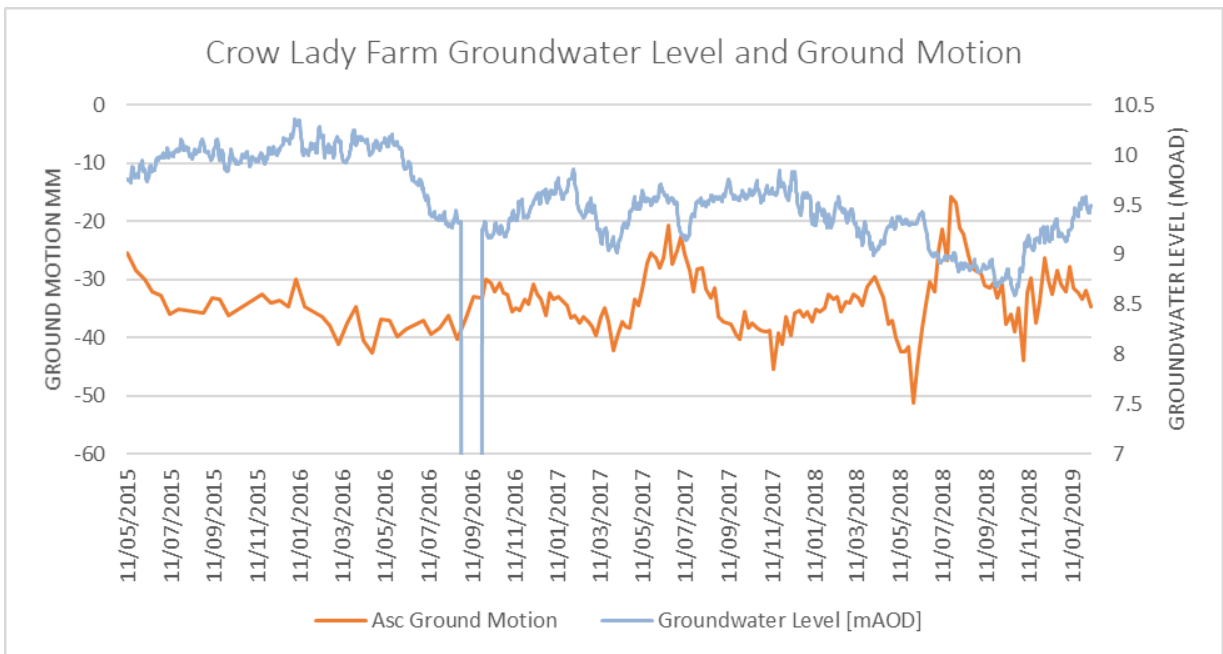


**Figure 66. Ascending ground motion time series compared to groundwater levels for Crow Lady Farm. © Environment Agency and database right 2019.**

The ascending time series for Crow Lady Farm (Figure 66) shows the same cyclical motion as observed in the time series for the underground reservoir next to the PNR site (as shown in

Figure 63 and Figure 64), even though these two locations are separated by approximately 10km. There is therefore a motion signal, which can be observed over spatial scales of at least 11km. Comparison of the groundwater and ground motion time series for Crow Lady Farm (Figure 66) and Bnfl (Figure 67) reveals a lack of direct correlation between the motion and changes in groundwater level. It is therefore unlikely that regional changes in groundwater levels are driving this apparent regional ground motion cyclical signal.

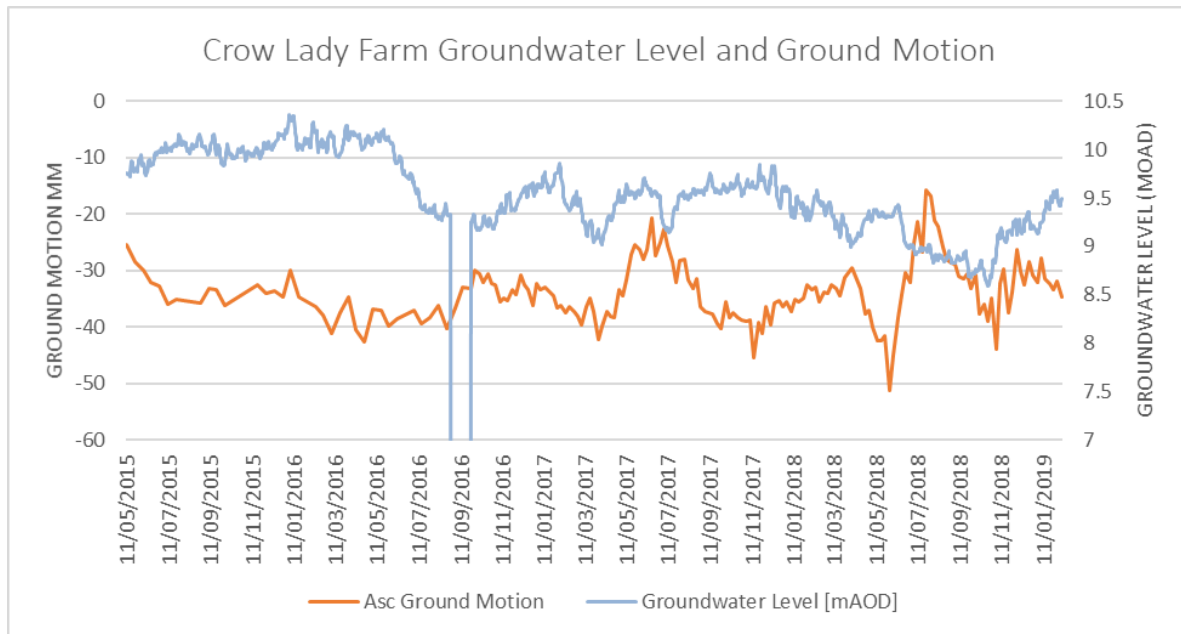


**Figure 67. Ascending ground motion time series compared to groundwater levels for ‘BNFL’.** © Environment Agency and database right 2019.

*Comparison of time series across the radar scene*

The time series near the PNR site (Figure 63 and Figure 64) and the time series for central Manchester show cyclicity (Figure 68), however the latter is of a smaller magnitude and the peaks and troughs are at different temporal positions. Therefore, there is not a consistent pattern to the observed cyclicity over the entire radar scene but there is consistency over shorter spatial wavelengths. This signal may therefore be related to yet un-identified causes of ground motion or atmospheric effects, which operate over the 10-20km range.

*Removal of the cyclic pattern from the signal*

Assuming that the cyclic component is a result of noise (either from the atmosphere or another source), we performed a frequency-domain signal analysis using the FFT algorithm on each point. FFT converted the time series from the time domain to the frequency domain where the amplitude and phase of each frequency can be retrieved. Frequencies higher than the 25<sup>th</sup> percentile in the frequency spectrum have been removed and the remaining signals used to reconstruct a filtered time series (Figure 69).

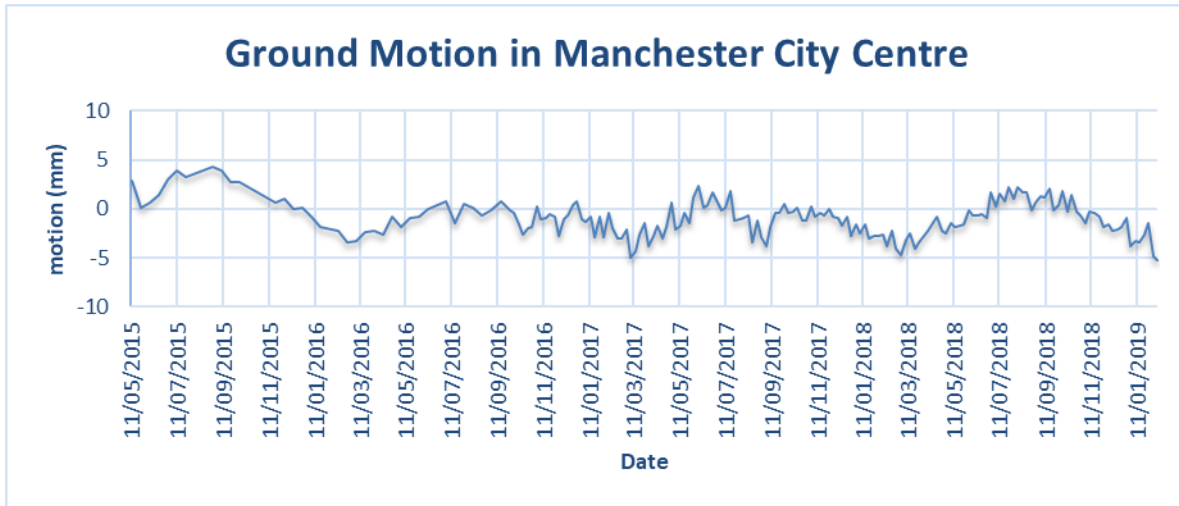


**Figure 68.** Ascending ground motion time series for points in the centre of Manchester.

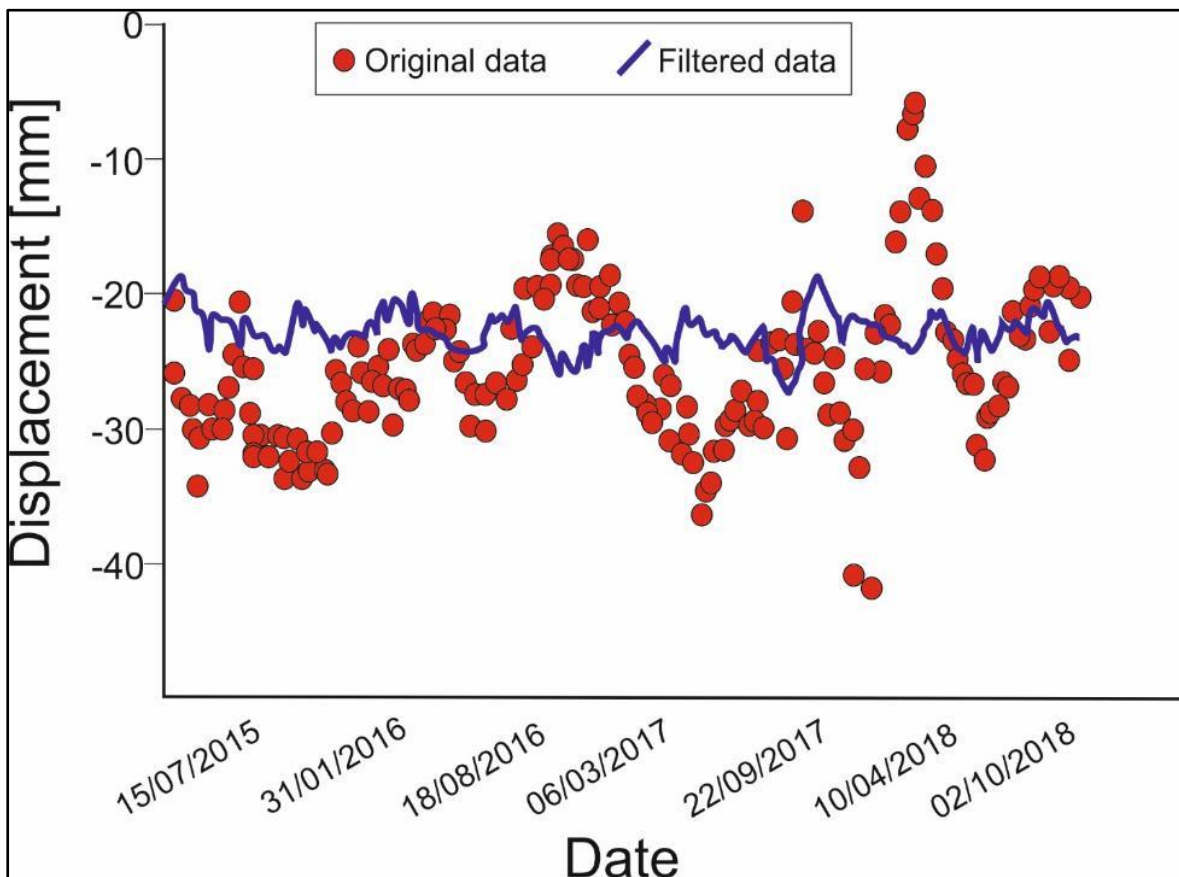


**Figure 69.** The original time series from the RapidSAR ascending data and the observed signal after the removal of the main cyclical components.

The filtered data for the PNR site displays a stable overall trend with a variation about the average of approximately 5-10mm. The cause of the noise is not known therefore its statistical removal may be too strong resulting in the removal of real ground motion signals, for this reason both raw and filtered data are used for the post hydraulic fracturing comparisons in the following sections.

### Changing the InSAR reference point

The reference point is a point within the processed data, which is assumed to be stable. All time series and velocities are referenced to this zero-motion point. If this point is far away from the area of interest then noise, such as atmospheric interference, can propagate and accumulate. It is therefore good practice to reference the data to a stable point close to the area under consideration. The ascending time series were re-referenced to a point closer to the shale gas operations (i.e. the reference point has been moved to the Kirkham Grammar School). The original reference point used was to the south of the radar frame close to Manchester.

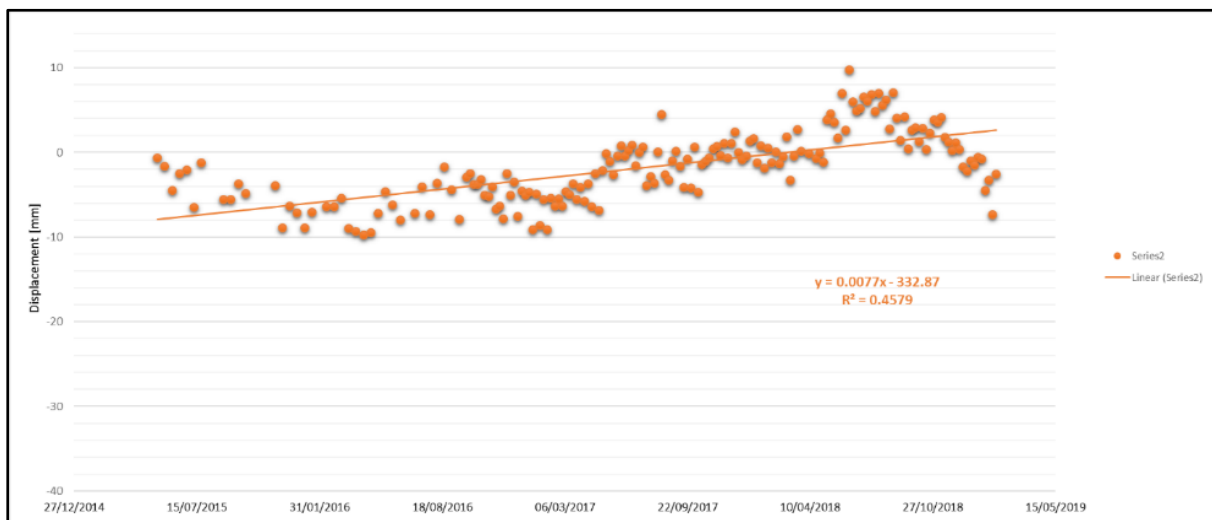


**Figure 70. Re-referenced ascending time series for points in the centre of the reservoir shown in Figure 62.**

The re-referenced ascending time series (Figure 70) still displays the same overall uplift trend as its original (Figure 63) but the cyclical peaks and troughs are reduced and the variation is much smaller. This therefore makes the interpretation of the motion within the period of shale gas operations more reliable. The re-referenced time series is used in the analysis in Section 5.4.

### 3.5.3 ISBAS results

Overall, the ISBAS data show the Flyde to be stable. Three areas of subsidence with average motion rates of up to 5mm per year are found in the southwest of the area (circled in Figure 71) these all correspond to golf courses. The golf courses are built upon superficial peat and wind-blown sands; it is therefore likely that the motion is related to water management at the golf courses. Regular watering of these areas during the dry periods experienced in 2018 may have led to differential ground motion.

The ISBAS time series data also has a variation (noise) of approximately 10-15mm (Figure 72). The first part of the plot shows that the noise is larger before the second Sentinel-1 satellite was launched (October 2016), which brought the revisit time down to 6 days rather than 11 days. However, at these locations we can clearly see that subsidence is occurring between September 2016 and August 2018.

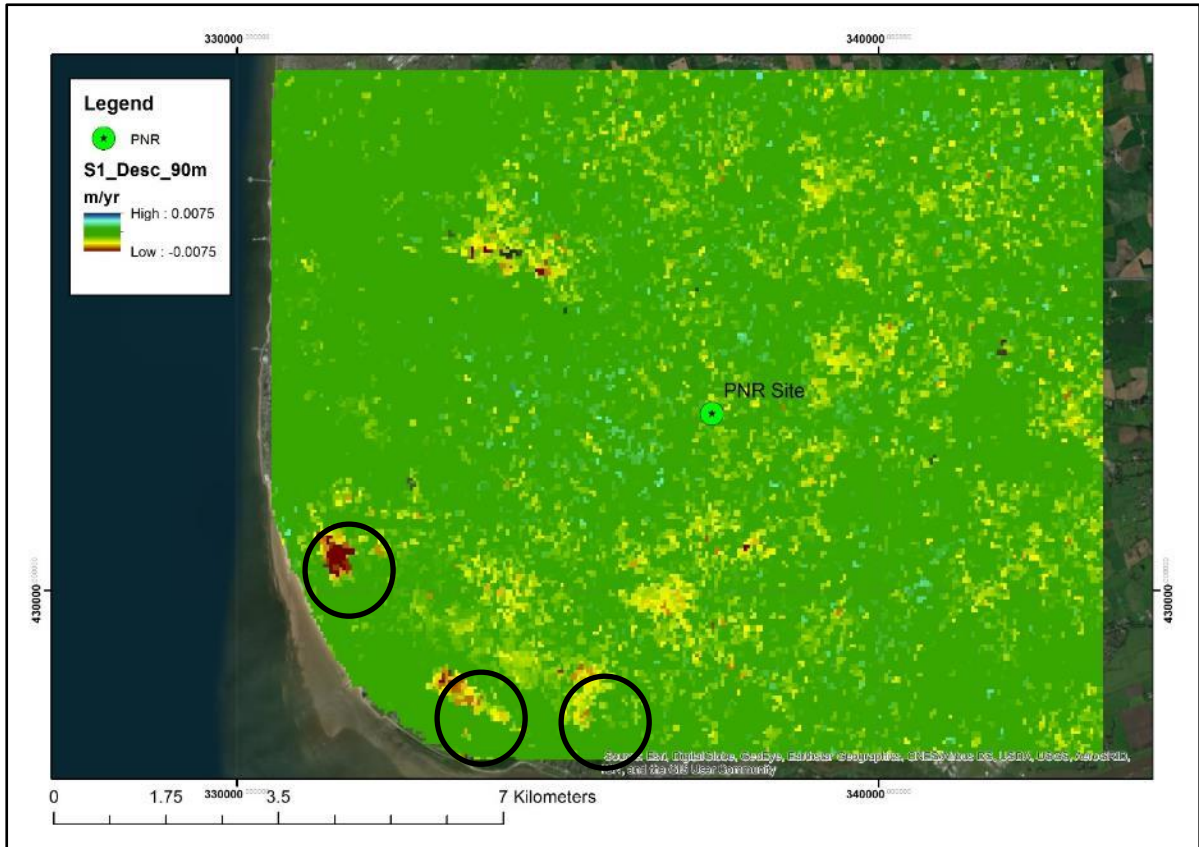


**Figure 71. ISBAS Sentinel 1 descending average velocities for the Flyde (projected to the vertical).**

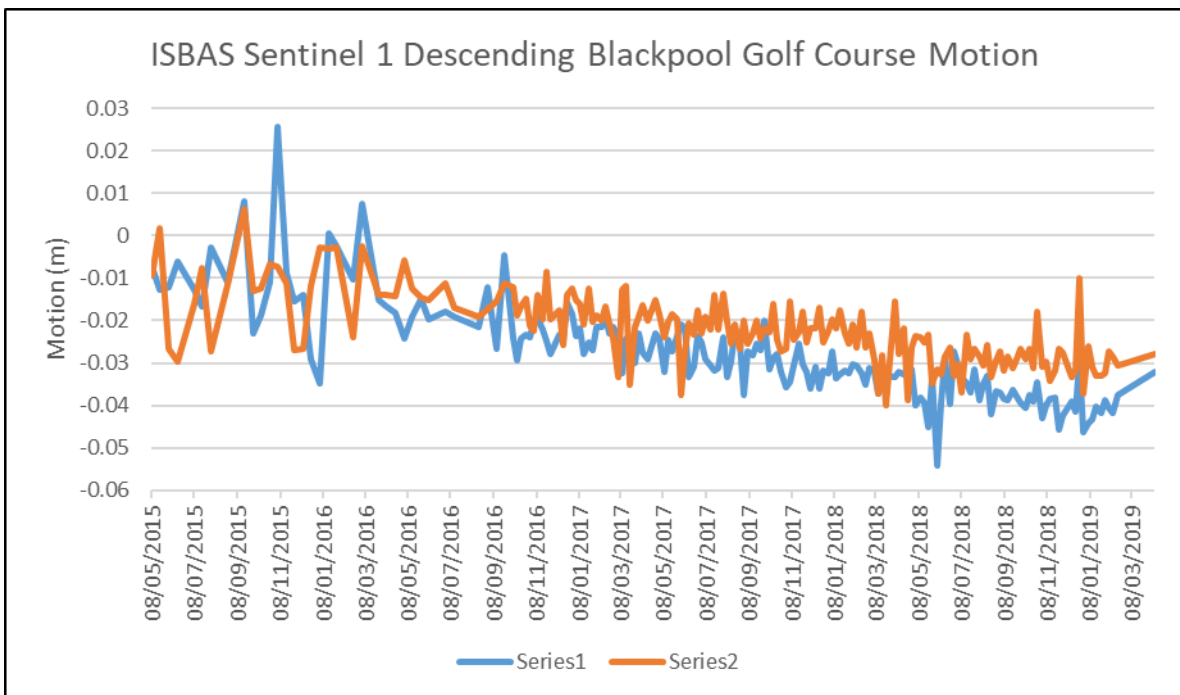


**Figure 72. ISBAS Sentinel 1 descending time series for points on the golf course the south of Blackpool (northern most circle in Figure 71).**

### 3.5.4 Post Baseline Ground Motion at the PNR site – RapidSAR Data

The time series for InSAR points at or near to the PNR site were examined (Figure 73) to establish whether or not hydraulic fracturing activities produced detectable ground motion. In particular the Sentinel-1 motion patterns for the period October 2018 – February 2019 were compared to the Sentinel-1 baseline of May 2015 – September 2018.

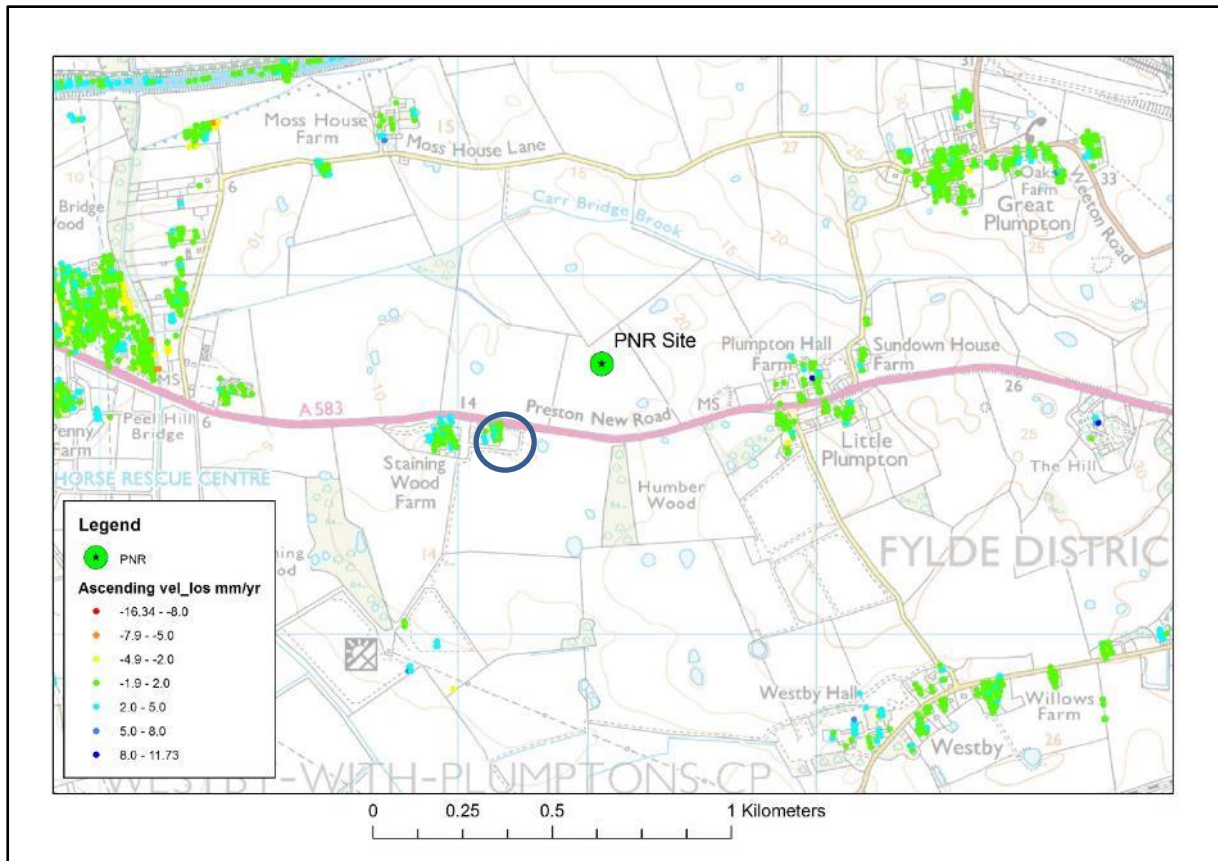


**Figure 73. Ascending ground motion time series for the region around the PNR site, showing locations of time series shown in Figure 74.**

Figure 74 reveals that, for the InSAR measurement points closest to the PNR site there is no significant change in the patterns of motion during the period of shale-gas activity compared to the baseline period (prior to operations). During the period of activity (October 2018 to January 2019) there is a variation in ground motion of approximately 10mm, this variation is within the magnitude of ~15mm variation observed during the baseline period.

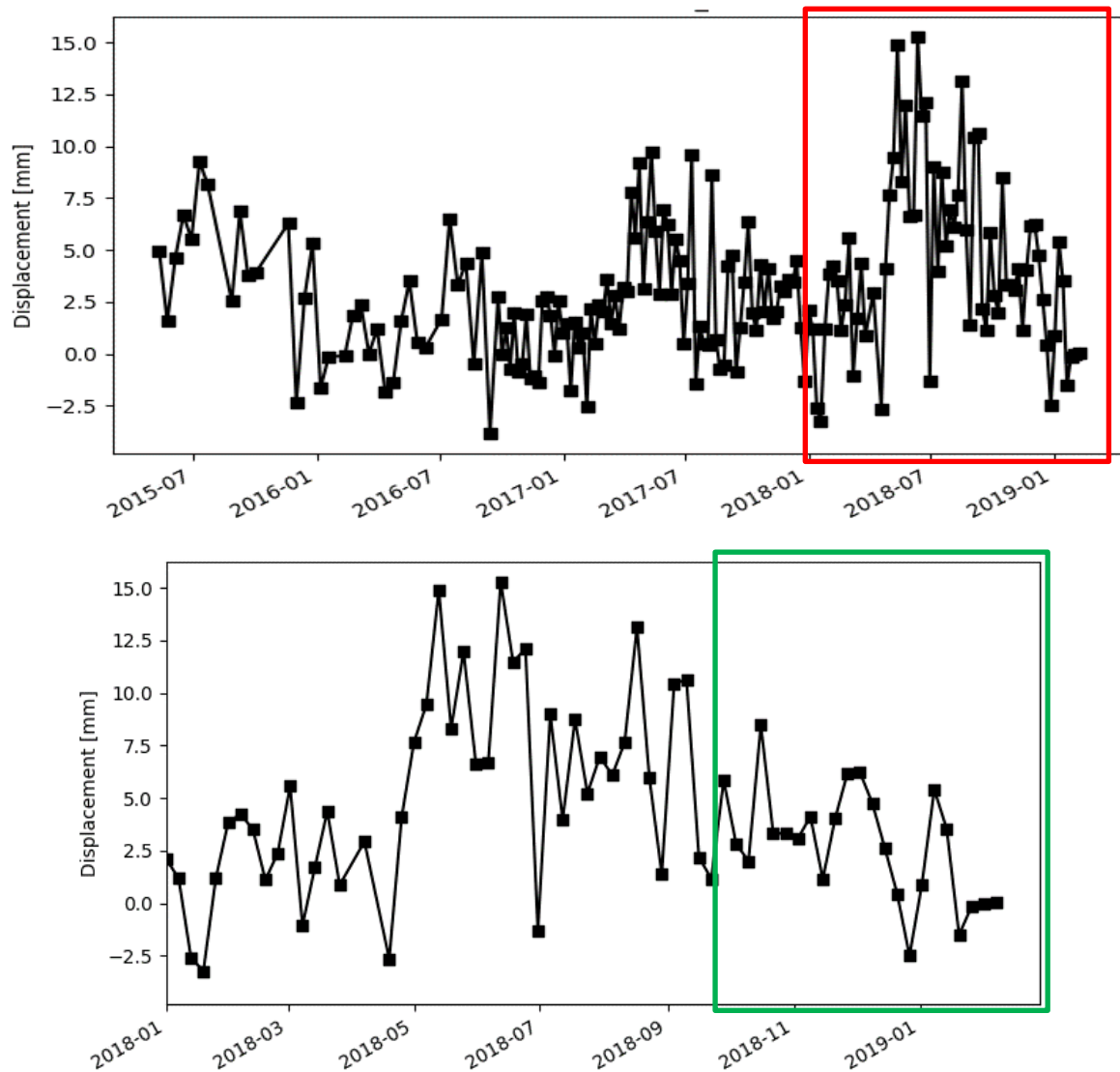


**Figure 74. High resolution ascending time series for points highlighted in Figure 73, the top plot shows the entire Sentinel 1 time series, the lower plot shows more detail for the red box including the time series for the period of hydraulic fracturing activity (highlighted by the green box).**

### 3.5.5 Comparison with 1992–2000 baseline

Comparisons of the hydraulic fracturing period with the ERS 1990’s data at the PNR site show that the site activity since October 2018 has not produced ground motion that differ from the long-term baseline. In the 1990’s the average motion at the detected points closest to PNR was within the range considered to be stable (Figure 75), the recent Sentinel-1 results also show the PNR site to be stable on average (over the 4 years processed). The ERS data (Figure 76), shows that the area was stable on average over the eight year period, however a variation of 20 mm was common during the 1990’s, a similar variation can be seen in the recent data (see Figure 74) and the variation for the hydraulic fracturing period is much less at only 10-12mm (see Figure 74).

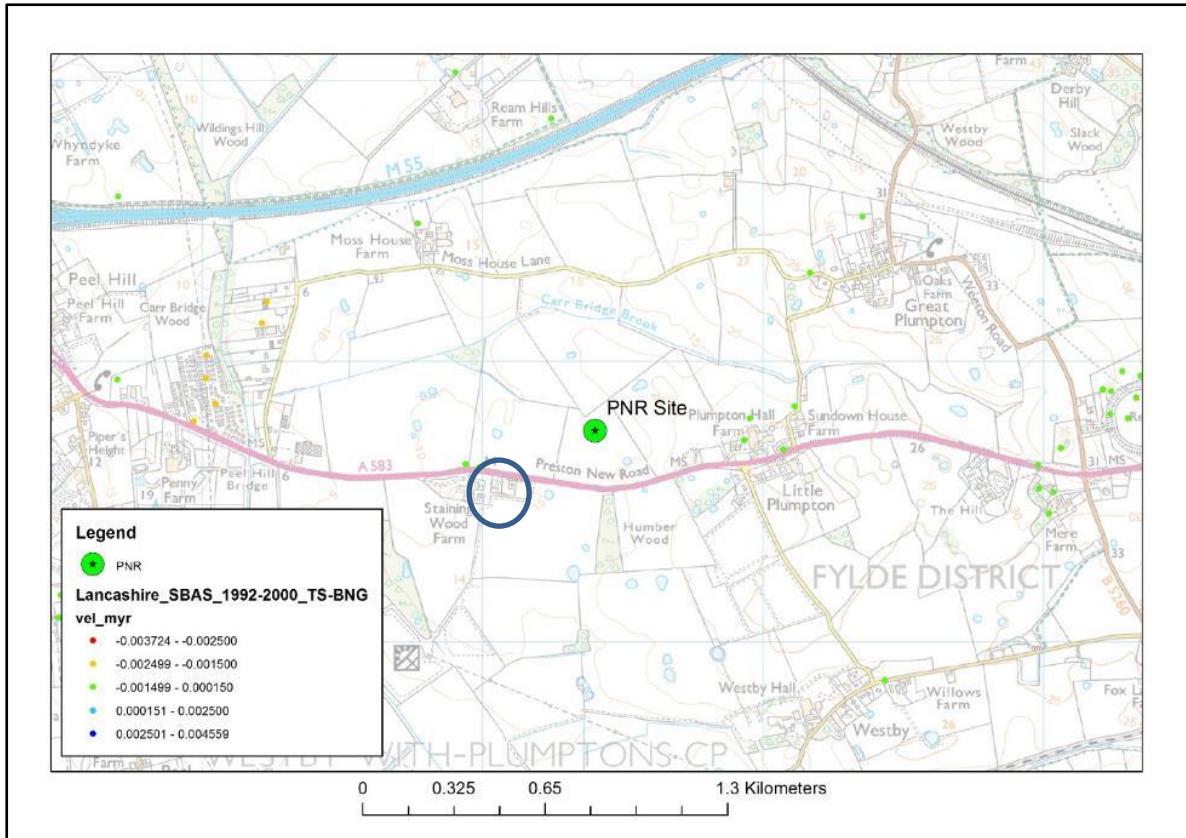


**Figure 75.** Ground motion average velocity points closest to the PNR site as derived from ERS data, 1992 – 2000. Circle highlights points for which time series are shown in Figure 76.

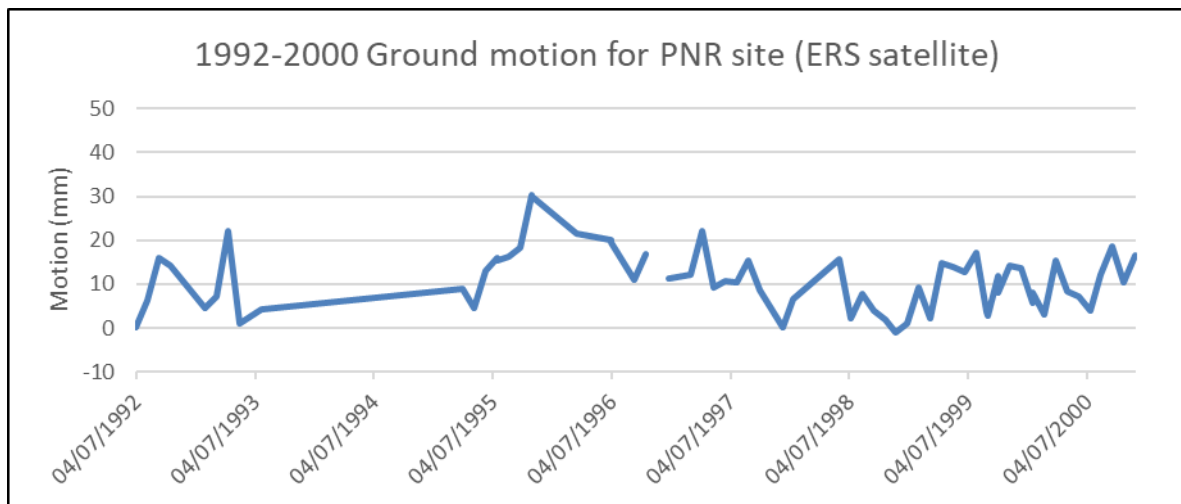
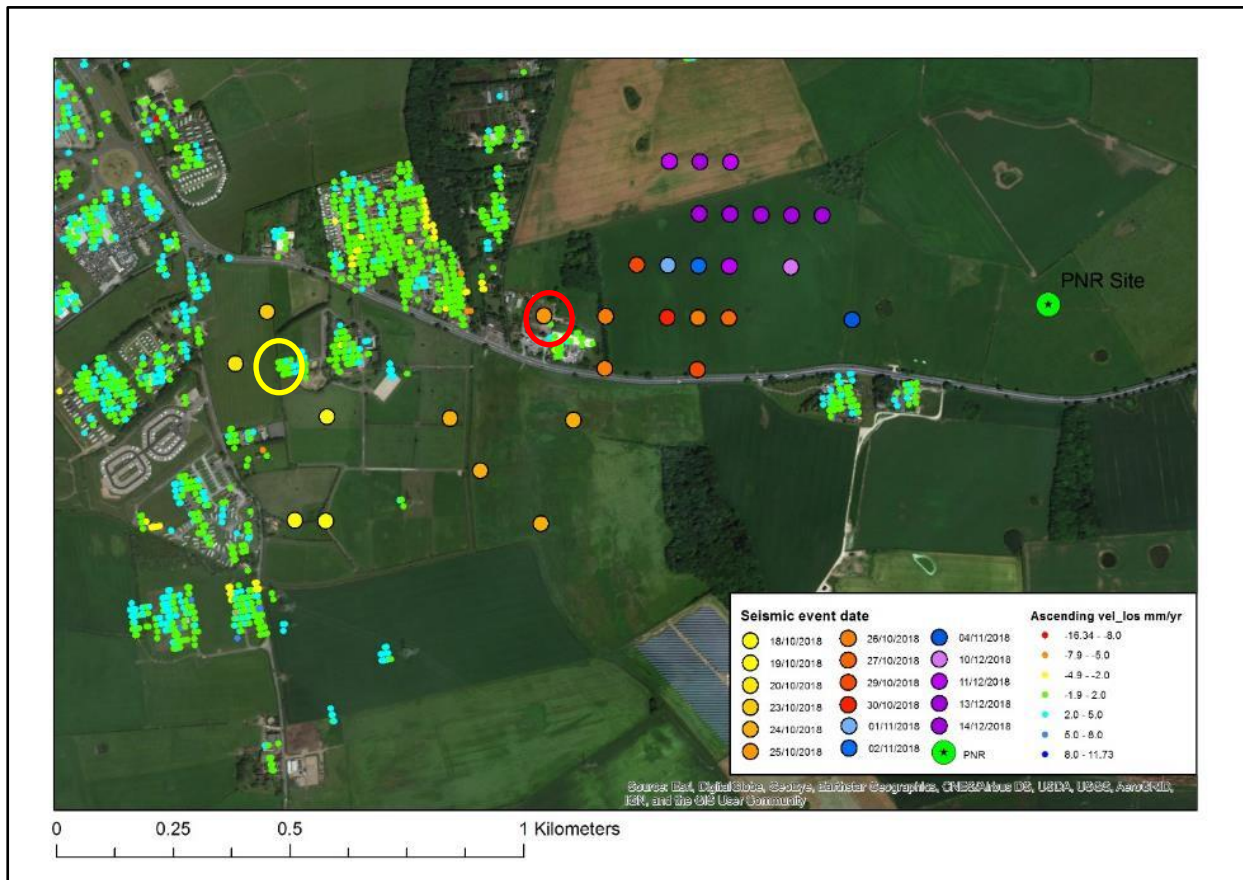


**Figure 76.** Ground motion time series for the points closest to the PNR site as derived from ERS data, 1992 – 2000.

### 3.5.6 Ground Motion at the locations of seismic events

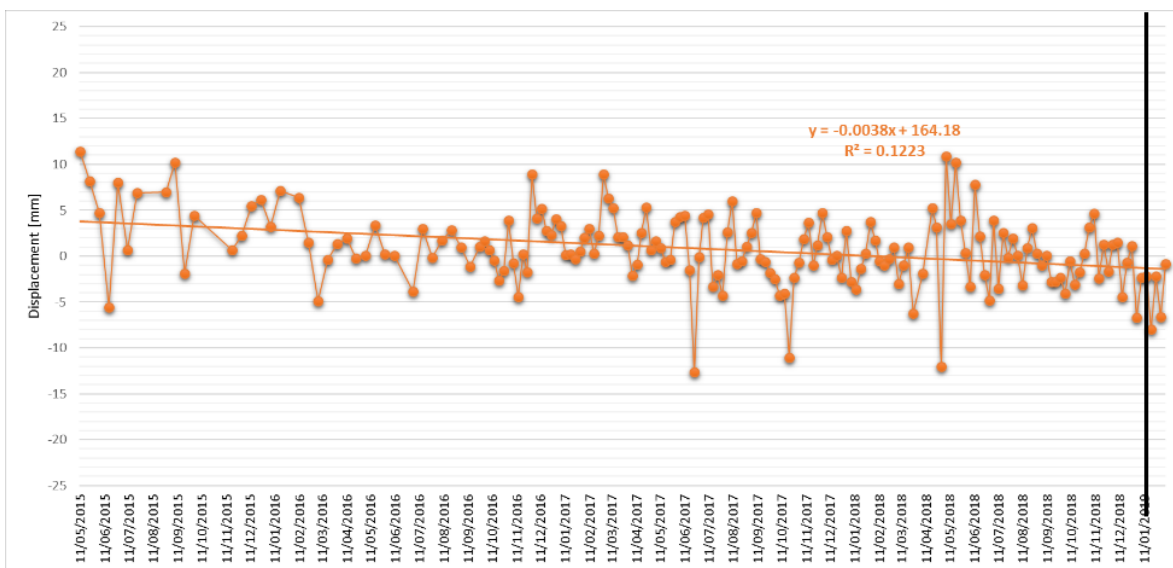
Hydraulic fracturing activities were halted several times during the fracturing phase of operations as the threshold for monitored seismic events was exceeded (seismic data from <http://www.earthquakes.bgs.ac.uk/earthquakes/dataSearch.html>). Figure 77 shows the

spatial location of the seismic events and the ground motion measurement points in the vicinity of these events.



**Figure 77. RapidSAR InSAR points displayed according to average velocity and seismic events in the PNR vicinity in October – December 2018.**

In Figure 77 the seismic events have been coloured according to the date on which they occurred. The ground motion time series for measurement points closest to the seismicity were analysed for these dates; some of the results are presented in Figure 78 and Figure 79.



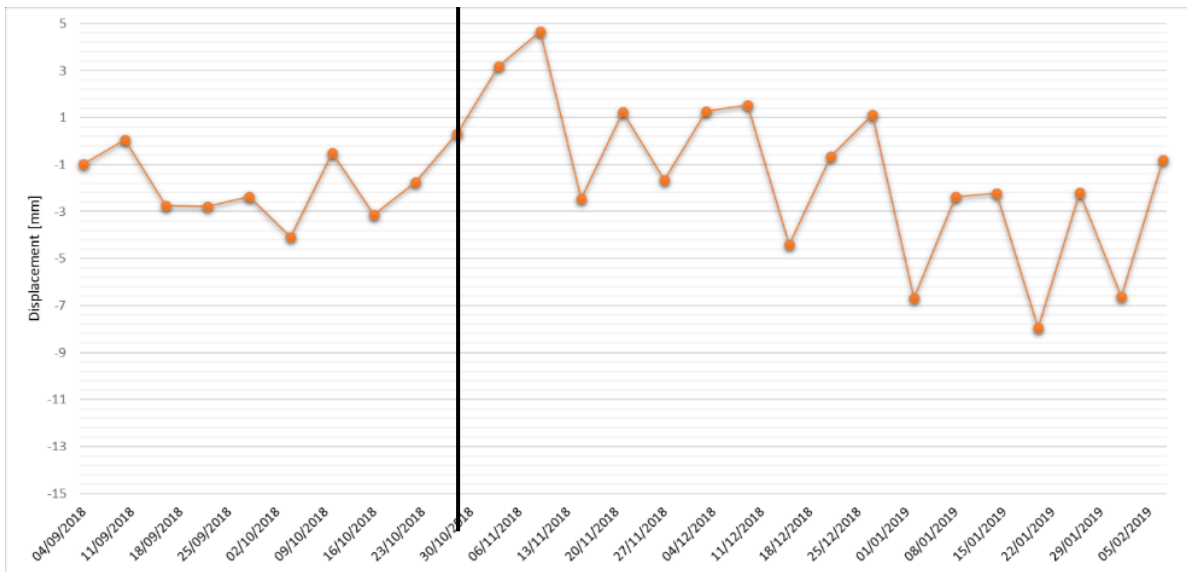


**Figure 78. RapidSAR InSAR time series for the points highlighted by red circle in Figure 77. The top plot shows the full raw time series and the bottom plot shows the raw time series for the period of activity. On both plots the black line indicates the date of the closest recorded seismic event (25/10/2018).**

The seismic events cannot be linked to significant ground motion detected by the InSAR data. Although InSAR measurements show surface uplift following the seismic events, this upwards motion does not deviate from, or exceed, the dynamic pattern of variation observed over the preceding three years.

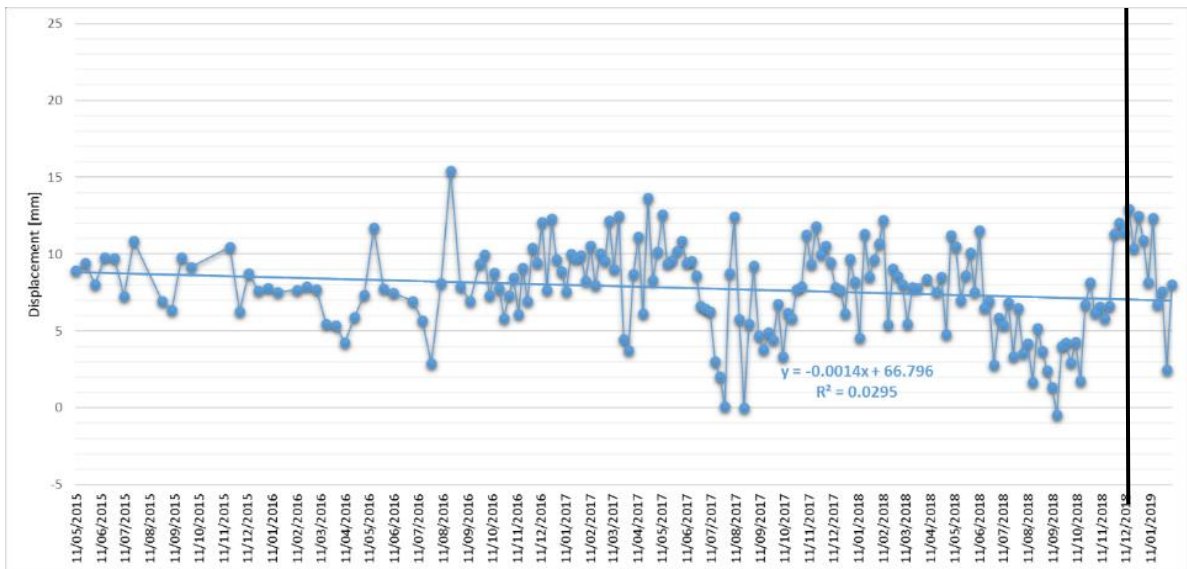


**Figure 79. RapidSAR InSAR time series for the points highlighted by yellow circle in Figure 77. The black line indicates the date of the seismic events closest to these points (18/10/2018-23/10/2018).**

The largest seismic event took place on the 11/12/2018 and was 1.5ML at a depth of 1.6km. The second largest, 1.1ML, took place on the 29/10/2018 at a depth of 2.9km. Both of these

events occurred at approximately the same location (largest purple circle on Figure 80). Once again the RapidSAR time series for points closest to this event shows no significant difference to the preceding period.

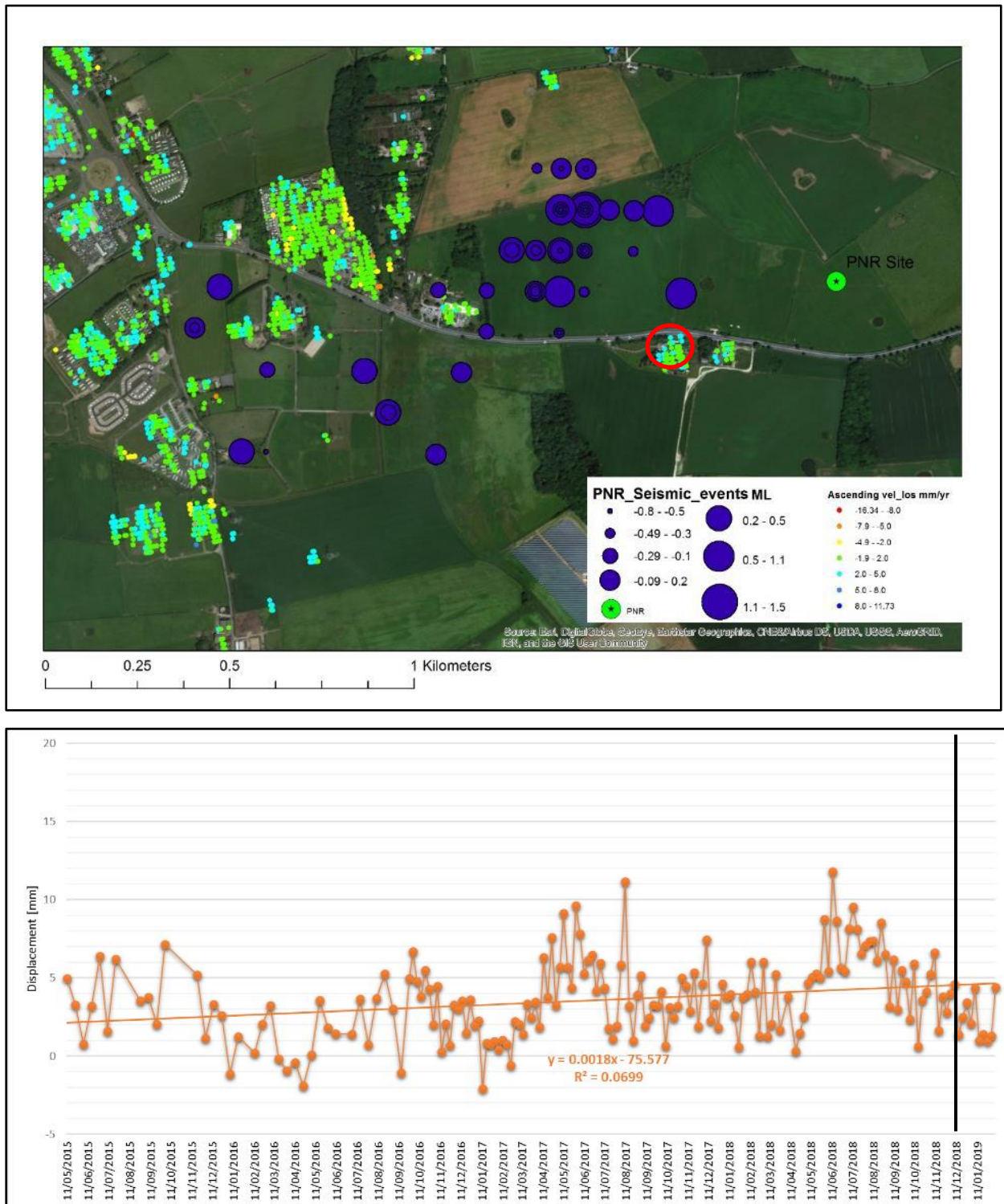


**Figure 80. Top: strength of seismic events denoted by size of circle; bottom: InSAR time series for the points highlighted by red circle. Black line on graph indicates date of seismicity.**

### 3.5.7 Post Baseline Ground Motion at the PNR site – ISBAS Data

#### 3.5.7.1 MOTION NEAR THE PNR SITE

The average annual motion for the 4 year period indicates that the site is stable (as shown by green points in Figure 81). The time series data also indicate average ground stability, while also displaying minor variability around that mean. This variability is within the range seen during the baseline period.

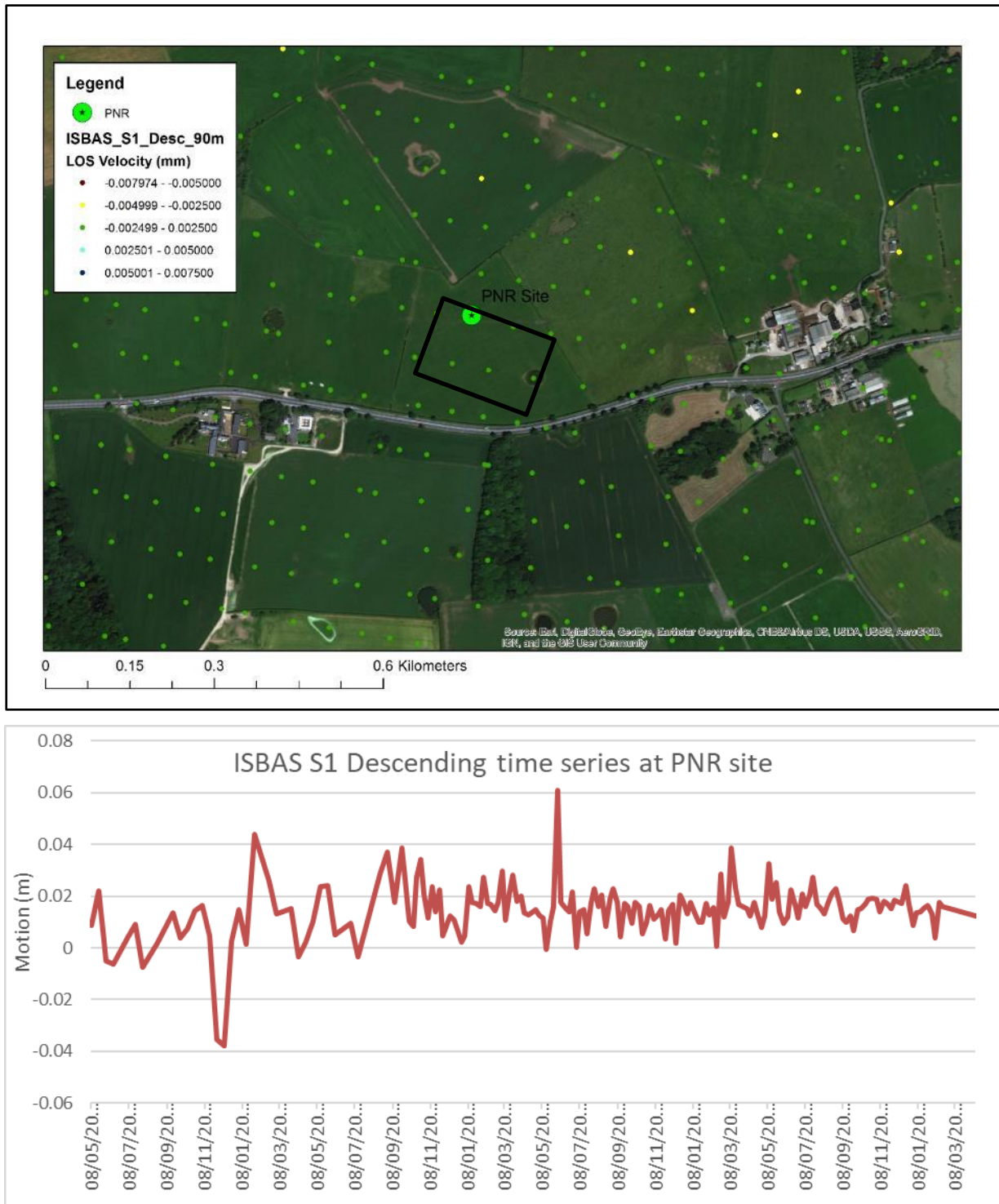


**Figure 81. ISBAS Sentinel-1 descending time series for points on the PNR site (points highlighted by black rectangle).**

### 3.5.7.2 MOTION AND SEISMIC ACTIVITY

As with the RapidSAR data, the ISBAS time series does not show any significant deviation from the baseline motion at the time and location of the strongest seismic event (Figure 82 and Figure 83).

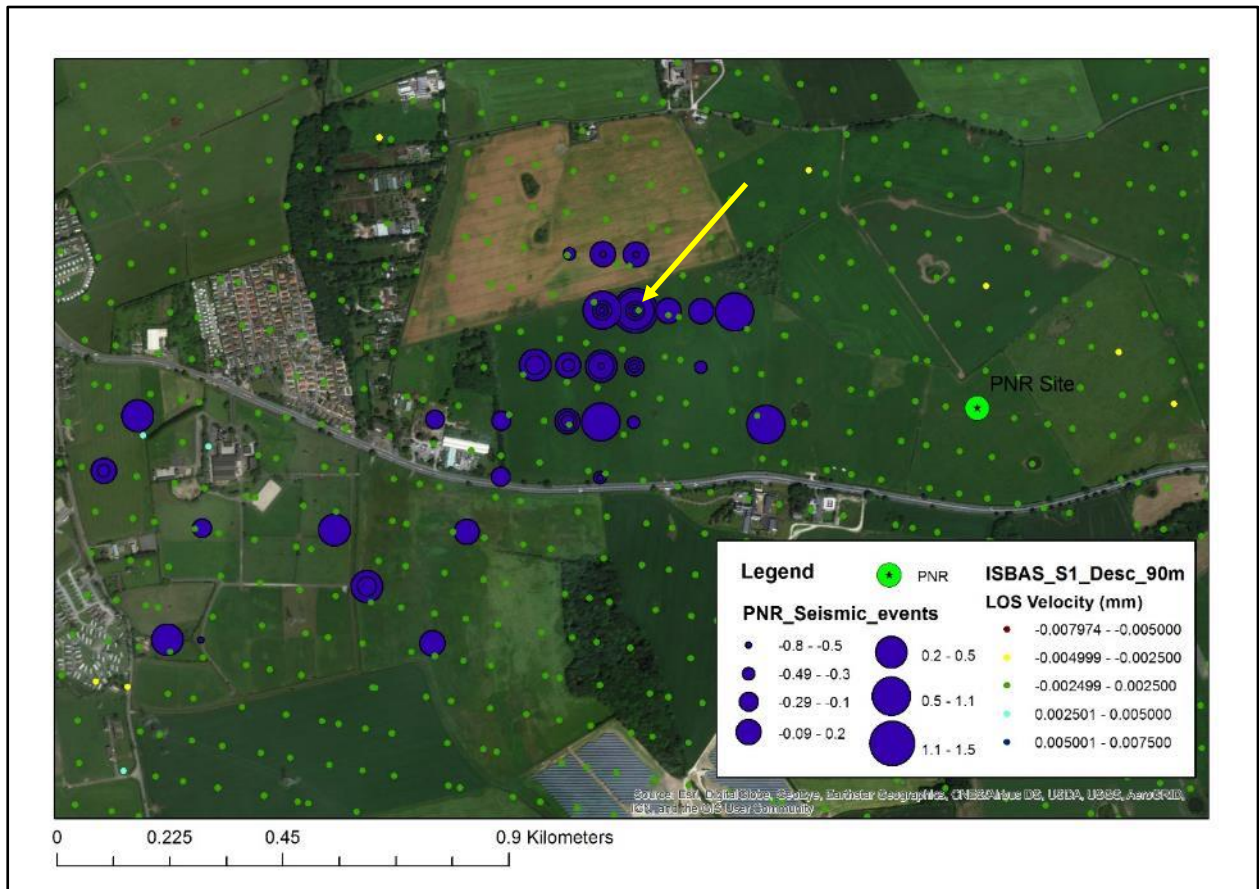


**Figure 82. ISBAS Sentinel-1 descending points and magnitude of seismic events.**

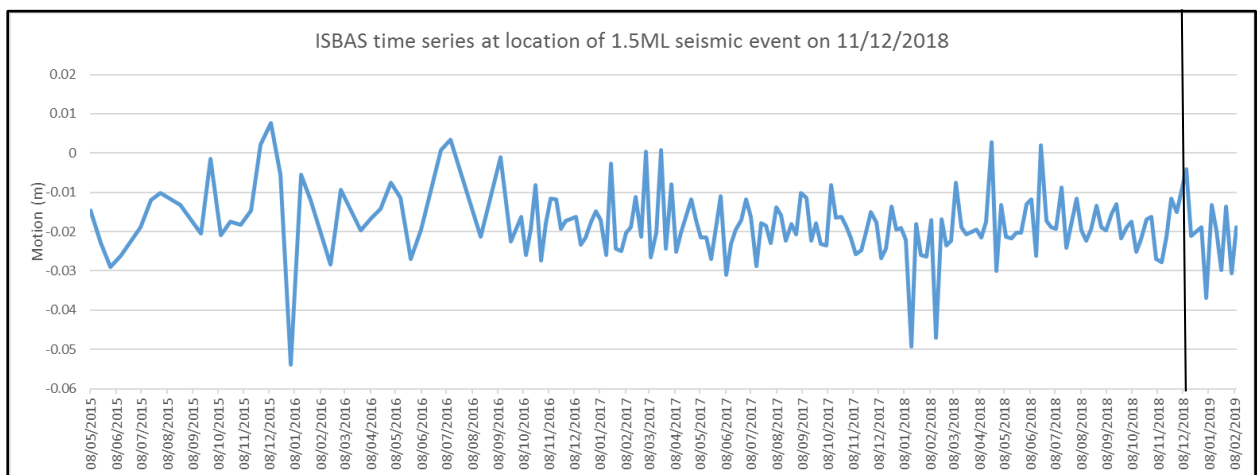


**Figure 83. ISBAS Sentinel 1 descending time series at the location of strongest seismic event (yellow arrow in Figure 80).**

## **3.6 DISCUSSION**

### **3.6.1 Vale of Pickering Baseline**

The Vale of Pickering InSAR ground motion analysis entailed processing three stacks of ERS-1/2, ENVISAT and Sentinel-1 radar satellite data using SBAS and ISBAS techniques (i.e. six levels of analysis in total). The ENVISAT data (2002-2009) consisted of 24 scenes; a stack size that is appropriate for InSAR processing but can be susceptible to atmospheric effects. The SBAS analysis indicated that the urban areas were predominantly stable in the time period. The areas of dispersed motion in the SBAS and ISBAS analyses are most likely due to atmospheric effects rather than genuine ground surface motion. Nevertheless, the zone of subsidence in the south of the monitoring area corresponds to known areas of compressible ground.

The ERS-1/2 Vale of Pickering dataset comprised 72 satellite radar scenes and it has therefore not been affected by atmospheric conditions. The SBAS analysis revealed that the urban areas and connecting roads are stable i.e. they are not affected by regional subsidence or uplift between 1992 and 2000. The ISBAS analysis also indicated that the area is predominantly stable apart from three zones that appear to display dispersed uplift. Our experience of this type of dispersed result is that it is not due to geological motion (which is more discrete) but it is most likely due to vegetation changes and agricultural practices.

The Sentinel-1A data offers the opportunity to extend the ground motion monitoring to the present day and beyond (the satellite is recording images of the UK). Since April 2015, there has been sufficient Sentinel-1A scenes to carry out InSAR investigation for this area of the UK. The InSAR processing of this new data results in an increased number of measurement points using both the SBAS and ISBAS techniques, when compared to ERS and ENVISAT InSAR results.

Within the Sentinel-1A InSAR results there is a great deal of information including a pattern of uplift in the Vale of Pickering, which is most likely linked to the groundwater, whether that be at shallow or greater depths.

A complete baseline has been established for ground motion in the Vale of Pickering. Shale gas operations are currently on hold in the area, therefore the InSAR analysis stopped in 2016, but it can be extended to the present day with Sentinel-1 data if and when operations start.

## **3.7 LANCASHIRE BASELINE**

The Fylde InSAR ground motion baseline analysis entailed processing one stack of ERS-1/2 (covering the period from 1992 to 2000) using SBAS and ISBAS techniques (i.e. two levels of analysis in total). The assessment indicates that zones within the wider region covered by the satellite image stack underwent both uplift and subsidence, while the majority of the region was stable. It is concluded that the uplift and subsidence in the Manchester area are related to coal mining, while the subsidence in the west of the Fylde relates to the presence of compressible ground. These examples provide evidence of the ground motion that this monitoring technique can detect.

Analysis of Sentinel-1 InSAR data for the pre-hydraulic fracturing period (2015–2018) reveals that the motion patterns observed in the 1990's data are still evident. However, their locations have shifted slightly (compressible ground to the west of the Fylde) or signal pattern switched from subsidence to uplift (Leigh) due to changing underground mining operations.

Analysis of the ERS and Sentinel-1 time series reveals a variability of ~20 mm around the mean trend of the ground motion. This is identified as the baseline variability within the InSAR time series data; any meaningful post hydraulic fracturing ground motion signals would

therefore need to exceed this variability or modify the style of motion observed within the time series results for it to be flagged as significant.

### **3.7.1 Lancashire post Baseline**

Two sources of InSAR ground motion data covering a four-year period have been processed and interpreted for the Preston New Road site and wider area. Two InSAR techniques were used (i.e. ISBAS and RapidSAR) to ensure that the best coverage of measurements was obtained both spatially and temporally. This approach was designed to provide the best chance of capturing motion that may be related to shale gas operations.

Analysis of the time series for the period (October 2018- December 2018) shows no appreciable difference following the hydraulic fracturing compared with the baselines established in both the Sentinel-1 and ERS time series. Examination of the Sentinel-1 time series for points closest to seismic events also showed no significant change at the time of seismic events.

## **3.8 CONCLUSIONS**

It was apparent at public engagement events in Lancashire and the Vale of Pickering that (i) there is concern that shale gas operations will cause ground motion and (ii) there is some confusion between seismic activity and ground motion. Many of the attendees link the two and presume that if there is seismic activity there must be ground motion and vice versa. It is therefore important to communicate the situation regarding baseline ground deformation and also provide evidence regarding the opportunities for independent monitoring in order to allay public fears. Part of this is the establishment of ground motion baselines along with monitoring of the situation throughout any shale gas operations. The baseline leads to an understanding of how the natural (and anthropogenic) processes may lead to ground motion. It provides evidence that ground motion already occurs, which may not impact on day-to-day life. It also offers comfort to the public that there is a record of the existing conditions so that if operations start there is a baseline with which to compare the up-to-date information.

The unique characteristics of satellite based InSAR have proven it to be a valuable technique in the establishment of a baseline of ground motion prior to exploitation of shale gas. There are four main benefits of using InSAR to detect and monitor ground motion:

1. In common with most remote sensing techniques, InSAR offers a regional view of the phenomena being measured. Ground deformation points are generated for the entire radar scene; this offers the opportunity to not only focus on ground motion for the immediate area surrounding the shale gas site, but also the wider area. This wider view allows an understanding of the processes, which drive the movement of the ground;
2. C-band satellites have been orbiting the Earth, and imaging the UK, since 1992-93. This data has been archived. It is therefore possible to process the archive data and ‘look back in time’ and retrospectively establish the patterns of ground motion for an area. This is simply not possible with other techniques such as GNSS where the survey equipment must be located on site with knowledge of the phenomena to be measured;
3. InSAR processing results in a dense network of opportunistic measurement points. For techniques such as SBAS the greatest densities are found over urban areas where the built environment act as good radar scatterers. However, recent advances in processing such as ISBAS increase the density of measurements, especially in rural areas, such as the Fylde. Each measurement point has an average velocity but also a time series, this

offers the opportunity to understand how the ground at each point has moved through time thereby enabling the interpretation;

4. The InSAR technique is non-invasive; it does not require access to shale gas operation sites to install monitoring equipment.

Within the Vale of Pickering and Lancashire C-band SAR data have been used to collect a baseline of the ground motion over 25 years and subsequently to characterise the deformation. This baseline shows that overall the areas have been stable. In each area, natural and man-made ground motion is observed which is linked to compressible ground, groundwater level changes and underground mining activities.

Comparison of time series in Lancashire for the period when hydraulic fracturing took place (October 2018 to January 2019) with the established baseline indicates that ground motion does not differ from that observed in the baseline. Examination of the ground motion time series for points closest to seismic events also shows no significant motion at the time of the events.

The InSAR data therefore demonstrates that to date the hydraulic fracturing activities at Preston New Road have not produced measurable ground motion that can be attributed to the shale gas activities within the time period of the monitoring. Also there is no measurable ground motion linked to the seismic events which occurred in October, November and December 2018.

Continued monitoring will be necessary to understand and evaluate the effects as the site potentially develops in the future.

### 3.9 ACKNOWLEDGEMENTS

ERS-1 data were obtained via a Category-1 ESA project ID:13543 ‘Enhancing landslide research and monitoring capability in Great Britain using C-band satellite SAR imagery and change detection, InSAR and Persistent Scatterers techniques’. Sentinel-1 data have been obtained via the Copernicus Program of ESA. The authors would like to acknowledge ©Geomatic Ventures Ltd and SatSense Ltd. who processed the ISBAS and RapidSAR data respectively.

### 3.10 REFERENCES

ALSHAMMARI, L., LARGE, D.J., BOYD, D.S., SOWTER, A., ANDERSON, R., ANDERSEN, R., MARSH, S., 2018. Long Term Peatland Condition Assessment via Surface Motion Monitoring Using the ISBAS DInSAR Technique over the Flow Country, Scotland. *Remote Sensing*, 10(7): 1103.

Arrick, A, Forster, A, Clark, D, Stewart, M and Lawrence, D. 1995. A geological background for planning and development in Wigan. Volume 2: A user’s guide to Wigan’s ground conditions. British Geological Survey Technical Report, No. WN/95/3.

BATESON, L., CIGNA, F., BOON, D. AND SOWTER, A., 2015. The application of the ISBAS InSAR method to the South Wales Coalfield. *International Journal of Applied Earth Observation and Geoinformation*, 34, pp.249-257.

BGS, 2000. PICKERING – ENGLAND AND WALES SHEET 53. SOLID AND DRIFT GEOLOGY.

GEE, D.; BATESON, L.; SOWTER, A.; GREBBY, S.; NOVELLINO, A.; CIGNA, F.; MARSH, S.; BANTON, C.; WYATT, L., 2017. Ground Motion in Areas of Abandoned Mining: Application of the Intermittent SBAS (ISBAS) to the Northumberland and Durham Coalfield, UK. *Geosciences*, 7, 85. <https://doi.org/10.3390/geosciences7030085>

JORDAN, H., CIGNA, F., BATESON, L. 2017. Identifying natural and anthropogenically-induced geohazards from satellite ground motion and geospatial data: Stoke-on-Trent, UK. *International Journal of Applied Earth Observations and Geoinformation*, 2017, 63: 90-103. <https://doi.org/10.1016/j.jag.2017.07.003>

LANCASHIRE COUNTY COUNCIL, 2017. Preston New Road shale gas exploration site, monitoring visit – 5 October 2017. Available at <https://www.lancashire.gov.uk/media/902939/monitoring-report-51017.pdf> [accessed on 1 April 2019]

MARSHALL, C., LARGE, DJ., ATHAB, A., EVERS, SL., SOWTER, A., MARSH, S., SJÖGERSTEN, S. 2018. Monitoring tropical peat related settlement using ISBAS InSAR, Kuala Lumpur International Airport (KLIA). *Engineering Geology*, 244. DOI: 10.1016/j.enggeo.2018.07.015

OGA, 2018. Consolidated Onshore Guidance, version 2.2. – June 2018. Available at [https://www.ogauthority.co.uk/media/4959/29112017\\_consolidated-onshore-guidance-compendium\\_vfinal-002.pdf](https://www.ogauthority.co.uk/media/4959/29112017_consolidated-onshore-guidance-compendium_vfinal-002.pdf)

ROSEN P.A., HENSLEY S., JOUGHIN I.R., LI F.K., MADSEN S.N., RODRÍGUEZ E., GOLDSTEIN R.M., 2000. Synthetic Aperture Radar Interferometry. *Proceedings of the IEEE*, v.88: 333-382.

SOWTER, A., L. BATESON, P. STRANGE, K. AMBROSE, AND M. F. SYAFIUDIN. 2013. DInSAR estimation of land motion using intermittent coherence with application to the South Derbyshire and Leicestershire coalfields, *Remote Sens. Lett.*, 4(10), 979–987.

SPAANS, K.; HOOPER, A., 2016. InSAR processing for volcano monitoring and other near-real time applications. *J.*

*Geophys. Res. Solid Earth*, 121, 2947–2960, doi:10.1002/2015JB012752.

VAJEDIAN, S., MOTAGH, M. AND NILFOUROUSHAN, F., 2015. StaMPS improvement for deformation analysis in mountainous regions: Implications for the Damavand volcano and Moshafault in Alborz. *Remote Sensing*, 7(7), pp.8323-8347.

WARD, R.S.; ALLEN, G.; BAPTIE, B.J.; DARAKTCHIEVA, Z.; JONES, D.G.; JORDAN, C.J.; PURVIS, R.M.; SMEDLEY, P.L.. 2016 Environmental baseline monitoring - Vale of Pickering: Phase I - final report (2015/16). Nottingham, UK, British Geological Survey, 96pp. (OR/16/002) (Unpublished)

WARD, R.S.; SMEDLEY, P.L.; ALLEN, G.; BAPTIE, B.J.; DARAKTCHIEVA, Z.; HORLESTON, A.; JONES, D.G.; JORDAN, C.J.; LEWIS, A.; LOWRY, D.; PURVIS, R.M.; RIVETT, M.O.. 2017 ENVIRONMENTAL BASELINE MONITORING PROJECT. PHASE II, FINAL REPORT. BRITISH GEOLOGICAL SURVEY, 163PP. (OR/17/049) (UNPUBLISHED)

Ward, R.S.; Allen, G.; Baptie, B.J.; Bateson, L.; Bell, R.A.; Butcher, A.S.; Daraktchieva, Z.; Dunmore, R.; Fisher, R.E.; Horleston, A.; Howarth, C.H.; Jones, D.G.; Jordan, C.J.; Kendall, M.; Lewis, A.; Lowry, D.; Miller, C.A.; Milne, C.J.; Novellino, A.; Pitt, J.; Purvis, R.M.; Smedley, P.L.; Wasikiewicz, J.M.. 2018 Preliminary assessment of the environmental baseline in the Fylde, Lancashire. Nottingham, UK, British Geological Survey, 104pp. (OR/18/020) (Unpublished).

## 4 Atmospheric composition

### 4.1 INTRODUCTION

This section discusses measurements of atmospheric composition (greenhouse gas and air quality indicator concentrations) sampled near the Preston New Road (PNR) and Kirby Misperton (KM) shale gas sites.

The third year of measurements has seen a change in activity at the Preston New Road site. Cuadrilla Resources Ltd commenced hydraulic fracturing activity at the PNR site in October 2018, resulting in a shift in analytical focus from baseline monitoring to operational-phase monitoring.

The data presented and interpreted in this report compare and contrast the three full years of atmospheric sampling conducted between February 1<sup>st</sup> 2016 and January 31<sup>st</sup> 2019. This period is split into three 12-month sections, consistent with Phase 2, Phase 3 and Phase 4 of the environmental monitoring project. Previous reports discussing the analysis of measurements during the first two annual phases of monitoring can be found in Ward et al., 2017 and Ward et al., 2018.

Significantly, three peer-reviewed journal articles discussing the 2016-2018 atmospheric baseline measurements have been submitted for publication (Lowry et al., 2019; Purvis et al., 2019; Shaw et al., 2019) in a special issue on environmental baselining of hydraulic fracturing in *Science of the Total Environment*. It is recommended that these open access articles be read alongside this project report. Purvis et al. (2019) discusses a baseline and pre-operational analysis of concentrations of NO<sub>x</sub> and other air quality indicators at the KM site. Lowry et al. (*in review*) identify and characterise pre-operational sources of methane around the PNR and KM8 sites using mobile surveys,  $\delta^{13}\text{C}$  and C<sub>2</sub>H<sub>6</sub> measurement. Shaw et al. (2019) discusses an analysis of baseline greenhouse gas measurements at both sites and presents a suggested algorithmic method for the identification of periods with elevated concentrations above the typical statistical range of baseline conditions. This facilitates an automated detection of periods/data of interest that may be related to greenhouse gas emissions events from the shale gas extraction facilities. This algorithm was used to determine that a period of enhanced CH<sub>4</sub> at PNR was related to emissions from the Cuadrilla shale gas extraction facility in January 2019. This event will be discussed briefly below and further analyses can be found in a supplementary BGS web publication (see Allen et al., 2019). The abstracts of the papers can be found in Appendix A.

### 4.2 SUMMARY OF MONITORING ACTIVITIES

Data have continued to be collected at both KM and PNR over the past 12 months (February 2018 – January 2019). Any technical or mitigating issues with the monitoring equipment and dataset provision experienced over the 12 months pertinent to Phase 4 are discussed below.

#### 4.2.1 Preston New Road

Monitoring has continued at the PNR site (see Figure 84). The current UGGA GHG-monitoring instrument was removed for laboratory testing in January 2018 and was returned on 17<sup>th</sup> May 2018; during this period, it was replaced by an identical unit calibrated using the same standards to ensure data continuity. The CO<sub>2</sub> eddy covariance (EC) instrument was removed on 30<sup>th</sup> May 2018 for routine servicing. It was replaced on 20<sup>th</sup> September 2018. The EC instrument experienced several issues related to writing files to the memory in December 2018 and January 2019; these have been rectified by updating the standard operating procedure. The EC

instrument is non-core (and redundantly additional, gratis) to the proposed site instrumentation, i.e. this does not represent a missing period of core monitoring data.

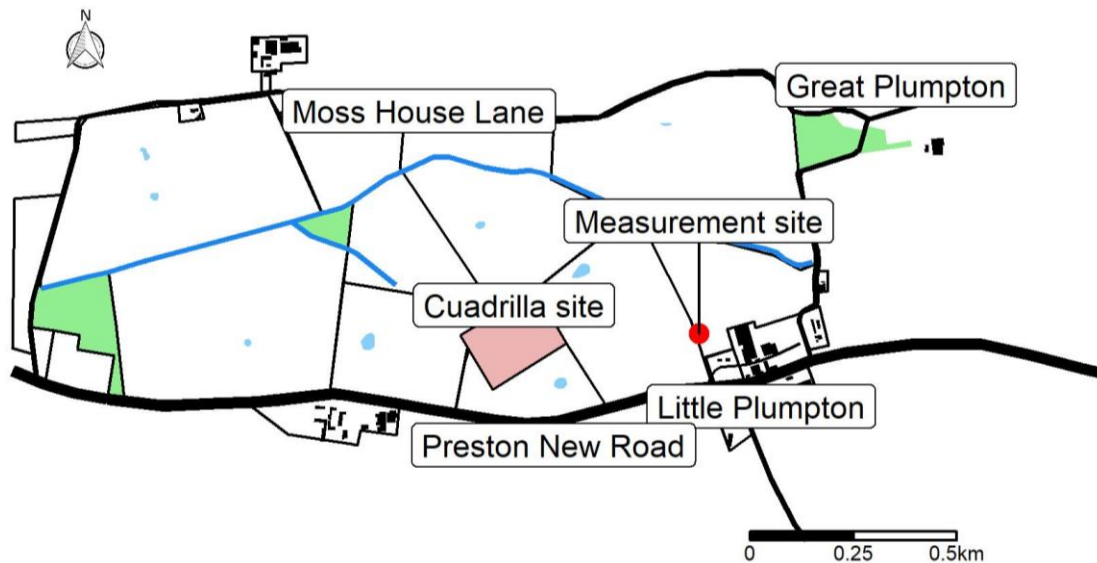


**Figure 84. Map showing the location of the measurement station at PNR relative to the Cuadrilla operated unconventional shale gas extraction facility. Other notable infrastructure is also shown.**

Various warnings on the NO<sub>x</sub> instrument relating to high box temperature occurred during summer 2018; these did not appear to have a significant adverse effect on data quality. The FIDAS instrument experienced various sample flow control issues beginning in December 2018 and was serviced in January 2019 by Air Monitors Ltd to rectify this. The NO<sub>x</sub> trap became inefficient in January 2019 leading to poor zero readings. This trap has now been replaced.

As part of a separately-funded project, a series of controlled experimental releases of small volumes of CH<sub>4</sub> gas were conducted in August and September 2018 to test new flux quantification methods using sampling by unmanned aerial vehicles and prototype instrumentation. The CH<sub>4</sub> was released from a field adjacent to the PNR monitoring station location. Greenhouse gas measurements during periods (amounting to a total of no more than 5 hours over 5 days) in which CH<sub>4</sub> was released were removed from the data prior to analysis in this report to avoid contamination of the dataset.

#### **4.2.2 Kirby Misperton**

Monitoring has continued at the KM site (see Figure 85). All GHG instrumentation operated normally with routine calibrations performed using reference standards and applied to the quality-assured public dataset used here (see following section).

There were several instrument issues over the reporting period. Both ozone and FIDAS instruments had faults over summer 2018 which resulted them being removed from site. The optics had failed on the FIDAS and was repaired. The ozone instrument had a leak on one of its valves which had resulted in lower ozone values being reported, this resulted in some data being removed from the dataset and as such ozone averages for this period.

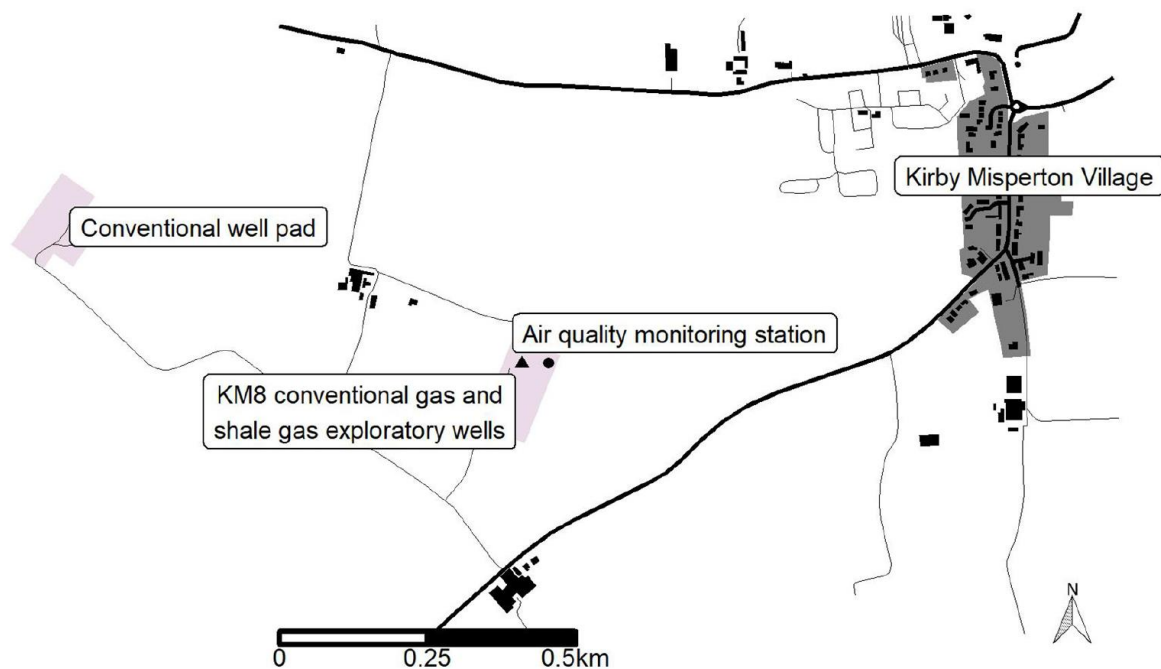


**Figure 85. Map showing the location of the measurement station on the KM8 shale gas site relative to the locality and other gas production infrastructure.**

#### **4.2.3 Data calibration and quality assurance**

The calibration and quality assurance procedures outlined in the Phase 2 report have continued to be upheld to ensure consistency and continuity in the dataset. Data from both sites employ quality assurance (QA) and quality control (QC) for air quality and greenhouse gas concentration data covering all aspects of network operation, including equipment evaluation, site operation, site maintenance and calibration, data review and ratification. All instrumental calibrations are traceable through an unbroken chain to international reference standards to ensure high accuracy, comparability with similarly calibrated high-precision instrumentation, and quantified uncertainties in the dataset. Metadata concerning the precision and guidance on use of the data is prepared for each measurement reported and made available to view publicly on the Centre for Environmental Data Analysis (CEDA) archive ([www.CEDA/ac/uk](http://www.CEDA/ac/uk)) after final QC approval.

Site visits occurred at 3-weekly intervals to check the condition of instruments and to perform checks on analyser accuracy, precision and response times, as well as calibration. A full list of instrument technical specifications and precision is available in the Phase 2 project report (Ward et al, 2017).

### **4.3 ANALYSIS AND DISCUSSION**

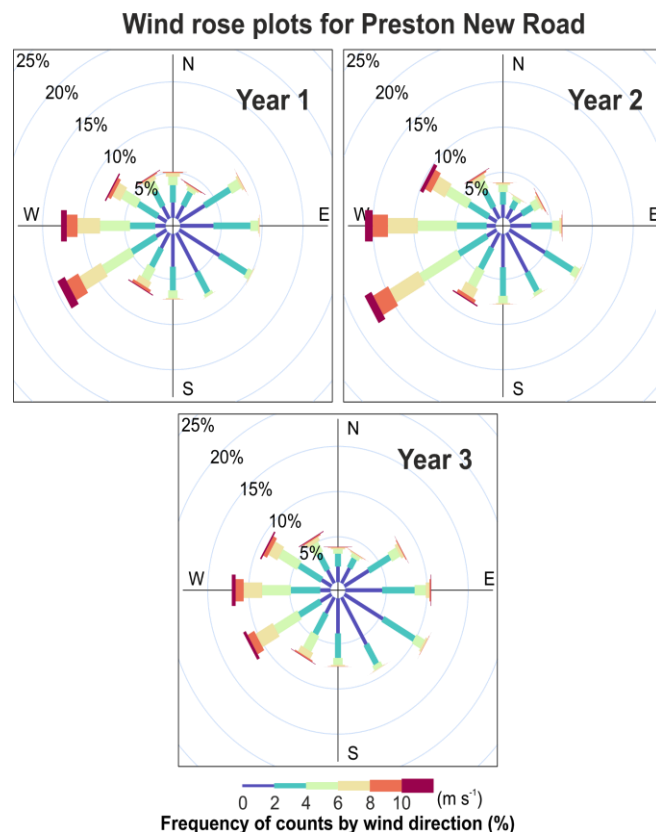
The following sections discuss the measurements from the previous three years. The data were analysed as three separate 12-month periods which are related to the different annual phases of baseline analysis. These 12-month periods begin in February and end in January of the following year. The three periods were analysed to examine inter-year baseline consistency, the nature of any variance in baseline conditions, and any changes due to operational industrial activity at either site.

Table 15 provides an overview of the three measurement periods, their start and end dates, and the “year number”, as referred to in many of the figures below. The style and analytical rationale of these figures has been established in previous project reports and it is assumed here that the reader is familiar with the approach. For further explanation of the type of figure presented here and how to interpret them, please consult Phase 2 and Phase 3 reports (Ward et al, 2017 and Ward et al. 2018).

**Table 15. Details of the three 12-month measurement periods.**

Period start	Period end	Year number	Reporting Phase
1 <sup>st</sup> February 2016	31 <sup>st</sup> January 2017	1	2
1 <sup>st</sup> February 2017	31 <sup>st</sup> January 2018	2	3
1 <sup>st</sup> February 2018	31 <sup>st</sup> January 2019	3	4

### 4.3.1 PNR wind climatology



**Figure 86. Wind rose plots for the Preston New Road site showing wind speed and direction statistics. Data from three 12-month periods defined in Table 15 are shown. The radii of the paddles illustrate the percentage of total sampling time in each of the 12 wind direction cones (30 degree increments relative to true North) and the colour of the paddle shows the wind speed (see colour legend). © University of Manchester (2019).**

The dominant wind direction at the PNR site continued to be from the west and south-west in Year 3 as expected (Figure 86). However, the relative frequency of these wind directions decreased slightly from the Year 1 and 2 values due to an elevated frequency of wind directions from the east and north-east. This is consistent with the spring and summer 2018 weather regime, which saw an increased incidence of blocking high pressure systems to the east of the UK and corresponding higher than long-term-average temperatures and drier conditions.

#### 4.3.2 KM wind climatology

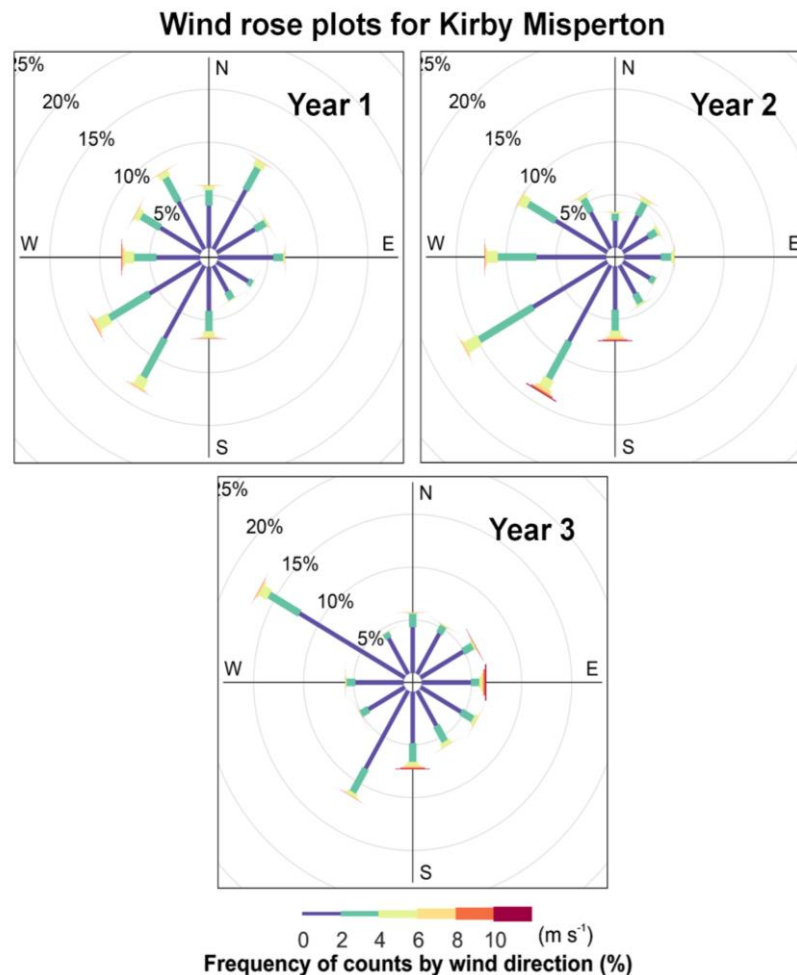


**Figure 87. Wind rose plots for the Kirby Misperton site showing wind speed and direction statistics. Data from three 12-month periods defined in Table 15 are shown. The radii of the paddles illustrate the percentage of total sampling time in each of the 12 wind direction cones (30 degree increments relative to true North) and the colour of the paddle shows the wind speed (see colour legend). © University of Manchester (2019).**

The pattern of wind directions at the Kirby Misperton site was somewhat different in Year 3 to the two previous years, with a far stronger north-westerly component at the expense of wind directions between 225° and 285° (south-west to west) (Figure 87). This effect appears to be consistent throughout the year and is likely to represent a change in on-site infrastructure rather than a real change in prevailing local meteorology. It is not possible to post-correct for the influences of surrounding infrastructure on wind measurements, but this impact must be considered when interpreting atmospheric data from this site, in particular when comparisons are being made between different data from different years. It is also an important consideration

for siting of monitoring equipment at/around sites that are likely to experience considerable infrastructure development. The impact of on-site infrastructure will general only affect sensors in close proximity to any infrastructure; the large distance between monitoring station and shale gas site at PNR represents an advantage in this case.

### 4.3.3 PNR greenhouse gases

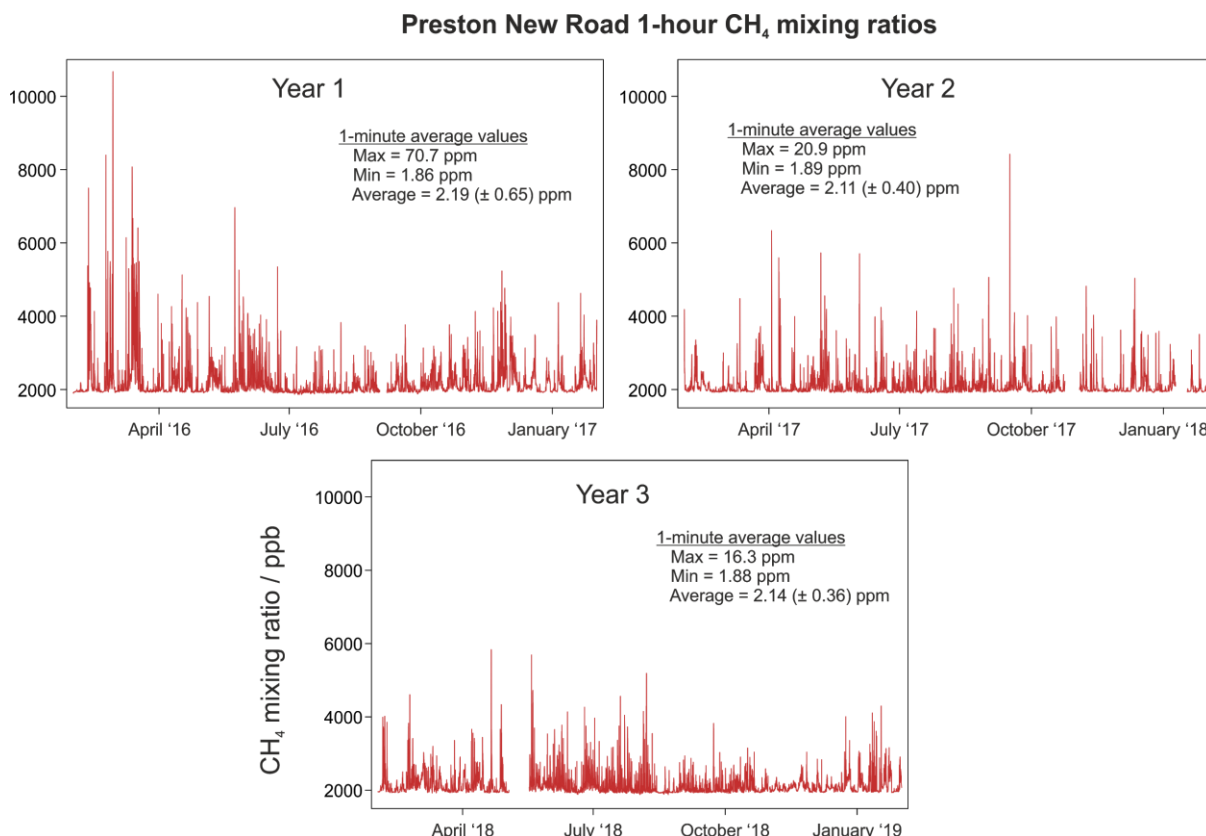


**Figure 88. Time series of one-hour averaged CH<sub>4</sub> mixing ratios measured at PNR for the three 12-month periods between 1<sup>st</sup> February 2016 and 31<sup>st</sup> January 2019.**  
© University of Manchester (2019).

Figure 88 shows time series of one-hour averaged CH<sub>4</sub> mixing ratios measured at PNR across the three year period. There is little significant variance in the global dataset mean concentration in Year 3, relative to Years 1 and 2. However, the frequency of one-hour average mixing ratios greater than 6 ppm can be noted to slightly decrease year-on-year, as did the frequency of measurements greater than 4 ppm. There are large variations in the mixing ratio on very short (less than 3 hour) temporal scales (visible as “spikes” in Figure 88); many of these changes were consistent with rapidly changing meteorological conditions, particularly when winds were from an easterly direction, consistent with previously reported local methane emissions associated with the nearby dairy farm ~200 m to the east of the measurement site. The yearly average CH<sub>4</sub> mixing ratio increases slightly from 2.11 ppm in Year 2 to 2.14 ppm in Year 3, and lower than the average in Year 1, of 2.19 ppm. Such variance in this year-to-year average is significantly smaller than the corresponding intra-year variance, meaning that variance in the inter-annual mean is not statistically significant or meaningful, especially considering the global rise in annual mean methane concentrations in the northern hemisphere, which is ~0.01 ppm.

Exploratory hydraulic fracturing operations began at PNR in October 2018. No obvious increase in the hourly CH<sub>4</sub> mixing ratios can be observed in the time series in Figure 88, when looking at such a plot of concentration data in isolation. In fact, there appeared to be fewer elevated spikes in the data time series to CH<sub>4</sub> mixing ratios greater than 3 ppm in Year 3 relative to Year 2. However, this is unlikely to be due to the commencement of operational activity and much more likely to be due to differences in the meteorology during those months in each year when compared on a monthly timescale. However, when discriminating the data for prevailing wind direction and the corresponding wind-correlated baseline, important deviations do emerge (discussed later, and in further detail in Allen et al., 2019).

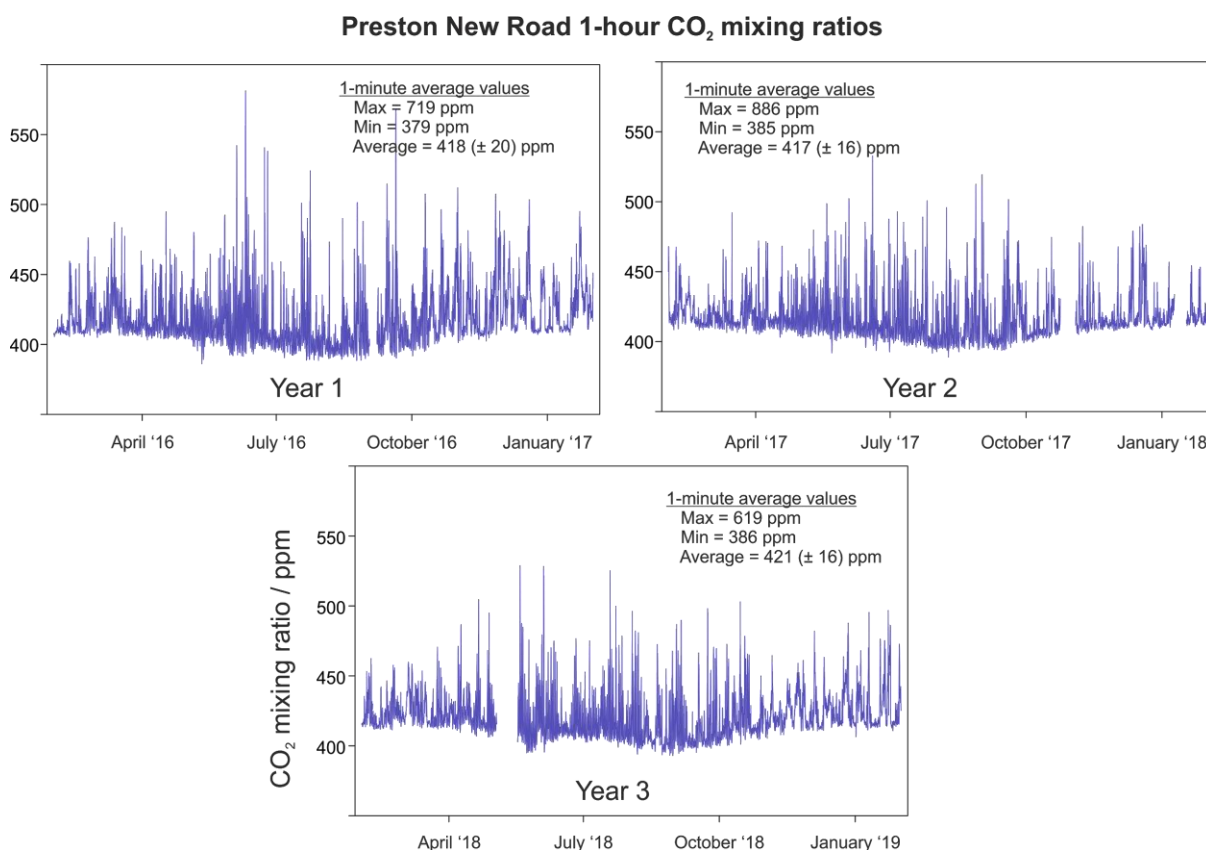


**Figure 89. Time series plots of one-hour averaged CO<sub>2</sub> mixing ratios measured at PNR for three 12-month periods between 1<sup>st</sup> February 2016 and 31<sup>st</sup> January 2019.**

© University of Manchester (2019).

As is the case for CH<sub>4</sub> in Figure 88, there were no statistically significant inter-annual changes in the CO<sub>2</sub> mixing ratio time series presented in Figure 89. The time series for each year show the expected distinct seasonal variation in CO<sub>2</sub> mixing ratios, with a decrease in background CO<sub>2</sub> concentrations in summer months due to northern hemisphere biospheric respiration. The average CO<sub>2</sub> mixing ratio is noted to increase between years 2 and 3, broadly consistent with the rate of global increase in background average CO<sub>2</sub> concentrations.

The exploratory hydraulic fracturing, beginning in October 2018, had no statistically significant impact on monthly-averaged CO<sub>2</sub> mixing ratios observed at the PNR monitoring station, relative to baseline CO<sub>2</sub> in years 2 and 3.

Figure 90 illustrates the frequency of the CH<sub>4</sub> mixing ratios associated with different wind directions. The three years are observed to be broadly consistent. Wind directions from the west generally resulted in CH<sub>4</sub> mixing ratios below 2.2 ppm for >90% of the total sampling

time in such wind regimes, whilst wind directions from the east resulted in a much greater proportion (>50%) of CH<sub>4</sub> mixing ratios above 2.2 ppm. This is consistent with conclusions made for earlier phases, which identify the local dairy farm to the east as being responsible for the highest (transient) enhancements, and longer-range (longer temporal and more chemically and dynamically mixed) urban and industrial pollution sources to the south east (including Manchester, Birmingham and London).

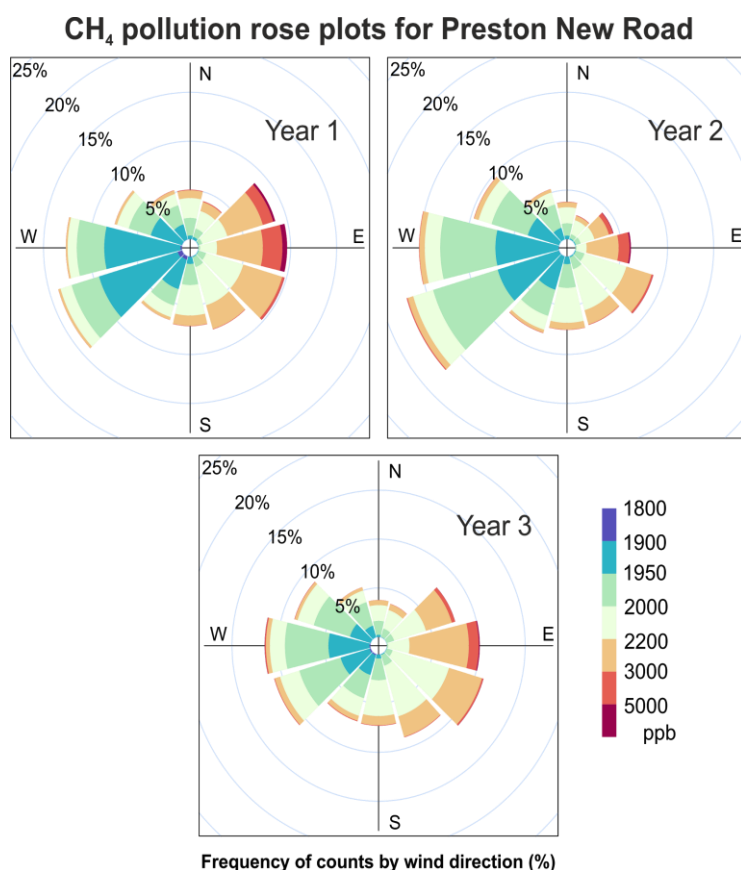


**Figure 90. CH<sub>4</sub> concentration-frequency and wind rose plots showing CH<sub>4</sub> mixing ratios as a function of wind direction for the three 12-month periods. The radii of the paddles illustrates the percentage of total time in each of the 12 wind direction cones (30 degree sections relative to true North) and the colour of the paddle shows the CH<sub>4</sub> mixing ratio (see colour legend). © University of Manchester (2019).**

There are no manifest statistically-significant differences across the three full year periods despite operational activity beginning in the last four months of Year 3. However, it is too early to identify annualised variance in the baseline climatology for Year 3 for westerly winds associated with PNR industrial activity, due to the fact that this only affects the final few months of Phase 4. Instead, a more focussed case study is required for those operational months, which is presented in Allen et al., 2019, and also the subject of ongoing analysis.

Figure 91 shows the frequency of CO<sub>2</sub> mixing ratios associated with 12 wind direction sectors. As for CH<sub>4</sub>, the dominant frequency (>50%) of mixing ratios >425 ppm is associated with easterly winds throughout the three year period. The dominance (>50%) of concentrations below 425 ppm is associated with westerly directions. There was no significant change in this general wind-correlated regime over the 3 years, and no discernible difference in the third year of measurements for westerly winds when operational activity commenced at PNR, for reasons described above in reference to CH<sub>4</sub>.

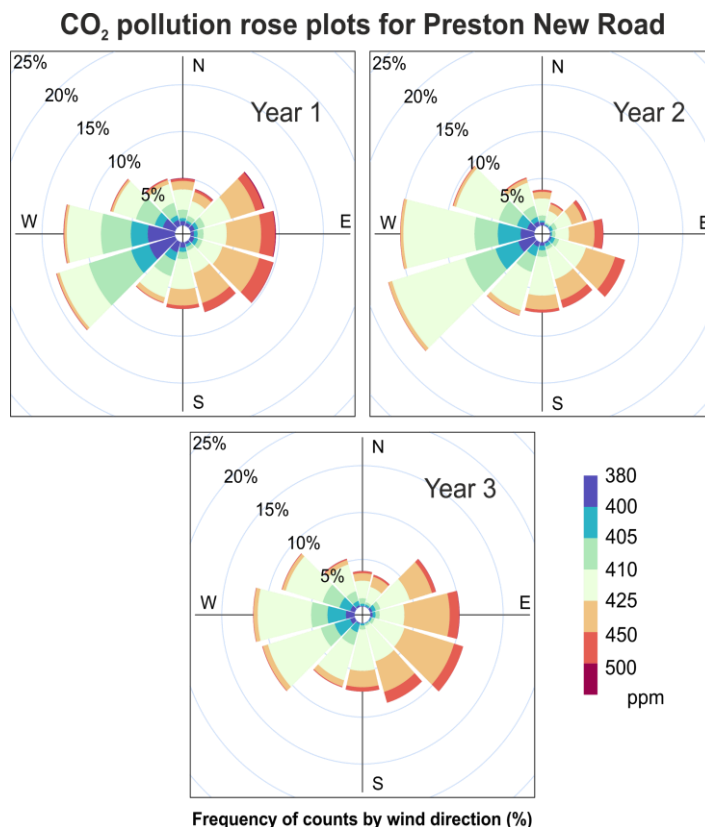


**Figure 91. CO<sub>2</sub> pollution rose plots showing CO<sub>2</sub> mixing ratios as a function of wind direction for three 12-month periods. The radii of the paddles illustrates the percentage of total time in each of the 12 wind direction cones (30 degree sections relative to true North) and the colour of the paddle shows the CO<sub>2</sub> mixing ratio (see colour legend). © University of Manchester (2019).**

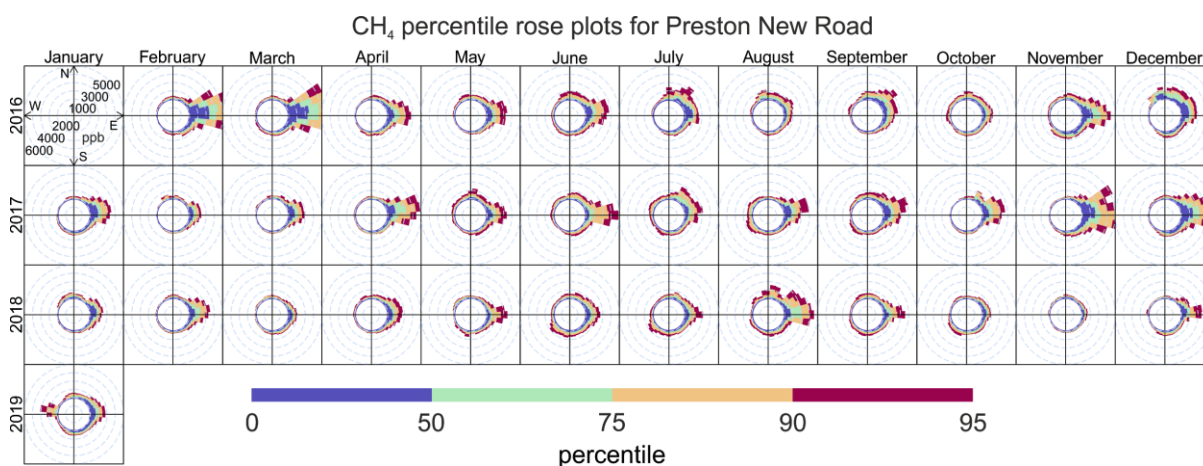


**Figure 92. Monthly CH<sub>4</sub> percentile rose plots showing percentile ranges in CH<sub>4</sub> mixing ratios as a function of wind direction for 36 monthly-averaged periods between 1<sup>st</sup> February 2016 and 31<sup>st</sup> January 2019. The radii of the paddles show the percentile ranges of absolute CH<sub>4</sub> concentrations (see coloured scale) in each of the 36 wind direction cones (10 degree sections). © University of Manchester (2019).**

Percentile rose plots (Figure 92) differ from concentration rose plots in that they do not solely illustrate the frequency of measurements occurring under different wind direction conditions. Instead, Figure 92 illustrates percentile ranges as a function of wind direction. Figure 92 shows 36 monthly-averaged percentile rose plots for CH<sub>4</sub> mixing ratios at PNR, allowing us to examine month-by-month variability and allowing us to deconvolve the months of operational activity at PNR since October 2018, from the wider baseline climatology.

It is immediately clear that the majority of higher mixing ratios is consistently associated with easterly wind conditions for every month in the baseline series. These mixing ratios can be attributed to local influence from the dairy farm to the east of the monitoring station, superimposed on a more polluted background of longer-range sources such as the major cities of England and Western Europe. Westerly winds, and to a lesser extent, both northerly and southerly winds, are generally much lower in terms of CH<sub>4</sub> mixing ratio.

Displaying the data at monthly resolution allows for the intercomparison of different years. February and March 2016 display much higher mixing ratios in easterly winds than the equivalent for 2017 and 2018. Mixing ratios in April, May, June, July and September were all highly comparable across each of the three years. CH<sub>4</sub> mixing ratios in easterly winds increased in August over the three years whilst easterly mixing ratios measured in October 2017 were much greater than those recorded in either of the two neighbouring years.

The most significant change occurred in January 2019, where mixing ratios under westerly wind conditions were measured to be significantly and anomalously higher than previous years for the same month. Indeed, the CH<sub>4</sub> mixing ratios in westerly winds recorded were greater than in any month during the three years of measurements.

The location of the Cuadrilla shale gas facility to the west of the monitoring station very strongly indicated that these enhanced mixing ratios were associated with emissions from the PNR facility. After detection of this anomaly, subsequent discussion between the project science team, the Environment Agency, and Cuadrilla, confirmed that the January 2019 observations were related to a nitrogen lift process used at PNR, which was carried out to clear the shale gas well. An attempt was made to flare the gas produced by this process but the flare could not combust the evolved gas. Therefore, the evolved gas was vented without combustion to atmosphere, explaining the observed methane enhancement and the lack of a CO<sub>2</sub> signal that might be expected should the gas have been successfully flared. Further information on the detection and analysis of this emission can be found in Allen et al., 2019; additional evidence for a CH<sub>4</sub> emission, measured using UAV sampling, is also described there. Further analysis, complete with CH<sub>4</sub> flux estimations, will be the subject of a future scientific paper.

An analogous plot (to Figure 92) for CO<sub>2</sub> is not available at the time of reporting here, but analysis presented in Figure 87 and Figure 88 earlier demonstrates that CO<sub>2</sub> percentile ranges remained largely consistent from month-to-month, even in January 2019.

Figure 93 shows the monthly median (solid line) measured CH<sub>4</sub> and CO<sub>2</sub> mixing ratios during only westerly wind conditions at PNR for the three year period. The 25<sup>th</sup> and 75<sup>th</sup> percentile ranges are shown by the darker transparent blocks, and the 5<sup>th</sup> and 95<sup>th</sup> percentile ranges are shown by the lighter transparent blocks.

Much like Figure 93, this plot shows the month-to-month comparability of CH<sub>4</sub> mixing ratios throughout much of 2016, 2017 and 2018. Summer months generally show greater ranges in both the interquartile and 5<sup>th</sup>/95<sup>th</sup> percentile ranges, with 95<sup>th</sup> percentile values of between 2.5 and 3.0 ppm during June, July and August. Winter months generally exhibited much smaller interquartile and 5<sup>th</sup>/95<sup>th</sup> percentile ranges, with 95<sup>th</sup> percentile values of approximately 2.2 ppm. The explanation for the wax and wane of this variability with the seasons is related to

northern hemispheric biospheric respiration activity, which is dynamic and active in the summer months and relatively dormant in winter.

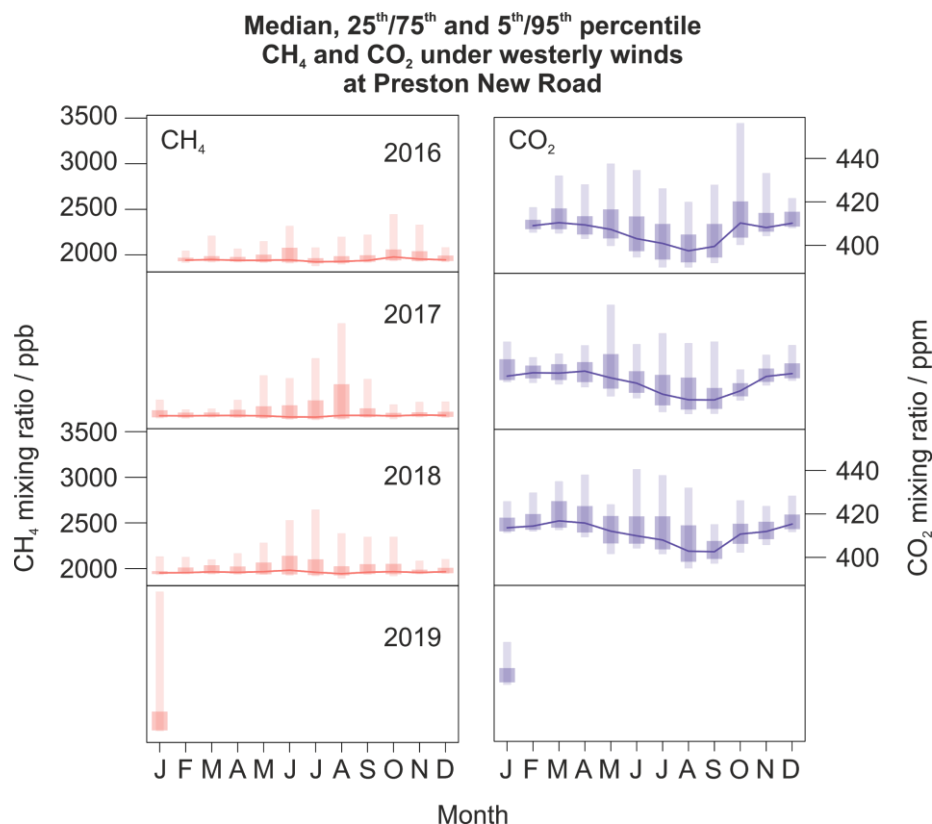


**Figure 93. Monthly median (solid line) percentile mixing ratios of CH<sub>4</sub> and CO<sub>2</sub> at PNR over the three year measurement period. 5<sup>th</sup>, 25<sup>th</sup>, 75<sup>th</sup> and 95<sup>th</sup> percentile values are indicated by the transparent boxes and whiskers. © University of Manchester (2019).**

January 2019 is again noteworthy as an anomalous outlier relative to all other monthly periods, including the more variable summer periods. The interquartile range for January 2019 is similar to that observed during summer months and is noted to be several times the interquartile ranges measured during both January 2017 and 2018. However, the 5<sup>th</sup>/95<sup>th</sup> percentile range during January 2019 far exceeds that seen in any other baseline month and is an order of magnitude larger than the equivalent range in January 2017 and 2018. This clearly highlights the nature of the enhancements in CH<sub>4</sub> observed in January 2019 under westerly wind directions and demonstrates the utility of the baseline measurements for the purposes of change detection. These enhancements were undoubtedly associated with operational activity occurring on the Cuadrilla Preston New Road shale gas extraction facility.

No concurrent changes in the CO<sub>2</sub> mixing ratio interquartile range, or 5<sup>th</sup>/95<sup>th</sup> percentile range, was observed during January 2019. This suggests that the emission from the shale gas facility likely took the form of non-combusted CH<sub>4</sub> i.e. it was not flared, consistent with the conclusions discussed for CH<sub>4</sub> above.

For further discussion and a final summary of the baseline climatological analysis for Phase 2 and Phase 3, please read Shaw et al., 2019 (2019). Shaw et al., 2019, also includes tables of baseline statistical thresholds and an emission event detection algorithm, which will be used by the project science team to automate event detection at PNR in future monitoring, and can

be adapted to the KM site when (and if) operational. This table, and the algorithm, are included in Appendix B.

#### 4.3.4 KM greenhouse gases

This section presents the baseline dataset for the KM site. As no hydraulic fracturing has yet taken place at the KM site, analysis here differs to that presented for PNR, where we discuss operational measurements since October 2018, and represents a continuation of baseline dataset gathering. Year 3 (Phase 4) is presented here and compared with Years 1 and 2 (previously reported in Phase 2 and 3 reports, respectively). A summary of the year 1 and 2 baseline at KM has now been submitted as a peer-reviewed journal article to Science of the Total Environment (Shaw et al., 2019). Further discussion can be found in that publication and a link to the study will accompany the final version of this published report. Wind roses and tracer correlations can also be found in that article and therefore only a summary of the statistical dataset at KMA is reported here.

The baseline climatology for both CH<sub>4</sub> and CO<sub>2</sub> in Year 3 is comparable with Years 1 and 2 with no significant variance in mean, interquartile or extreme statistical ranges in any month or year-to-year. The general background trends in CO<sub>2</sub> and CH<sub>4</sub> and seasonal variations intra-year are comparable to those discussed for PNR earlier, for the same underlying reasons related to northern hemispheric biospheric controls and general meteorological regimes.

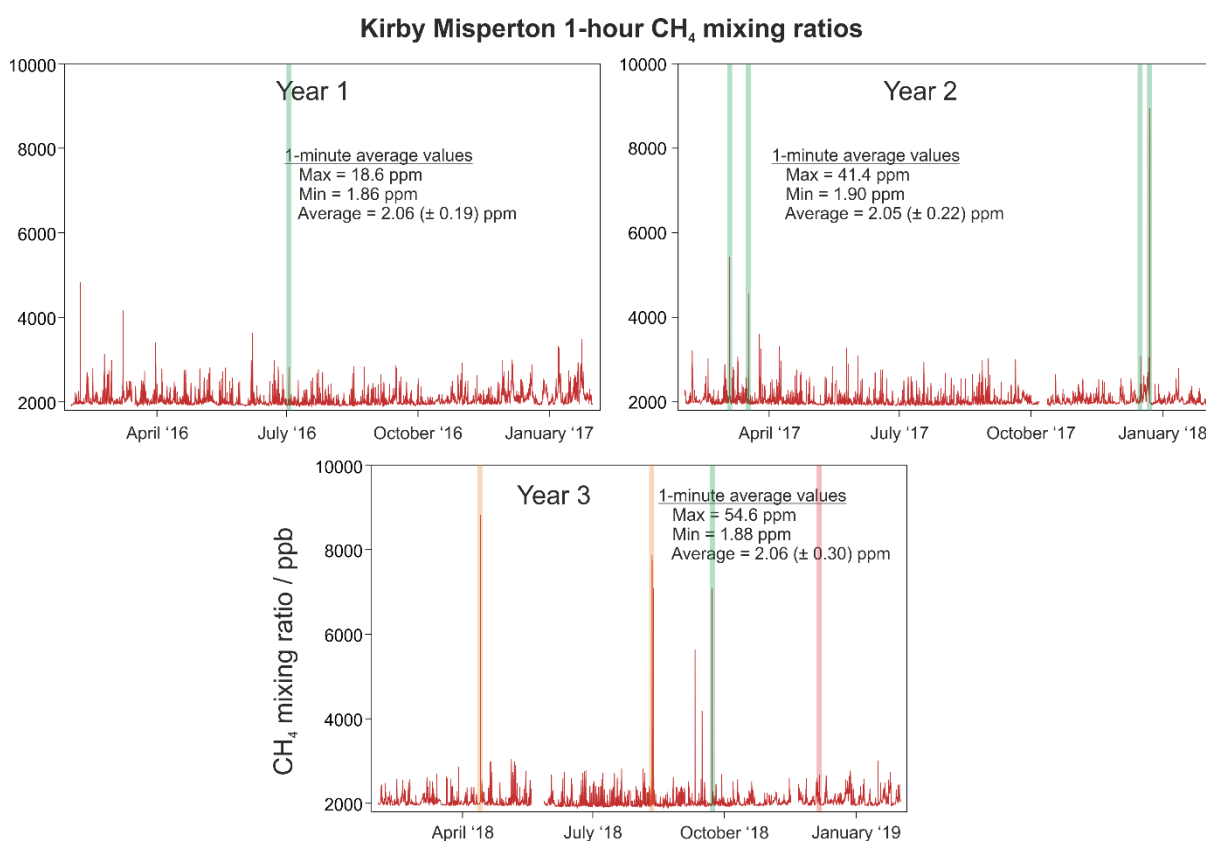


**Figure 94. Time series plots of one-hour averaged CH<sub>4</sub> mixing ratios measured at KM for three 12-month periods between 1<sup>st</sup> February 2016 and 31<sup>st</sup> January 2019.**

© University of Manchester (2019).

Figure 94 shows a time series of hourly CH<sub>4</sub> mixing ratios measured at KM for the three year period. The data are comparable year-to-year. The large (but transient) enhancements, where

CH<sub>4</sub> mixing ratios reached hourly values greater than 4 ppm, have been confirmed to be due to emissions from controlled venting of a nearby conventional wellhead at the KMA facility. Periods which were flagged as exceeding the CH<sub>4</sub> change detection algorithm are highlighted: green indicates periods which were flagged and confirmed to be due to CH<sub>4</sub> venting by the operator; orange indicates periods which were flagged but have not been confirmed to be due to CH<sub>4</sub> venting by the operator; red indicates periods which were reported to involve CH<sub>4</sub> venting but were not flagged by the change detection algorithm (because of unfavourable wind direction).

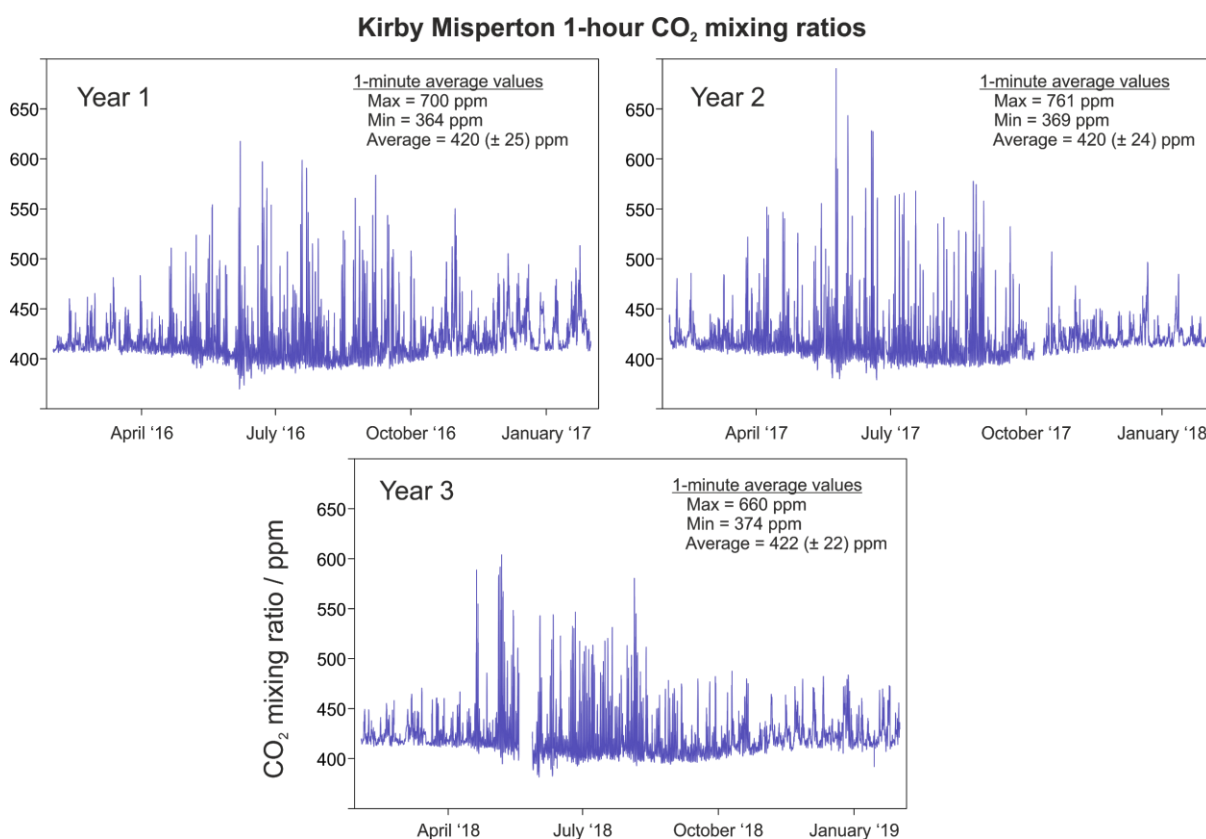


**Figure 95. Time series plots of one-hour averaged CO<sub>2</sub> mixing ratios measured at KM for three 12-month periods between 1<sup>st</sup> February 2016 and 31<sup>st</sup> January 2019.**  
© University of Manchester (2019).

Figure 95 shows the time series of CO<sub>2</sub>. The seasonal background is clear and directly comparable to measurements at the same time at PNR. Similar transient enhancements, peaking at around 600 ppm are seen, peaking in frequency in spring and summer months. This is more pronounced at KM, compared with PNR, which sees roughly similar frequency of transient CO<sub>2</sub> enhancements throughout the year. These transient CO<sub>2</sub> enhancements indicate local and regional sources of CO<sub>2</sub> at both sites. However, at KM, land-based anthropogenic CO<sub>2</sub> emissions are expected to be observed for all wind directions, unlike PNR, where this would not be expected in westerly winds (of maritime air mass origin). The KM data do suggest that there are local and regional sources of CO<sub>2</sub> that are more dominant in summer months than those seen at PNR, and such sources are associated with westerly winds at KM, not observed at PNR.

Figure 96 illustrates the month-to-month statistical variance over the 3 year baseline period (not discriminated for wind direction), showing very similar trends to those seen and discussed at PNR, with the exception of January 2019 where hydraulic-fracturing-related emissions were

observed at PNR. While the patterns and trends in variability are similar with season at both sites, the magnitudes of this variability are different - smaller ranges are observed at KM, compared with PNR in the case of CH<sub>4</sub>. This is due to the absence of a dominant local CH<sub>4</sub> source (i.e. the dairy farm at PNR) at KM; notwithstanding infrequent but large transients associated with controlled venting at KMA.

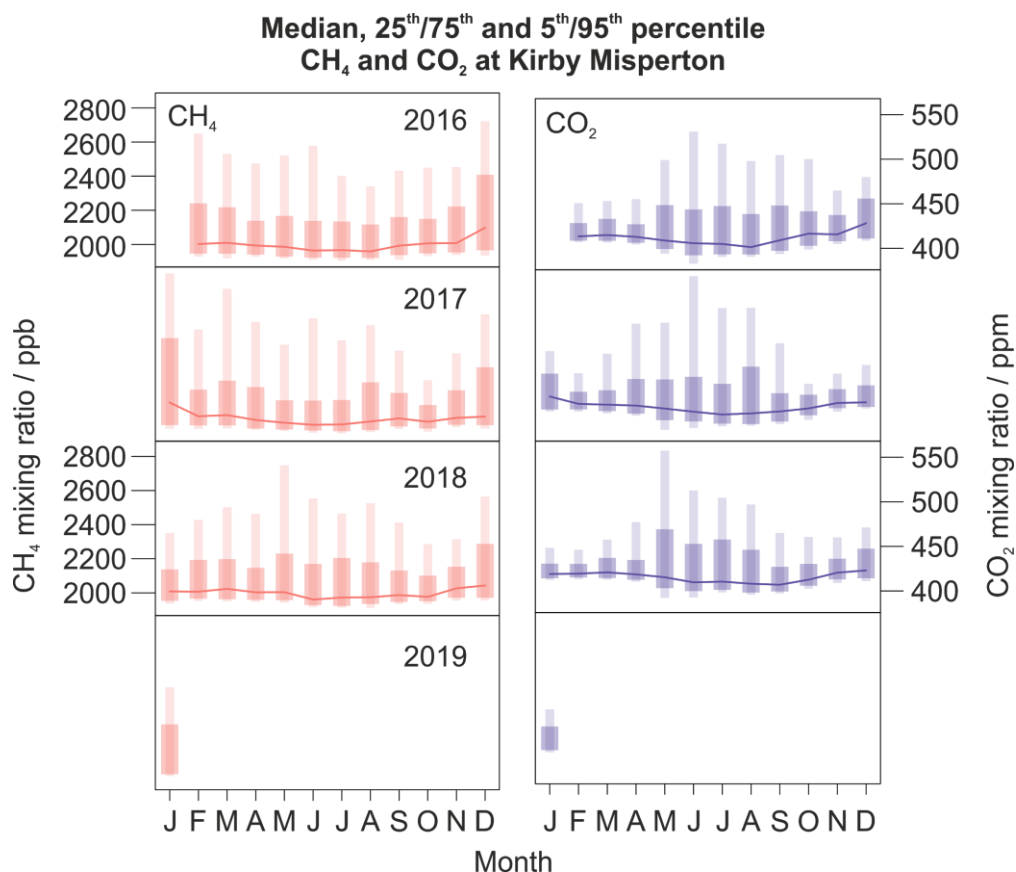


**Figure 96. Monthly median percentile mixing ratios of CH<sub>4</sub> and CO<sub>2</sub> at KM over the three year measurement period. 5<sup>th</sup>, 25<sup>th</sup>, 75<sup>th</sup> and 95<sup>th</sup> percentile values are indicated by the transparent boxes. © University of Manchester (2019).**

Further analysis of the year 1 and 2 baseline at KM can be found in Shaw et al., 2019. As for PNR, tables for statistical baseline thresholds from KM can be found in the Appendix B. In summary, the year 3 baseline at KM is highly comparable with years 1 and 2, with little statistical variance in trends with wind direction or season. This does suggest that a 12-month baseline is a suitable time frame for baseline characterisation for a single site, as concluded in earlier reports for Phase 2 and Phase 3. Therefore, a comparative analysis against this baseline is concluded to be appropriate should KM become operational; and the event detection algorithm now developed for PNR can be adapted for use at KM.

#### 4.4 MOBILE METHANE MEASUREMENT SURVEYS

Mobile methane baseline surveys were carried out by RHUL, and samples collected for isotopic analysis on the following dates:

- Fylde, Lancashire: 17<sup>th</sup> and 18<sup>th</sup> July 2018 (17 samples), 22<sup>nd</sup> and 23<sup>rd</sup> August 2018 (34 samples), 17<sup>th</sup> and 18<sup>th</sup> October 2018 (23 samples), 15<sup>th</sup> and 16<sup>th</sup> January 2019 (33 samples), 6<sup>th</sup> and 7<sup>th</sup> March 2019 (20 samples)

- Vale of Pickering, North Yorkshire: 18<sup>th</sup> and 19<sup>th</sup> July 2018 (14 samples) 14<sup>th</sup> and 15<sup>th</sup> November 2018 (22 samples), 5<sup>th</sup> and 6<sup>th</sup> March 2019 (19 samples).

Real-time measurements of methane mole fraction were made by cavity ringdown spectroscopy using a Picarro 2301 instrument, and of ethane mole fraction by off-axis optical spectroscopy using an LGR UMEA instrument. Samples of air from the located methane plumes were collected in Flexfoil bags (SKC Ltd.) so that sources could be isotopically characterised, as well as at locations where a stable background mole fraction was measured so that baseline  $\delta^{13}\text{C}$  could be identified. The instrumentation and technique are based on that described by Zazzeri et al., (2015). The August 2018 Fylde campaign was undertaken to coincide with drone-testing of a new instrument to detect plume emissions from release of cylinder methane gas, the October 2018 campaign took place within the first week of hydraulic fracturing and the January 2019 campaign during the period of flowback testing by Cuadrilla. The November 2018 Kirby Misperton campaign coincided with the public outreach event.

The bags of air from the campaigns were analysed for methane mole fractions using a Picarro G1301 CRDS and  $\delta^{13}\text{C}$  of methane using gas chromatography isotope ratio mass spectrometry (CF-GC-IRMS, Fisher et al., 2006). Maps of the methane excess in ppb above the baseline for the region during the sampling period (where the baseline was defined as the 2<sup>nd</sup> percentile of recorded mole fractions during the period ten minutes either side of each measurement point) were produced using Arc-GIS.

Between the final surveys of Phase 3 in February/March 2018 and the first surveys of Phase 4 in July 2018 there were some significant changes in sources, particularly with many major gas leaks identified during Phase 3 being fixed. This is the case for the A6 leak near Catterall, Lancashire, and the A169 leak near Keldholme, North Yorkshire. The ongoing repairs/replacement of the pipeline running along the south side of Preston New Road to the east and west of Little Plumpton, moved along from west of the PNR shale gas pad in January 2018 to the east of it in July 2018. Evidence of work on the pipe had ceased by August 2018, but a gas leak was detected near to the bus stop next to Plumpton Hall Farm, with emission from a roadside grate, and these continued throughout the Phase 4 survey period. The Pickering gas offtake station continues to be a significant source of emissions through Phase 2, 3 and 4.

Changes have been seen in major landfill sources during the Phase 4 period. Notable reductions in the excess  $\text{CH}_4$  over background have been noted in Fylde at the Fleetwood (Jameson Road) landfill, since the start of Phase 4, and in Ryedale at the Knapton Quarry landfill, which shows evidence of landscaping and reduction in activity between November 2018 and March 2019. Both sites are now emitting methane that is more enriched in  $^{13}\text{C}$ , in the range -56 to -54‰, typical of closed landfills with some cover oxidation, compared with signatures of -61 to -57‰ when these sites were active. More focus in Phase 4 was given to the Midgeland restored landfill in Blackpool. While not covering a large area a peak of 17 ppm  $\text{CH}_4$  was sampled, with an isotopic signature of -55‰, typical of closed landfills. Given that this site is only 2.8 km west of the PNR site and the size of the peak encountered it is likely that under inversion conditions that plumes from this source will be encountered at the continuous PNR measurement site coming from the same direction as the well pad, but it is isotopically distinct and does not contain ethane. This means that all landfill sites in both study areas have no further waste input and emit as closed or restored landfills.

Dairy farming and associated waste / manure sources have remained largely unchanged during Phases 3 and 4. Manure piles recur in the same locations each year. Emissions from the agricultural source are influenced by climate. The manure piles emit more  $\text{CH}_4$  during warm and wet conditions when anaerobic activity is prevalent. Warmer spring and autumn conditions mean that cattle spend longer in fields with an associated reduction in dispersed  $\text{CH}_4$  emissions,

compared to the periods of confinement in barns. Milking time then becomes a focus of emissions. As such the isotopic signature is variable between the eructation signature close to -70‰ and the animal waste signature close to -51 ‰. Signatures of -64‰ for the combined emission seen downwind of barns was consistent in both survey areas in the second half of Phase 4, suggesting that proportions of 65% breath to 35% waste is an appropriate default scenario for dairy farms in these regions.

#### 4.4.1 Fylde – Baseline period

##### 4.4.1.1 DATA PROCESSING METHODS (METHANE MOLE FRACTION AND ETHANE/METHANE RATIOS)

The dataset from the multiple surveys in the Fylde has been split into two main datasets: a pre-hydraulic fracturing operational (baseline) dataset and an ongoing operational dataset. In order to make sense of the baseline dataset as a whole, the 9 campaigns (18 survey days) which contribute to this portion needed to be combined in a way as to minimise any sampling bias as multiple surveys have covered the same routes and were conducted under a variety of meteorological conditions.

##### *Combining CH<sub>4</sub> mole fraction surveys*

Each survey can only give a snapshot of the methane emissions as the vehicle surveying makes each pass, however by combining all of the surveys we can begin to build a picture of the average reach of various methane sources. In order to achieve this, the point data from all the surveys has been averaged into 10 m<sup>2</sup> bins and then the 10 m<sup>2</sup> bins averaged into 100 m<sup>2</sup> bins. The underlying concept is that the resulting map will show areas which are most impacted at vehicle inlet height by sources of methane and gives some idea of emission consistency for the very frequently surveyed roads. The most prevalent wind directions will be captured more often by the surveys, and therefore the final result should capture a realistic impact of the prevailing wind. Data is filtered out at the initial averaging stage where the background value of methane is higher than 2 ppm as methane that has built up under overnight inversion conditions will highly bias the end dataset. An example of the data downscaling is shown in Figure 97.

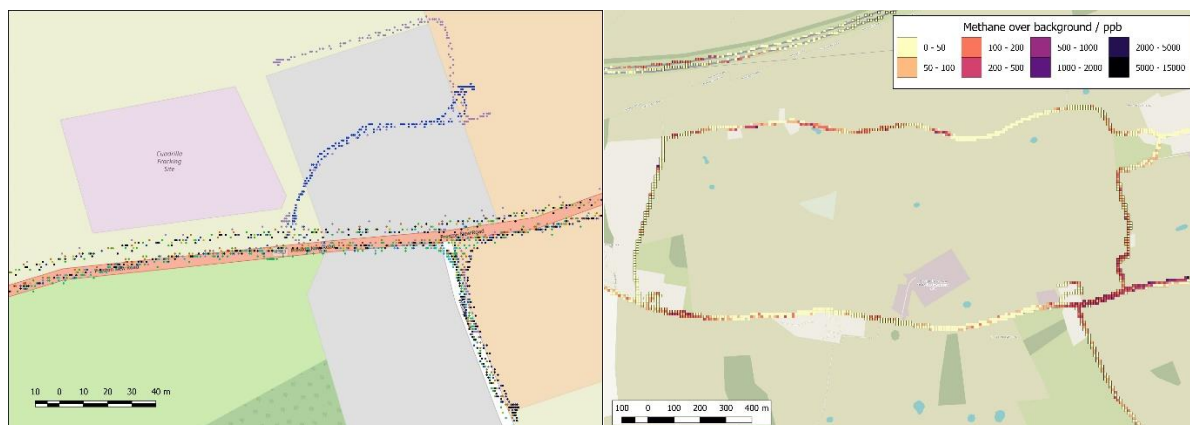


**Figure 97. Left: Very close up view of multiple survey passes, each point represents a single data point of CH<sub>4</sub>. Right: Downscaled data to give 10 m<sup>2</sup> averages from the point data depicting the average methane above background measured on the circuit around the shale gas site, darker colours represent higher average mixing ratios of CH<sub>4</sub>.**

© RHUL (2019).

### Combining isotopic data

The isotopic data collected from campaigns FY1 to FY9 can be analysed in isolation to give interesting and relevant data (such as seasonal analysis of cattle). However, it is also useful to consider the dataset as a whole to generate isotopic maps which characterise the whole region. In order to combine isotopic data points from differing surveys requires a re-analysis using the Miller-Tans method (Miller and Tans, 2003) rather than the Keeling plot method (Keeling, 1961) used in previous single campaign reports. The Miller-Tans method requires allocation of a background isotopic and mixing ratio data point to be assigned to each elevated methane data point, the background points were allocated manually using surveying and analysis notes. New isotopic datasets from the 9 surveys were then created based upon both geographic data and location notes to create datasets where the same methane source was thought to have been surveyed on multiple surveys. The resulting datasets for each methane source were plotted as Miller-Tans plots where the slope of the linear regression represents the source  $\delta^{13}\text{C}_{\text{CH}_4}$  signature. The resulting overview of source signatures for the region are shown in Figure 98 and Figure 99.

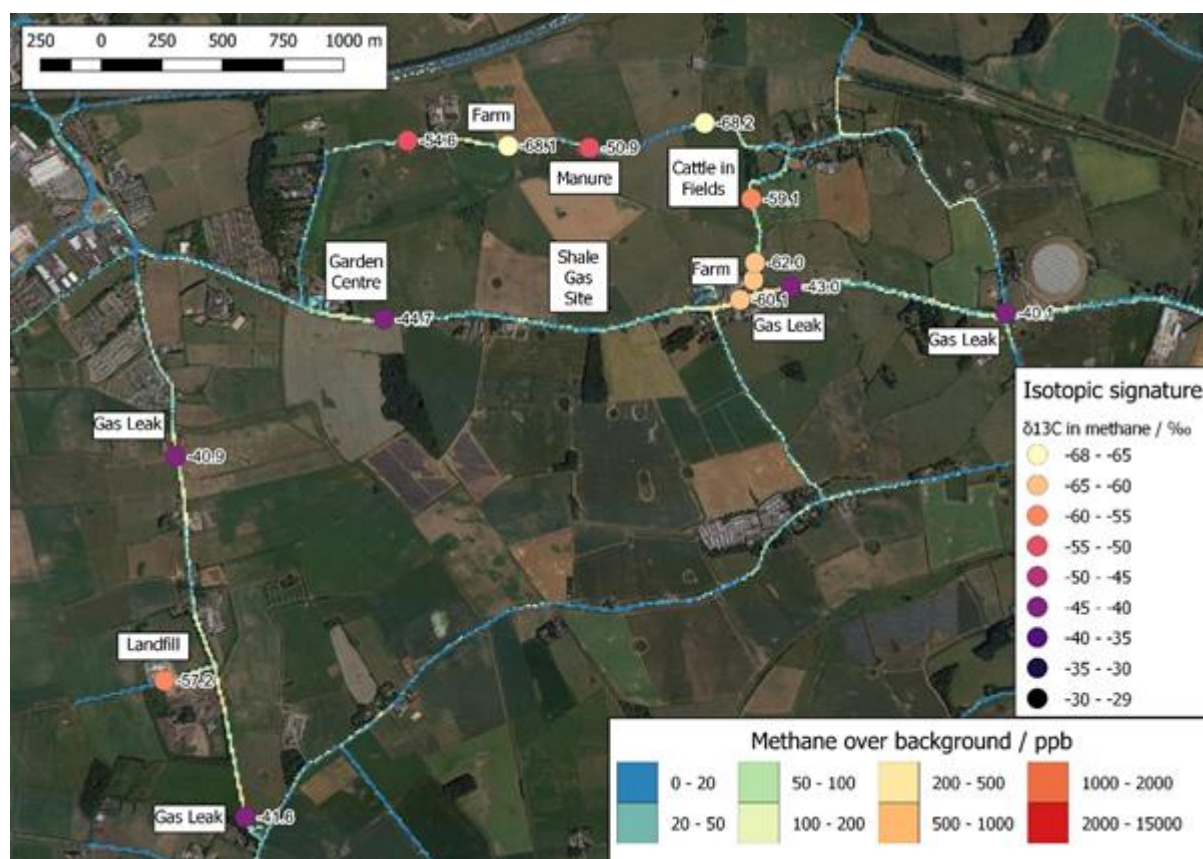


**Figure 98. Isotopic signatures and averaged enhanced methane mole fraction map in the area around the shale gas extraction site. Labels represent known sources and associated  $\delta^{13}\text{C}_{\text{CH}_4}$  source signature determined from Miller-Tans analysis. © RHUL (2019). Using ethane:methane tracer as a mapping tool of emissions**

The presence or absence of ethane associated with methane is a well-established tool to predict whether the origin of the methane is from a thermogenic or biogenic source (see Table 16). However, it has only recently become possible to include an instrument capable of measuring

ethane in a mobile laboratory at a precision useful for such studies. A Los Gatos Research Ethane-Methane analyser was fitted to the RHUL mobile laboratory from campaign FY4 onwards and the data has been collated to produce ethane:methane maps as shown in Figure 100. To produce the overview maps, the data has been filtered to remove data where the ethane < 50ppb and/or methane < 200ppb enhanced over the background mole fractions. This enables us to focus on the areas of emission and not mis-identify / mis-focus on interesting ratios caused by fluctuations in instrument noise (instrument precision is 30ppb (1-σ, 1s) for ethane). The data for enhanced ethane and methane is shown at the same scale as the isotope maps (Figure 99 and Figure 100) to demonstrate both the ability and consistency of using an ethane:methane tracer map as both a complementary and as an alternative to spot sampling for isotopes.

**Table 16. Literature values for ethane:methane ratios. In Summary: <0.01 Probably Biogenic, >0.03 Probably Thermogenic.**

C <sub>2</sub> H <sub>6</sub> : CH <sub>4</sub>	Source
0.08	Gas Plants <sup>1</sup>
0.03	Compressor Station <sup>1</sup>
0.1	Thermogenic coal <sup>2</sup>
0.03	UK Gas Distribution <sup>3</sup>
0.15	Oil Fields <sup>3</sup>
0.005	Biogenic Coal <sup>2</sup>
0.118	Gas Fields <sup>4</sup>

<sup>1</sup>Lopez et al. 2017, <sup>2</sup>Stapoc et al. 2007, <sup>3</sup>Xiao et al. 2008, <sup>4</sup>Rella et al. 2015

The continuous nature of the ethane:methane data set is especially useful where plumes of methane of differing provenance merge into each other, such as gas leaks and landfill on Peel Road (Figure 102) and also Treales gas offtake station and the local farm (Figure 103).

The ethane:methane dataset for the campaigns FY4-FY9 is shown in Figure 104 to highlight the general trends between ethane and methane for emissions in the Fylde region observed during the baseline period. There appears to be four dominant trends within the ethane:methane ratio, the two trends with ethane:methane ratios of 0.045 and 0.07 are most interesting as it suggests that there may be two different thermogenic sources in the region which have been measured during the baseline studies, possibly suggesting a change in the source mix of gas in the local pipelines over the baseline period (Figure 104). This is in contrast to the data from Kirby Misperton where the gas signature for ethane appears to have been very stable during the same period.

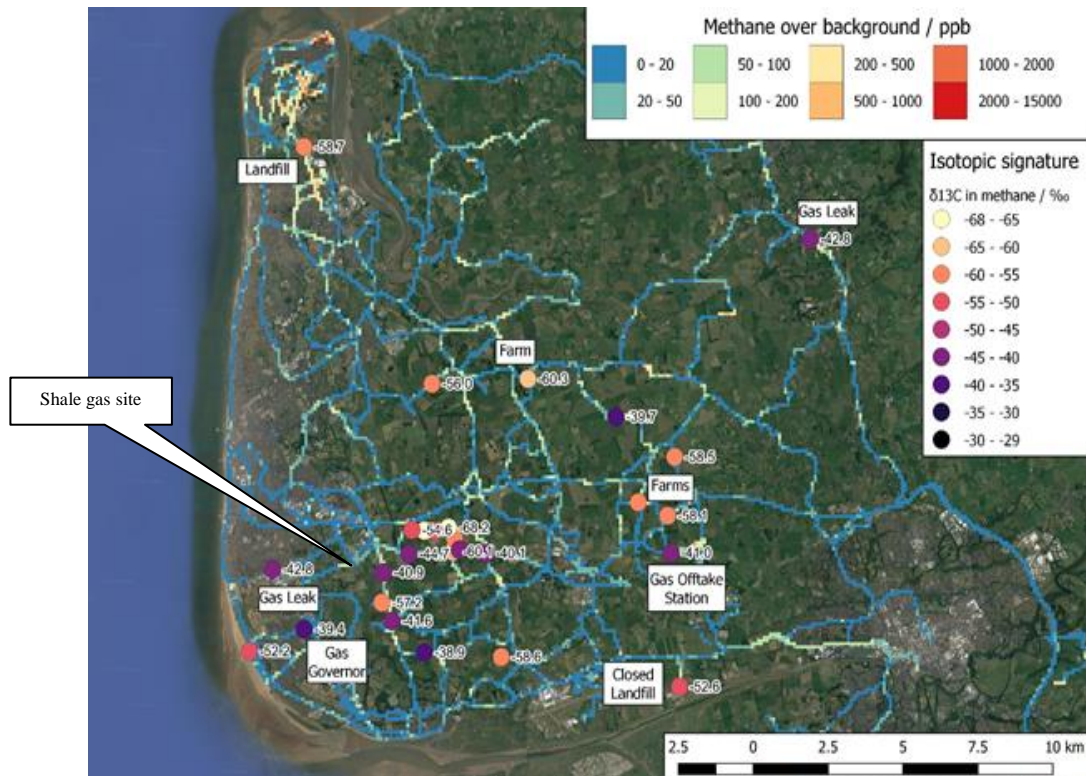


Figure 99. Regional isotopic and averaged enhanced methane mole fraction map in the Fylde region. Labels represent known sources and associated  $\delta^{13}\text{C}_{\text{CH}_4}$  source signature determined from Miller-Tans analysis. © RHUL (2019).

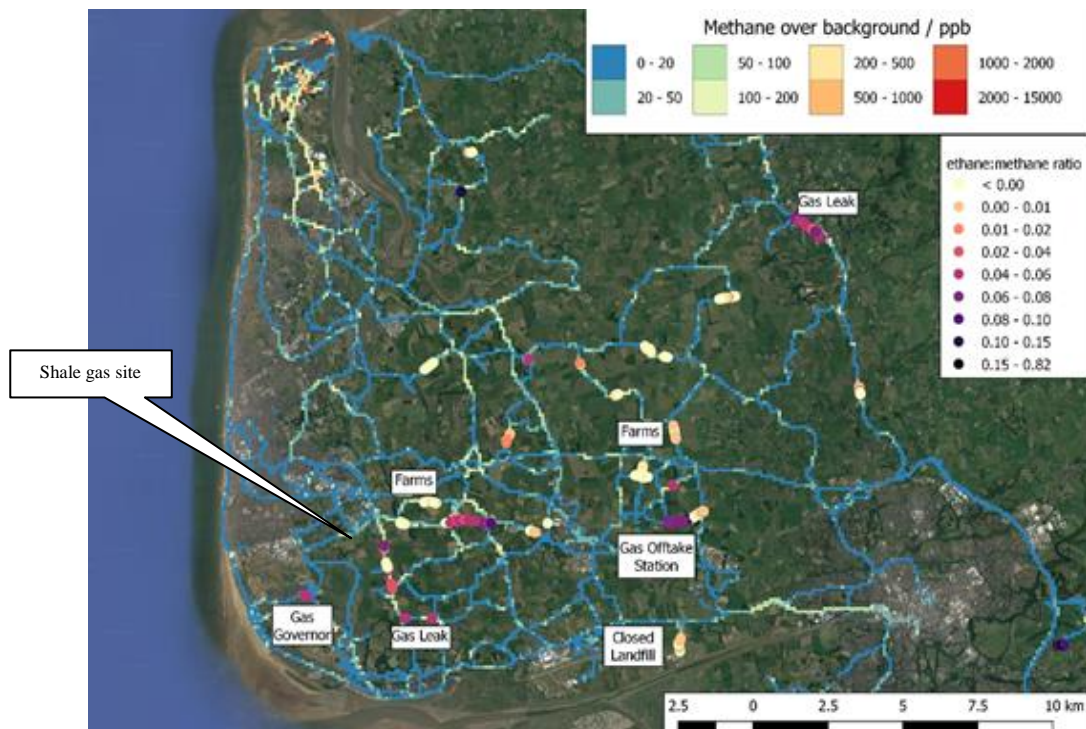
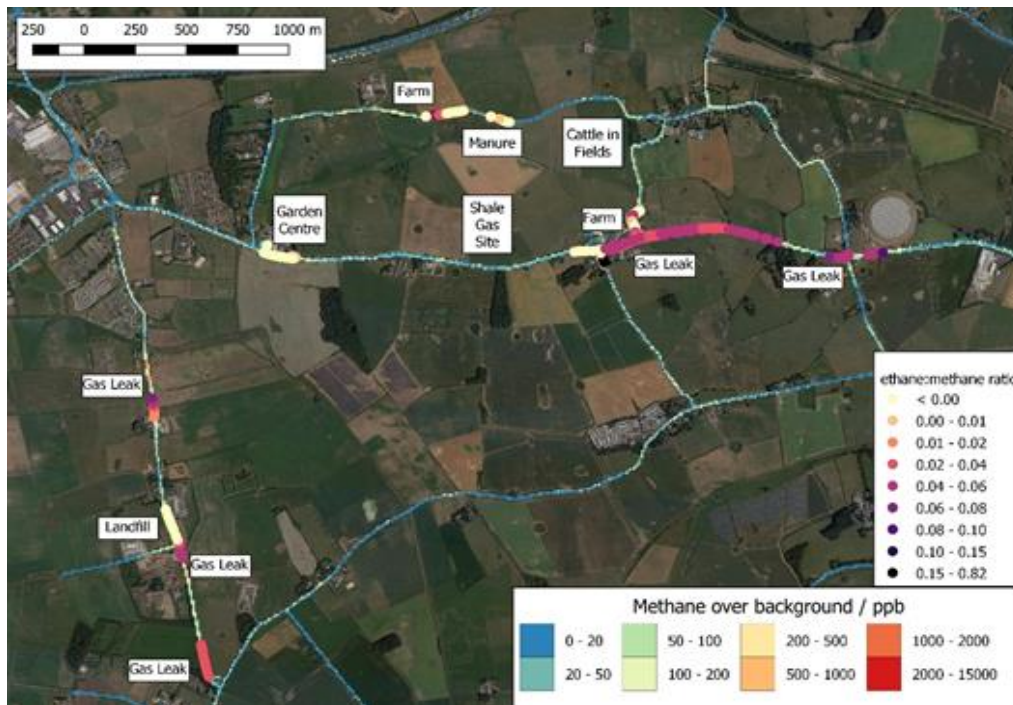
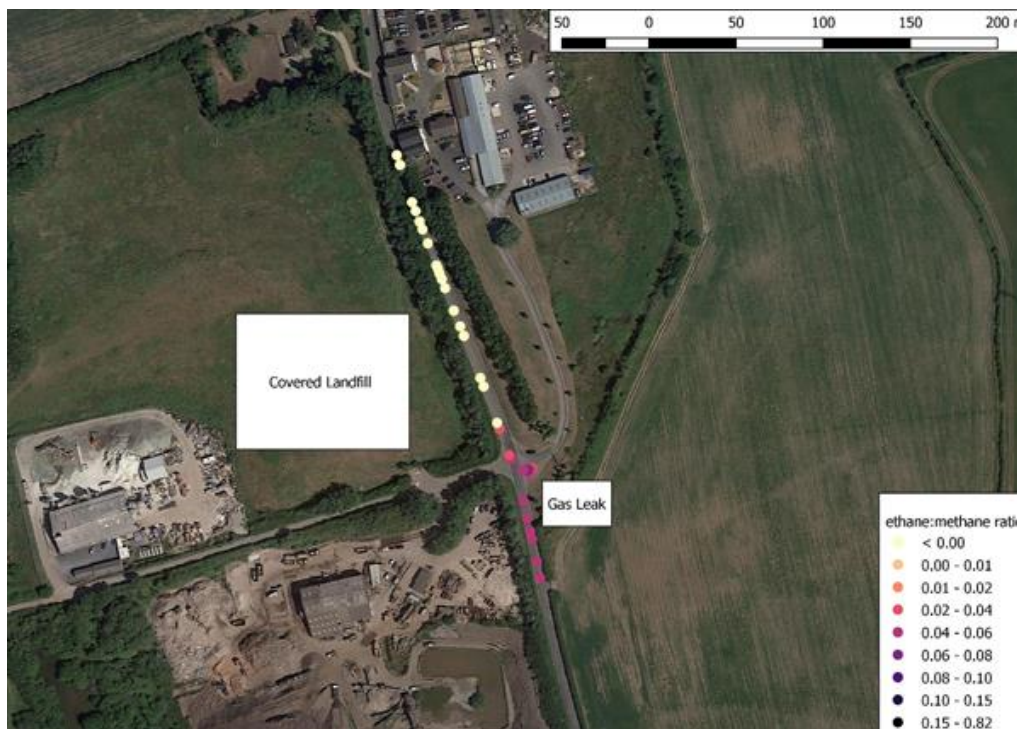


Figure 100. Overview map of ethane:methane ratios superimposed on the average enhanced methane mole fraction for the Fylde region. Labels represent known sources as examples. Light colours represent biogenic sources and darker colours more thermogenic sources of methane. © RHUL (2019).



**Figure 101. Overview map of ethane:methane ratios superimposed on the 10m<sup>2</sup> average enhanced methane mixing ratios for the local area around the shale gas extraction site. Labels show known sources of methane. Light colours represent biogenic sources and darker colours more thermogenic sources of methane. © RHUL (2019).**



**Figure 102. Demonstrating the value of mobile continuous ethane and methane ratios, here we can see the sudden change in ratio as the vehicle goes through what may have been otherwise considered a continuous plume, but is in fact a change from a gas leak source to a landfill source in the centre of the map. © RHUL (2019).**

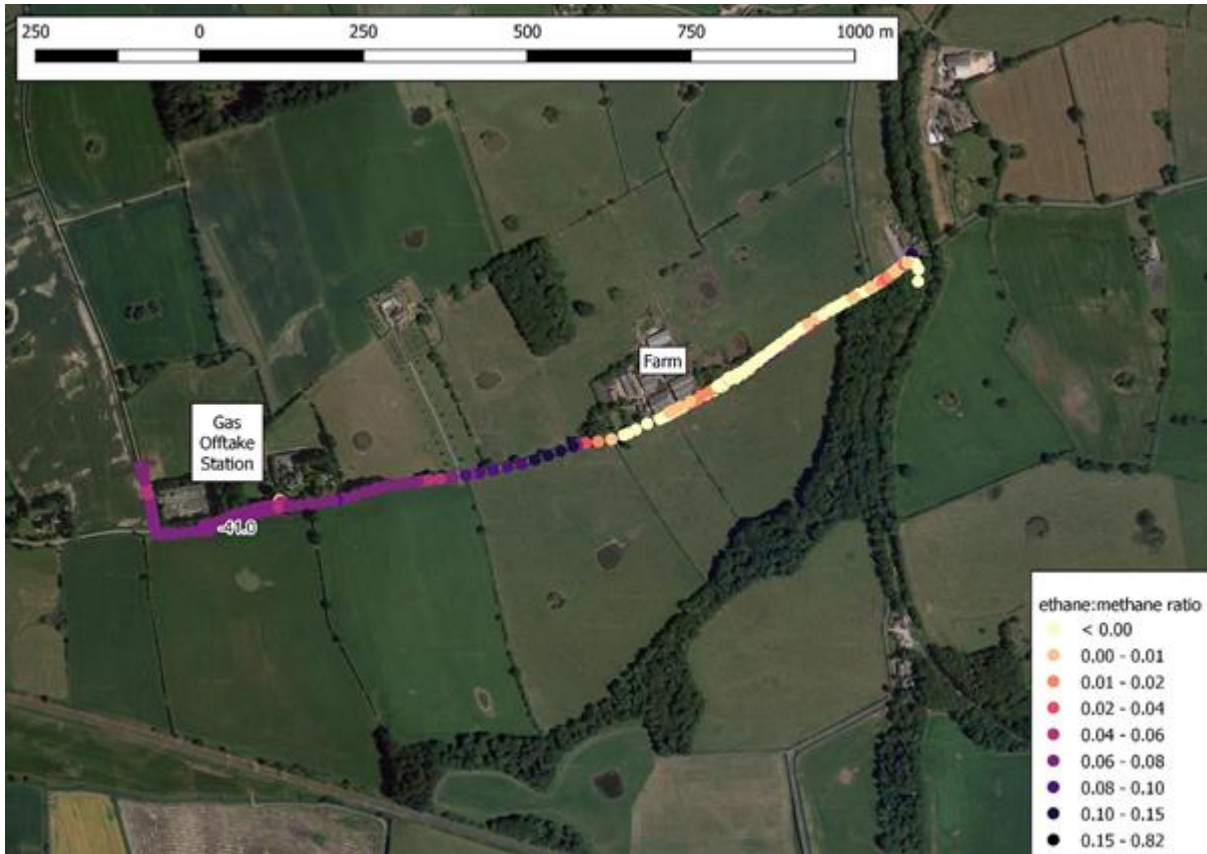


**Figure 103. Ethane and methane ratios near the Treales gas offtake station and the nearby plume of methane from the local farm. The plume sources are easily distinguished using the ethane:methane ratios from the mobile measurements. © RHUL (2019).**

Figure 104 shows the ethane-methane relationship of over six sampling campaigns (FY4 to FY9). The main trends of thermogenic gas emissions stand out and are marked by black lines. These have  $C_2H_6:CH_4$  ratios between 0.045 and 0.07 and appear to be related to gas leaks and thermogenic gas sources. Two additional trends are observed; enhanced methane without ethane (ratio of  $< 0.005$ , associated with biogenic sources such as landfill and farms), and enhanced ethane with little relative enhancement in methane associated with vehicle exhausts or filling stations. The range of  $C_2H_6:CH_4$  may indicate that there are mixed gas and biogenic plumes. This scenario occurs for the W-MW sector at PNR where farm and gas emissions overlap in downwind plumes.

#### **4.4.2 Fylde - Operational period (during and post hydraulic fracturing)**

Although methane emissions from the nitrogen lift were observed at the stationary site intermittently in mid-January, these were not observed during the period of the mobile campaign on the afternoon of 15<sup>th</sup> and the morning of 16<sup>th</sup> January 2019 (Figure 105). No new methane sources were detected on the mobile surveys. The main sources detected around the shale gas extraction site remain the mains gas pipeline leaks on Preston New Road and Peel Road and localised farm emissions.

Identified sources in March 2019 (Figure 106) remained the same as in the baseline period. No noticeable emissions were observed from the PNR shale gas site.

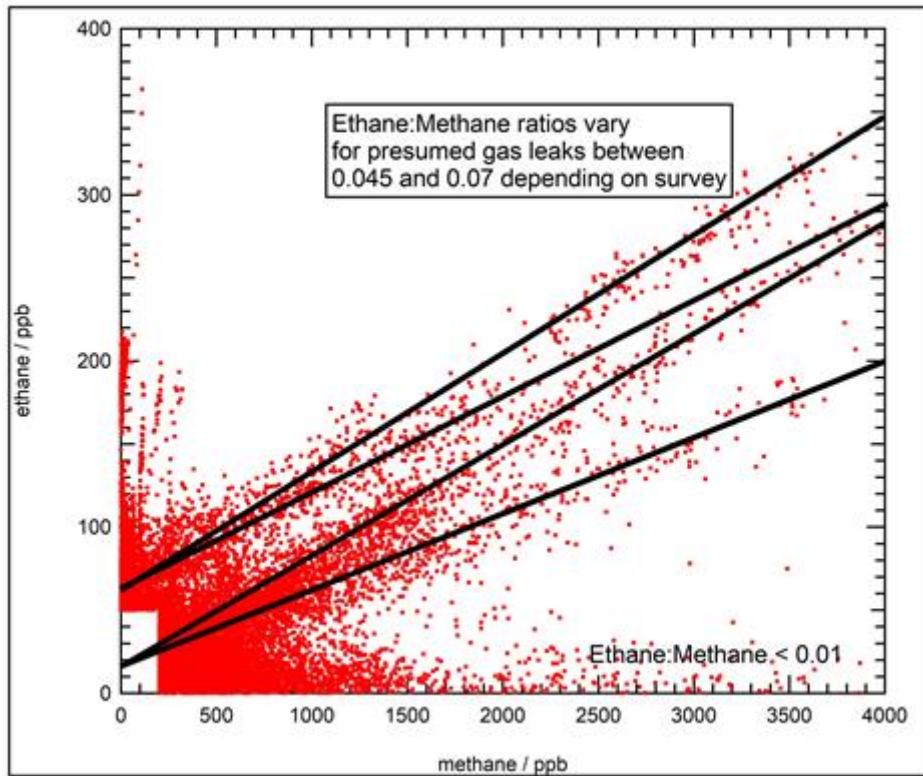


Figure 104. Ethane vs Methane for data collected across FY4 to FY9 using the Los Gatos UMEA instrument. Data is filtered to only include points where either CH<sub>4</sub> > 200ppb or C<sub>2</sub>H<sub>6</sub> > 50ppb. © RHUL (2019).

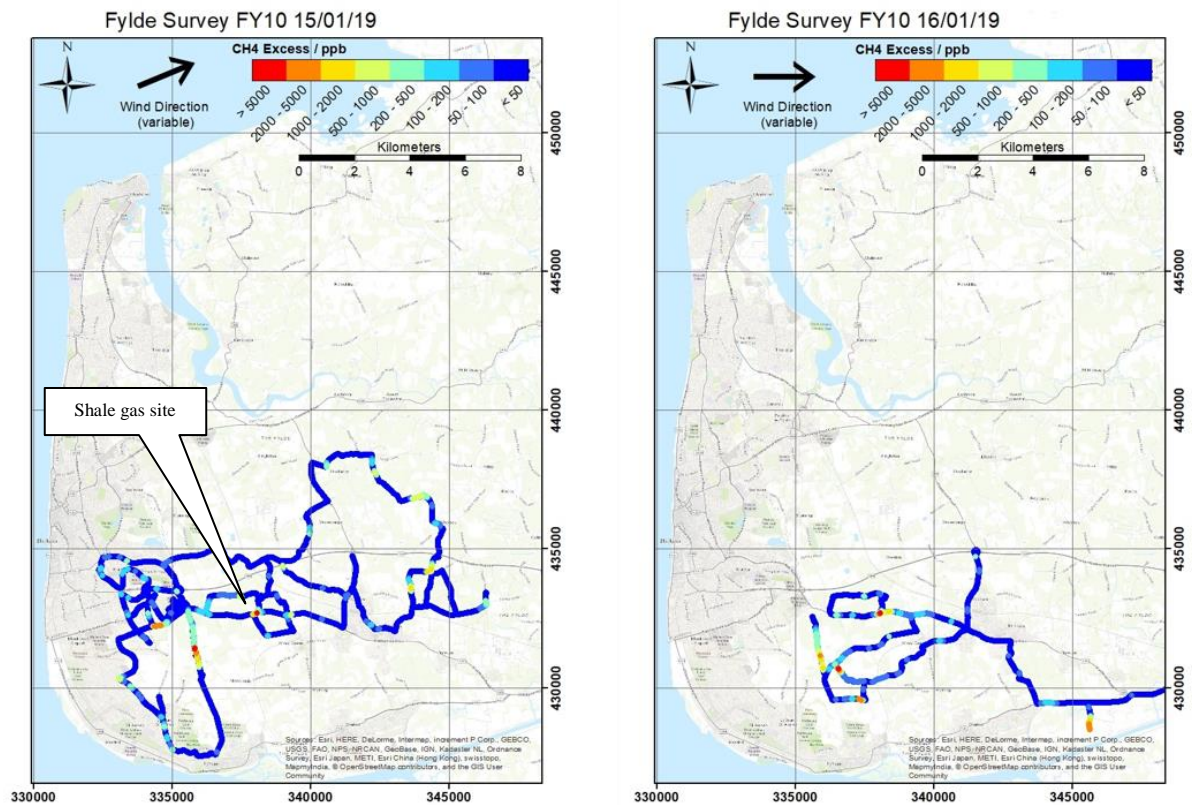
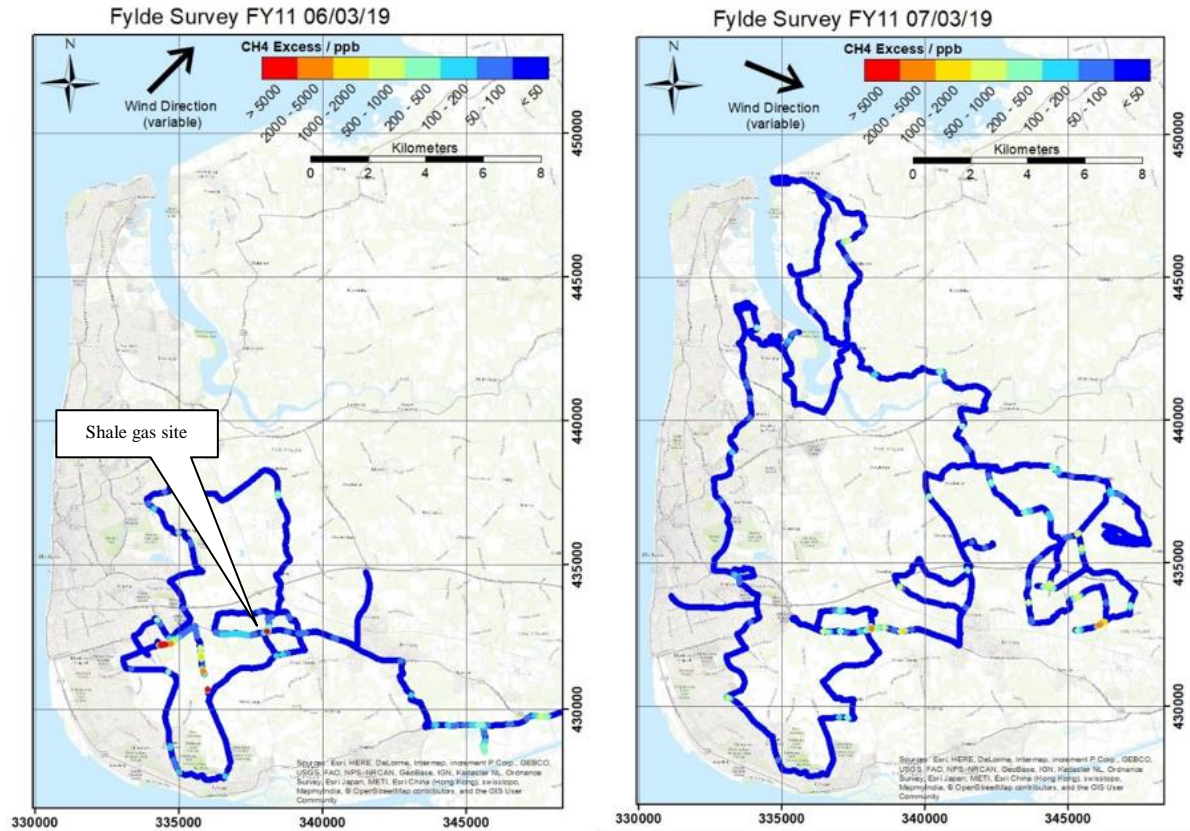


Figure 105. Methane elevations above baseline measured in the Fylde during FY10, 15<sup>th</sup> and 16<sup>th</sup> January 2019. © RHUL (2019).



**Figure 106.** Methane elevations above baseline measured in the Fylde during FY11, 6<sup>th</sup> and 7<sup>th</sup> March 2019. The large peak observed on 6 March 2019 is the Midgeland closed landfill site, 2.8 km west of the PNR site. © RHUL (2019).

Table 17 shows the consistency of the isotopic source signatures of the main emissions in the Fylde region throughout the monitoring period.

**Table 17.** Isotopic signatures of the main methane sources seen on each campaign in the Fylde identified from Keeling plot analysis. On some campaigns different signatures were identified for cows in barns<sup>(a)</sup> and cows in fields<sup>(b)</sup>.

Source	Location (Lat, Long)	$\delta^{13}\text{C}$ signatures (‰)										
		Mar 2016	Jul 2016	Jun 2017	Oct 2017	Jan 2018	Feb 2018	July 2018	Aug 2018	Oct 2018	Jan 2019	Mar 2019
Dairy farms	Many	-60.2 <sup>a</sup> -64.4 <sup>b</sup>	58.4	-59.1	-60.9	-66.2	-61.0	-62.7	-59.1 <sup>a</sup> -67.9 <sup>b</sup>	-62.9	-62.2	-62.6
Manure piles	Many	-51.6		-53.1		-58.6		-55.9	-51.6			

Gas leaks	Many	-41.2		-40.9	-42.8	-42.6	-40.6	-40.8	-40.5	-39.4	-40.8	-39.6
Clifton landfill (closed)	53.75 3°N2. 825° W	-55.1				-55.5		-55.8				-52.0
Anna's Rd Landfill (closed)	53.77 5°N2. 976° W						-59.8				-57.2	-57.5
Midgeland Landfill (closed)	53.78 2°N2. 993° W										-55.3	-55.0
Fleetwood landfill (active)	53.91 0°N3. 027° W	-57.8	-58.4	-58.3				-58.7		-54.3		

#### 4.4.3 Vale of Pickering

The main sources in the vicinity of the Kirby Misperton site (KMA) continue to be gas leaks from the Pickering offtake station, dairy farms and the Knapton landfill site. Examples of the maps of methane excess for July 2018 and March 2019 are shown in Figure 107 and Figure 108.

Vale of Pickering Survey KM7 18/07/18

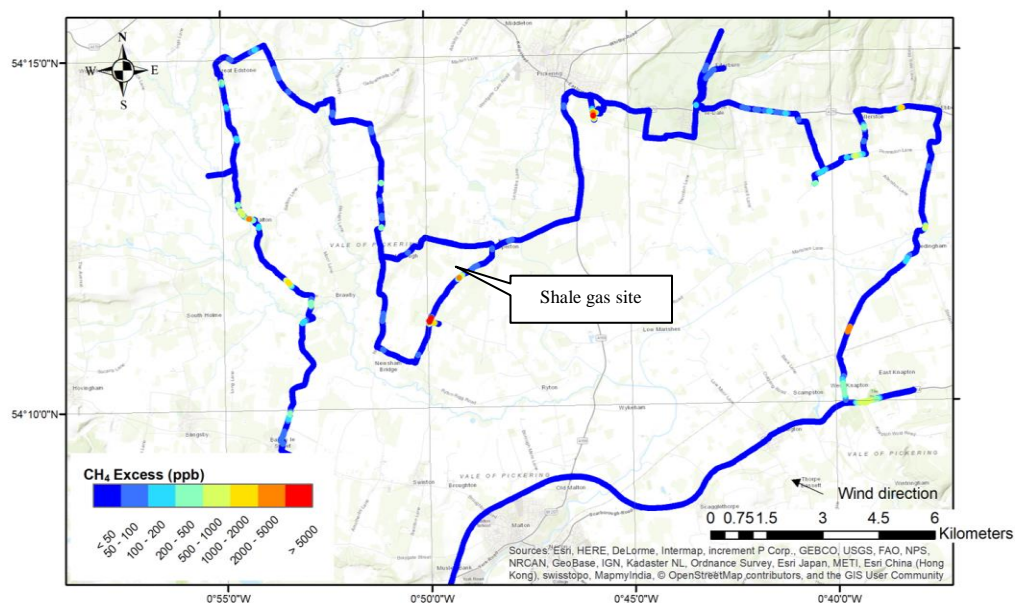


**Figure 107. Methane elevations above baseline measured in the Vale of Pickering on 18<sup>th</sup> July 2018. Methane  $\delta^{13}\text{C}$  measured in the bags collected is also shown. © RHUL (2019).**

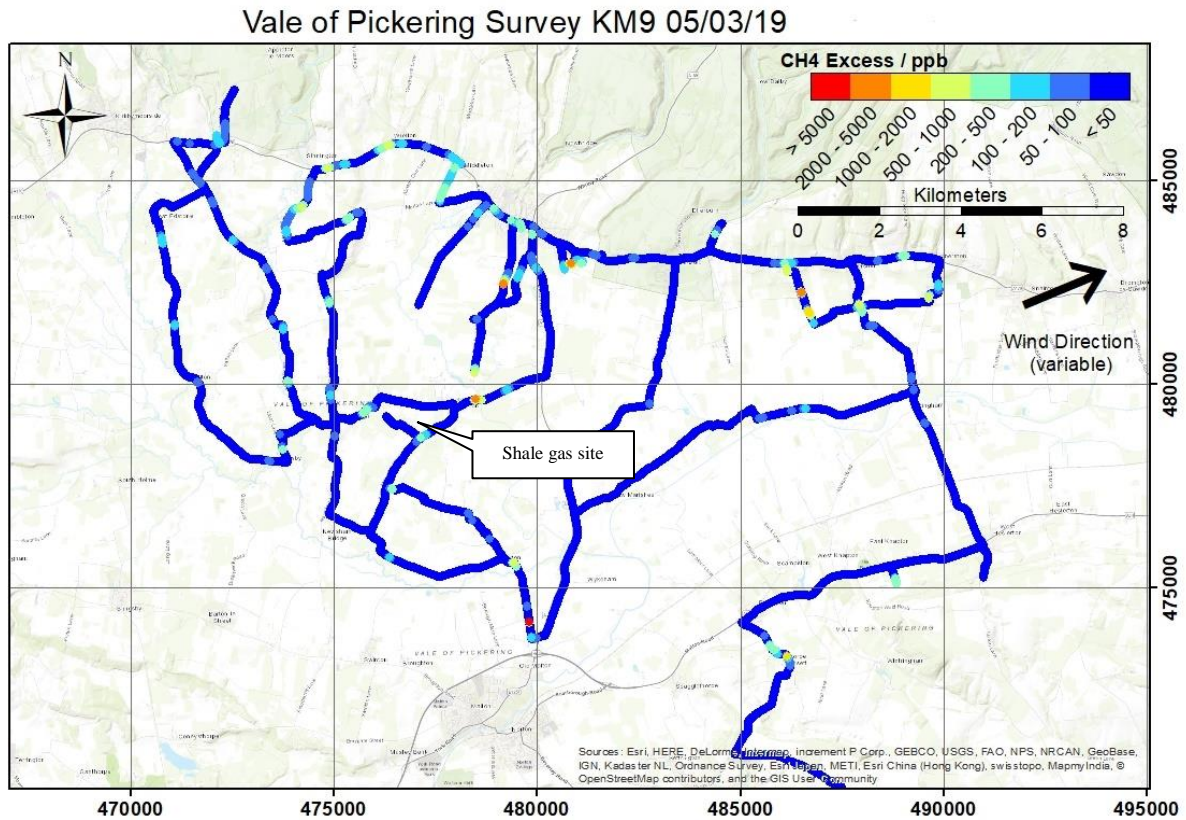


**Figure 108. Methane elevations above baseline measured in the Vale of Pickering on 5<sup>th</sup> March 2019. © RHUL (2019).**

Elevations in ethane occur when the methane emissions are from the gas distribution network. The crossplot of ethane:methane from surveys KM4 to KM9 identifies the ethane:methane ratio for gas leaks in the Vale of Pickering as consistent at around 0.07. Higher ratios of ethane:methane may be from combustion (bonfires or occasional vehicle emissions), with low ratios from biogenic sources (farms or landfill).

Figure 109 shows the ethane-methane relationship of over six sampling campaigns (KM4 to KM9). Four significant trends stand out; enhanced methane without ethane (associated with biogenic sources such as landfill and farms),  $C_2H_6:CH_4 \sim 0.07$  to 0.08 related to leaks in the gas supply network,  $C_2H_6:CH_4$  of related to bonfires, and enhanced ethane with little relative enhancement in methane which appears to be associated with vehicle or filling station emissions.

Table 18 shows the consistency of the isotopic source signatures of the main emissions in the Vale of Pickering region throughout the monitoring period.

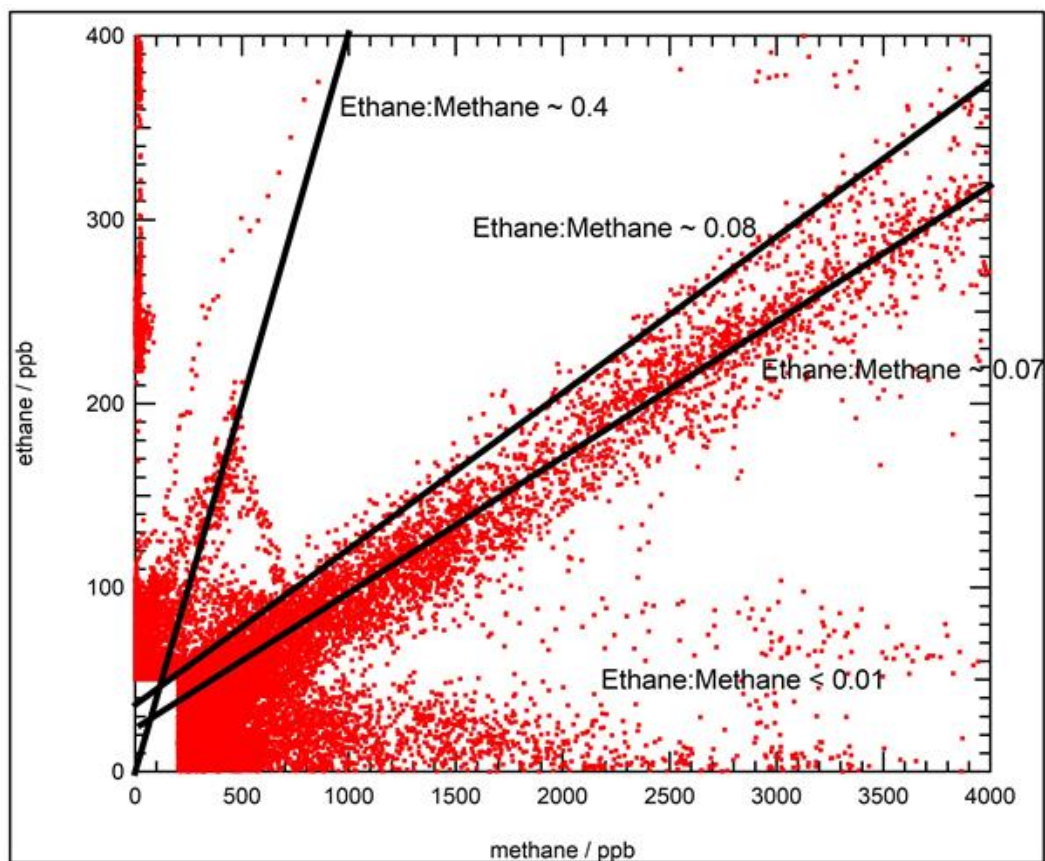


Figure 109. Ethane vs Methane for data collected across KM4 to KM9 using the Los Gatos UMEA instrument. Data is filtered to only include points where either CH<sub>4</sub> > 200ppb or C<sub>2</sub>H<sub>6</sub> > 50ppb. © RHUL (2019).

Table 18. Isotopic signatures of the main methane sources seen on each campaign in the Vale of Pickering identified from Keeling plot analysis

Source	Location (Lat, Long)	CH <sub>4</sub> δ <sup>13</sup> C signatures (‰)								
		Oct 2016	Jan 2017	Jun 2017	Oct 2017	Jan 2018	Mar 2018	Jul 2018	Nov 2018	Mar 2019
Dairy farms	Many	-63.6	-59.3	-64.7	-66.2	-67.3	-65.5	-67.0	-64.1	-63.9
Manure piles	Many			-49.7	-56.7		-50.1	-63.4		-51.2
Pickering gas offtake station	54.236°N 0.762°W	-41.7	-42.4	-40.6	-42.9	-42.0	-42.0	-41.9	-41.2	-41.4 -40.4
Gas leak A170	54.264°N 0.905°W				-41.4	-41.5	-41.6			

<b>Gas leak, Kirby Misperton Rd</b>	54.207°N 0.798°W			-39.9			-44.2			
<b>Caulklands landfill (closed)</b>	54.242°N 0.711°W	-57.4	-57.3	-59.0			-57.9			
<b>Knapton landfill (active)</b>	54.162°N 0.644°W			-58.5	-58.6	-59.6	-61.1	-58.7	-61.4	-56.2

There was evidence of reduction in activity at Knapton landfill between November 2018 and March 2019. It is now emitting methane that is more enriched in <sup>13</sup>C, at -56 ‰, typical of closed landfills with some cover oxidation, compared with signatures of -61 to -58 ‰ when the site was active.

A clear separation of 2 plumes from the Pickering offtake station during southerly winds in March 2019 (Figure 110) allowed two separate peaks to be identified at the western and eastern sides of the Pickering gas offtake station when surveying outside of the perimeter fence. This suggests at least two emission points at the site. This was hinted at during previous south-westerly airflow suggesting that this has been the case throughout Phases 3 and 4 of the project. At further distances the plumes merge together and the availability of downwind roads meant that the plume could be traced 800-900m north of the site with more than 100 ppb CH<sub>4</sub> excess.

#### 4.5 SUMMARY OF MOBILE SURVEYS SINCE 2016

The main methane sources within a 10 km radius of the PNR and KM drill sites have persisted through phases 2, 3 and 4.

Fugitive gas network emissions - only the largest observed gas leaks are fixed (enhancements >10ppm measured). Smaller leaks and fugitive emissions from known gas installations persist. Largest peaks detected up to 1 km downwind.

Waste sources - the active landfills in both Fylde and Ryedale have closed to waste delivery in recent years with an associated significant reduction in emissions (possibly >80%) and an enrichment in <sup>13</sup>C associated with increased methane oxidation from thick cover soils. Older closed landfills continue to emit methane. Largest peaks detected up to 1.5 km downwind.

Farm sources - these remain largely unchanged from Phase 2 with barns being the focus of emissions, representing a mix of animal eructations and waste emissions. The spatial distribution varies with season and climate, with more dispersed animal emissions from fields and regular sites populated by manure piles outside of the winter months. Barn sources detected up to 500m downwind.

Hydraulic-fracturing-related emissions - none was detected during the survey periods; it is expected that these can be distinguished using isotopic or ethane proxies, but this would not be definitive until production samples are available for comparison.

### Pickering gas offtake plume KM9 06/03/19



**Figure 110. A rare southerly wind on 6 March 2019, allowed two separate peaks to be identified at the western and eastern sides of the Pickering gas offtake station when surveying outside of the perimeter fence. © RHUL (2019).**

## 4.6 REFERENCES

- Allen, G., Shaw, J., Shah, A., Pitt, J., Ricketts, H., Williams, P., Ward, R.S 2019. Environmental baseline monitoring project: Methane enhancements detected at Little Plumpton air monitoring site. Nottingham, UK, British Geological Survey. <https://www.bgs.ac.uk/news/item.cfm?id=9410>.
- Fisher, R, Lowry, D, Wilkin, O, Sriskantharajah S and Nisbet. EG (2006) High-precision, automated stable isotope analysis of atmospheric methane and carbon dioxide using continuous-flow isotope-ratio mass spectrometry, *Rapid Comm. Mass. Spec.* 20, 200-208.
- Purvis, R.M., Lewis, A.C., Hopkins, J.R., Wilde, S.E.; Dunmore, R. E.; Allen, G.; Pitt, J.; Ward, R. S 2019 Effects of ‘pre-fracking’ operations on ambient air quality at a shale gas exploration site in rural North Yorkshire, England. *Science of The Total Environment*, 673. 445-454.
- Shaw, J., Allen, G., Pitt, J., Mead, M.I., Purvis, R.M., Dunmore, R., Wilde, S.E., Shah, A., Barker, P., Bateson, P., Bacak, A., Lewis, A.C., Lowry, D., Fisher, R.L., Lanoiselle, M., Ward, R. S. 2019. A baseline of atmospheric greenhouse gases around prospective UK shale gas sites. *Science of The Total Environment*, 684. 1-13.
- Ward, R.S., Smedley, P.L., Allen, G., Baptie, B.J., Daraktchieva, Z., Horleston, A., Jones, D.G., Jordan, C.J., Lewis, A., Lowry, D., Purvis, R.M., Rivett, M.O. 2017. Environmental baseline monitoring project: Phase II final report. Nottingham, UK, British Geological Survey, 163 pp. (OR/17/049) (Unpublished).
- Ward, R.S., Smedley, P.L., Allen, G., Baptie, B.J., Cave, M.R., Daraktchieva, Z., Fisher, R., Hawthorn, D., Jones, D.G., Lewis, A., Lowry, D., Lockett, R., Marchant, B.P., Purvis, R.M., Wilde, S. 2018. Environmental baseline monitoring: Phase III final report (2017-2018). Nottingham, UK, British Geological Survey, 143pp. (OR/18/026) (Unpublished).
- Zazzeri, G, Lowry, D, Fisher, RE, France, JL, Lanoisellé, M & Nisbet, EG (2015) Plume mapping and isotopic characterisation of anthropogenic methane sources, *Atmospheric Environment*, 110, 151-162. DOI: 10.1016/j.atmosenv.2015.03.029.

## 5 Air Quality

### 5.1 INTRODUCTION

This section reports the Air Quality dataset for both the Kirby Misperton (KM) and Preston New Road (PNR) measurement sites.

The statistical analysis of the AQ dataset for both sites is presented and interpreted in the context of sources of emissions using meteorological data to aid analysis. The analysis provides information on the annual climatology of air pollution at both locations along with representative insight into shorter-term variability in air pollution. The baseline analysis is framed specifically with reference to the attainment of the European Commission (EC) Air Quality Directive limits at both locations. This uses a range of metrics including annual, 1 day and 8-hour mean concentrations.

For LP there was a change from baseline monitoring to operational monitoring in October 2018 when hydraulic fracturing began. The dataset for LP has been analysed for changes arising from this hydraulic fracturing cycle.

A research paper entitled “*Effects of ‘pre-fracking’ operations on ambient air quality at a shale gas exploration site in rural North Yorkshire, England*” has been published in *Science of the Total Environment* in April 2019 (Purvis et al, 2019) describing the impacts of the pre-operational phase at KM.

### 5.2 THE BASELINE DATASET

The dataset used in this report was collected using surface monitors located at KM and LP and covers the observation period from 1 February 2018 until 31 January 2019. However as identified above, the data at LP from the 15th October 2018 will not be considered as baseline but are referred to as “fracking”. The dataset has been further refined to account for drilling and preparation periods. The dataset includes local meteorology (2 m above ground), nitrogen oxides (NO and NO<sub>2</sub>, collectively NO<sub>x</sub>), particulate matter (PM) in a number of aerodynamic size ranges, ozone (O<sub>3</sub>), speciated non-methane hydrocarbons (NMHCs) and from 2017 hydrogen sulphide (H<sub>2</sub>S). The data are archived and publically accessible at the NERC Centre for Environmental Data Analysis (CEDA). Measurements are available at 1 minute intervals, except NMHCs which are reported as weekly values, see: <http://browse.ceda.ac.uk/browse/badc/envbaseline>. The environment baseline is first examined on a site by site basis followed by comparison of the climatologies of pollution at each site.

### 5.3 RESULTS AND DISCUSSION

Managing and improving air quality in the UK is driven by European (EU) legislation on ambient air quality standards and also commitments to limit transboundary emissions, through the National Emissions Ceiling Directive and the UNECE Convention on Long-Range Transport of Air Pollution (CLRTAP), often referred to as the Gothenburg protocol. The 2008 ambient air quality directive (2008/50/EC) sets legally binding limits for outdoor air pollutants that impact on human health and includes NO<sub>2</sub>, O<sub>3</sub>, benzene, 1,3 butadiene, PM<sub>10</sub> and PM<sub>2.5</sub>. All these species have been measured as part of the baseline project. Within the UK, ambient air quality is managed with the aspiration that all locations should meet either the prescribed Limit Values or Target Values depending on the species. EU Limit values are legally binding concentrations that should not be exceeded. There are prescribed averaging times associated with each pollutant and for some pollutants a number of exceedances are allowed in each year.

Target values are meant to be attained where possible by taking all necessary measures not entailing disproportionate costs, often reflecting natural impacts on those pollutants that can lie outside of regulatory controls. All EU directive standards are listed here: <http://ec.europa.eu/environment/air/quality/standards.htm>. The UK air quality objectives for data parameters measured as part of the air quality baseline are shown in Table 19.

**Table 19. UK National air quality objectives**

Pollutant	Concentration	Averaging period	Legal nature	Permitted exceedances	Approx conversion to ppb <sup>a</sup>
Fine particles (PM <sub>2.5</sub> )	25 µg/m <sup>3</sup>	1 year	Limit value	none	n/a
Nitrogen dioxide (NO <sub>2</sub> )	200 µg/m <sup>3</sup>	1 hour	Limit value	18 per year	104.7 ppb
	40 µg/m <sup>3</sup>	1 year	Limit value	none	20.9
PM <sub>10</sub>	50 µg/m <sup>3</sup>	24 hours	Limit value	35 per year	n/a
	40 µg/m <sup>3</sup>	1 year	Limit value	none	n/a
Benzene	5 µg/m <sup>3</sup>	1 year	Limit value	none	1.88ppb
Ozone	120 µg/m <sup>3</sup>	Maximum daily 8 hour mean	Target value	25 days averaged over 3 years	60.1 ppb

### 5.3.1 Summary of annual means of air pollutants at KM and LP

Table 20 shows a summary of the Phase IV measurement mean values for various air pollutants at KM and LP and a restatement of the annual Directive limit value.

**Table 20. Summary of annual statistics for KM and LP locations for various air pollutants and comparison against annual mean limit values \* Ozone annual mean appears low due to missing summer data.**

Pollutant	Annual Mean at KM Feb 2018 - Jan 2019	Annual mean at LP Feb 2018 - Jan 2019	Annual mean Limit value
Ozone*	16.4 ppb	21.3 ppb	60.1 ppb
PM <sub>2.5</sub>	8.6 µg/m <sup>3</sup>	6.9 µg/m <sup>3</sup>	25 µg/m <sup>3</sup>
PM <sub>10</sub>	11.5 µg/m <sup>3</sup>	8.0 µg/m <sup>3</sup>	40 µg/m <sup>3</sup>
NO	0.9 ppb	1.75	No limit value

NO <sub>2</sub>	2.7 ppb	6.14	20.9 ppb
NO <sub>x</sub>	3.7 ppb	7.37ppb	No limit value
Benzene	ppb	ppb	1.88 ppb
H <sub>2</sub> S	0.8 ppb	0.44 ppb	
SO <sub>2</sub>	0.2 ppb	1.23 ppb	

The annual means for the Phase IV period are shown in Table 20. It should be noted that the ozone instrument at KM was unserviceable for the summer period so the annual average is likely to be lower than previous years.

**Table 21. Exceedance of UK air quality standards.**

<b>Pollutant</b>	<b>Number of 8-hours exceedances KM</b>	<b>Number of 8-hours exceedances LP</b>	<b>8-hour limit</b>
Ozone	0	1	60.1 ppb
	<b>Number of 24-hours exceedances KM</b>	<b>Number of 24-hours exceedances LP</b>	24 hour limit
PM <sub>10</sub>	2	0	50 µg/m <sup>3</sup>
	<b>Number of 1-hours exceedances KM</b>	<b>Number of 1-hours exceedances LP</b>	
NO <sub>2</sub>	0	0	200 µg/m <sup>3</sup>

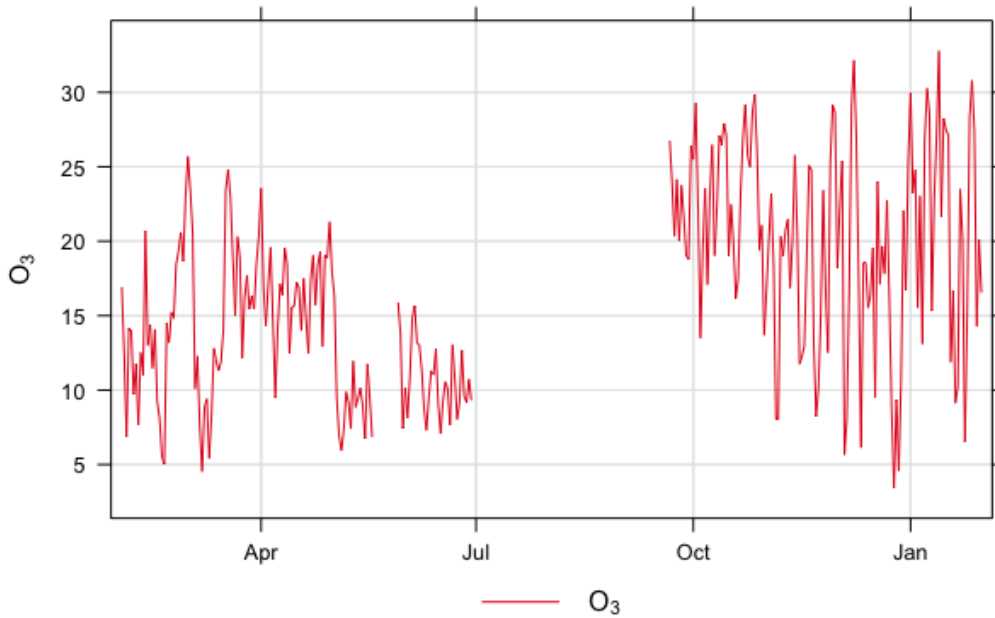
Within this measurement period there were no NO<sub>2</sub> exceedances at either site (Table 21). On 26<sup>th</sup> June 2018 the O<sub>3</sub> at LP exceeded the 8-hour average threshold. This was due to the UK experiencing a heat wave and anticyclonic weather conditions which result in a build-up of pollution and increased O<sub>3</sub> production. The instrument at KM was not in service at this time but other measurement sites around the UK also showed high O<sub>3</sub> readings.

The 24-hour mean limit value for PM<sub>10</sub> was exceeded on 3<sup>rd</sup> and 4<sup>th</sup> March 2018 at KM. Although there was not an exceedance at LP, it did show elevated values, so it is likely that this was a UK-wide episode similar to this that occurred in March 2016 and February 2017 at both sites.

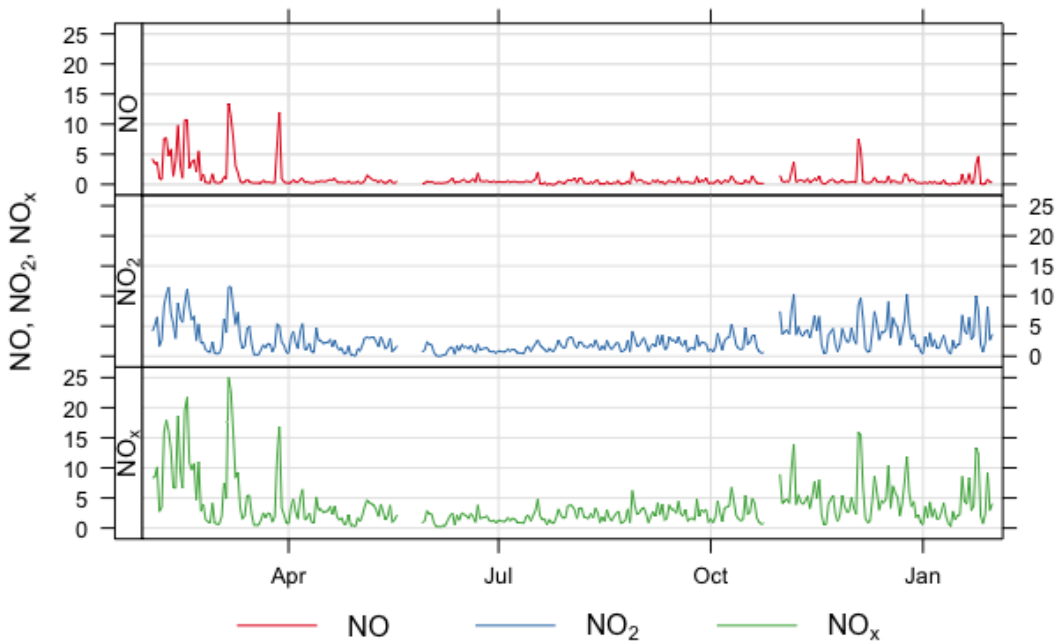
#### 5.3.1.1 SPATIALLY RESOLVED AIR POLLUTION CLIMATOLOGIES

The annual mean values for air pollution allow for comparison against national targets. NO<sub>x</sub>, O<sub>3</sub>, PM, H<sub>2</sub>S and meteorological data have all been collected at 1-minute time resolution and this is advantageous for data analysis as a more detailed climatology of air pollution can be constructed at the local scale.

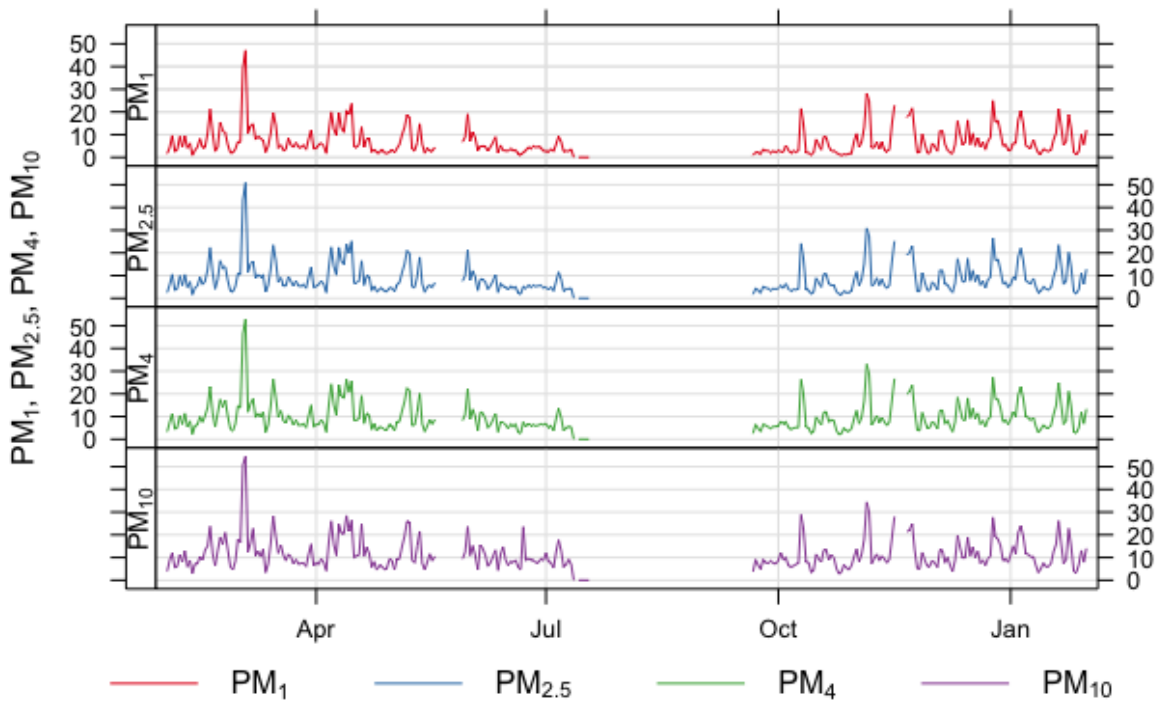
The daily average for the Phase IV period is shown in Figure 111 and Figure 112. The  $O_3$  at LP (Figure 112) is highest in June and July, and this coincides with a heat wave across the UK. The higher temperatures and anticyclonic weather conditions result in a build-up of pollutants ( $NO_x$  and VOCs) which can then lead to an increase in  $O_3$ . Ozone can be transported long distances by the wind, so rural areas (where titration by  $NO$  is minimal) often experience highest  $O_3$  concentrations in these conditions.



(a)

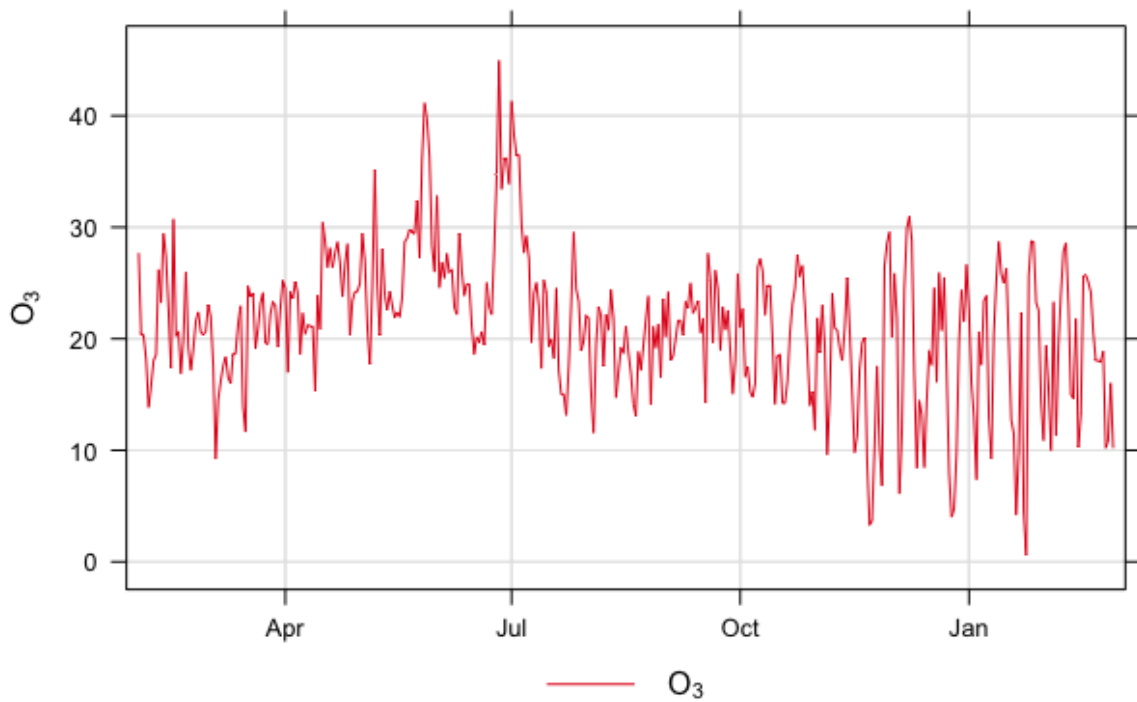


(b)

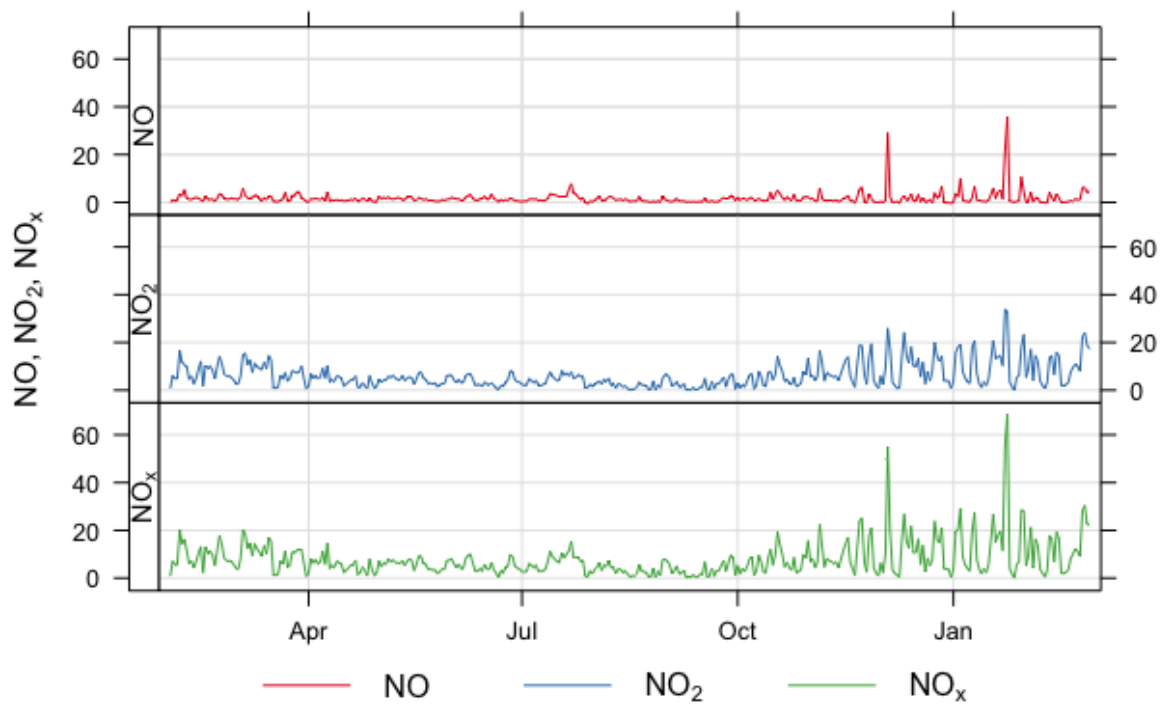


(c)

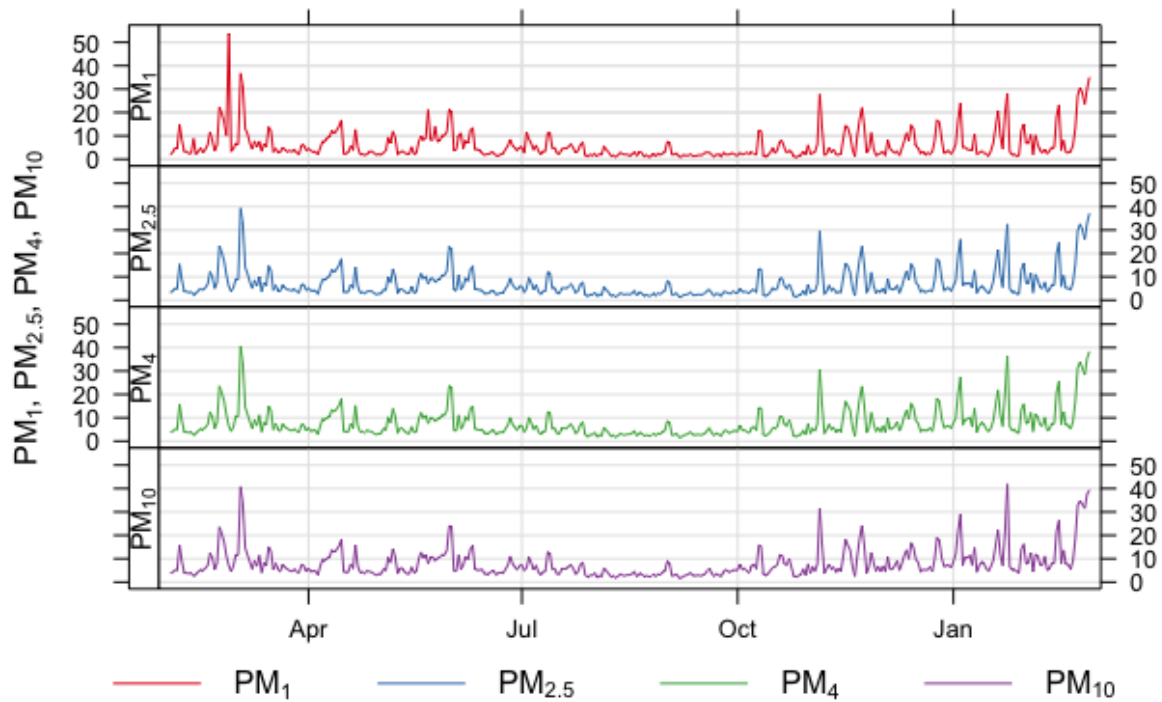
**Figure 111. Phase 4 daily time series at the KM site for (a) O<sub>3</sub>, (b) NO, NO<sub>2</sub>, NO<sub>x</sub>, (c) PM<sub>1</sub>, PM<sub>2.5</sub>, PM<sub>4</sub>, PM<sub>10</sub> and PM<sub>Total</sub>. © University of York (2019).**



(a)



(b)



(c)

**Figure 112. Phase 4 daily time series at the LP site for (a) O<sub>3</sub>, (b) NO, NO<sub>2</sub>, NO<sub>x</sub>, (c) PM<sub>1</sub>, PM<sub>2.5</sub>, PM<sub>4</sub>, PM<sub>10</sub> and PM<sub>Total</sub>. © University of York (2019).**

### 5.3.1.2 KIRBY MISPERTON DETAILED ANALYSIS

There has been no additional operational activity at the KM site during the Phase 4 project period. The hydraulic fracturing equipment was removed from the site in early 2018 and no activity has taken place at the shale gas well site (KMA). There have been significant maintenance issues with the Thermo O<sub>3</sub> instrument over this period, resulting in poor data coverage over the summer period, for this reason the ozone measurements have been removed from the detailed analysis (Figure 111). The instrument was found to have a leaking internal valve which has since been fixed.

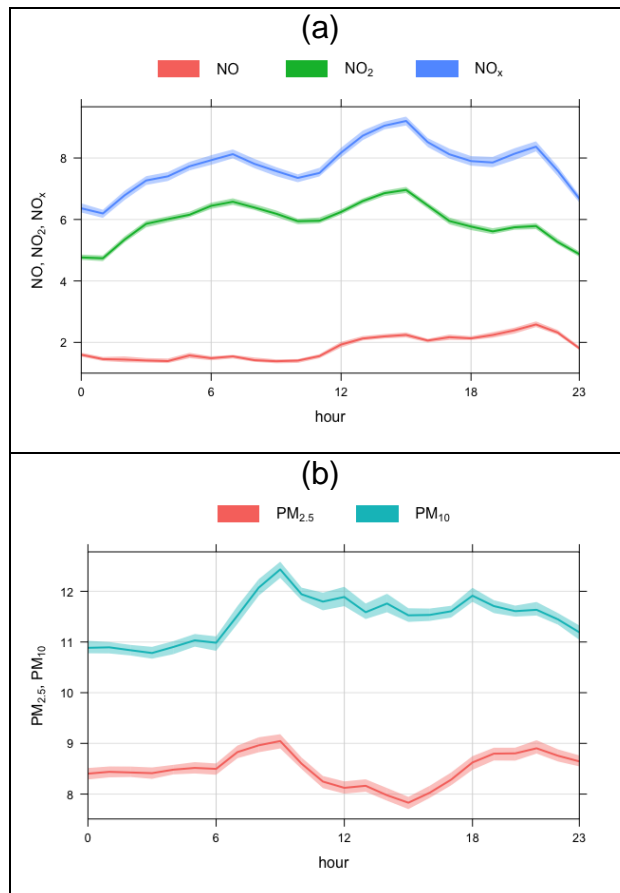
To enable a full baseline climatology of air pollution to be established it is important to examine the influence of wind direction. Table 20 reports the annual means for pollutants measured under the Air Quality Directive, whereas Table 22 reports those metrics by individual wind sector. In the UK it is most common for air from the East (E) and south-east (SE) to be most polluted as these often bring air from the SE of England and from continental Europe. The lowest concentrations of air pollution are typically observed during periods of high-wind-speed Atlantic westerly airflow. The measurements at KM have returned to a similar pattern to that observed during Phase II, with the highest concentrations of NO<sub>x</sub> to the S and SE of the site as a result of there being no influence from activity on the site itself (W).

**Table 22. Phase IV wind sector averages at KM.**

	N	NE	E	SE	S	SW	W	NW
O <sub>3</sub> (ppb)	24.8	23.3	24.0	22.1	22.6	21.5	22.0	24.8
NO (ppb)	1.6	1.8	1.9	1.9	1.9	1.8	1.7	1.8
NO <sub>2</sub> (ppb)	5.1	6.1	5.6	6.7	6.0	6.6	5.9	5.7
NO <sub>x</sub> (ppb)	6.6	7.9	7.6	8.6	7.9	8.4	7.6	7.5
PM <sub>2.5</sub> (µm/m <sup>3</sup> )	7.1	10.2	14.0	11.2	7.5	6.5	5.2	5.9
PM <sub>10</sub> (µm/m <sup>3</sup> )	10.1	13.0	17.8	14.2	10.3	9.6	8.2	8.9
H <sub>2</sub> S (ppb)	0.5	0.6	0.5	0.6	0.6	0.5	0.6	0.6
SO <sub>2</sub> (ppb)	1.1	1.1	0.9	1.5	1.4	1.5	1.3	1.4

#### *Diurnal Variation of air pollution at KM*

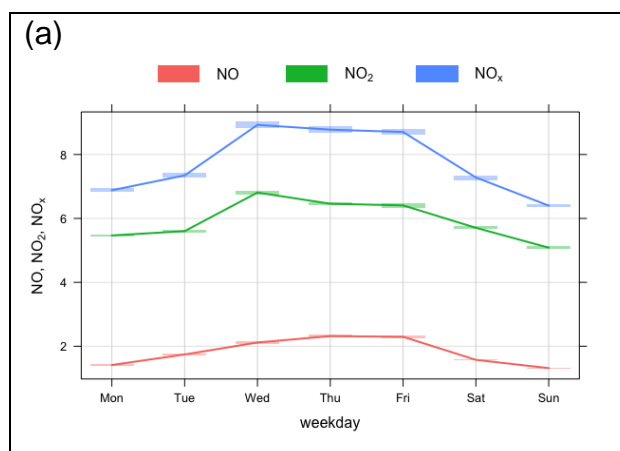
The diurnal variation in concentrations for the NO<sub>x</sub> and PM are similar to those observed in Phase II (Figure 113). The fact that these are different in profile is the first indication that the PM and NO<sub>x</sub> may have different sources at times. The NO<sub>x</sub> diurnal shows NO and NO<sub>2</sub> increasing in the morning and late afternoon, which is probably due to the boundary layer height and local traffic sources. The relative distribution of NO to NO<sub>2</sub> is balanced towards NO<sub>2</sub> indicating that very close-by combustion sources are not dominating the local NO<sub>x</sub>. This is the opposite to Phase III where it was balanced towards NO due to emissions arising from activities on the KMA site. This changed once the equipment that was on site last year for the hydraulic fracturing ceased operating and was removed.



**Figure 113. Diurnal variations at KM for (a) NO<sub>x</sub> and (b) PM. © University of York (2019).**

### *Hebdomadal Cycles at KM*

Higher air pollution concentrations during the working week (Mon - Fri) are clear from the NO<sub>x</sub> measurements with NO<sub>x</sub> being highest during the week and decreasing at the weekend (Figure 114). PM has a less pronounced weekly cycle.



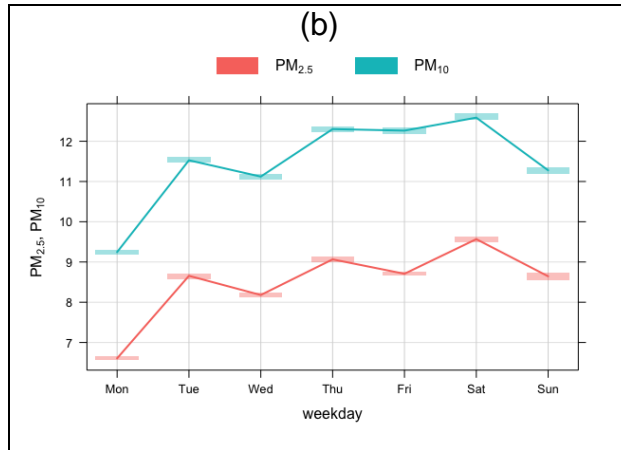


**Figure 114. Hebdomadal Cycles at KM for (a) NO<sub>x</sub> and (b) PM. © University of York (2019).**

*Annual Cycles at KM*

KM has previously shown annual typical cycles that would be expected for UK air quality, and these are shown in Figure 115. Both NO<sub>x</sub> and PM show highest concentrations during the winter months and minima in the summer, although the lowest months are off-set between the two pollutant types.

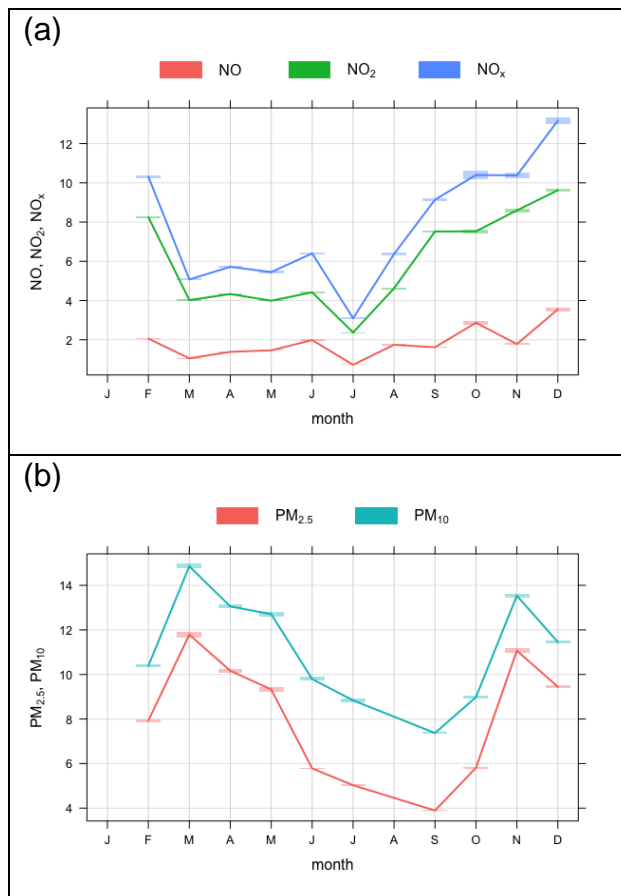


**Figure 115. Annual cycles at KM for (a) NO<sub>x</sub> and (b) PM. © University of York (2019).**

### Source Locations for KMA

Figure 116 shows polar plots for the same pollutants, with concentrations (colour scale), wind direction (radial scale) and wind speed. For many situations concentrations would be expected to decrease with increasing wind speed due to increased dilution but there are some instances where this process can lead to increases, for example due to plume grounding or the transport of air over long distances. Combining the two types of data analysis gives some indication of source regions of pollutants.

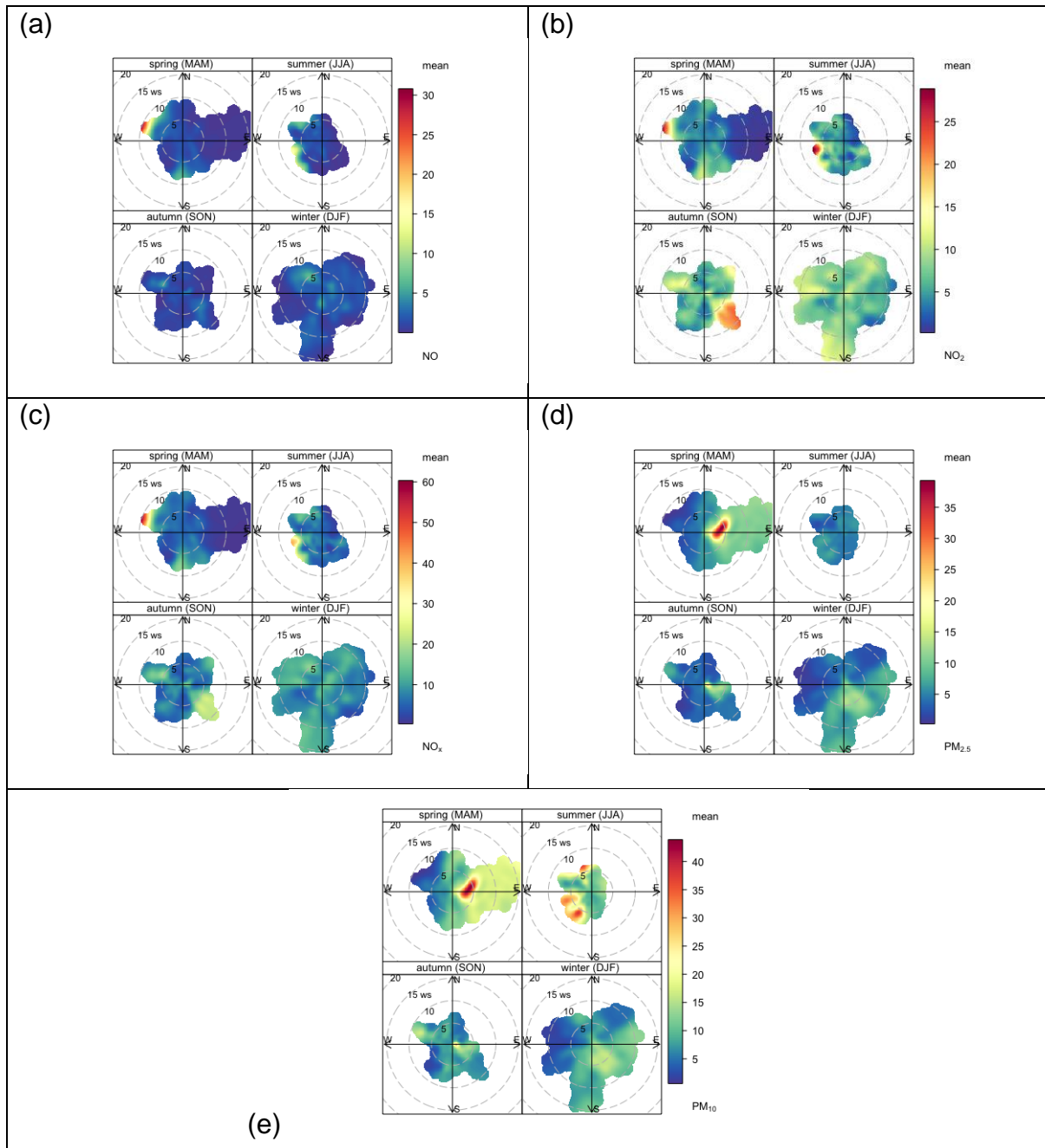


**Figure 116. Polar plots for LP (a) NO (b) NO<sub>2</sub>, (c) NO<sub>x</sub>, (d) PM<sub>2.5</sub>, (e) PM<sub>10</sub>. © University of York (2019).**

By breaking the plots down into season it can be seen that the peaks in PM are in the Spring (PM<sub>2.5</sub> and PM<sub>10</sub>) and Summer (PM<sub>10</sub>). NO<sub>x</sub> does not show the same maximums so it can be assumed that the sources of the high PM concentrations are not due to road traffic. As particle

suspension can increase with increasing wind speed, this could be due to sea spray from the east coast or particles from spoil heaps, wind blown dust or similar. It may also reflect an agricultural source to the east of the site, and this would coincide when ammonia emissions are generally at their highest from muck spreading.

There appear to be some sources of NO<sub>x</sub> which were not present in previous reports; these are visible in the spring and summer and at higher wind speeds. From map analysis there does not seem to be obvious new source of this NO<sub>x</sub>, that was not there previously.

### 5.3.2 Little Plumpton detailed analysis

#### 5.3.2.1 METRICS

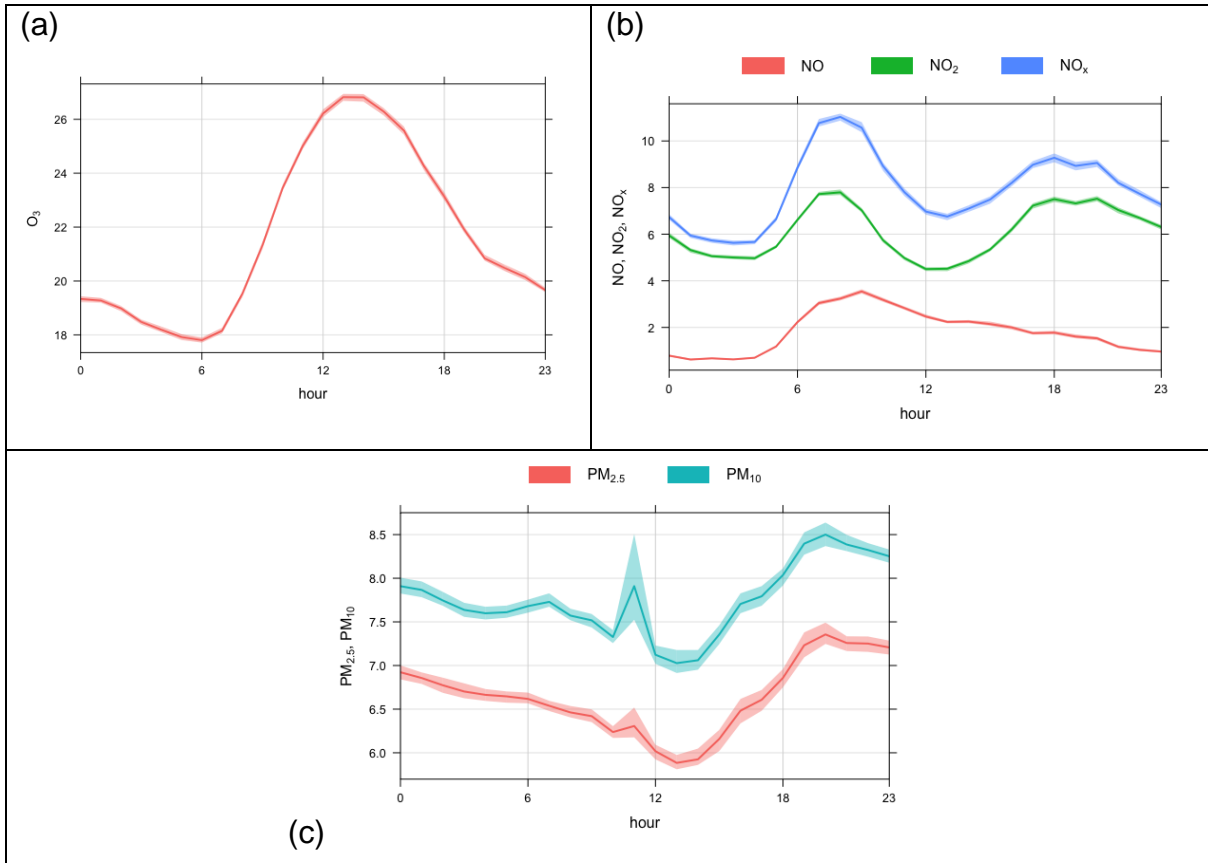
Table 23 reports those metrics by individual wind sector. These are very similar to the Phase III results and same conclusions are drawn. There is a slight reduction in the PM average concentrations for air arriving from the S. Air flow from the SE has the highest NO<sub>x</sub> and PM measurements once more. The LP site also has the influence of the major road that is to the south of the site and its influence can be clearly seen in the NO<sub>x</sub> and PM measurements from those wind sectors.

**Table 23. Phase IV wind sector averages at LP.**

	N	NE	E	SE	S	SW	W	NW
O <sub>3</sub> (ppb)	20.3	20.8	19.1	16.1	20.2	24.8	25.0	27.051
NO (ppb)	0.9	1.2	2.1	3.2	2.2	1.0	2.0	0.6920
NO <sub>2</sub> (ppb)	4.3	5.5	9.1	11.0	6.9	2.6	3.9	2.616
NO <sub>x</sub> (ppb)	5.2	6.7	11.3	14.2	9.1	3.6	5.8	3.308
PM <sub>2.5</sub> (µm/m <sup>3</sup> )	4.9	6.8	10.9	9.7	5.6	4.3	4.3	4.140
PM <sub>10</sub> (µm/m <sup>3</sup> )	5.3	7.8	12.0	10.9	6.8	5.6	5.4	5.142
H <sub>2</sub> S (ppb)	0.4	0.5	0.7	0.6	1.8	0.6	0.4	0.4
SO <sub>2</sub> (ppb)	0.8	0.8	0.9	1.5	1.3	1.1	1.1	0.9

#### *Diurnal variation of air pollution at LP*

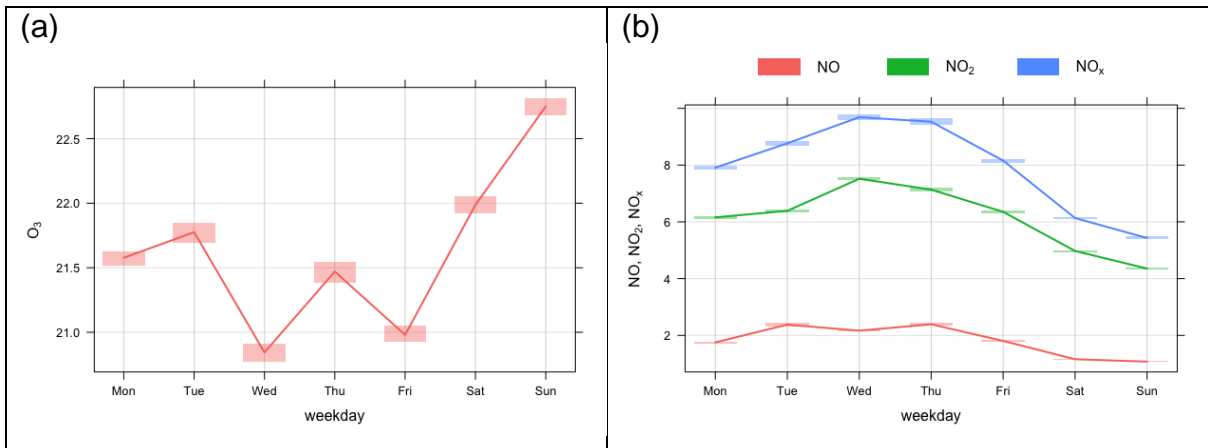
All diurnals are similar to those observed in Phase III except the PM which has a spike just before midday, and may be the influence of a small number of high concentration values in the data set. This is not seen in the NO<sub>x</sub> diurnal so is unlikely to be traffic related (Figure 117). As previously, the O<sub>3</sub> diurnal is lowest at night and peaks just after midday, as previously discussed this is expected in the context of UK oxidative air chemistry. The NO<sub>x</sub> diurnal at LP is heavily influenced by road traffic, with NO<sub>x</sub> increasing in the morning, due of the boundary layer and local traffic sources. The early evening peak is again due to the evening rush hour.



**Figure 117. Diurnal variations at LP for (a) O<sub>3</sub> (b) NO<sub>x</sub> and (c) PM. © University of York (2019).**

*Hebdomadal variation of air pollution at LP*

As in previous reports, the working week is clear in the NO<sub>x</sub> and PM measurements, highest during the week and decreasing at the weekend (Figure 118). Conversely ozone peaks on Sundays, a result of lower titration from NO.



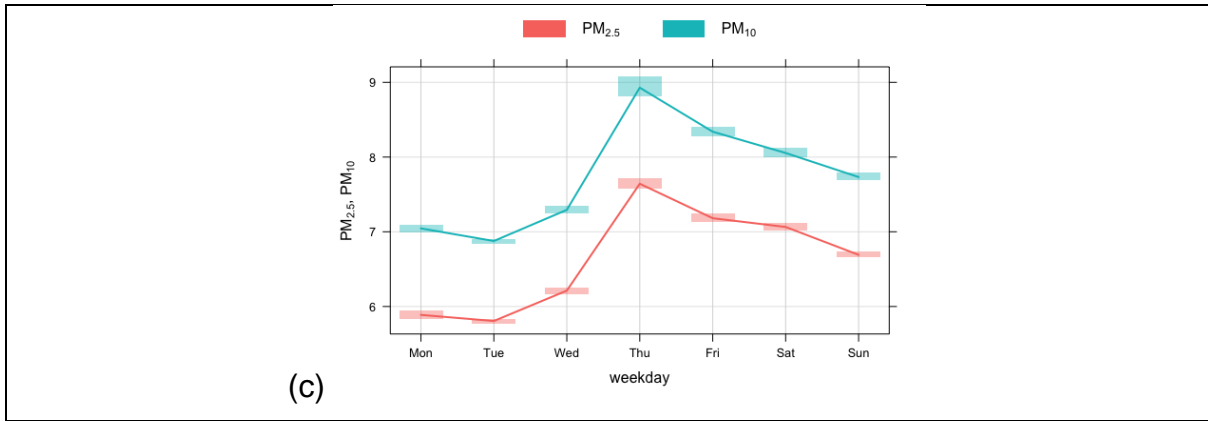


**Figure 118. Hebdomadal Cycles at LP for (a) O<sub>3</sub> (b) NO<sub>x</sub> and (c) PM. © University of York (2019).**

*Annual variation of air pollution at LP*

These show typical cycles in the context of UK air quality as discussed in the KM section earlier (Figure 119). However, it is worth noting that in the Phase IV observations PM is lower in the summer months and both PM and NO<sub>x</sub> have a steeper increase in September. As hydraulic fracturing operations started at the PNR site began in October 2018, this period will be investigated further.

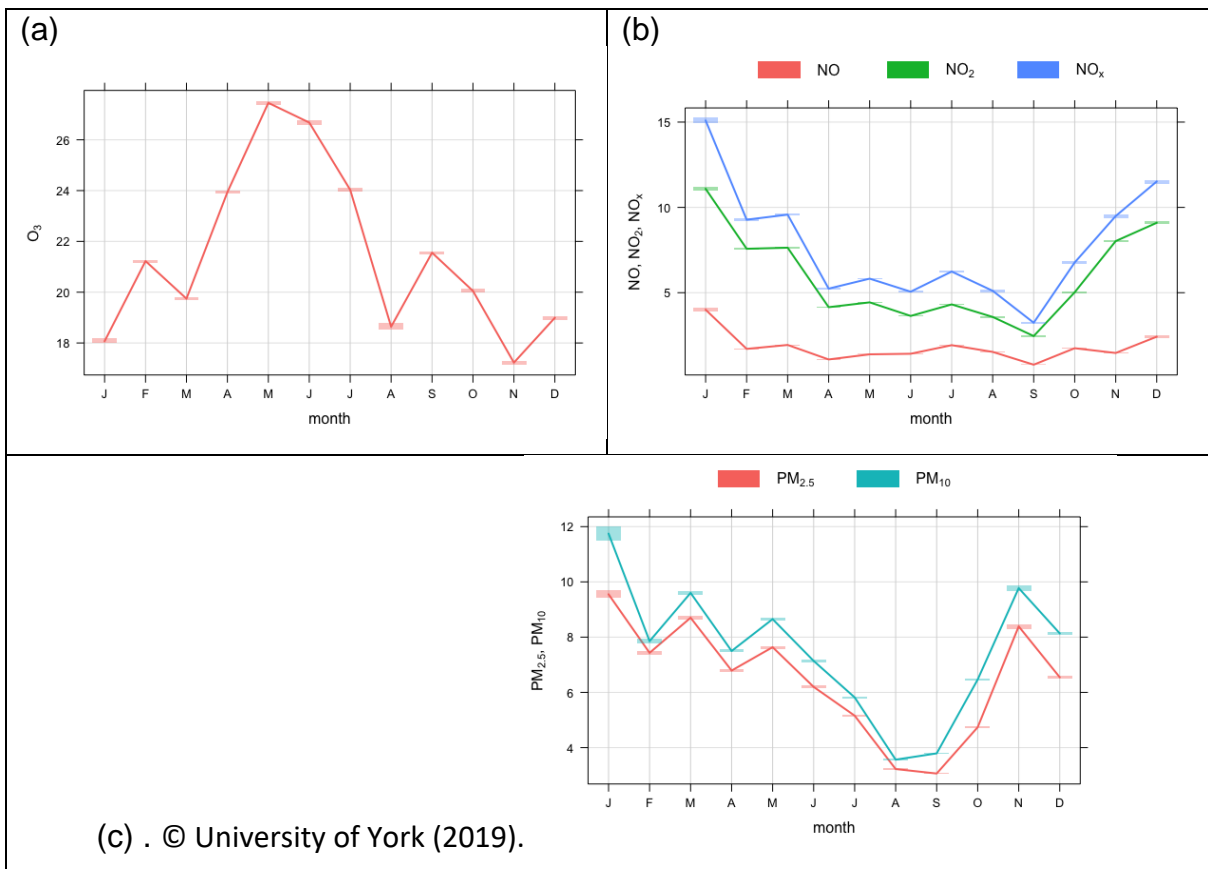


**Figure 119. Annual cycles at KM for (a) O<sub>3</sub>, (b) NO<sub>x</sub> and (c) PM**

### Source Locations for LP

NO<sub>x</sub> sources are seen to the south east of the site. This is attributed to road transport, and this is also true for the PM observations (Figure 120). There does not appear to be an additional strong source to the west of the site when hydraulic fracturing was taking place (October - December) in contrast to the observations at KM where NO<sub>x</sub> was enhanced during pre-hydraulic fracturing operations. The LP monitoring site is further away from the shale well-site than at the KM and this will have some influence in determining the detectability of emissions. The local LP environment in general also more polluted than at KM, making small incremental increases difficult to discern.

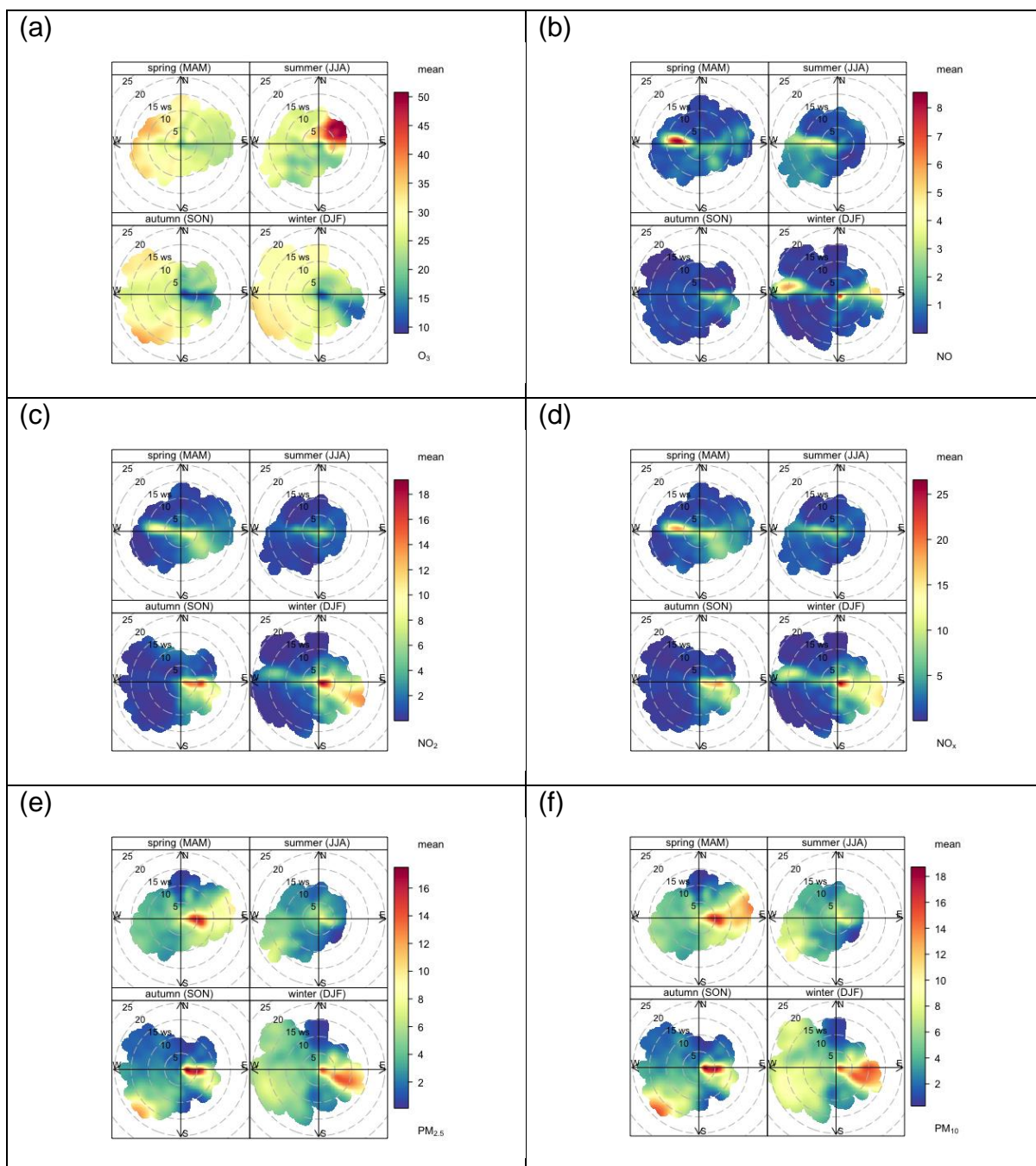


**Figure 120. Polar plots for LP (a) O<sub>3</sub>, (b) NO (c) NO<sub>2</sub>, (d) NO<sub>x</sub>, (e) PM<sub>2.5</sub>, (f) PM<sub>10</sub>. © University of York (2019).**

The enhanced concentrations of PM to the south east of the site has been visible in previous data, which will be local influence as well as the enhanced regional PM sources in Easterly air masses. The higher concentrations of PM at highest SW windspeeds may be due to the influence of the Atlantic air masses, especially in the coarser fraction.

The largest difference between the two phases appears in O<sub>3</sub> which has higher values in in the summer 2018. This is due to a more limited dataset in Phase 3 as the instrument was offline during June and July when the highest concentrations are expected due to photochemical production of O<sub>3</sub> in high temperatures and anticyclonic conditions.

The polar plot for H<sub>2</sub>S (Figure 121) shows one source area which is to the east of the monitoring station, with no source to the west where the well site is situated. This ties in with the information from Cuadrilla that sour gas (H<sub>2</sub>S rich gas) was not expected from the well-site.

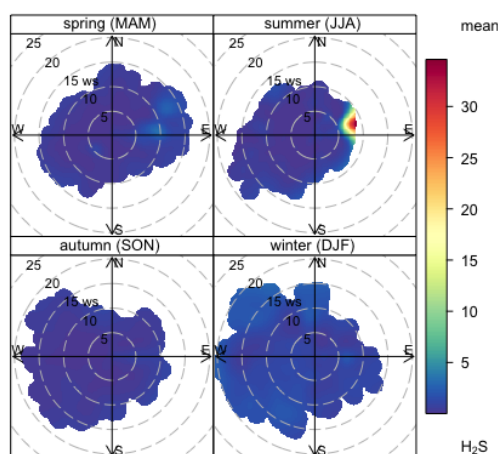


**Figure 121. Polar plot for H<sub>2</sub>S in LP. © University of York (2019).**

### 5.3.3 Non methane hydrocarbons at KM and LP

Non methane hydrocarbon (NMHC) samples have been taken on a weekly basis at both sites. A summary of NMHC for KP and LP is shown in Table 24 and Table 25. NMHCs can give an indication of air mass origin, in areas of oil and gas production higher lighter alkanes such as ethane and propane may be due to fugitive emissions. Alkanes are saturated hydrocarbons including methane, ethane, propane, and higher members. In cases where the observed value was below the minimum detection limit, half this value was used in averaging (0.005 ppb).

Mean hydrocarbon mixing ratios at KM are generally lower than at LP. At both sites alkanes had the highest mean and maximum values. LP seems to show more variation between the highest and lowest observed mixing ratios compared to KM. From Figure 122 median values are largely similar between the two sites, however the maximum values are much higher at LP, which has the effect of increasing the mean mixing ratio but is excluded in the median. In particular, n-pentane and iso-pentane were unusually high at LP during April and September respectively. During April 2018, high values of ethane, propane and butanes were also observed. However, in September enhancements in other species were much smaller, meaning at present the source of the sharp increase in iso pentane is unclear.

**Table 24. Summary of NMHC measurements for 2018 at KM, N = 36. All NMHC have an uncertainty of < 10%**

Hydrocarbon	Phase IV Mean (ppb)	Minimum Value (ppb)	Maximum Value (ppb)
Ethane	2.4	0.8	7.0
Ethene	0.6	0.2	1.5
Propane	1.5	0.2	9.7
Propene	0.2	0.02	0.9
Isobutane	0.5	0.05	2.8
N-butane	0.6	0.07	4.4
Isopentane	0.5	0.03	5.7
N-pentane	0.2	0.02	1.8
Benzene	0.2	0.05	1.6
Toluene	0.2	0.03	1.2

**Table 25. Summary of NMHC measurements for 2018 at LP, N = 37. All NMHC have an uncertainty of < 10%.**

Hydrocarbon	Phase 4 Mean (ppb)	Minimum Value (ppb)	Maximum Value (ppb)
Ethane	3.4	1.1	5.6
Ethene	0.7	0.2	1.7
Propane	3.1	0.3	20.4
Propene	0.3	0.01	1.5
Isobutane	1.3	0.06	7.1
N-butane	1.6	0.1	11.0
Isopentane	3.6	0.05	37.5
N-pentane	2.4	0.04	34.9
Benzene	0.6	0.08	5.4
Toluene	0.9	0.03	6.3

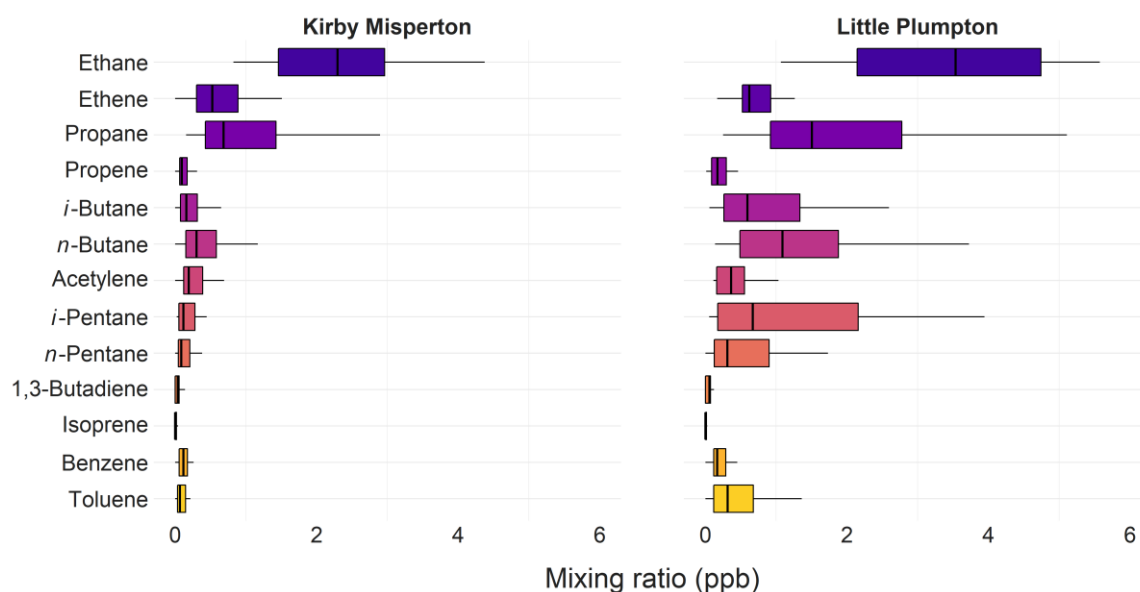


**Figure 122. Selected hydrocarbon boxplot of annual hydrocarbon mixing ratios measured at KM and LP during phase 4 (2018). Vertical bars are median values. The left and right edges of the box correspond to the 25<sup>th</sup> and 75<sup>th</sup> percentiles respectively. The horizontal whiskers show the largest or smallest values no further than 1.5 times the interquartile range respectively. Data beyond the end of the whiskers are not included here. © University of York (2019).**

Figure 123 highlights the seasonal cycle in hydrocarbon mixing ratios. The highest values are generally observed in the winter months where the boundary layer is shallow and oxidation is slowest, and decreases in the summer months when the boundary layer is deeper and oxidation rates are faster. Mixing ratios peak during March 2018, with enhancements in acetylene, 1,3-butadiene and toluene, which are typically associated with vehicle emissions.

The seasonal cycle at LP, shown in Figure 124, appears less pronounced than at KM due to a greater effect from local road traffic sources. High mixing ratios were observed throughout Spring 2018 during the preparation stage of the hydraulic fracturing cycle. Similar to KM, minimum values of most hydrocarbons were observed during the summer months, when the oxidation is most rapid. During the latter half of 2018, hydraulic fracturing commenced at LP. Maximum values of the aromatic compounds toluene and benzene were observed during May 2018, however other compounds do not appear to show this trend and so more analysis is required to understand these enhancements. It is understood that propane was added to the flare gas (shale gas recovered during on-site operations) to aid combustion, however any increases in propane emissions are not evident in the hydrocarbon data shown here. Propane mixing ratios peaked during April 2018 and were much lower during winter 2018 when flaring would have occurred.

However, it is worth noting that hydrocarbon samples are collected once per week, between 9:30 am – 11:30 am on a Monday. Whilst this type of sampling is enough to identify changes in mixing ratios as a response to changes in broad atmospheric conditions throughout the year, it is unlikely to be of a sufficient time resolution to pick up enhancements due to short-term events happening on the shale gas site itself. In addition to this, although the monitoring station is positioned downwind of the predominant wind direction of the gas well site, any specific events will only be possible to identify provided the wind direction transports air from the exploration site to the monitoring station.

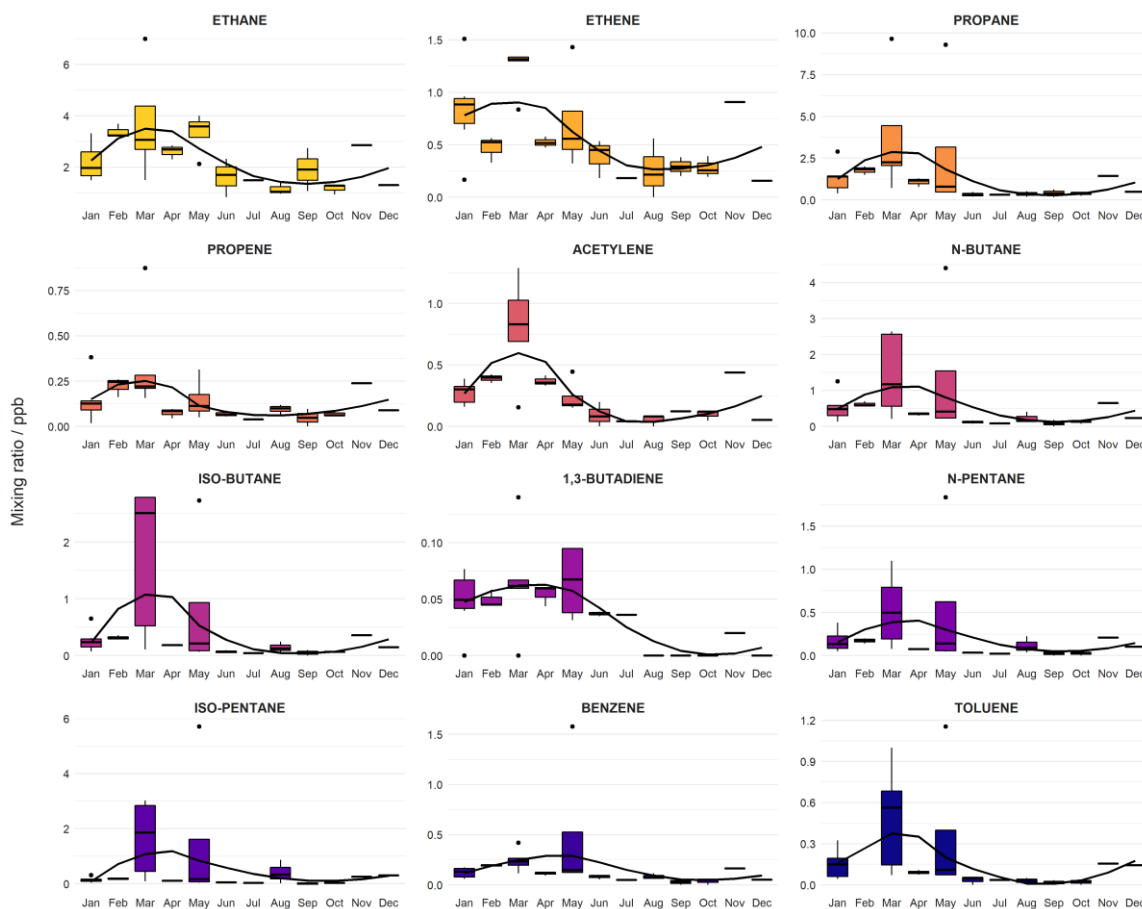


**Figure 123. Monthly variation in selected hydrocarbons at KM for 2018. © University of York (2019).**

*Breakdown of activities at LP*

As hydraulic fracturing has now taken place at LP it is possible to look at the different phases of the operational cycle, the dates for these periods are explained in **Error! Reference source not found.**

**Table 26. Breakdown of the recent operation cycles at PNR**

Dates	Period	Explanation
1/2/16 – 4/1/17	Baseline	No activity was happening at the PNR site
5/1/17 – 16/8/17	Preparation	The PNR site was being cleared and prepared for drilling to take place
17/8/17 – 17/7/18	Drilling	Two vertical and horizontal wells drilled at PNR
18/8/18 – 14/10/18	Pre-operation	Drilling completed and hydraulic fracturing equipment brought on site
15/10/18 – 31/1/19	Hydraulic fracturing	Hydraulic fracturing began at the site

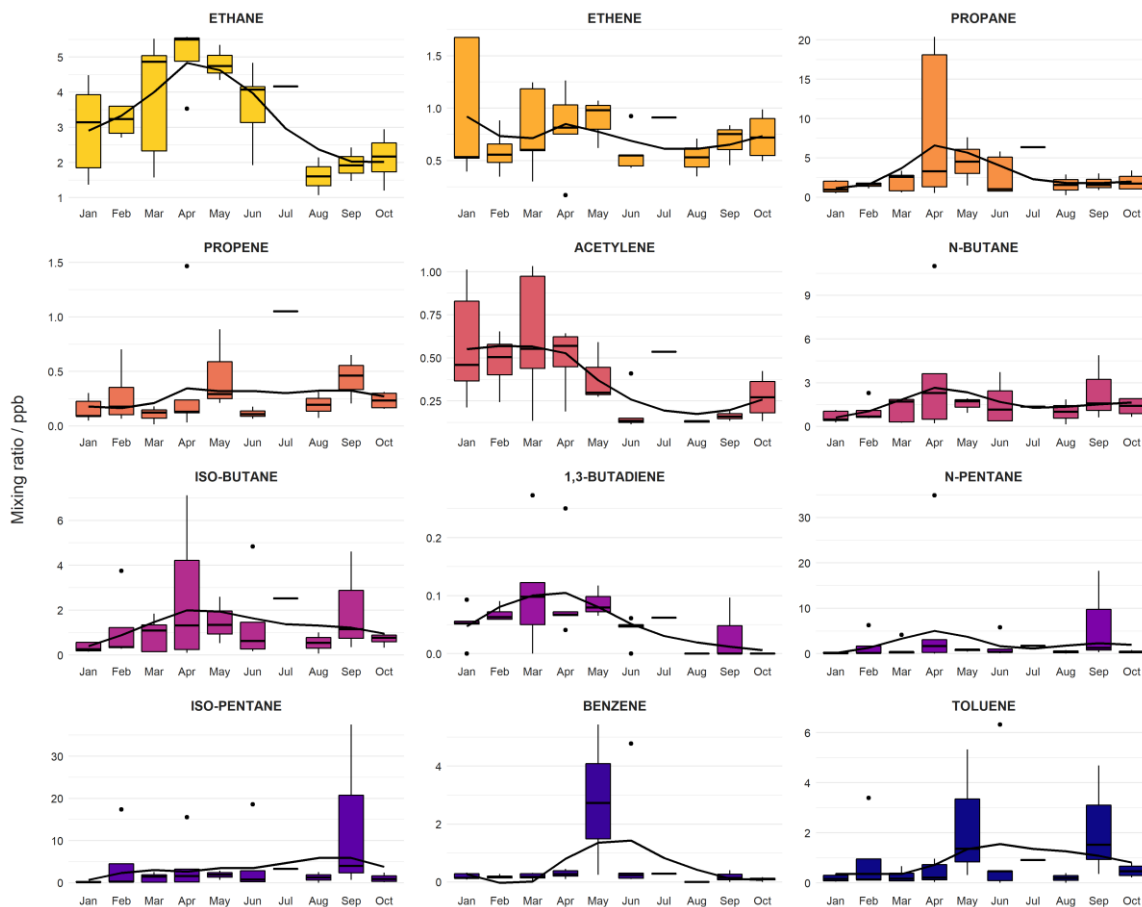


**Figure 124. Monthly variation in selected hydrocarbons at LP for 2018. © University of York (2019).**

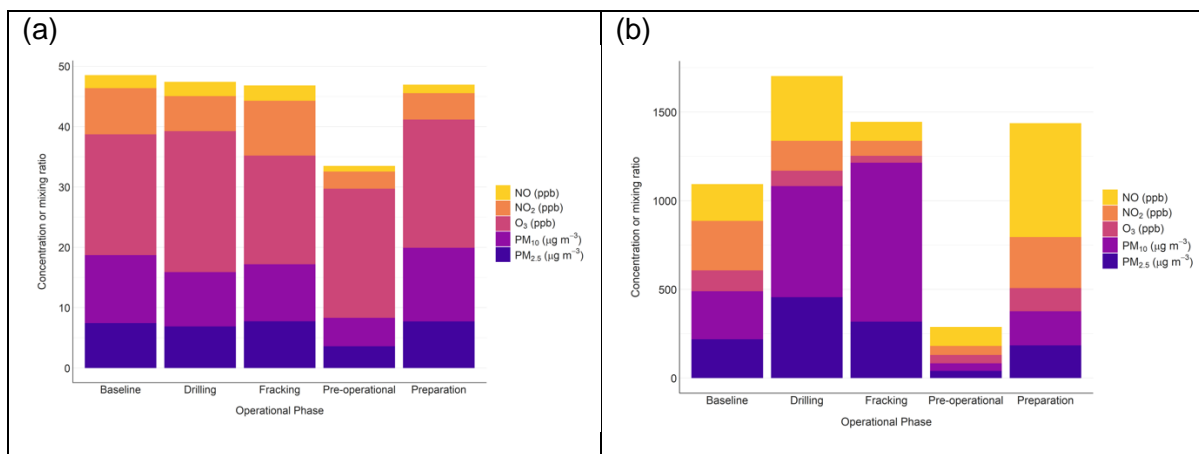


**Figure 125. Baseline concentrations compared against four distinct operational phases (a) period mean values (Error! Reference source not found.) over each period and (b) 1-minute maximum peak values during each period. © University of York (2019).**

The hourly average for each air pollutant has been calculated for the five distinct periods along with the maximum values (the maximum value for the hourly dataset for the period) and these are shown as a cumulative air pollution amount in Figure 125.

There are no major differences in the period-averaged values for the five different stages, with little difference in air quality values between the baseline period, and subsequent activity phases on site. A different picture emerges when just the minute peak maximum values for each period are considered. NO<sub>x</sub> maximum values are higher during some phases than the baseline period for, notably preparation and drilling whilst highest PM maximum values were seen during the hydraulic fracturing and drilling phase.

Due to the differing times during the year that these individual operational phases occurred it care is needed in drawing exact like-for like comparisons, since some seasonal effects are likely to be overlaid. The hydraulic fracturing occurred over the 4 months in winter whereas the baseline and drilling period was over a whole year. To attempt to correct for this, data was taken from previous corresponding baseline periods, measurements taken at the same time of year as the hydraulic fracturing and the drilling periods. The dates for the new analysis period are shown in Table 27.

**Table 27. Breakdown of time periods of different phases used to compare Drilling and Hydraulic fracturing against baseline conditions from similar periods in a previous year at LP**

Dates	Period	Explanation
15/10/16 – 31/1/17	Baseline	No activity was happening at the LP site
15/10/17 – 31/1/18	Drilling	Two vertical and horizontal wells drilled at LP
15/10/18 – 31/1/19	Hydraulic fracturing	Hydraulic fracturing began at the site

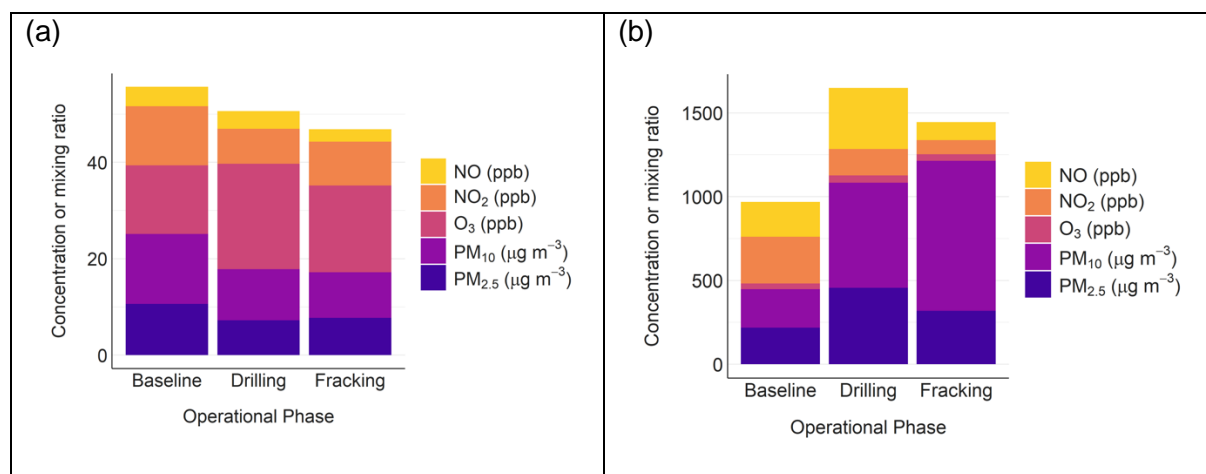


**Figure 126. Two LP operational phases compared to the corresponding baseline period from the previous year (a) period-averaged values and (b) 1-minute maximum concentrations. © University of York (2019).**

Figure 126 shows that there is no indication of large-scale enhancements in air pollution during either the drilling or hydraulic fracturing phases, when taken as an average concentration over that period of activity and compared to the corresponding baseline period from the previous year. The maximum observed values, as represented by the highest observed 1-minute concentration during each phase (and previous year's corresponding baseline) are higher during the drill and hydraulic fracturing phases, largely through an enhancement in PM.

The LP monitors are to the west of the well-site so if observations are influenced by activity at the well-site the wind direction must be broadly westerly in direction. The air quality data was subsequently filtered to only show those observations when the measurements were influenced by the well-site (defined as any air mass coming from the NW, W or SW). The results of this filtered analysis are shown in Figure 127. As previously, when an average is taken over the full period of each phase, there is no indication of any significant increase in air pollution during drilling or hydraulic fracturing. When the maximum minute values are considered, there are some enhancements in maximum values during the drill and hydraulic fracturing phases.

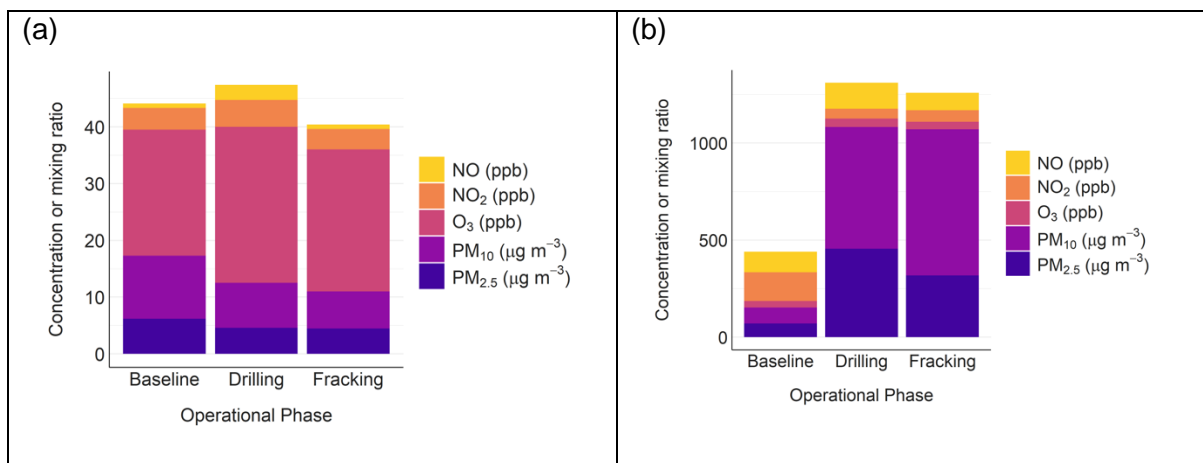


**Figure 127. A comparison of previous baseline values (2017), drill and frack phases filtered for air masses from NW, W and SW that passed over the well-site before arriving at the monitors. (a) average values for representative baseline period and each phase and (b) maximum 1-minute values for baseline and each phase. © University of York (2019).**

#### 5.4 METHANE EVENT AT LP

As described in Section 4 of the report (atmospheric composition), methane enhancements were observed at the monitoring station and were associated with wind passing over the LP site towards the monitoring station. A major event took place between 11 and 17 January 2019. The event is now known to have been a release of methane to air as a result of the gas not igniting in the flare stack.

Initial analysis shows that the NO<sub>x</sub> concentrations show a similar profile to the methane measurements (Figure 128). It is thought the NO<sub>x</sub> source may be from the exhaust emissions of pumping systems used at the site. The peak NO<sub>2</sub> (40 ppb) was at 08:30. PM measurements do not show similar enhancements for this period.

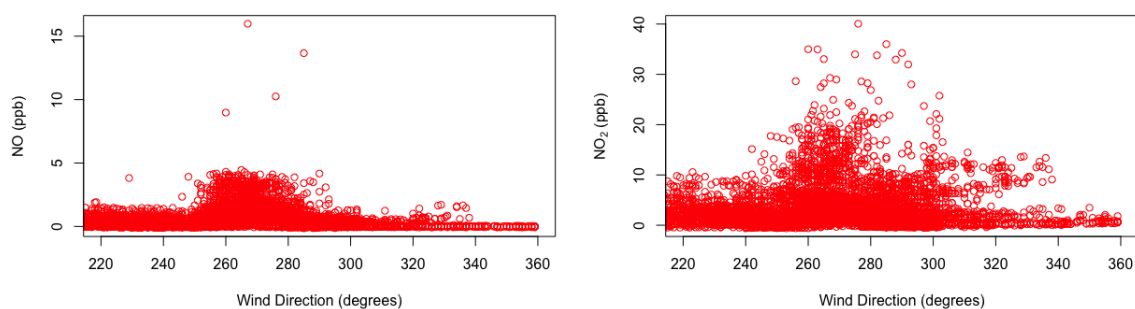


**Figure 128. NO and NO<sub>2</sub> from the 11 – 15<sup>th</sup> January 2019 methane enhancement was observed at the LP monitoring station. © University of York (2019).**

There was no enhancement of H<sub>2</sub>S observed during this period, with concentrations typically 2 ppb or below (Figure 129).

University of York are working with University of Manchester to investigate this event further.

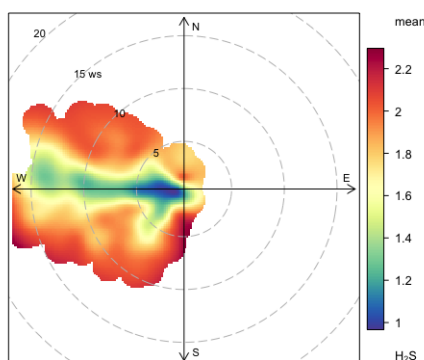


**Figure 129. H<sub>2</sub>S measurements during the LP event. © University of York (2019).**

## 5.5 MOBILE SURVEYS

In October 2018 the WASP (WACL Air Sampling Platform), shown in Figure 130 and Figure 131, was available for use. A Nissan NV400SE L3H2 was modified in order to make it suitable for mobile air quality measurements. The rear of the van was fitted with a refrigeration system capable of temperatures between -18 °C and +18 °C and 50 mm of insulation was fitted throughout. The overall interior dimensions are length 3450 mm x width 1650 mm x height 1750 mm and the approximate payload is 1000 kg. A front facing sample inlet, 2 m off the ground was fashioned using approximately 6 m of PTFE tubing with an outside diameter of 1/2 inch. A pump draws air from outside at a flow rate of around 40 L min<sup>-1</sup> through the inlet, from which scientific instruments mounted within a standard 19-inch rack sample from at the specific flow rate required. Gas phase measurements of O<sub>3</sub>, NO<sub>2</sub>, H<sub>2</sub>S, CH<sub>4</sub>, CO<sub>2</sub> and C<sub>2</sub>H<sub>6</sub> (ethane) were made using the instruments listed in Table 28.



**Figure 130. WACL Air Sampling Platform at the KMA Monitoring Site. © University of York (2019).**

**Table 28. WASP instrumentation**

Pollutant	Instrument	Precision	Measurement Period
O <sub>3</sub>	2B Technologies Model 202 Ozone Monitor	2 % of reading above 1.5 ppb	0.1 Hz
NO <sub>2</sub>	Teledyne Model T500U CAPS NO <sub>2</sub> Analyser	0.5% of reading above 5 ppb	1 Hz
H <sub>2</sub> S	Teledyne Model T101 UV Fluorescence H <sub>2</sub> S Analyser	0.5% of reading above 50 ppb	0.05 Hz
CH <sub>4</sub> , CO <sub>2</sub>	Los Gatos Research Ultra Portable Greenhouse Gas Analyser (UGGA)	< 2 ppb	1 Hz
Ethane	Aerodyne Research QC-TILDAS Ethane Monitor (ICL)	0.05 ppb	1 Hz

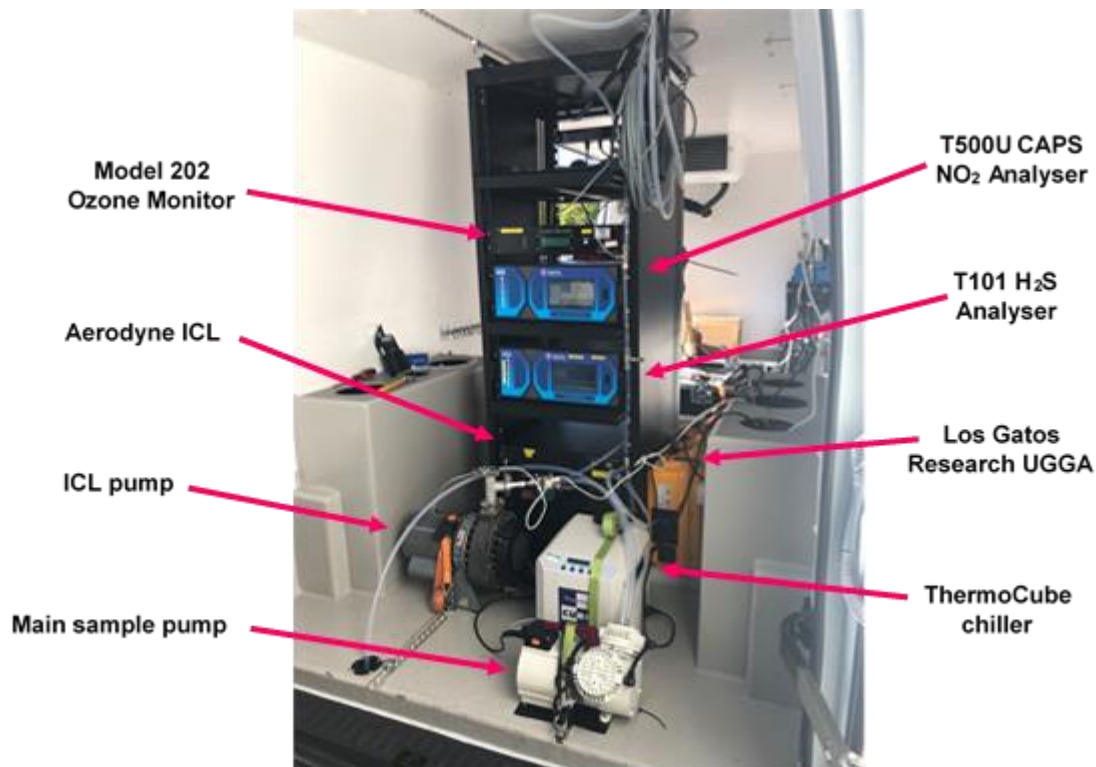


**Figure 131. Instrument layout in the van.. © University of York (2019)**

In October 2018 Cuadrilla confirmed that hydraulic fracturing (fracking) had begun at the Preston New Road shale gas exploration site and was expected to last approximately three months. In addition to the permanent monitoring station housed 0.3 km east of the site, a number of mobile surveys were conducted in an attempt to measure any emissions as a result of hydraulic fracturing operations. The route was chosen to include a loop directly around the site as well as additional smaller loops to evaluate the local background.

A difficulty with the analysis was limited knowledge on the timing of specific activities being undertaken at the site. On days that the van was available and there was hydraulic fracturing taking place, the short duration of each phase of testing meant that operations had ceased before the van could be fully deployed.

Two surveys were conducted on consecutive days with the aim of identifying key emissions sources in the area, with the potential of observing a plume from the site itself. Figure 132 and Figure 133 show the route taken on each day. For both surveys, consistent sources to the Southeast and Southwest of the site were present despite opposite wind directions, suggesting this is independent of the site. On 17th October 2018, enhancements in CH<sub>4</sub> and ethane were seen to the North of the site. No ethane, CO<sub>2</sub> or NO<sub>2</sub> was present in this plume, suggesting this is emissions from cattle farming in the area as observed and not as a result of combustion.

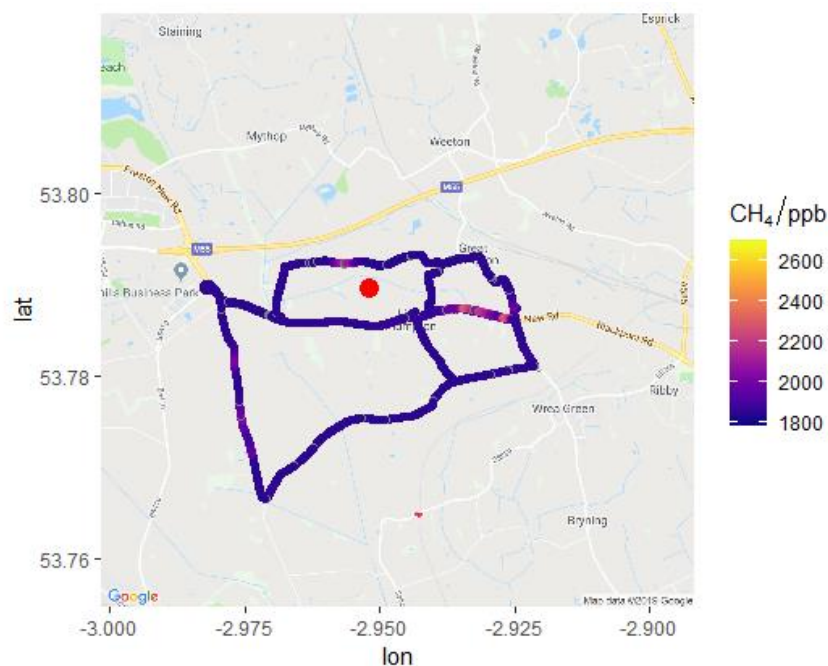


**Figure 132. Drive track coloured by CH<sub>4</sub> on 17/10/18. The red circle designates the position of the shale gas site. © University of York (2019).**

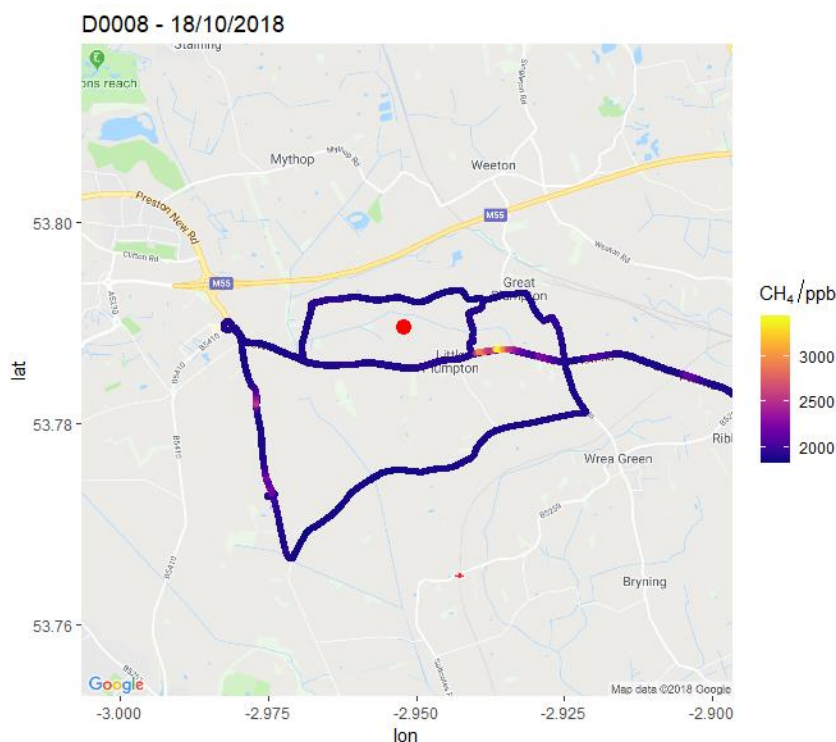


**Figure 133. Drive track coloured by CH<sub>4</sub> on 18/10/18. The red circle designates the position of the shale gas site. © University of York (2019).**

Figure 134 shows the observed time series of pollutants on 17th October 2019. All enhancements in ethane corresponded to enhancements in CH<sub>4</sub>, however there were some notable peaks of CH<sub>4</sub> that were not correlated with ethane, CO<sub>2</sub> or NO<sub>2</sub>, suggesting at least two different source contributions, possibly including a biogenic source. Enhancements of CH<sub>4</sub> are

not well correlated with CO<sub>2</sub>, however in general CO<sub>2</sub> plumes contained some NO<sub>2</sub>, indicating a combustion source, likely to be traffic emissions along Preston New Road. From these drives it is unlikely that any potential emissions from the site were captured, however the main purpose of this was to test the setup of the mobile monitoring platform which performed well throughout. The position of some key sources in the area were established, which can be compared to any future surveys. Data from the permanent monitoring station can also be compared to mobile observations, which could help to distinguish regional and local sources.

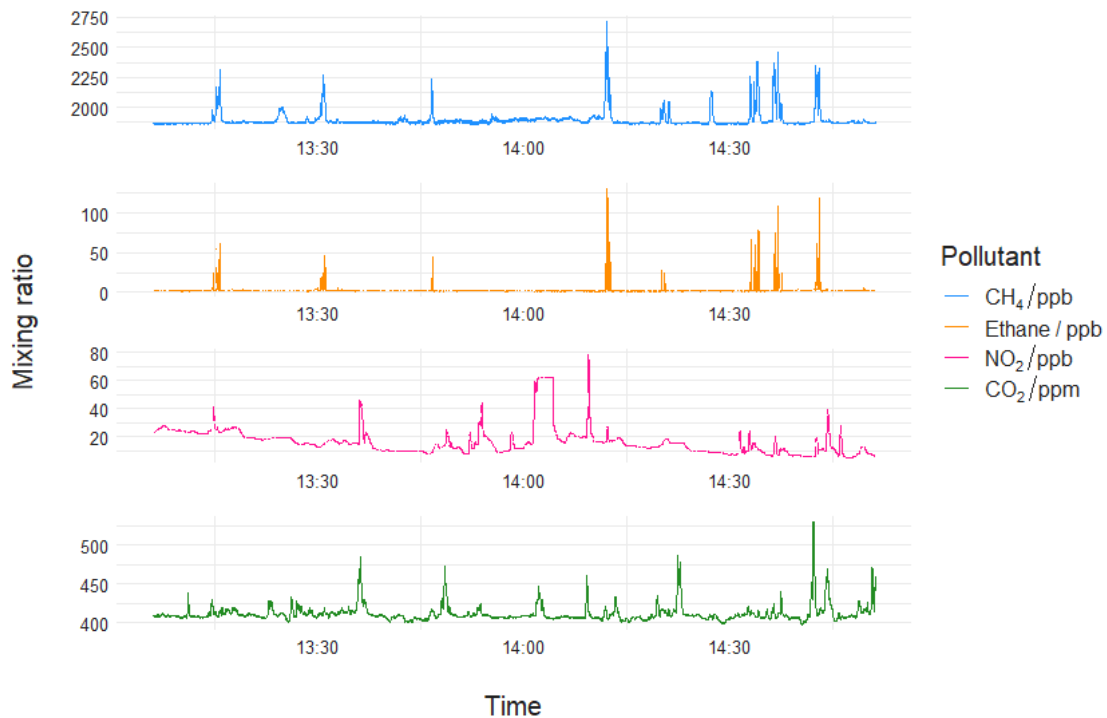


**Figure 134. Measured mixing ratios of pollutants throughout the survey of the hydraulic fracturing site on 17/10/18. © University of York (2019)**

## 5.6 CONCLUSIONS

Data at KM has continued to be collected but there has been no further activity by the shale gas operator in the area since the last report. The measurements can therefore continue to be classed as baseline. A research paper has been published on the effects of pre-hydraulic-fracturing at KM in April 2019 (Purvis et al, 2019).

As hydraulic fracturing has taken place at LP it has been possible to evaluate the effects of various different periods of activity in terms of air quality changes measured downwind. Local changes in air quality were much less pronounced than seen during the pre-operational phase at LP. The relative complexity of sources in that region, coupled to a monitoring site further away from the well-site that at KM, means the data needed to be filtered by wind direction first to identify any potential effects during drilling or hydraulic fracturing periods. As the hydraulic fracturing operations took place over a 3-month period in the winter, seasonality could have an impact when looking at changes over the baseline. In this analysis we have gone back to previous years of baseline measurement to create a directly comparable seasonal climatology

against which the operational periods could be compared, highlighting the critical importance of long-term baseline measurement prior to activities beginning.

From the observations made, there were no measured exceedances of any national air-quality limits at LP during the period of hydraulic fracturing, and no significant differences seen in averaged air quality over the period of drilling when compared to a similar climatological period of baseline from the year before, although there was an increase in maximum values. During the hydraulic fracturing and drilling phases at LP, the maximum minute values were enhanced when wind direction was from the west. This is likely to be from activity on site.

During the methane emission event at LP on January 2019, increases in NO<sub>x</sub> were detected for the same time period and wind direction. However, this was to maximum values of only 30 ppb, well below the short-term 1-hour limits value. PM was not affected. Further work is being carried out to investigate these findings.

Although mobile measurements were made around LP it was difficult to coordinate with site activities as the authors were not provided with this information in advance. To make measurements of this kind more meaningful, the authors recommend that the mobile laboratory be located in the shale gas area for a specific time period, other supporting measurements carried out at the same time (isotopic ratios, UAV measurements, soil gas) and information on proposed site activities provided in the form of advance reports of the next day's planned activities.

## **5.7 REFERENCES**

Purvis *et al.*, Effects of 'pre-fracking' operations on ambient air quality at a shale gas exploration site in rural North Yorkshire, England, Science of the Total Environment, 2019

# 6 Radon

## 6.1 INTRODUCTION

Radon,  $^{222}\text{Rn}$ , a radioactive, colourless and odourless gas with a half-life of 3.82 days is the largest source of radiation exposure for most of the UK population and is the second highest cause of lung cancer after smoking (Darby et al., 2005).

Public Health England (PHE) reviewed the potential public health impact of possible chemical and radiological pollutants resulting from shale gas activities in 2014 (PHE-CRCE-009). The PHE review recognised that radon would be released to air but expected this to be at a low concentration. PHE could not envisage a plausible mechanism in which shale gas extraction processes could significantly change the amount of radon entering properties from the ground. PHE also recognised, however, that people might measure radon in their home after such activities start and miss-attribute any high levels to the shale gas activities rather than from existing natural sources. Radon measurements in outdoor air and in homes were recommended, in order to assess the baseline and provide evidence on radon distributions before shale gas extraction began.

The Vale of Pickering is an area which has been selected for shale gas extraction. Whilst the majority of the area of the Vale does not have naturally elevated radon potential, there are areas of naturally elevated radon potential, called radon Affected Areas, at around 5 to 8 km to the north and to the south of the proposed site (KMA). In radon Affected Areas at least 1% of homes are expected to have radon levels at or above the UK Action Level of  $200 \text{ Bq m}^{-3}$ . To determine the effect (if any) of shale gas extraction on levels of radon, baseline monitoring of radon levels within these radon Affected Areas is required prior to commencement of shale gas extraction in order to compare with results at the same locations after shale gas extraction has begun. PHE has been monitoring indoor and outdoor radon levels at various locations in the Vale of Pickering since October 2015.

Indoor radon concentrations exhibit diurnal, monthly and seasonal variation (Miles and Algar, 1988), thus long-term testing gives a better estimate of the annual average radon concentration. PHE has recruited householders who have agreed to receive standard packs of passive detectors by post for several consecutive periods of 3 months. In addition, each home has been issued a further two passive detectors for householders to carry out monitoring over a longer period of up to a year. Some 121 properties in the Vale of Pickering were included in the fourth phase of the monitoring from April 2018 to March 2019. Measurements in this study follow the PHE Validation scheme (Daraktchieva et al, 2018) for handling, placement and reporting of results for homes.

Outdoor radon levels have been assessed using passive radon monitors very similar to those used routinely in homes. The detectors have been placed in small aluminium-wrapped weatherproof plastic pots in discreet but open-air positions in a number of locations in the Vale of Pickering and also around Oxfordshire (acting as a control). The detectors have been left in position for several consecutive periods of 3 months, or longer, to measure the radon concentrations in the open air.

An active radon monitor (AlphaGUARD) and passive detectors were placed in the enclosure at the KMA site to assess the short-term variation and long-term average radon concentration at the site.

## 6.2 INDOOR RADON MONITORING

### 6.2.1 Results from the four consecutive 3-month tests (December 2017 to December 2018)

Four areas were selected for indoor radon monitoring in the Vale of Pickering: Kirby Misperton and Little Barugh, Yedingham, Pickering and Malton. Pickering and Malton are both areas of established elevated radon potential.

Results from the four 3-month tests covering the period from December 2017 to December 2018 are presented in Table 29. The annual average radon concentrations were calculated employing seasonal correction factors as outlined in the PHE Validation scheme (Daraktchieva et al, 2018).

The distribution parameters assuming log-normality confirm that homes in Kirby Misperton and Little Barugh are situated in areas with low radon potential. The monitoring in the 11<sup>th</sup> period (June 18 - September 18) identified that one house in Yedingham (an area with low radon potential) had a result which was above the UK radon Action Level of 200 Bq m<sup>-3</sup>. The result for the same house in the same period for 2017 was similar. The results for all other periods including the 12<sup>th</sup> period (September 18- December 18) were below the Action Level. It should be noted that there is a small possibility of houses having radon levels above the UK radon Action Level even when they are in the lowest radon probability areas.

Pickering and Malton are situated in areas with higher radon potential (Miles et al, HPA-RPD-033, 2007). Pickering has been confirmed as a radon Affected Area. Malton is also a radon Affected Area but on the third phase of the project there were insufficient properties retained to provide good statistics. To rectify the reduced statistical power more participants were recruited in the autumn 2017. The results from the 11th period (June 18–September 18) indicated that indeed Malton is situated in an area with elevated radon potential.

**Table 29. Range and distribution of estimated annual average indoor radon measurements from December 2017 to December 2018.**

Area (number of homes)	Ninth 3-month reported results (Dec 17-Mar 18) Bq m <sup>-3</sup>			Tenth 3-month reported results (Mar 18-Jun 18) Bq m <sup>-3</sup>			Eleventh 3-month reported results (Jun 18 -Sep 18) Bq m <sup>-3</sup>			Twelfth 3-month reported results (Sep 18 -Dec 18) Bq m <sup>-3</sup>		
	Range	GM	GSD	Range	GM	GSD	Range	GM	GSD	Range	GM	GSD
Kirby Misperton and Little Barugh (25/24/24/21)	10-50	22	1.5	7-70	20	1.6	14-110	35	1.5	17-80	39	1.5
Yedingham, surrounding (25/24/23/21)	7-70	22	1.9	8-120	23	2.1	12-240	42	2.1	12-140	37	1.9
Pickering (37/31/29/29)	6-350	38	2.6	6-170	31	2.5	10-250	48	2.7	9-260	55	2.4
Malton (23/17/19/19)	14-70	33	1.7	12-90	32	1.7	12-200	37	2.0	20-109	48	1.7

GM = geometric mean; GSD = geometric standard deviation

### 6.2.2 Seasonality of indoor radon

Seasonality of indoor radon was studied using the twelve 3-month consecutive measurements in each home, without seasonal correction. Data were only included from the 56 homes where

results were available for all of the measurement periods (November/December 2015 to December 2018).

The average radon concentrations were calculated by combining the results for homes in each of the areas of Kirby Misperton and Little Barugh (KM-LB), Yedingham, Pickering and Malton for each of the measurement periods. The results are presented in Figure 135. From the plot it is evident that homes in Kirby Misperton and Little Barugh, and also in Yedingham showed rather small seasonal variation. The seasonality in Pickering in contrast is well pronounced, however all areas follow the normal UK seasonal pattern with a minimum in summer and maximum in winter (Miles et al, 2012). The number of results for Malton is rather small (only 3 households participated in all of the measurements) compared to the other areas where results were assessed, hence the uncertainty in the results is higher. It should be noted that the average values for each 3-month measurement period for the first year (November /December 2015 to December 2016) show good agreement with the values for the second year (December 2016 to December 2017) and third year (December 2017 to December 2018).

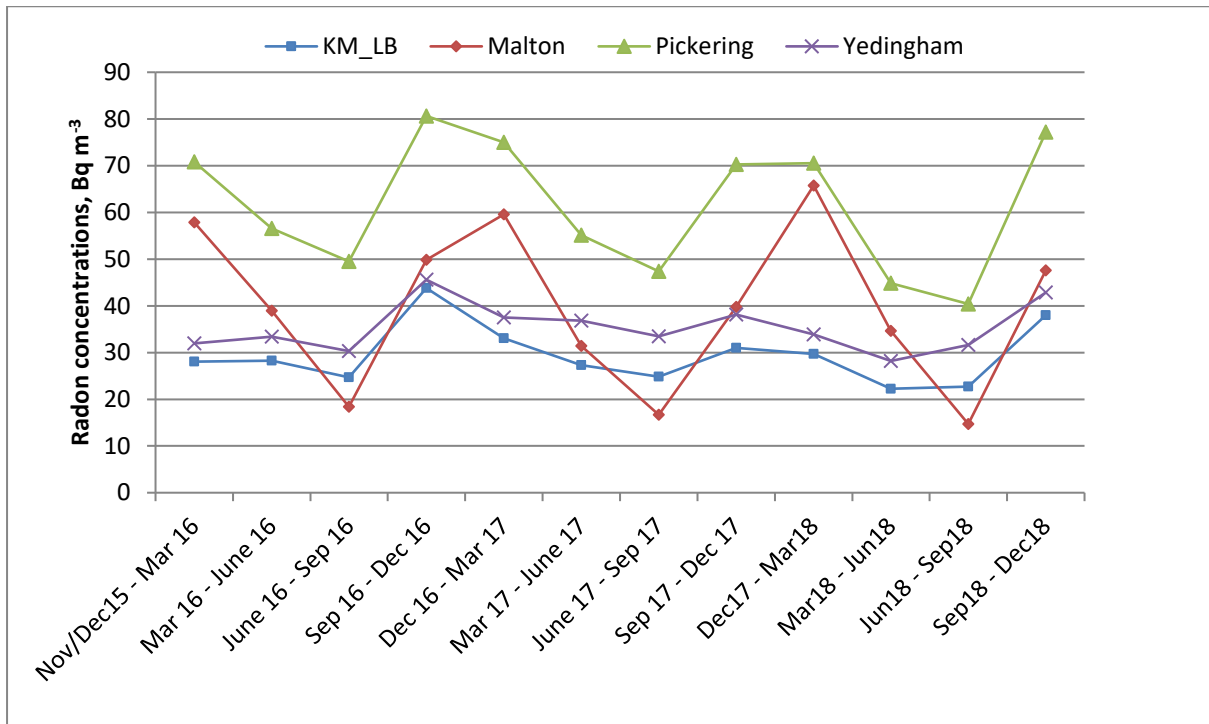


**Figure 135. Seasonal variation of average indoor radon concentrations in the area of Kirby Misperton and Little Barugh (KM\_LB), Yedingham, Pickering and Malton.**  
© PHE (2019)

### 6.3 OUTDOOR RADON MONITORING

Four sites were selected for outdoor radon monitoring in the Vale of Pickering around Kirby Misperton (the area closest to the KMA site), Yedingham (control site), Pickering and Malton (sites in radon Affected Areas). One in Oxfordshire was selected as an additional control. A total of four 6-month and four 1-year passive detectors were used to record radon concentrations at each sampling point since April 2017. The locations of the monitoring points in the Vale of Pickering are shown in Figure 136.

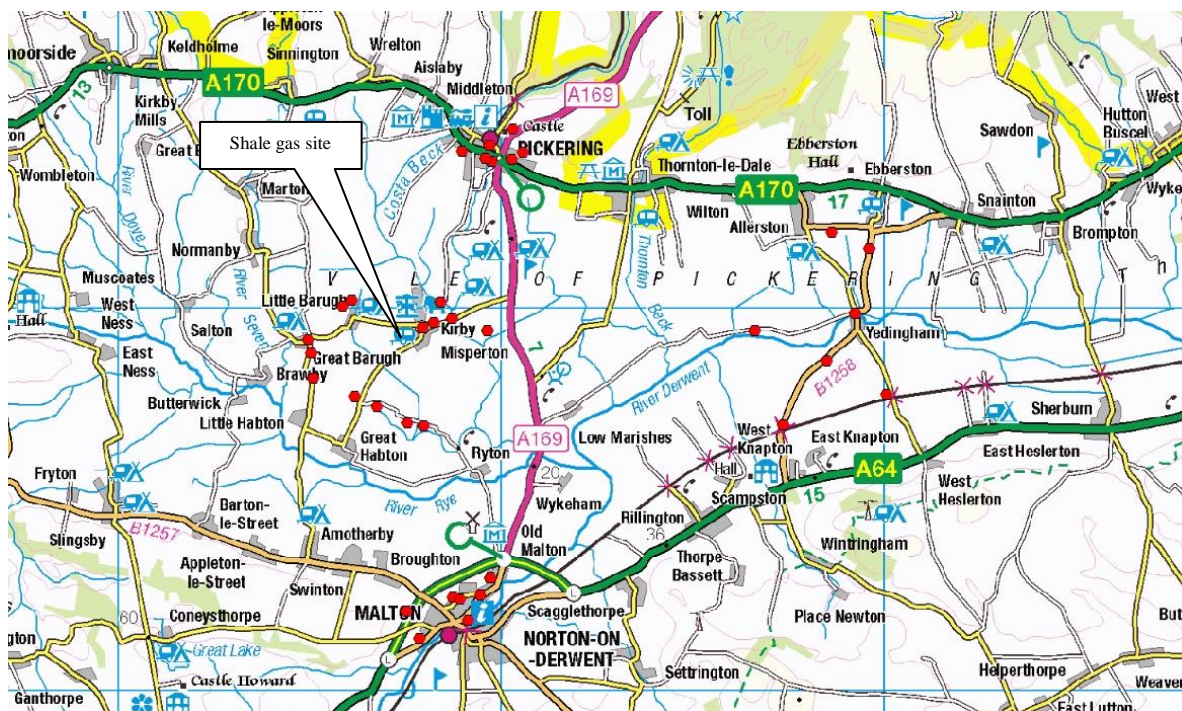


Figure 136. Outdoor radon sampling points in the Vale of Pickering. © PHE (2019)

### 6.3.1 Outdoor measurements in the monitoring period April 2018 to April 2019

In April 2017 the monitoring was changed from 3-monthly to 6-monthly monitoring. The results from the third (April 2018-October 2018) and fourth (October 2018- April 2019) 6-month monitoring periods were plotted and compared with the results obtained from two 1-year tests (April 2017 to April 2018) and (April 2018 to April 2019) where these were available. The information for each sampling point in the area around Kirby Misperton, Yedingham (control area), Pickering and Malton are shown in Figure 137 to Figure 140, respectively. The results for each location for each period were averaged and plotted. It was not possible to obtain results for all sites as some of the detectors were removed or damaged during the measurement period due to vandalism. This was most evident in the Malton area. Some sites where this damage occurred were re-located; for these monitoring points the 1-year monitoring results were not available.

Some of the detectors showed quite high results during the third and fourth 6-month tests, and 1-year test (April 18- April 19). It was noticed that these high results deviated significantly from the results measured with other passive detectors placed at the same locations during the same measurement periods (Figure 137 to Figure 140) which resulted in increased uncertainties of the overall result.

The results from the control area in Oxfordshire are shown in Figure 141. The points were located in private gardens. Monitoring was carried out for 21 months from April 2017 to January 2019. In January 2017 three new participants joined the programme.

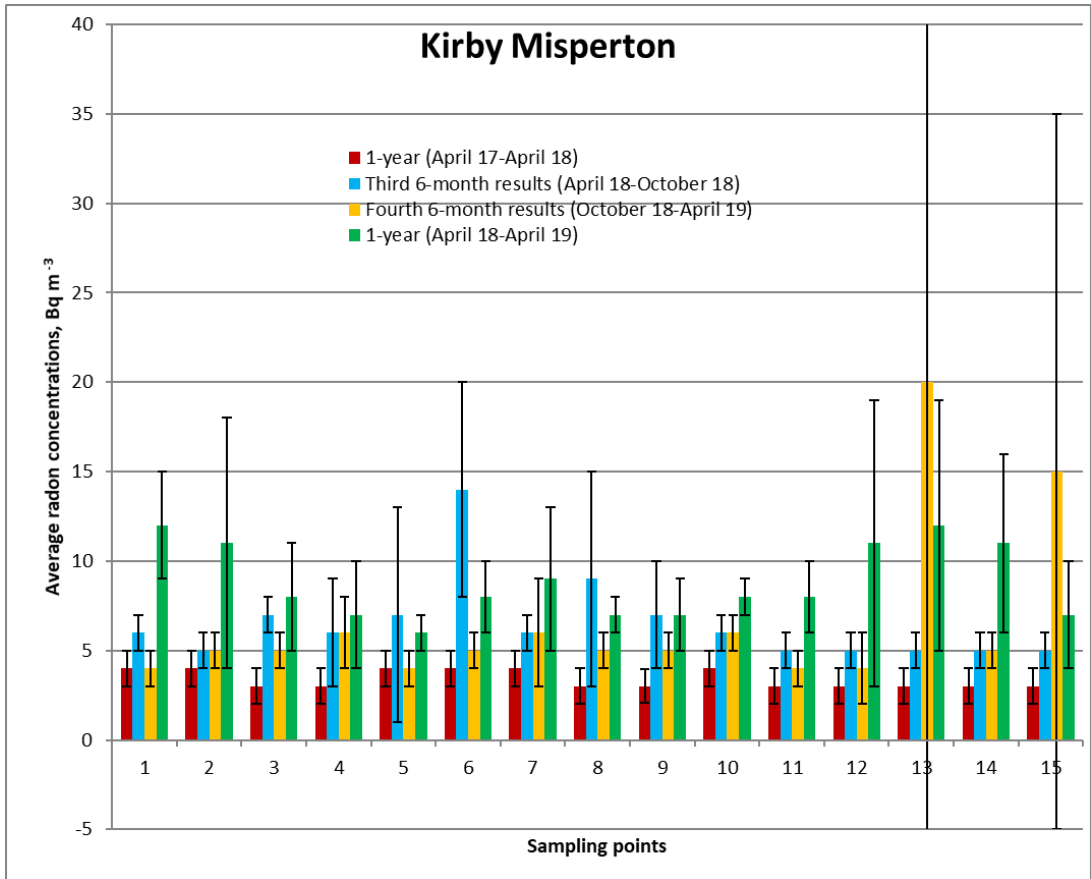


Figure 137. Average radon concentrations at the sampling points around Kirby Misperton. © PHE (2019)

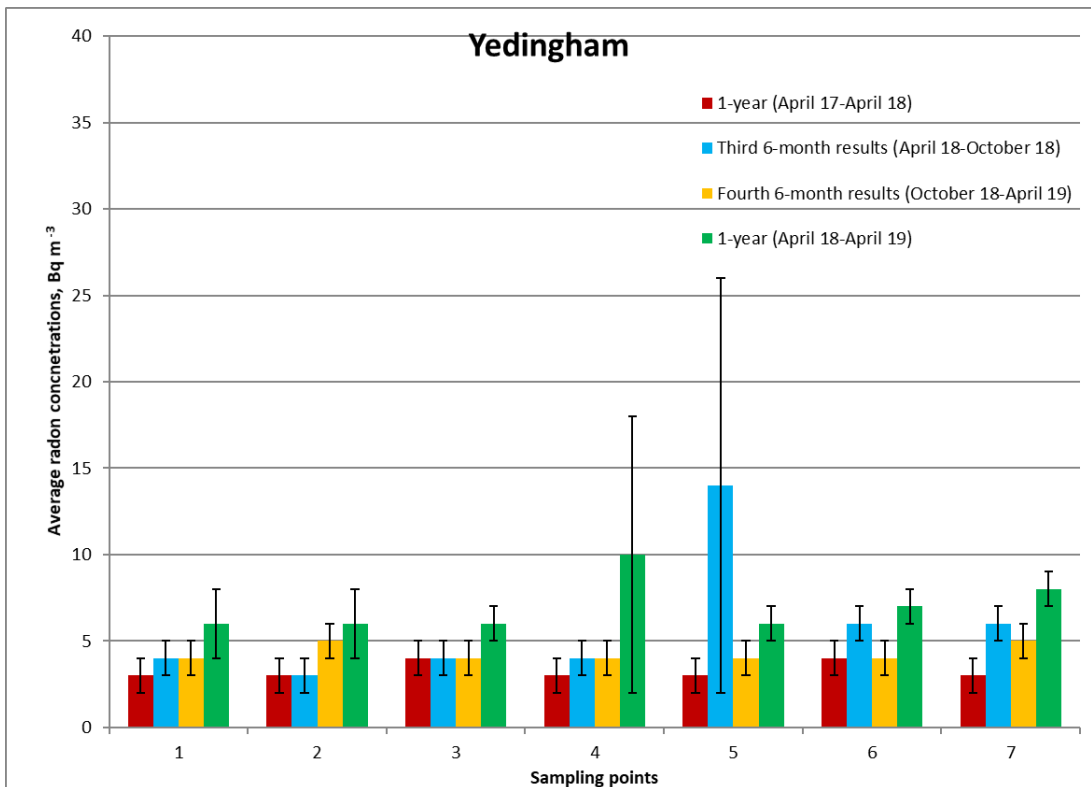
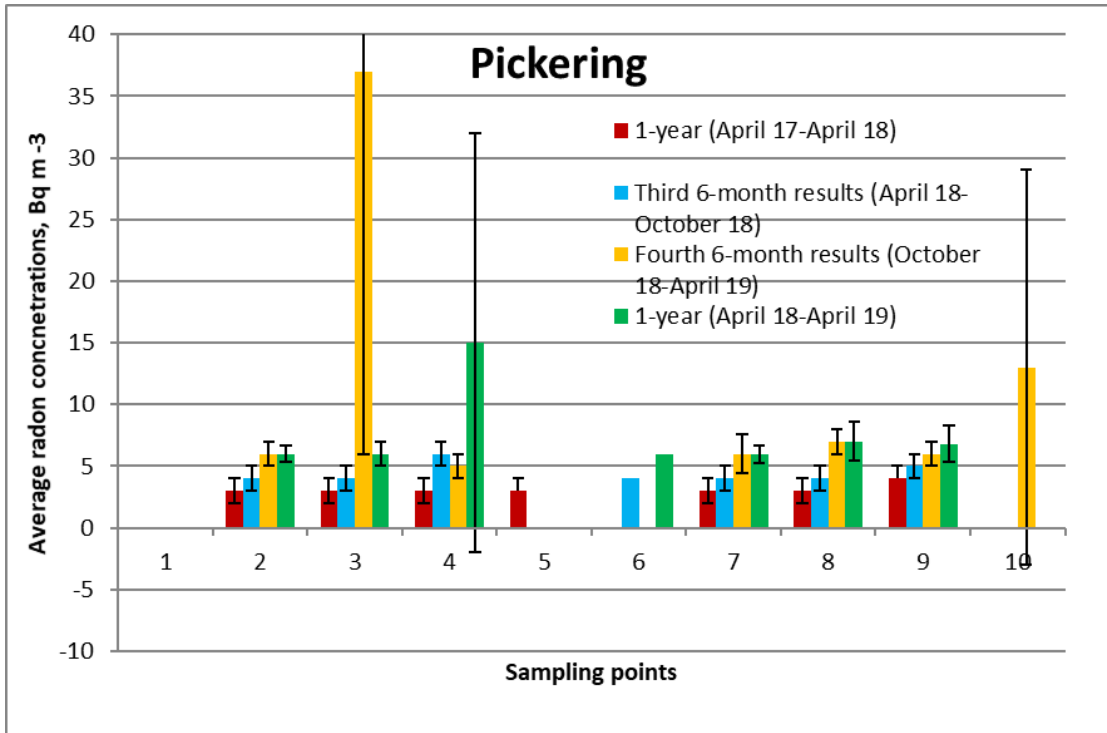
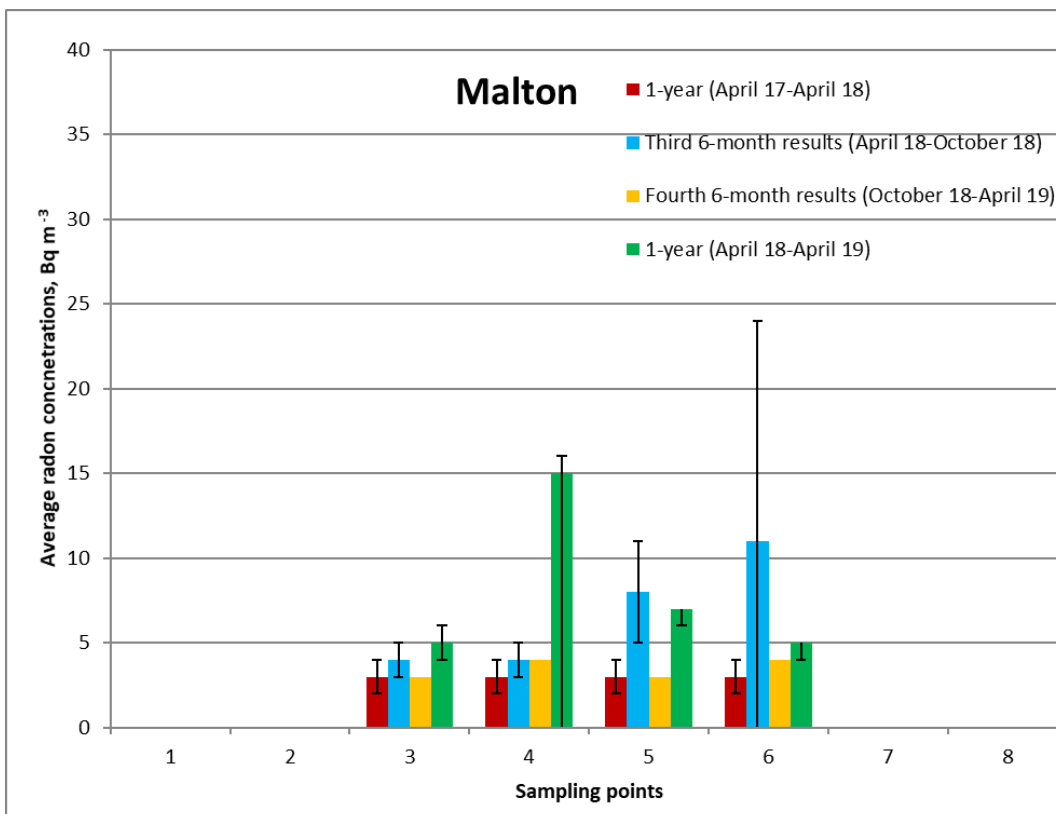


Figure 138. Average radon concentrations at the sampling points around Yedingham. © PHE (2019)



**Figure 139. Average radon concentrations at the sampling points around Pickering.**  
© PHE (2019)



**Figure 140. Average radon concentrations at the sampling points around Malton.**  
© PHE (2019)

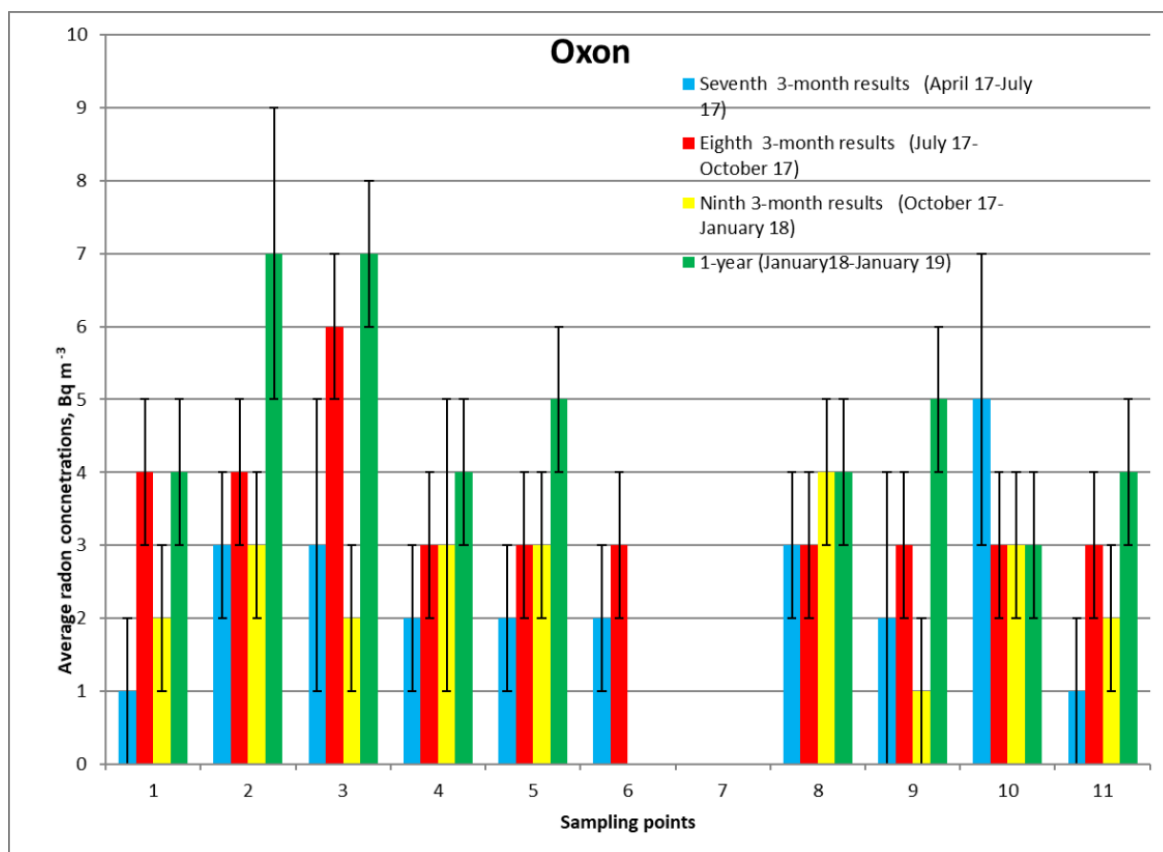


**Figure 141. Average radon concentrations at the sampling points in Oxfordshire.**  
© PHE (2019)

## 6.4 MONITORING AT THE KMA ENCLOSURE

The data from the AlphaGUARD continual radon monitoring instrument, placed in the enclosure at the KMA site for the period between April 2017 and April 2019 were analysed. The inherent background of the instrument resulting from the longer half-life alpha-emitting radionuclides (from environmental exposure and materials within the instrument), was taken into account when data were processed. The radon data, taken at 1 hour intervals, are log-normally distributed. The distribution parameters for two 3-month periods (April 2017- July 2017 and July 2017-October 2017) and one 6-month period (October 2018- April 2019) are given in Table 30. The average radon concentrations measured over the above monitoring periods was  $5 \text{ Bq m}^{-3}$ . In order for a comparison to be made between the outdoor radon concentrations measured with the instrument and the other outdoor results, passive monitors were also placed in the enclosure at the KMA site.

The average radon concentrations measured using 10 passive detectors are similar to the arithmetic means (AM) of the distributions measured with the AlphaGUARD for the three periods as shown in Table 30. This demonstrates a good agreement between the two different measurement techniques.

A graph showing the raw data obtained from the AlphaGUARD, without background correction, is given in Figure 142. No data were collected between end of July and beginning of November 2018 due to a fault in the instrument. The instrument was replaced in November 2018.

**Table 30. Range and distribution of radon measurements made with AlphaGUARD and passive detectors in the KMA enclosure.**

Period of monitoring	AlphaGUARD			Passive detectors		
	Range	Arithmetic Mean (AM)	Geometric Mean (GM)	Geometric Standard Deviation (GSD)	Arithmetic Mean (AM)	Standard Deviation (SD)
April 17-July17	1 - 47	5	3	2.4	-	-
July 17-October17	1 - 38	5	3	2.4	7	1
October18-April 19	0 - 41	5	4	2.6	5	1

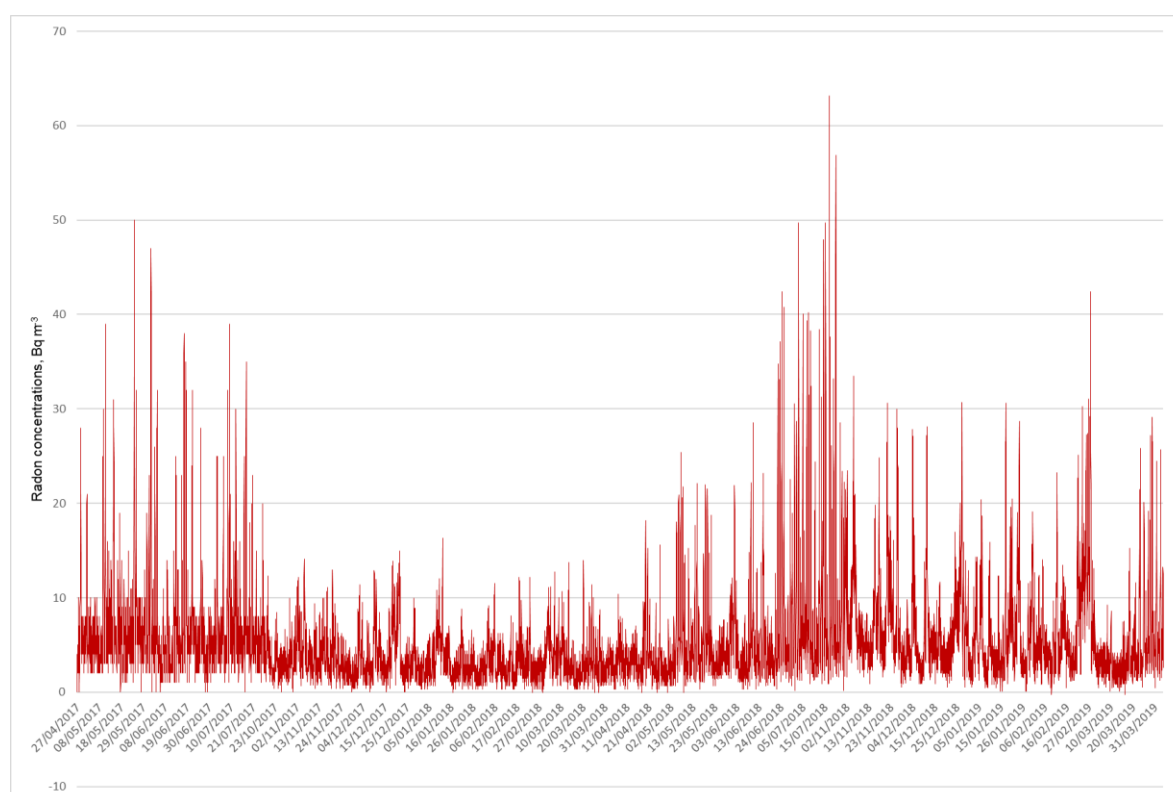


**Figure 142. Time series of radon concentrations recorded by AlphaGUARD between April 2017 and April 2019. © PHE (2019)**

### 6.5 COMPARISON OF YEAR 1, YEAR 2 AND YEAR 3 RESULTS

Year to year variation of indoor radon was studied with measurements from 56 homes where results were available for all twelve measurement periods. The indoor radon levels did not show any obvious difference between the first year (November/December 2015- December 2016), second year (December 2016- December 2017) or third year (December 2017- December 2018) of monitoring (see Figure 135).

There is an indication of year to year variability of outdoor radon. The results from the first year of monitoring (October 2015 to October 2016) were about 1.5 times higher than the radon

concentrations measured during the second year (October 2016 to October 2017) and similar to the third year of monitoring (October 2017 to April 2019).

## **6.6 CONCLUSIONS**

### **6.6.1 Indoor radon**

The analysis of the results for about 110 homes measured in the Vale of Pickering showed distributions of indoor radon concentrations consistent with the usual log-normal distribution for indoor radon.

The results for Kirby Misperton and Little Barugh area are consistent with their status as not being radon Affected Areas.

Results for Yedingham (an area with low radon potential) are also below the Action Level except for a house which had results which were above the UK radon Action Level of 200 Bq m<sup>-3</sup> for the seventh and eleventh monitoring periods (June 17 - September 17) and (June 18 - September 18), respectively. The results for all other periods for this house were below the Action Level. This result demonstrates the variability of radon when measured over a long period. We are aware that year-to-year variability of indoor radon of up to 40 % (Hunter et al) is possible.

The results for Pickering confirmed the prior status as a radon Affected Area with radon concentrations spread over a wider range from about 10 to 350 Bq m<sup>-3</sup> and several homes were found to have results exceeding the Action Level. Each householder was given standard advice on any action required; those with high radon levels were given additional information on reducing their radon concentrations.

Radon levels above 200 Bq m<sup>-3</sup> were measured in some homes in Malton at the beginning of this study and in the eleventh monitoring period which confirmed our classification as a radon Affected Area; standard advice to reduce radon levels was issued to the occupiers of these homes.

Seasonal variation of indoor radon was also studied for all areas. Results indicated that there is little seasonal variation in measurements made in homes in the areas of Kirby Misperton and Little Barugh, and also in Yedingham. The seasonal variation observed in Pickering was higher. All areas follow the normal seasonal pattern in the UK with the highest radon concentrations in winter and lowest radon concentrations in summer. It should be noted that the number of results for Malton is rather small compared to the other areas where results were assessed.

### **6.6.2 Outdoor radon**

The results from the first year of monitoring (October 2015 to October 2016) of 3-month back-to-back measurements of outdoor air are about 1.5 times higher than the radon concentrations observed previously in the UK of 4 Bq m<sup>-3</sup> (Wrixon et al., 1988). The results from the second year of the monitoring (October 2016 to October 2017) indicated levels closer to those previously measured. However, the results from the latest monitoring (October 2017 to April 2019) indicated that outdoor radon levels are above the levels of the second year and closer to the levels of the first year. There is no indication of elevated outdoor radon concentrations in the Pickering or Malton radon Affected Areas. The analysis of results for another control site in Oxfordshire showed similar concentrations.

### **6.6.3 Monitoring at the KMA site**

Results from an AlphaGUARD active monitor and passive detectors, placed in the KMA enclosure are in good agreement with the average outdoor radon concentrations within the area of Kirby Misperton. The active monitoring showed significant variations over time, however the annual average measured at KMA was consistent whichever of the techniques was used.

## **6.7 REFERENCES**

Daraktchieva Z, Howarth C B, Gooding T D, Bradley E J and Hutt N (2018) Validation Scheme for Organisations Making Measurements of Radon in UK Buildings: 2018 Revision, PHE-CRCE-040.

Darby S, Hill D, Auvinen A, Barros-Dios J M, Baysson H, Bochicchio F. et al. (2005) Radon in homes and risk of lung cancer: collaborative analysis of individual data from 13 European case-control studies. *BMJ*, 330 :223.

Miles J C H and Algar R A (1988) Variations in radon-222 concentrations. *Journal of Radiological Protection* 8 (2), 103-106.

Miles J C H, Appleton JD, Rees DM, Green BMR, Adam KAM, Myers AH (2007) Indicative Atlas of Radon in England and Wales, Chilton, HPA-RPD-033.

Miles J C H, Howarth C B and Hunter N (2012) Seasonal variation of radon concentrations in UK homes. *J. Radiol. Prot.* 32, 275-287

Hunter N, Howarth C B, Miles J C H, Muirhead C R (2005) Year-to-year variations in radon levels in a sample of UK houses with the same occupants. Seventh International Symposium on the Natural Radiation Environment(NRE-VII). In: *Radioactivity in the Environment Book Series*, vol. 7. Elsevier, 438-447.

Kibble A, Cabianca T, Daraktchieva Z, Gooding T, Smithard J, Kowalczyk G, McColl N P, Singh M, Mitchem L, Lamb P, Vardoulakis S and Kamanyire R (2014) Review of the Potential Public Health Impacts of Exposures to Chemical and Radioactive Pollutants as a Result of the Shale Gas Extraction Process, Chilton, PHE-CRCE-009

Wrixon A D, Green B M R, Lomas P R, Miles J C H, Cliff K D, Francis E A, Driscoll C M H, James A C and O’Riordan M C (1988) Natural Radiation Exposure in UK Dwellings. Chilton, NRPB-R190

# 7 Soil gas

## 7.1 INTRODUCTION

The soil gas element of the project seeks to establish baseline conditions for the concentrations of gases in the soil, flux of key gases from the soil to the atmosphere, and near-ground atmospheric levels of gases. There is therefore some overlap with the atmospheric composition (greenhouse gas) monitoring (Section 4). Since radon was measured at a subset of the surveyed locations there is also some linkage to the radon work (Section 6).

Baseline soil gas measurements, like those for other elements of the project, provide a basis against which to assess any future changes that might result from shale gas activities. Although of low probability, there is the potential for gas to escape from depth along geological pathways (faults, fractures and other higher permeability zones) or man-made features, especially wells (either pre-existing or drilled for shale gas exploration, evaluation or development). Whilst large faults may be known from existing geological maps and/or data acquired during hydrocarbon exploration (e.g. 3-D seismic data), or become apparent from seismicity or ground motion studies, smaller faults and fractures may be present but unknown. The completion (plugging and abandonment) of existing deep boreholes can also be of variable quality depending on the age of the well and there are wells in the Vale of Pickering that are more than 50 years old. New wells also represent a potential migration pathway if not constructed properly.

It is very difficult to predict where gas migration from depth might reach the surface whether it follows natural or man-made pathways. Natural seepage of gas along faults tends to occur at limited sites, metres to tens of metres across, along only a very small proportion of the fault length (e.g. Annunziatellis et al., 2008; Johnson et al., In press; Ziogou et al., 2013). Borehole leaks can occur at the wellhead or, if fluid escapes from the annulus of the well, can reach the surface up to several kilometres away (e.g. Allison, 2001).

Although soil gas monitoring is not a statutory requirement for shale gas activities, it is necessary at landfill sites (Environment Agency, 2010) and is often used to satisfy regulatory requirements for monitoring at geological CO<sub>2</sub> storage sites (European Union, 2009a, b). In the context of shale gas, it provides an additional line of evidence for detecting impacts that might arise from sub-surface leakage from shale gas infrastructure and to support interpretation of air monitoring (greenhouse gas and radon) data.

## 7.2 SITE SELECTION

Site selection was based on a mixture of scientific and pragmatic considerations and the general principles are described in more detail elsewhere (Smedley et al., 2015). At the KM8 and PNR shale gas sites, the continuous monitoring equipment was located close to the air quality and greenhouse gas monitoring stations. An additional site in the Vale of Pickering is located close to a set of groundwater monitoring boreholes and the multilevel samplers boreholes near Kirby Misperton where naturally high baseline methane concentrations have been measured (Section 2). In addition, three locations in Vale of Pickering, and two locations in the Fylde (around the PNR sites and close to Roseacre), formed the basis of the repeat baseline surveys.

## 7.3 MONITORING ACTIVITIES

Table 31 provides an overview of baseline soil gas monitoring activities between 2015 and 2019. Repeat broad-scale grid survey data has been collected in 2016 and 2018. This includes

point measurements of CO<sub>2</sub> flux, soil gas (principally CO<sub>2</sub> and CH<sub>4</sub>, combined with O<sub>2</sub> and other gases including Rn), along with mobile laser surveys of near-ground atmospheric CO<sub>2</sub> and/or CH<sub>4</sub>. Surveys are combined with temporal data from continuous monitoring systems i.e. automated flux chambers and a scanning methane laser system at KM8, a soil gas monitoring station at a site to the east of Kirby Misperton, and an eddy covariance (EC) system close to the PNR site.

**Table 31. Overview of soil gas monitoring 2015-2019. \*post-hydraulic fracturing, †data acquisition from the Kirby Misperton soil gas station is ongoing but can no longer be accessed remotely and requires manual download; March 2019 data will be reported in Phase 5.**

Region	Survey mode Mobile laser surveys, and broad scale soil gas and flux grids	Continuous monitoring
Vale of Pickering Kirby Misperton and KM8	November 2015 March 2016 (no data) June 2016 August 2016 October 2016	Kirby Misperton soil gas station: August 2016 to February 2019 <sup>†</sup> KM8 CO <sub>2</sub> flux station: October 2016 to May 2018 KM8 Open path scanning CH <sub>4</sub> laser: November 2016 to March 2017
Fylde, Lancs Preston New Road (PNR) and Roseacre (RLG)	August 2015 September 2016 September 2018 (PNR only) December 2018 (mobile laser PNR only)*	PNR Eddy covariance: January 2016 to March 2019

\*post-hydraulic fracturing

†data acquisition from the Kirby Misperton soil gas station is ongoing but can no longer be accessed remotely and requires manual download; data for March 2019 will be reported in later reports.

## 7.4 RESULTS AND DISCUSSION

### 7.4.1 Performance of monitoring techniques

Soil gas monitoring in survey mode is highly mobile and increasingly responsive. Over the baseline monitoring period, the soil gas facility has employed an evolving range of techniques to develop a body of baseline data for the Vale of Pickering and Lancashire that enables natural (e.g. diurnal and seasonal) variations to be evaluated, and against which any changes resulting from shale gas activities can be assessed.

Survey equipment generally performed well because it included built-in redundancy for critical parameters. The major challenge with survey mode is weather dependency and the level of staff effort required. During the monitoring programme, the optimum time for soil gas surveys has been found to be autumn; an attempted survey in March 2015 yielded no useful data due to unfavourable weather, and baseline soil gas in late spring/summer tends to be dominated by CO<sub>2</sub> produced by biological respiration during the growing season, whereas this declines during autumn. Winter typically yields little useful data as soil gas becomes trapped in ‘lenses’ underground and soil to air flux is impeded due to water-logging. Given fugitive emissions during shale gas operations could occur at any time of the year, sufficient baseline soil gas monitoring data is needed as far as possible from across the seasons to allow natural/seasonal variations to be accounted for, or to enable a process-based approach (Romanak et al., 2012) to be sensibly interpreted.

There have been some modifications made in the 2018 (Phase 4) surveys to account for planned or actual shale gas operator activities, specifically the focussing on work around the PNR site rather than Roseacre and the Vale of Pickering, and changes to points around the PNR well-pad (addition of new or substituted points) as a result of site activities and field boundary changes. The mobile CH<sub>4</sub> and CO<sub>2</sub> lasers also demonstrated their value including extremely short notice deployment of the CO<sub>2</sub> laser in response to a pause in shale gas activities outside the normal soil gas survey season (December 2018).

Some continuous monitoring techniques proved more successful than others. The eddy covariance system at Little Plumpton (Lancashire) has operated almost continuously since its installation, with only rare losses in data because of scheduled maintenance, occasional data download failure or data corruption problems.

The soil gas monitoring station installed to the east of KM8 also performed consistently throughout the monitoring period. Only occasional gaps in data were observed for individual buried gas probes, the most notable being related to a seal failure that required the probe to be returned to the manufacturer, or localised waterlogging due to unusual weather conditions. Telemetry also functioned well for most of the monitoring period, although more recently manual downloads of data have been undertaken.

Almost continuous data was also obtained from the flux system at KM8 during its deployment. It was decommissioned for maintenance between September 2017 and January 2018 as Third Energy were planning major site changes including moving the monitoring cabinet. Additionally, one of the four flux chambers developed a fault and was not reinstalled. The flux kit was decommissioned again in May 2018 and the decision to reinstall was deferred until plans for development and hydraulic fracturing of the KM8 shale gas wells became clearer. Because permissions were granted for operations at PNR, attention over the reporting period has increasingly focussed on monitoring in Lancashire.

The deployment of the methane scanning laser system at KM8 has been less successful because of a combination of technical issues with the system, exacerbated by shale gas site activities that resulted in loss of line of sight for the laser paths due to the installation of well-pad equipment and the sound wall. The latter meant decommissioning the system completely until it could be properly re-sited. Ultimately the decision to do so was deferred until plans for development at KM8 and Preston New Road became clearer. As a result, data is available for a short period between November 2016 and March 2017 only.

In summary, continuous monitoring (CO<sub>2</sub> flux and scanning laser) at the KM8 site was scaled back/suspended (i.e. decommissioned equipment was not subsequently recommissioned) because of lack of activity at this site. While scaling back or suspending soil gas monitoring is not ideal, it is unlikely to impact significantly on the robustness of the overall baseline since its estimation is not solely reliant on soil gas instruments, but is considered in the light of data generated by air quality and radon monitoring. For the KM8 site, at least 12 months of continuous soil gas data is available and this has allowed the baseline to be characterised and reported.

Elsewhere, soil gas monitoring near Kirby Misperton to the east of KM8, and eddy covariance at Little Plumpton, has continued largely uninterrupted during the Phase 4 period. The re-focussing of resources has also allowed additional surveys (one full baseline survey before hydraulic fracking began, one rapid response laser survey during an interlude in hydraulic fracking and one after the hydraulic fracturing of the PNR-1z well had been completed) to be added to the monitoring programme at Preston New Road. The most recent full soil gas survey

was undertaken in April 2019. Preliminary data are provided in this report, but a more detailed analysis of the data will be reported at a later date.

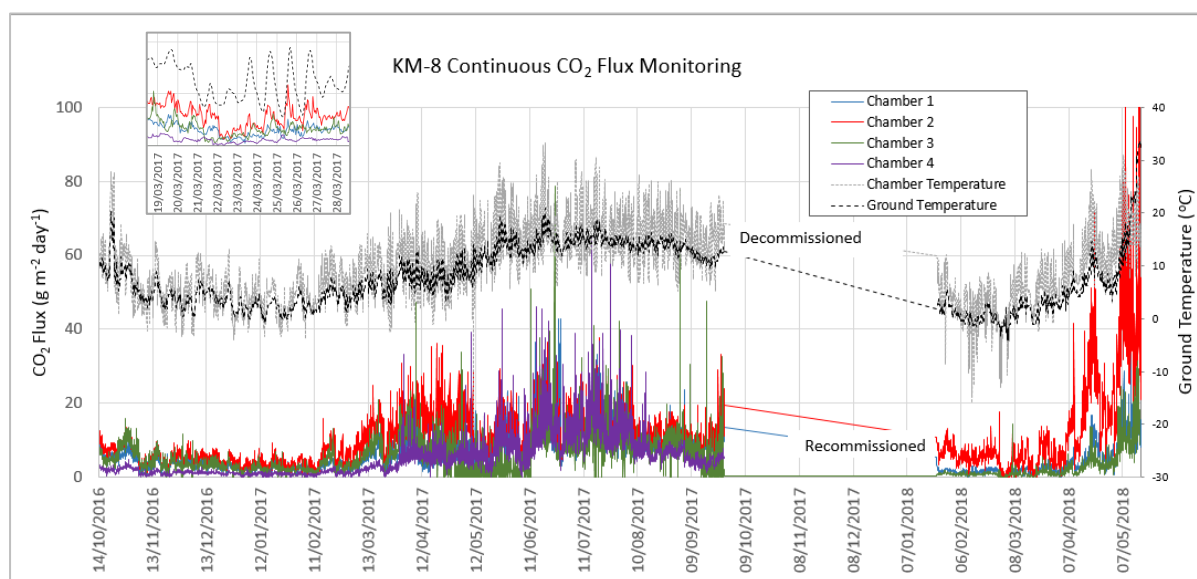


**Figure 143. Continuous time series plot of CO<sub>2</sub> flux from chambers 1, 2, 3 and 4, along with ground and chamber temperature, and 10 day period in March 2017 showing flux changes in response to diurnal cycles and weather events (inset).**

#### 7.4.2 Continuous CO<sub>2</sub> flux monitoring at KM8

Figure 143 shows CO<sub>2</sub> flux from all four long-term flux chambers installed at KM8. With the exception of chamber 4, which suffered a seal failure and was not reinstalled following scheduled maintenance in September 2017, data is more or less continuous throughout the period October 2016 to May 2018. The measured fluxes are relatively low, with chamber 2 typically displaying slightly elevated values compared to other chambers (Figure 148). The reason for this may lie in the heterogeneous nature of the KM8 site and/or the new tree planting in the vicinity of the chambers.

Generally fluxes across all the KM8 chambers have been consistent with one another and overall trends from all four flux chambers are broadly similar (Figure 143 and Figures 144 to 147), displaying lower CO<sub>2</sub> flux during the colder autumn and winter months, when plant growth and microbial activity is reduced and less biogenic CO<sub>2</sub> is produced. Higher fluxes are shown in all four chambers during spring and summer months, corresponding with elevated ground temperatures (note that ground temperature from the chamber 1 sensor is plotted for all four chambers) and associated plant growth and microbial activity. This observed seasonal pattern of CO<sub>2</sub> flux throughout the year is as would be expected for the UK climate.

The inset in Figure 143 shows discernible diurnal components to the CO<sub>2</sub> flux, along with longer lasting features which likely reflect passing weather systems. Heavy rain in particular can cause the ground to become saturated, resulting in water ‘sealing’ the surface and preventing the migration of gas to the atmosphere. This effect may be seen as a short term decrease in flux in all four chambers e.g. in March (inset) or June 2017 where a sharp short term decrease in flux is seen coincident with a drop in both atmospheric pressure and ground temperature.

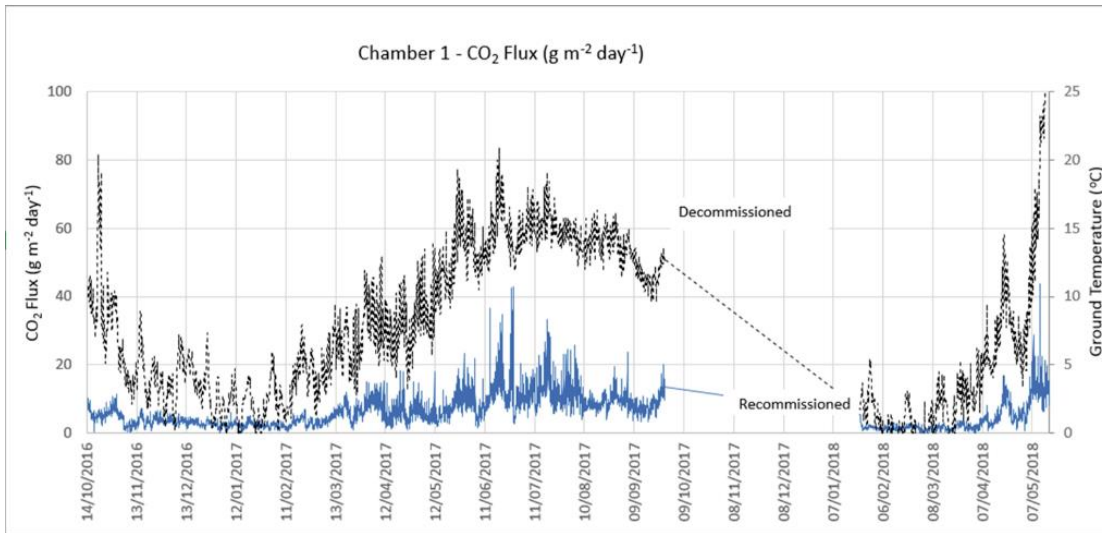


**Figure 144. Individual time series plot of KM8 CO<sub>2</sub> flux from Chamber 1, along with ground temperature**

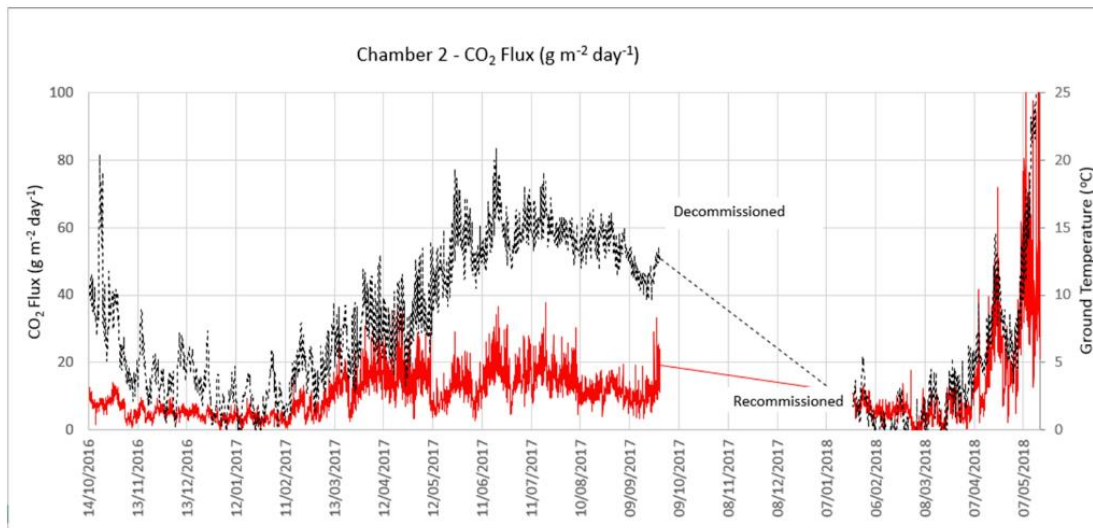


**Figure 145. Individual time series plot of KM8 CO<sub>2</sub> flux from Chamber 2, along with ground temperature**

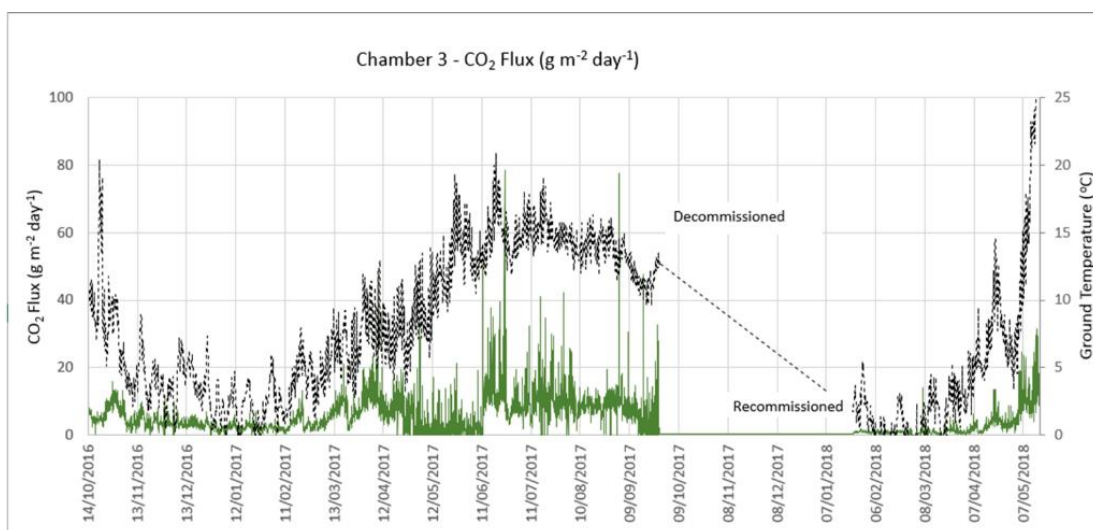


**Figure 146. Individual time series plot of KM8 CO<sub>2</sub> flux from Chamber 3, along with ground temperature**

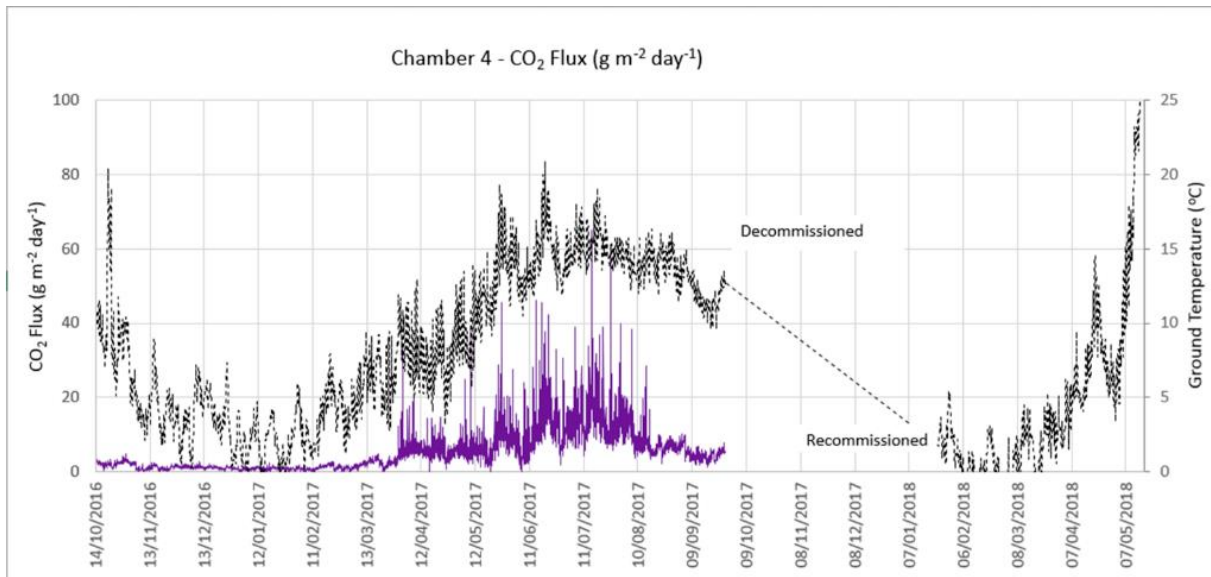


**Figure 147. Individual time series plot of KM8 CO<sub>2</sub> flux from Chamber 4, along with ground temperature**

The KM8 flux values are in good agreement with CO<sub>2</sub> flux measured during the discrete grid surveys at nearby farms. This illustrates the increase in CO<sub>2</sub> flux during the summer months where crop and surface vegetation growth, and accompanying microbial activity, are at their highest rate, resulting in a greater contribution of biogenic CO<sub>2</sub> from the soil to the atmosphere. Peak values observed at KM8 are typically between 40 and 60 g m<sup>-2</sup> day<sup>-1</sup> during the months May – August, which is similar to the bulk of data shown in the spatial maps of CO<sub>2</sub> flux in Figure 152.

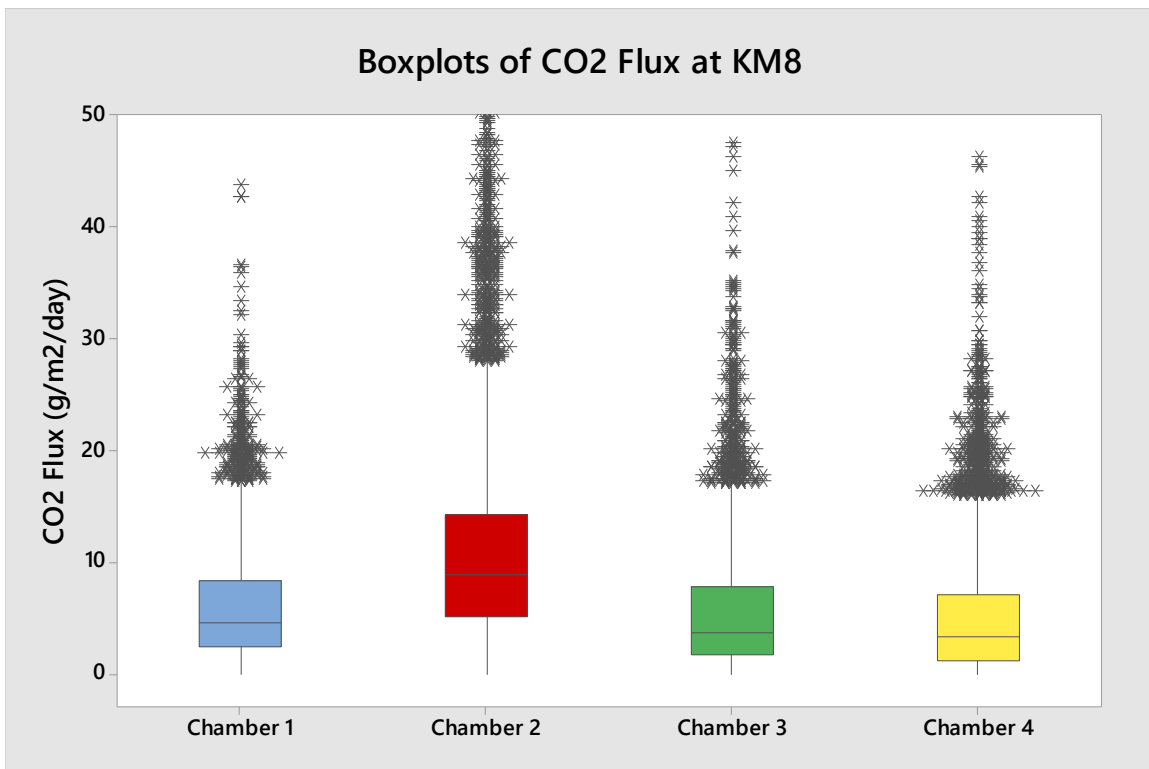


**Figure 148. Summary of long term CO<sub>2</sub> flux at KM8, October 2016 to May 2018.**

### 7.4.3 Continuous soil gas monitoring: Kirby Misperton soil gas station

The soil gas monitoring station was installed on farmland to the east of KM8 in August 2016 and consists of four hard-wired soil gas probes connected to a remotely-accessed central station. The station configuration was adapted in early May 2017 (Figure 149) and, despite major changes at the surface, short gaps for maintenance and repair and occasional downtime for individual probes, the station has operated more or less continuously since (Figure 150). The only data manipulation has been to exclude data that are clear electrical artefacts coinciding with brief losses in signal for one of the probes that result in an artificial CO<sub>2</sub> concentration of 100%. Excluded data is available on request. Data continues to be collected remotely, however the station no longer transmits automatically and data needs to be manually downloaded during a site visit. The most download is scheduled for June 2019 (covering the period February - May 2019) and will be reported in Phase 5.

The most noticeable feature in CO<sub>2</sub> concentrations across the baseline monitoring period is the steep rise in CO<sub>2</sub> concentration displayed by probe 3 in early spring 2018, which then became unresponsive. This proved to be due to waterlogging, in fact probe 3 was found to be completely submerged, and the elevated CO<sub>2</sub> concentrations are most likely the result of a build-up of soil gas that water sealing prevented from migrating to the atmosphere. Ultimately the probe dried out and resumed operation of its own accord.

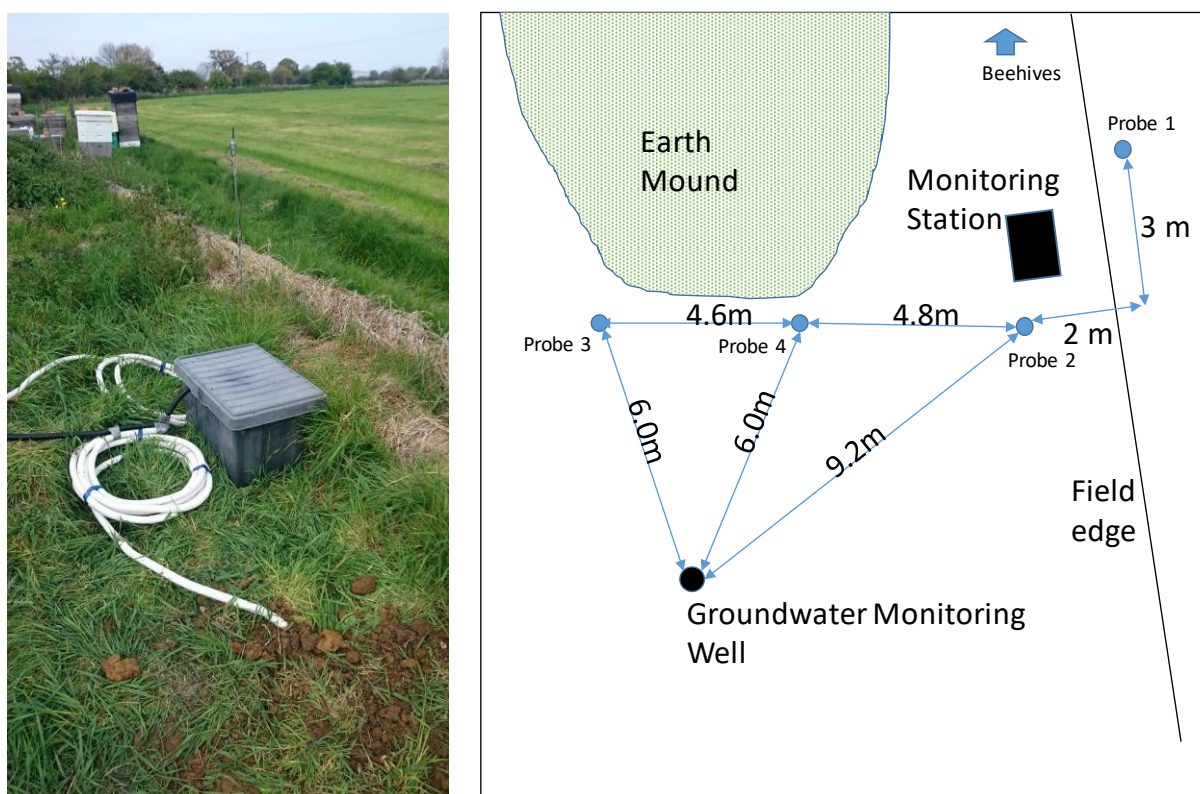


**Figure 149. Soil gas monitoring station appearance (left) and layout in 2017-18 (right).**

Otherwise, the long term pattern in soil gas CO<sub>2</sub> (2016 - 2019) was one of diurnal fluctuations overlaying seasonal ground temperatures and weather patterns. This is illustrated by higher CO<sub>2</sub> recorded in spring and summer when higher ground temperatures encourage microbial activity and biological respiration, and produce relatively more biogenic CO<sub>2</sub>; lower CO<sub>2</sub> during autumn and winter as biological respiration winds down. Ignoring waterlogged probe 3, CO<sub>2</sub> concentrations peaked between 4 and 6% in spring and summer, whereas CO<sub>2</sub> concentrations in colder months are typically 1 to 2% or less, depending on the probe. Differences between the probes, and possibly also some differences in their patterns of response, are likely to reflect small-scale variability in ground conditions (e.g. being located on hard-standing, at field margin, Figure 149). Conversely, coincident peaks and troughs of CO<sub>2</sub> concentration seen between probes could probably be tied in with specific events such as rainfall accompanying the passage of weather systems.

Long term soil gas patterns are also in broad agreement with patterns in long term CO<sub>2</sub> flux obtained at KM8, particularly for gas probe 3. It is unclear why this gas probe 3 should show a better correlation than other probes (Figure 151), but it is presumably related to its position (e.g. on hard-standing) relative to the other three gas probes (Figure 149), rendering it more sensitive and any correlation appearing more obvious.

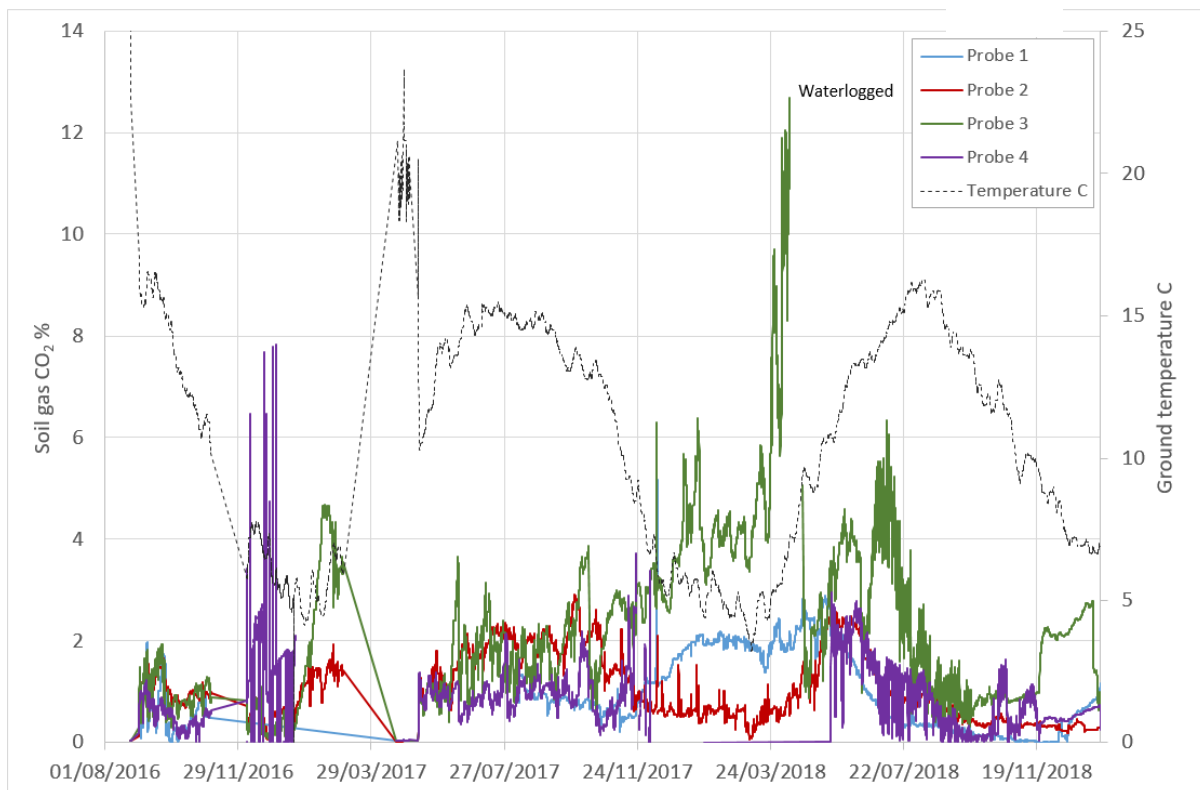


**Figure 150. Summary of all continuous soil gas data from the monitoring station east of Kirby Misperton, August 2016 to January 2019.**

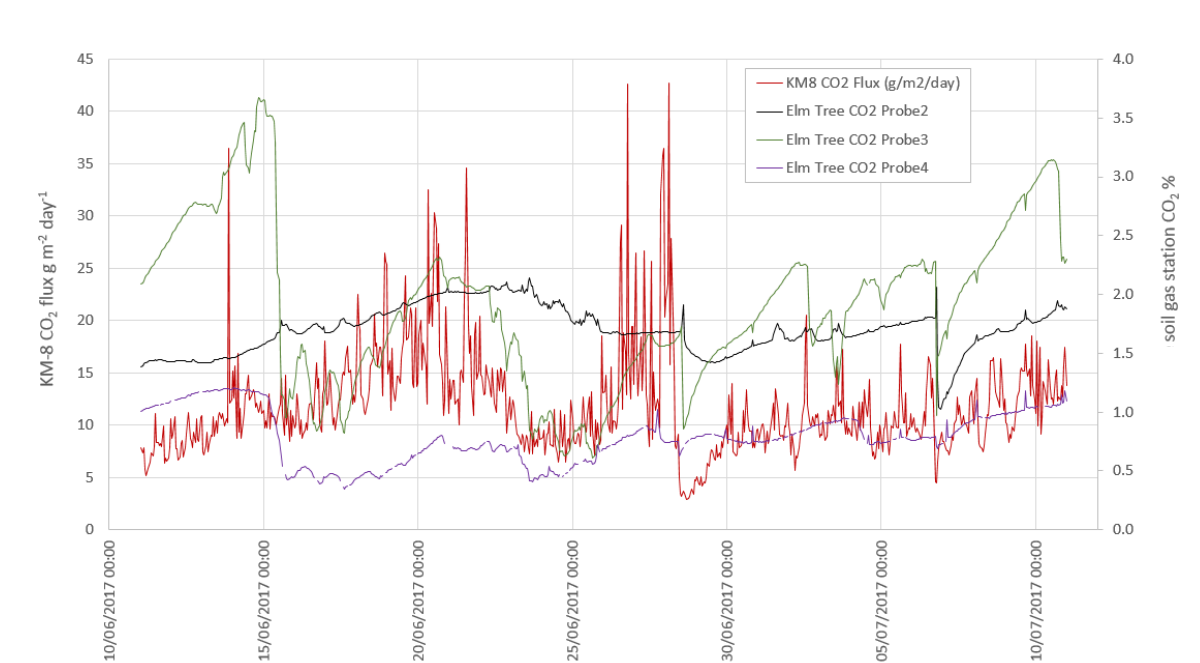


**Figure 151. Illustration of broad agreement between KM8 CO<sub>2</sub> flux and Kirby Misperton soil gas station CO<sub>2</sub> in soil gas from June 2017.**

#### 7.4.4 Soil gas surveys

Soil gas baseline monitoring in survey mode consisted of repeated broad scale grids of CO<sub>2</sub> flux and soil gas point measurements, along with mobile laser surveys. The latter is a rapid screening exercise conducted over wide areas; the facility typically uses this method to identify anomalies that can be followed up with more detailed point measurements, but it was also used specifically in an attempt to ascertain surface manifestations of the impacts of shale gas activities (see Section 7.4.9).

#### 7.4.5 Vale of Pickering: CO<sub>2</sub> flux

Table 32 provides a summary of 476 individual CO<sub>2</sub> flux measurements obtained during the Vale of Pickering soil gas surveys. The general pattern of higher average CO<sub>2</sub> flux found in the 2016 summer campaigns (June and August), and lower average flux found in the autumn campaigns (November 2015 and October 2016), compare well with measurements obtained from the four long term flux chambers operating in continuous monitoring mode at KM8 during similar periods the following year (Figure 143). This reflects the seasonal increase and decline in biogenic contributions to CO<sub>2</sub> flux, as well as the influence of saturated conditions impeding CO<sub>2</sub> migration to the atmosphere during periodic or seasonal weather events, the latter noted for the November 2015 survey.

**Table 32. Summary of CO<sub>2</sub> flux data from soil gas surveys in Kirby Misperton. \*negative value suggests soil acting as CO<sub>2</sub> sink**

Survey	n	Minimum CO <sub>2</sub> flux g m <sup>-2</sup> day <sup>-1</sup>	Maximum CO <sub>2</sub> flux g m <sup>-2</sup> day <sup>-1</sup>	Mean g m <sup>-2</sup> day <sup>-1</sup>
2015 November	142	3.37	34.71	13.18
2016 June	115	2.48	142.28	32.01
2016 August	116	-24.51*	98.19	19.07
2016 October	103	-30.55*	40.56	12.44

To illustrate how CO<sub>2</sub> flux is distributed spatially across the sampling grid, CO<sub>2</sub> flux obtained for each of the 2016 surveys are mapped in Figure 152. The maps show that, point for point, CO<sub>2</sub> flux values were generally lower in the October 2016 campaign than in the two summer campaigns. There are also a small number of points in the easternmost grid that, by comparison, showed relatively high CO<sub>2</sub> flux (>75 g m<sup>-2</sup> day<sup>-1</sup>) in the summer campaigns; this is very likely due to ongoing agricultural activities (e.g. cropping and soil amendment) at the time of sampling.

Inferred geological faults in the area are also shown in Figure 152 since these represent a potential migration pathway for geogenic CO<sub>2</sub> produced at depth. There is no obvious correlation between inferred faults and measured CO<sub>2</sub> flux; the distribution of radon in soil gas also shows no obvious correlation with known faults (data not shown), however unknown faults in the survey area are also a possibility.

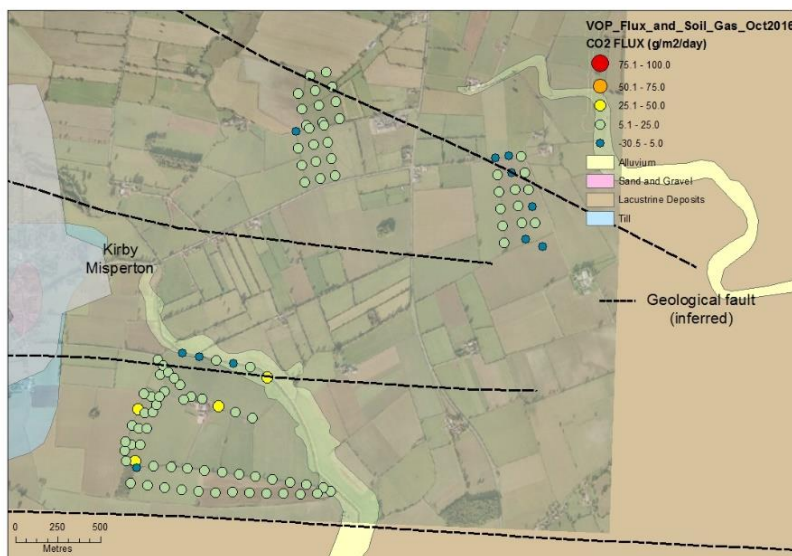
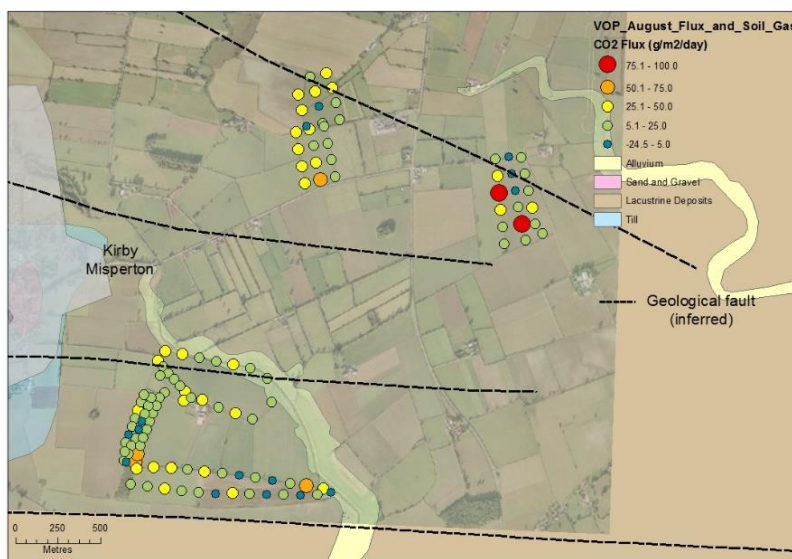
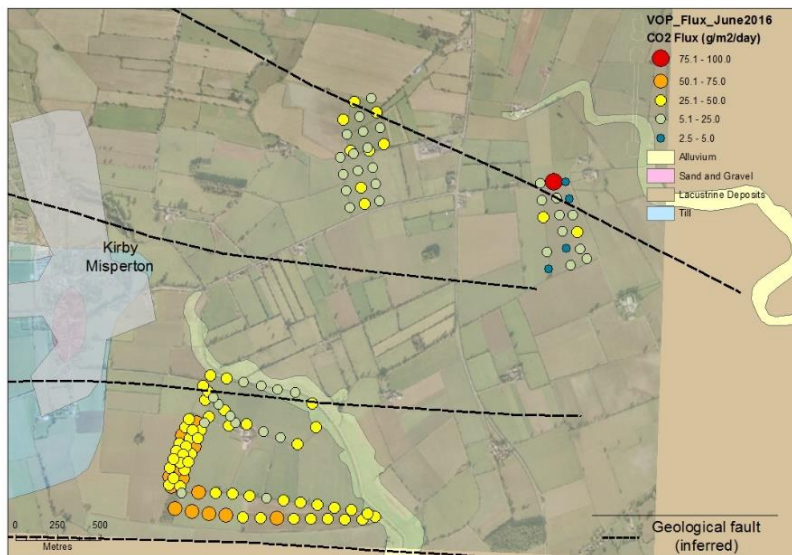


**Figure 152. Geospatial distribution of CO<sub>2</sub> flux measured over three 2016 field surveys at Kirby Misperton. Top to bottom: June 2016, August 2016, October 2016**

#### 7.4.6 Vale of Pickering: soil gas

Soil gas samples are collected by driving a 1.5 m hollow steel push probe into the ground to access gas within the soil pore spaces well below the surface, beyond the influence of atmospheric gas. For the Vale of Pickering, a total of 440 soil gas samples were obtained across the four surveys summarised in Table 32. All but three soil gas samples were collected at our standard depth i.e. between 60 (if avoiding buried infrastructure) and 90 cm below the soil surface. Of the three shallow samples (depth <40 cm), one appeared from its composition to be atmospheric gas rather than soil gas. However, since the impact of this one sample on subsequent data analysis was deemed negligible, all samples were included in the subsequent data analysis.

**Soil gas data was collected during 2015 and 2017 for the Vale of Pickering. Further surveys were not carried out in 2018 as no shale gas operations were expected at the KM8 sites. Instead resources were re-focused on the area around the PNR site. Data available for the Vale of Pickering are summarised in box and whisker plots in Figures 153 and 154. There appear to be no major differences in the soil gas concentrations of CO<sub>2</sub>, O<sub>2</sub> or methane between sites (**

Figure 153). The combined data for all sites (Figure 154) indicate baseline CO<sub>2</sub> concentrations range up to 10%, with an average of 1.8%.

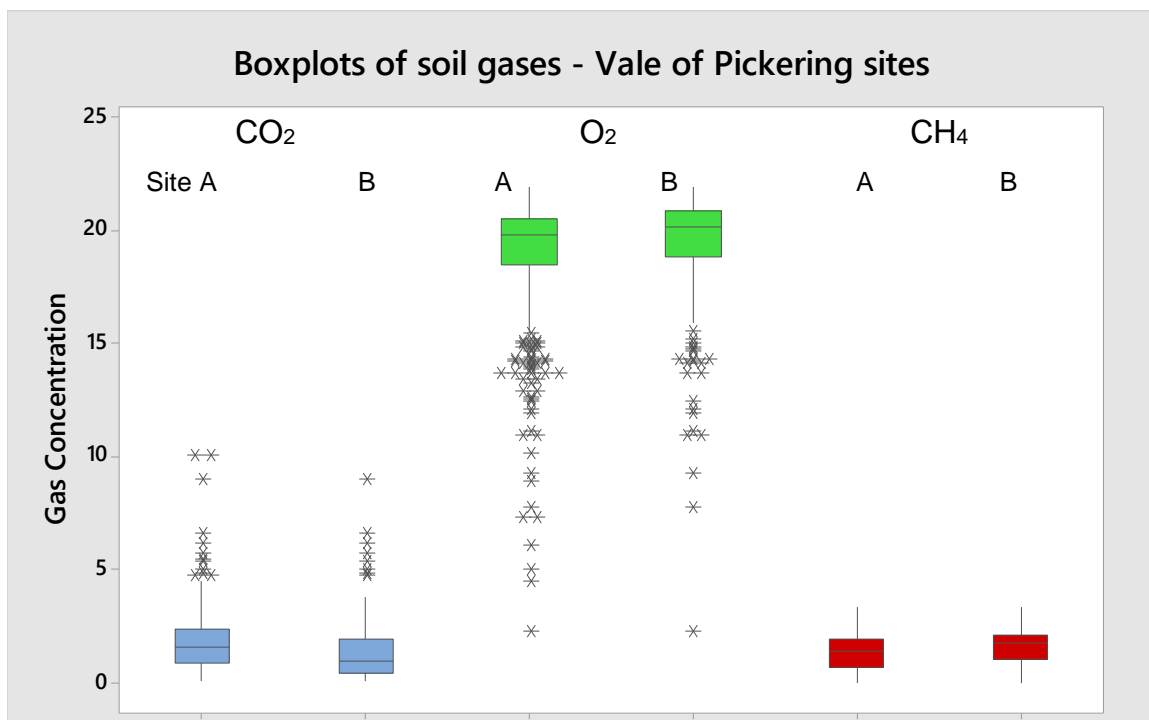


**Figure 153 Compiled Vale of Pickering soil gas CO<sub>2</sub> (%), O<sub>2</sub> (%) and CH<sub>4</sub> (ppm) data, separated by site**

The relationship between concentrations of different soil gases, in this case CO<sub>2</sub> and O<sub>2</sub>, can provide an indication of the predominant processes influencing the concentration of CO<sub>2</sub> in soil gas (Romanak et al., 2012). 155 suggests that much of the CO<sub>2</sub> measured during the Vale of Pickering surveys originates from biogenic sources in the shallow subsurface, as its relationship with soil gas oxygen lies along the biological respiration line. As expected, the strength of the relationship varies between seasons; the relationship is stronger in summer than in autumn, when the relationship is more mixed towards the oxidation of methane.

The concentrations of methane in soil gas averaged 1.3 ppm (range 0-3.3 ppm, n = 448). Typical atmospheric methane concentrations in the area are c.1.8 to c.2.4 ppm. This suggests there are no

discernible point sources of elevated soil gas methane and, possibly, that if methane has been present, it is oxidised to CO<sub>2</sub>. The relationship between soil gas CO<sub>2</sub> and O<sub>2</sub> would seem to support this, with some samples lying along the CH<sub>4</sub> oxidation line in 155. There was also very little detectable methane flux across the Vale of Pickering sampling grid for any of the soil gas campaigns (data not shown).

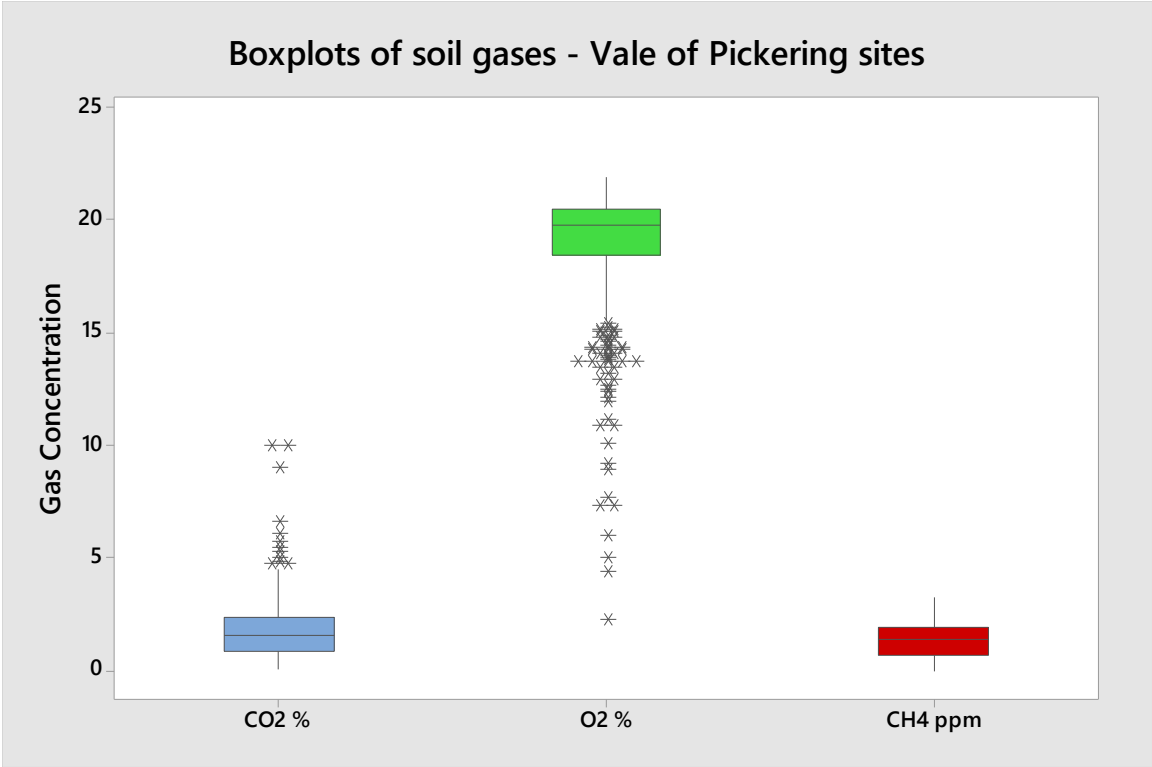


Figure 154 Compiled Vale of Pickering soil gas data, all sites

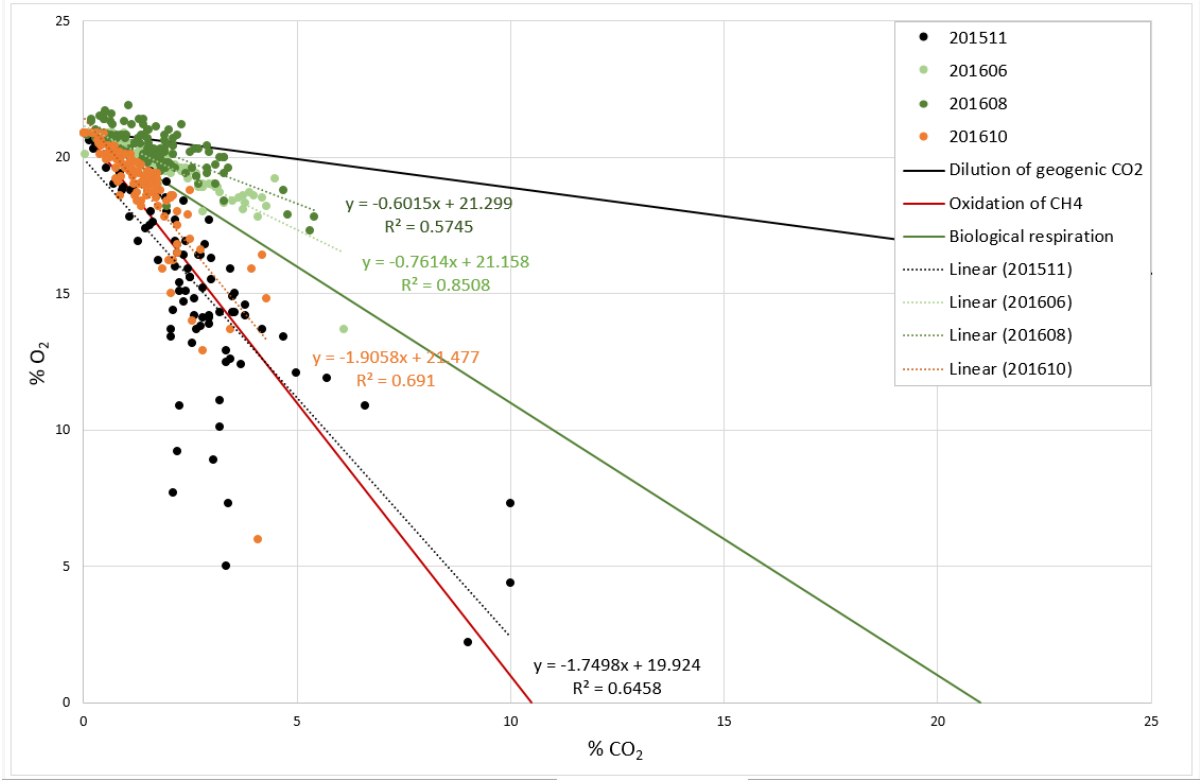
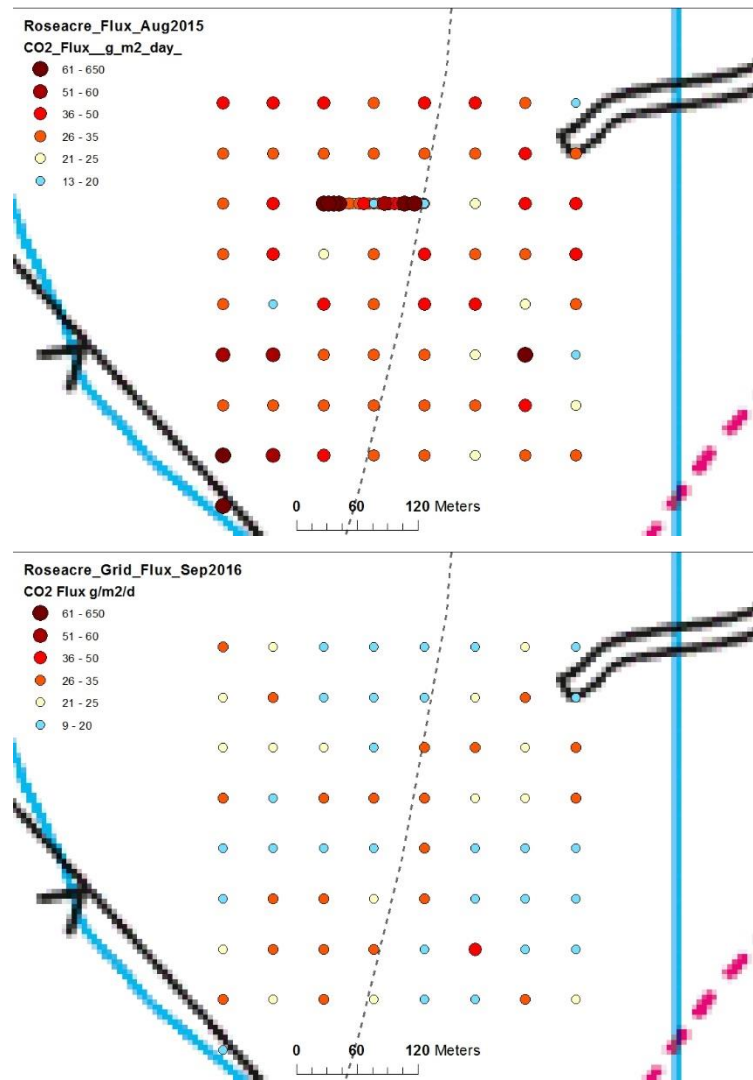


Figure 155 Binary plot of soil gas compositions, Vale of Pickering, by survey



**Figure 156. Geospatial distribution of CO<sub>2</sub> flux measured over two 2016 field surveys at Roseacre, dashed line denotes location of linear fault.**

#### 7.4.7 Lancashire: CO<sub>2</sub> flux

A total of 376 CO<sub>2</sub> flux samples were obtained across three surveys in Lancashire. Sampling focussed on two fields to the west of the PNR well-pad (directly above the lateral extent of the shale gas wells), and at a site near Roseacre (August 2015 and September 2016 only at Roseacre). 33 provides a summary of CO<sub>2</sub> flux for both sites across all surveys. The highest flux observed was 650 g m<sup>-2</sup> day<sup>-1</sup> in the low-lying northern boundary of the eastern field at Preston New Road in August 2015, an area that is often waterlogged. The average CO<sub>2</sub> flux is marginally higher in the late summer than in the early autumn, again likely due to warmer temperatures driving the production of biogenic CO<sub>2</sub> in the shallow subsurface. The temporal differences between surveys are less striking than seen in the Vale of Pickering, presumably due to the timing of the surveys. This is even clearer if the single highest flux value is excluded; this reduces the maximum to 178.32 and the average to 30.68 g m<sup>-2</sup> day<sup>-1</sup>.

The spatial distribution of CO<sub>2</sub> flux is shown for Roseacre in Figure 156 and for Preston New Road in Figure 157. Similarly, for both the Lancashire sites, CO<sub>2</sub> flux is higher overall in August 2015 than in the later September surveys. There also appears to be little spatial correlation between CO<sub>2</sub> flux (or radon, data not shown) and the path of a known geological fault across the Roseacre site although, like Vale of Pickering, unknown faults are also a possibility in this survey area.

**Table 33. Summary of CO<sub>2</sub> flux data from soil gas surveys in Lancashire. \*negative value suggests soil acting as CO<sub>2</sub> sink**

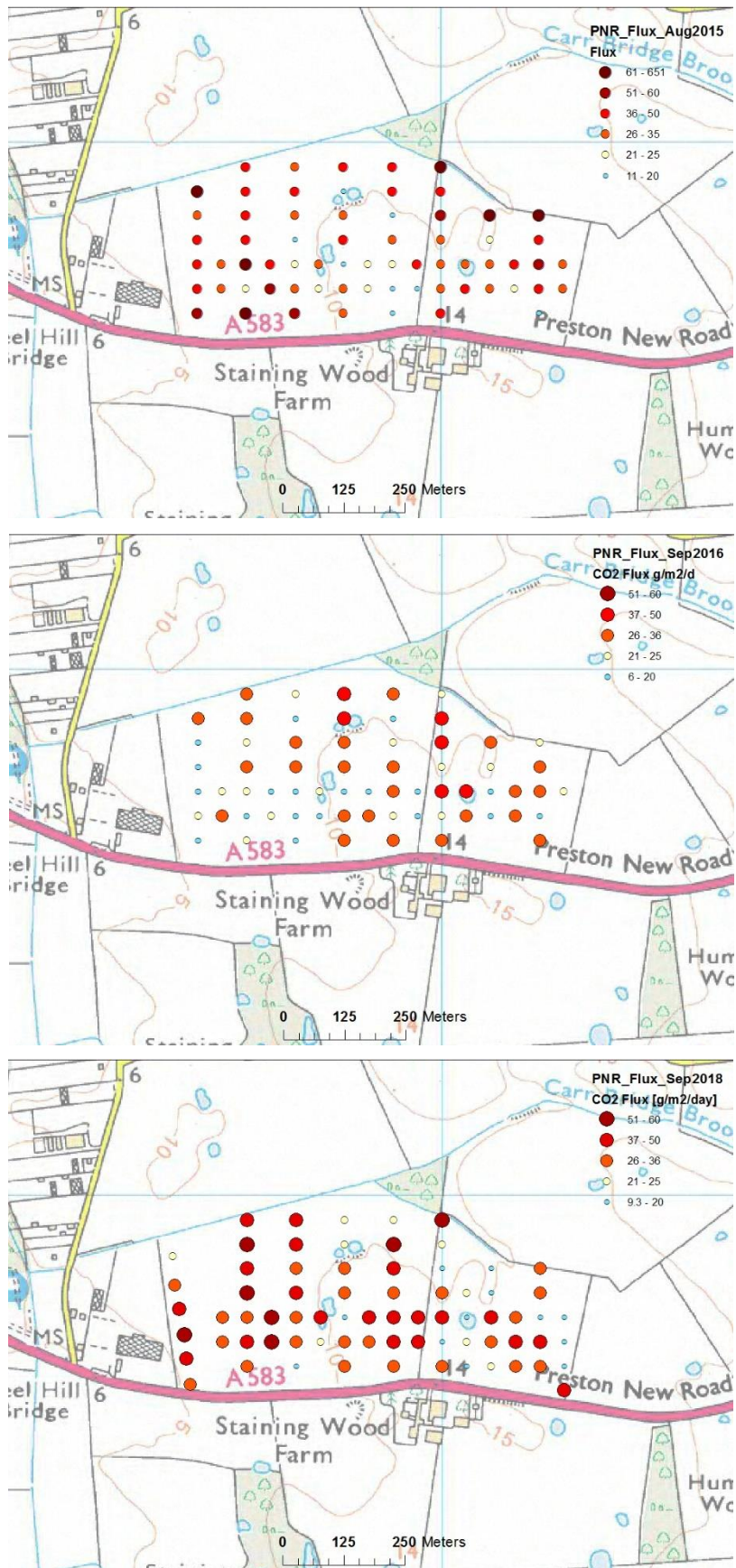
Survey	n	Minimum CO <sub>2</sub> flux g m <sup>-2</sup> day <sup>-1</sup>	Maximum CO <sub>2</sub> flux g m <sup>-2</sup> day <sup>-1</sup>	Mean g m <sup>-2</sup> day <sup>-1</sup>
2015 August	152	11.25	650.60	41.72
2016 September	152	-70.99*	45.20	23.02
2018 September	72	9.31	59.59	32.16

In Lancashire, a total of 357 soil gas samples were collected with eight soil gas samples obtained at shallower depth than our standard 70-90 cm. The eight shallow ( $\leq 40$  cm) samples were all collected in September 2018 and, of these, one sample appeared from its composition to be atmospheric gas rather than soil gas. Again, since the impact of this one sample on subsequent data analysis was deemed negligible, all 357 samples were included in the subsequent data analysis.

Soil gas data for Lancashire are summarised into box and whisker plots in Figures 158 and 159. As seen with soil gas data from the Vale of Pickering, there appears to be no major differences between sites. The combined data for both sites (Figure 159) indicates baseline CO<sub>2</sub> concentrations range up to 18%, with an average of 3.18%.

A process-based approach has been applied to the Lancashire data in an attempt to apportion the source of observed soil gas CO<sub>2</sub>. 160. suggests that much of the CO<sub>2</sub> measured during the Lancashire surveys originates from biogenic sources in the shallow subsurface, as its relationship with soil gas oxygen lies mainly along the biological respiration line with some mixing towards the CH<sub>4</sub> oxidation line. Given the spread of CO<sub>2</sub> concentrations measured, the biogenic relationship is more obvious in data from the September 2016 survey. We would again expect the relationship to vary between seasons, and for the relationship is stronger in spring and summer than in autumn, but enough data is not yet available for Lancashire to demonstrate this.

Concentrations of methane in soil gas averaged 1.3 ppm. This is a little lower than typical atmospheric methane concentrations and suggests there are no point sources of elevated soil gas methane. The methane range was 0 to 6.5 ppm, with the highest methane in the low lying, often waterlogged, northern boundary of the western Preston New Road site. Very little methane flux was detected for the Lancashire sites (data not shown).



7.4.8 Figure 157. Geospatial distribution of CO<sub>2</sub> flux measured over three field surveys at Preston New Road. Top to bottom: August 2015, September 2016, September 2018 Lancashire: Soil gas

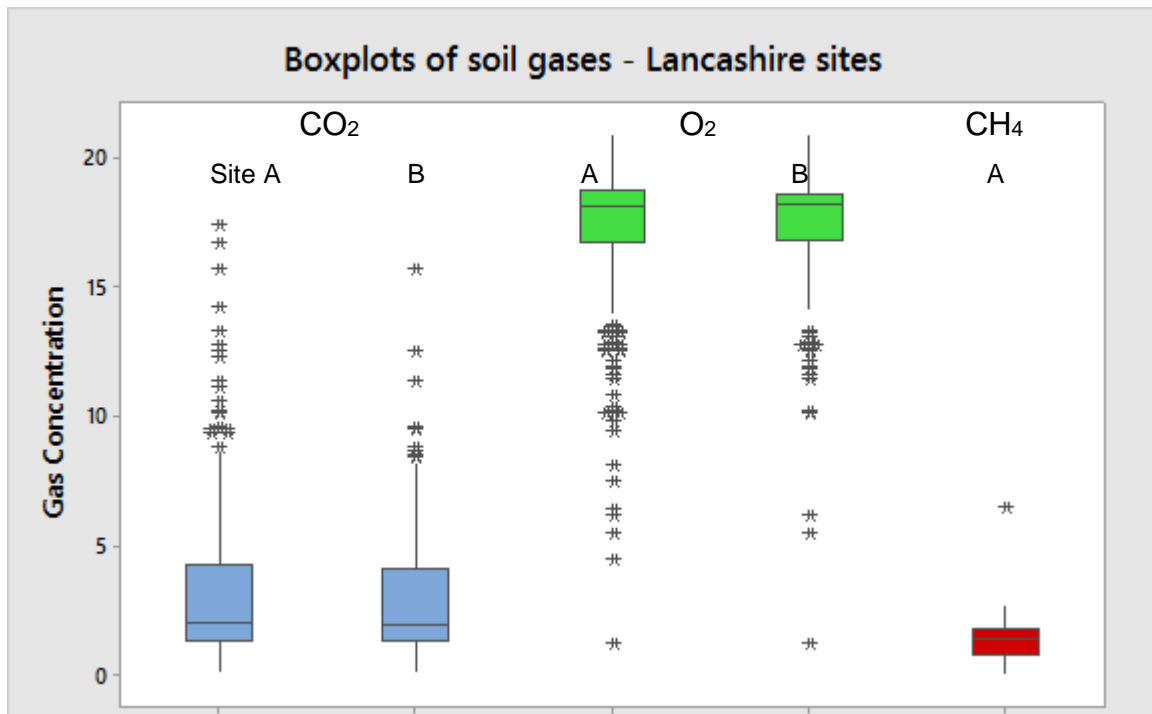


**Figure 158. Compiled Lancashire soil gas CO<sub>2</sub> (%), O<sub>2</sub> (%) and CH<sub>4</sub> (ppm) data, separated by site. No CH<sub>4</sub> data are available for Site B.**

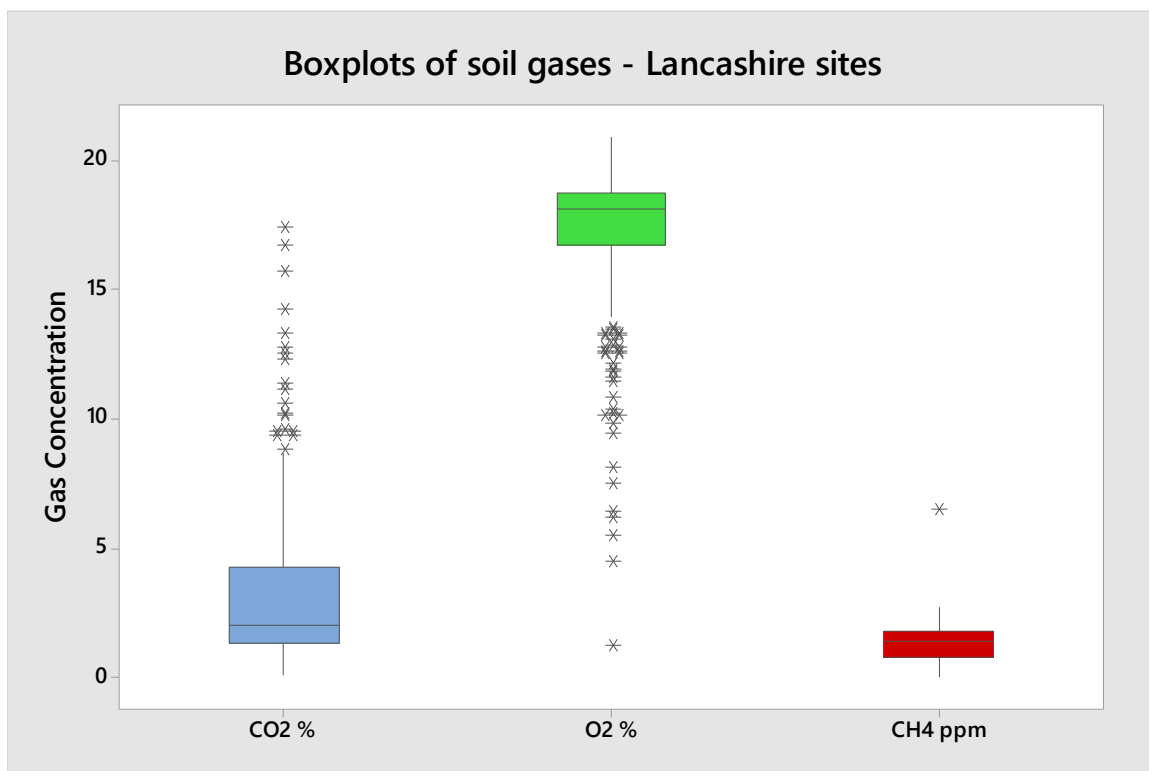


**Figure 159. Compiled Lancashire soil gas data, all sites combined**

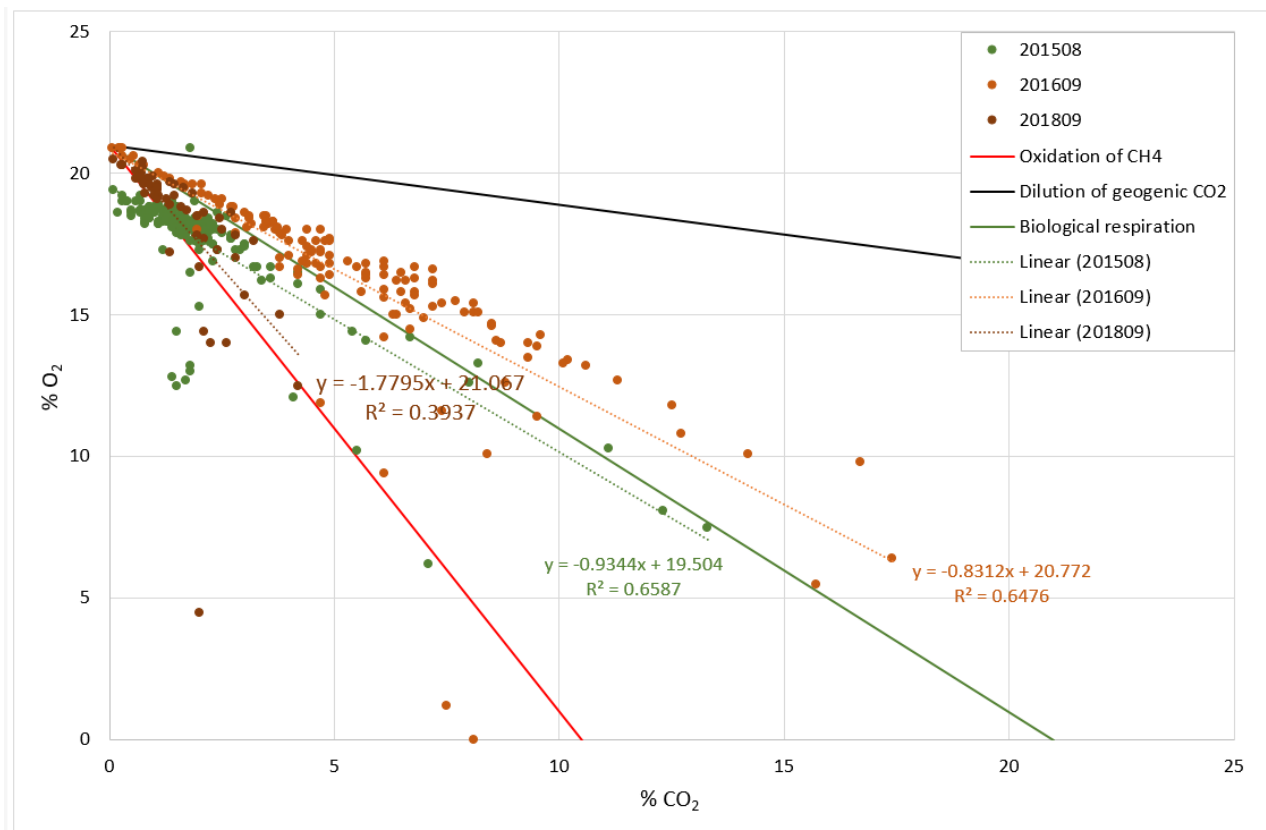


**Figure 160. Binary plot of soil gas compositions, Lancashire, by survey**

#### 7.4.9 Shale gas activity and near surface CO<sub>2</sub> concentrations at PNR

The mobile CO<sub>2</sub> laser system was deployed 4-5 December 2018. There was no suggestion that fugitive emissions were likely, but the opportunity arose to rapidly assess near ground CO<sub>2</sub> concentrations against available baseline data during a pause in operations at PNR, when the PNR-1z well was expected to be under pressure following injection of hydraulic fracturing fluids and the well being shut-in.

The upper panel in Figure 161 shows the mobile laser CO<sub>2</sub> data from the baseline soil gas survey in September 2018. Before injection, there is a general pattern of higher CO<sub>2</sub> in the westernmost field compared to the east field that borders the PNR well pad, following the field boundary; this pattern is consistent with the September 2016 soil gas survey. Taken alongside the Lancashire gas compositions, which predominantly fall along the biogenic CO<sub>2</sub> line (160.), this further suggests the difference in CO<sub>2</sub> seen in the baseline data are related to land-use rather as opposed to a geogenic input.

The mobile laser survey conducted in December 2018, during the pause in injection, suggests marginally higher CO<sub>2</sub> across the field adjacent to the well pad (overlaid in lower panel, Figure 161). However, the prevailing conditions (extremely wet particularly in this easternmost field) were not favourable for soil gas measurements generally, and CO<sub>2</sub> concentrations at the near surface were not significantly greater than the baseline values.

Even if fugitive gas were present, it is difficult to predict where fluid migration from depth might reach the surface, whether it will follow natural or man-made pathways. In this case, the spatial distribution of CO<sub>2</sub> is diffuse and constrained by the field boundary, which suggests a relationship with land-use and shallow biological activity, rather than to shale gas activities in the area. If a further opportunity arises, there would be merit in combining the mobile laser survey with collection on soil gas for composition and isotopic analysis to provide further information on the likely source of CO<sub>2</sub>.



**Figure 161. Mobile laser CO<sub>2</sub>, September 2018 (upper panel) and December 2018 (lower panel). CO<sub>2</sub> values are concentration in ppm.**

#### **7.4.10 April 2019 CO<sub>2</sub> flux and $\delta^{13}\text{C}$ isotopes in CO<sub>2</sub> - Preliminary Data**

A further survey was carried out in April 2019 (delayed from March due to poor weather) after hydraulic fracturing and flow testing operations on the PNR-1z well had been completed. The repeat CO<sub>2</sub> flux measurements taken in April 2019 (Figure 162) are comparable, if not generally lower, than those obtained during the three 2015 to 2018 surveys shown in Figure 157. Viewed alongside soil gas data from the survey, including stable carbon isotope  $\delta^{13}\text{C}$  in CO<sub>2</sub> analysis (average -27.41, range -25.57 to -28.48‰), this indicates CO<sub>2</sub> originating from a biogenic source, most likely related to routine farming activities and in line with landowner reports of recent application of fertiliser which would markedly increase biological activity. While this is a

preliminary interpretation of the data, there is no evidence of impact on soil gas from the shale gas operations carried out at the PNR site up until April 2019. .

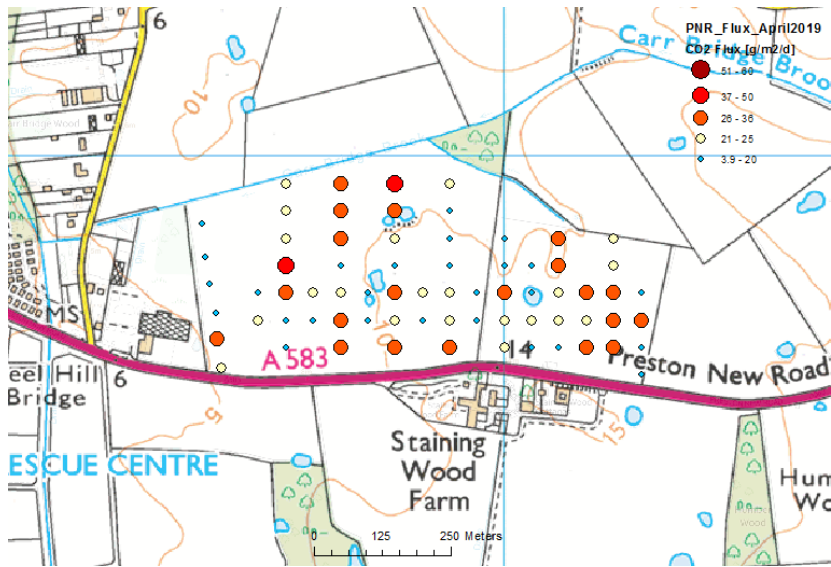


**Figure 162. Preliminary: Geospatial distribution of CO<sub>2</sub> flux measured at Preston New Road, April 2019**

### **7.5 GEOSTATISTICAL ANALYSIS OF SAMPLING REQUIREMENTS FOR SOIL GAS SURVEY MEASUREMENTS**

A statistical evaluation of soil gas datasets was carried out to examine spatial and temporal variability. The spatial distribution of survey observations was assessed on the basis of a geostatistical model using prior information on likely sources of variation and analysis of the data. The developed model can potentially be used to support decisions on sampling requirements for any future monitoring required during baseline and operational phases of shale gas development.

A critical consideration in ongoing monitoring of soil gas concentrations or fluxes (i.e. the parameters) is the number and frequency of measurements (i.e. sample design) required to produce a meaningful estimate of the soil gas status. The accuracy of any estimate of soil gas status will vary according to the number of measurements and the amount of variation in the parameter values. With measurements available from more than two years of monitoring in the Vale of Pickering, we are in a position to assess the degree of spatial and temporal variation in the observations and the implications for our sampling requirements.

The first stage of such an assessment is to decide the exact spatial and/or temporal scale over which we wish to predict the soil gas concentrations. For instance, we might wish to determine the field scale average concentrations or to continuously map the variation in concentration. Both estimates will be subject to uncertainty. For example, Figure 163 (left) shows a geostatistical prediction of the variation of CO<sub>2</sub> flux across a field in November 2015. Note that geostatistical models require that observations are normally distributed whereas the CO<sub>2</sub> fluxes are highly skewed. Therefore, we shifted and log-transformed the data prior to predicting this map. Figure 163 (right) indicates the uncertainty associated with the predictions at each site. It is clear that the expected errors increase as the predictions move away from the measurement sites (although larger errors are also evident at the field edges).

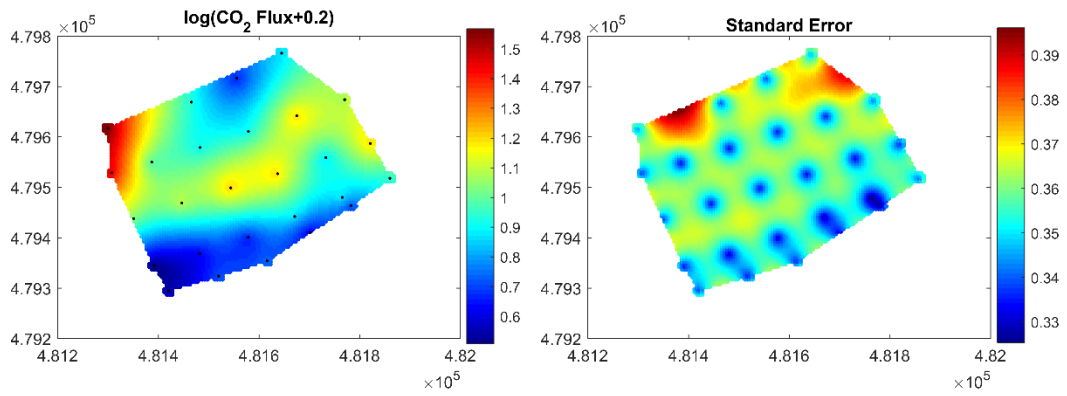


**Figure 163. Geostatistical prediction of log (CO<sub>2</sub> flux +0.2) with measurement locations denoted by black dots (left) and associated standard errors (right). Units are log(g m<sup>-2</sup> d<sup>-1</sup>).**

Both the predictions and the standard errors shown in Figure 163 depend on the spatial variability or correlation of the flux measurements. This spatial variation can be expressed in terms of a variogram (Webster & Oliver, 2007). The variogram describes how the expected squared difference between two observed values increases as the distance between the two measurements increases. The variograms shown in Figure 164 for log (CO<sub>2</sub> flux +0.2) were estimated by residual maximum likelihood (Lark & Cullis, 2006) from the measurements made in each field campaign. Some differences in these variograms from different campaigns are evident. The total variation is largest in the June 2016 and August 2016 campaigns whereas measurements made a small distance apart are most similar for the November 2015 and October 2016 campaigns.

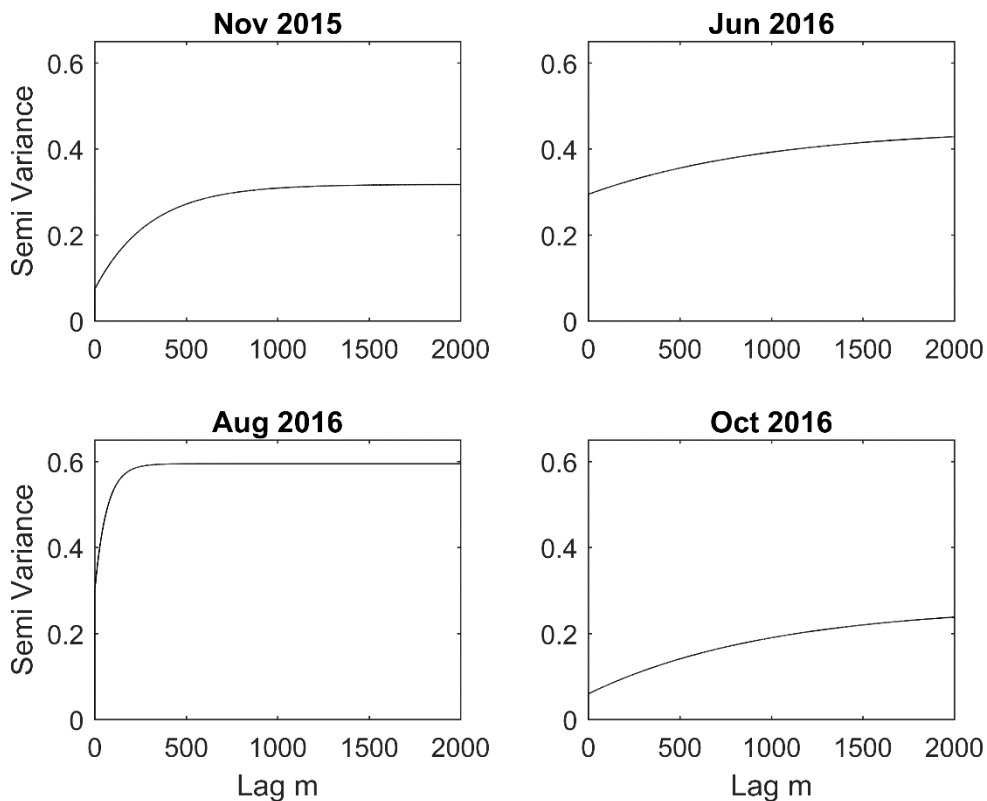


**Figure 164. Maximum likelihood estimates of variograms for of log (CO<sub>2</sub> flux +0.2).**

Once we know the variogram for a particular variable it is possible to use it to calculate the uncertainty associated with spatial predictions of that variable based on any proposed set of measurement sites. For example, we consider 81 soil gas measurements positioned on a regular square grid and the prediction of the CO<sub>2</sub> flux at the very centre of that grid so that the prediction

site is equidistant from the four closest measurements. If we increase the grid-spacing we can explore how the standard errors increase as the measurement intensity decreases (Figure 165).

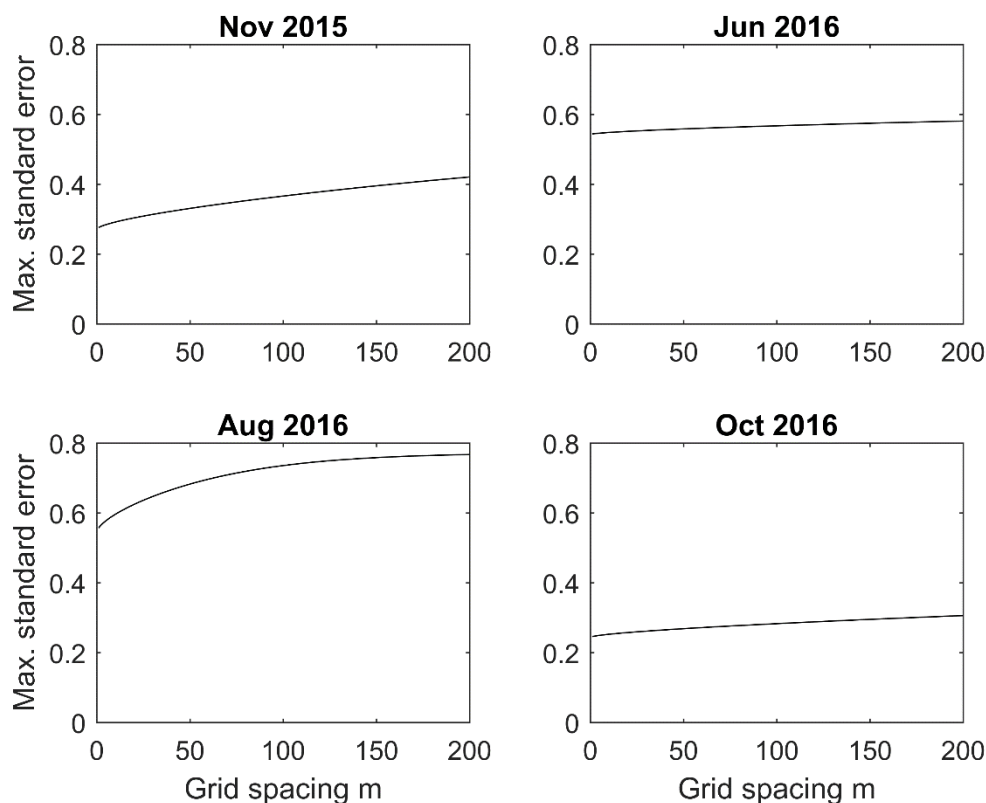


**Figure 165. Standard errors for spatial log (CO<sub>2</sub> flux +0.2) predictions at the centre of 81-point regular square grids of different sizes.**

The rate of increase in errors reflect the variograms shown in Figure 164, with the largest errors occurring in June and August when the fluxes are more variable. Figure 166 shows the results for a similar exercise using CO<sub>2</sub> concentrations.

Although based on a relatively small number of surveys, these results likely reflect the higher biological activity (plant and microbial) in the main spring and summer growing seasons compared with lower levels of activity in the autumn. They support previous studies (e.g. Beaubien et al, 2013) in suggesting that the autumn is the optimal time for detecting any emissions resulting from shale gas (or other) operations as natural background is at its lowest. The variation in error with grid spacing was again more significant for spring and summer surveys. The errors associated with the relatively wide spacing of soil gas and flux measurements (200 m) will be offset by the lower errors arising from more closely spaced mobile laser data (typically 10 m spacing).

The same approach can also be used to assess the implications of different temporal frequencies of measurements using the data from the continuous CO<sub>2</sub> flux and concentration monitoring stations at KM8 and a site to the east, respectively. In this case, we predict the gas variable half-way between two measurement times and consider the implications of increasing the gap between measurements (Figure 167 and Figure 168). The benefits of a high frequency of measurements are evident in each case. A very low standard error applies at the 1 hour rate of sampling used for the soil gas and flux measurements and would also be expected for the 30 minute averages derived from the very high (10 Hz) data acquisition rates of the eddy covariance system.

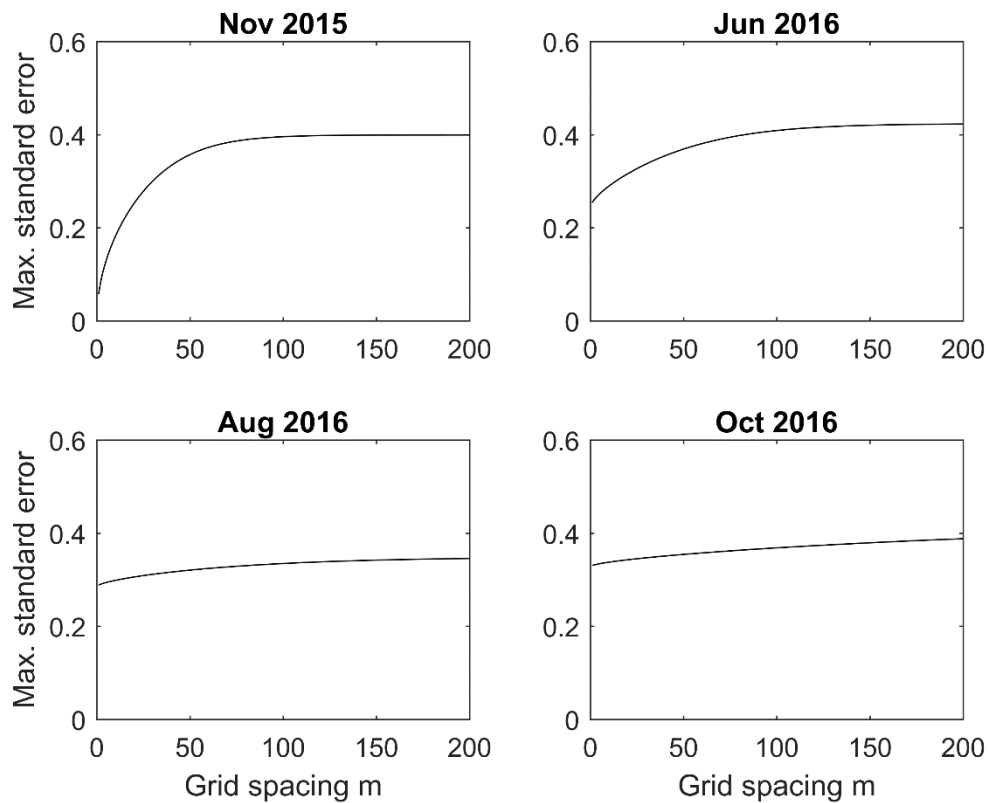


**Figure 166. Standard errors for spatial log (CO<sub>2</sub> conc +0.2) predictions at the centre of 81-point regular square grids of different sizes. Units are log (%).**

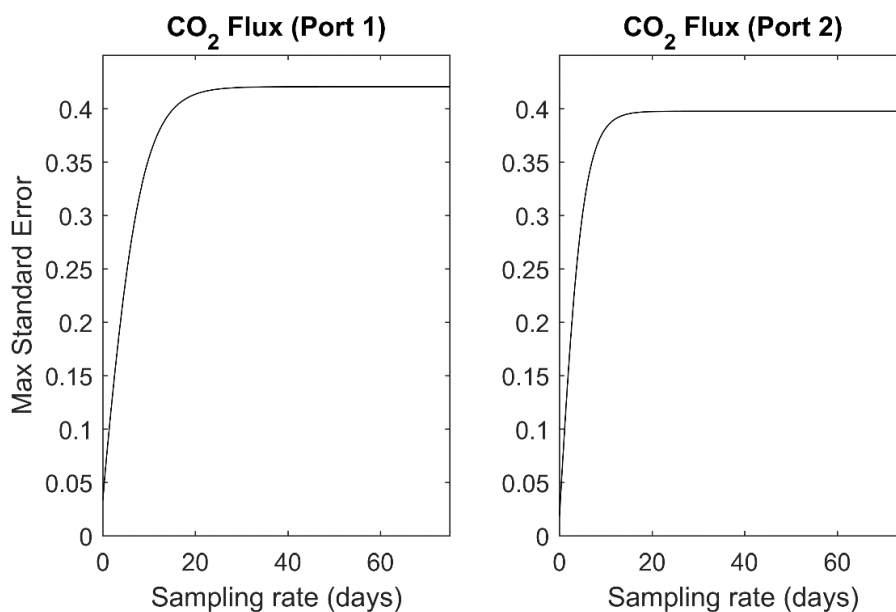


**Figure 167. Standard errors for temporal log (CO<sub>2</sub> flux +0.2) predictions at the time midway between two measurements as a function of time between measurements.**

In conclusion, now that datasets illustrating the spatial and temporal variation of gas concentrations and fluxes are available we are in a position to use geostatistical techniques to estimate the expected errors that will result from spatial or temporal prediction of these properties over any specified scale under the assumption that these future surveys follow the same patterns of variation. This can be used to guide future surveys or continuous measurements and the analysis can be refined by incorporating the data from that monitoring.

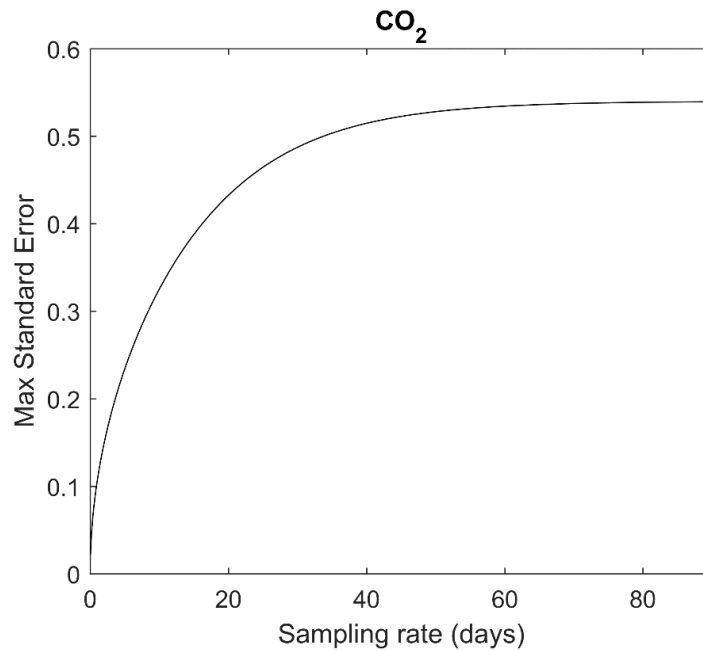


**Figure 168. Standard errors for temporal log (CO<sub>2</sub> concentration +0.2) predictions at the time midway between two measurements as a function of time between measurements.**

## 7.6 SUMMARY AND CONCLUSIONS (SOIL GAS)

Over the baseline monitoring period, the soil gas monitoring activity has employed an evolving range of techniques to develop an initial body of baseline soil gas data for the Vale of Pickering and Lancashire shale gas sites. The application of survey and continuous monitoring techniques across the monitoring period is summarised in Table 31 in Section 7.3, and is included again below for convenience; it reflects a change in priorities as the project has progressed and reflecting progress with industrial activity at the KM8 and PNR shale gas sites. While not always continuous, taking data available from all techniques, in parallel with overlapping air quality and radon monitoring techniques, the data obtained throughout the monitoring period enables natural (e.g. diurnal and seasonal) variations in soil gas to be evaluated, thereby providing a baseline against which any shale gas related impacts can be distinguished.

### 7.6.1 CO<sub>2</sub> flux and soil gas surveys

Soil gas monitoring in survey mode is highly mobile and has become increasingly responsive. It has been possible, from the survey data, to begin to ascertain baseline conditions before shale gas activities occur and an initial estimate of the baseline CO<sub>2</sub> flux and soil gas has been developed for both Kirby Misperton (see the summary CO<sub>2</sub> flux data in Table 32 and soil gas maps, boxplots and binary plots in Figures 153 to 155) and Preston New Road (33 and Figures 158 to 160.), against which the impact of shale gas activities can be assessed. Tables and boxplots and example maps are again included below for convenience but please note that these are examples and cannot be taken in isolation. A robust assessment of any impact from hydraulic fracking activities needs to take account of seasonal and diurnal variations using all the data available. Gas composition analysis indicates that baseline CO<sub>2</sub> primarily originates from biological processes in the shallow subsurface, with a smaller contribution from the oxidation of CH<sub>4</sub>, depending on the time of year (Section Figures 155 and 160.).

The challenge with survey mode is weather dependency. The optimum season for UK soil gas surveys has been found to be autumn; at a practical level, winter campaigns in the UK typically yield little useful data (soil gas becomes trapped and flux to atmosphere is impeded). Statistical analysis of Vale of Pickering data suggests autumn campaigns are least sensitive to changes in

grid spacing. Early summer is also favourable statistically; while variation in parameter values is higher overall (because of the growing season), it is less sensitive to changes in distance between measurements compared with November and August. On the other hand, baseline soil gas in late spring/summer tends to be dominated by CO<sub>2</sub> produced by biological respiration, but still yield valuable baseline data.

**Table 34. Overview of soil gas monitoring 2015-2019.**

Region	Survey mode Mobile laser surveys, and broad scale soil gas and flux grids	Continuous monitoring
Vale of Pickering Kirby Misperton and KM8	November 2015 March 2016 (no data) June 2016 August 2016 October 2016	Kirby Misperton soil gas station: August 2016 to February 2019 <sup>†</sup> KM8 CO <sub>2</sub> flux station: October 2016 to May 2018 KM8 Open path scanning CH <sub>4</sub> laser: November 2016 to March 2017
Fylde Preston New Road (PNR) and Roseacre (RLG)	August 2015 September 2016 September 2018 (PNR only) December 2018 (mobile laser PNR only)*	PNR Eddy covariance: January 2016 to March 2019

\* post-hydraulic fracturing

<sup>†</sup>data acquisition from the Kirby Misperton soil gas station is ongoing but can no longer be accessed remotely and requires manual download; data for March 2019 onwards will be reported in later reports.

**Table 35. Summary of baseline CO<sub>2</sub> flux data from soil gas surveys in Kirby Misperton.**  
\*negative value suggests soil acting as CO<sub>2</sub> sink

Survey	n	Minimum CO <sub>2</sub> flux g m <sup>-2</sup> day <sup>-1</sup>	Maximum CO <sub>2</sub> flux g m <sup>-2</sup> day <sup>-1</sup>	Mean g m <sup>-2</sup> day <sup>-1</sup>
2015 November	142	3.37	34.71	13.18
2016 June	115	2.48	142.28	32.01
2016 August	116	-24.51*	98.19	19.07
2016 October	103	-30.55*	40.56	12.44

**Table 36. Summary of baseline CO<sub>2</sub> flux data from soil gas surveys in Lancashire.**  
\*negative value suggests soil acting as CO<sub>2</sub> sink

Survey	n	Minimum CO <sub>2</sub> flux g m <sup>-2</sup> day <sup>-1</sup>	Maximum CO <sub>2</sub> flux g m <sup>-2</sup> day <sup>-1</sup>	Mean g m <sup>-2</sup> day <sup>-1</sup>
2015 August	152	11.25	650.60	41.72
2016 September	152	-70.99*	45.20	23.02
2018 September	72	9.31	59.59	32.16

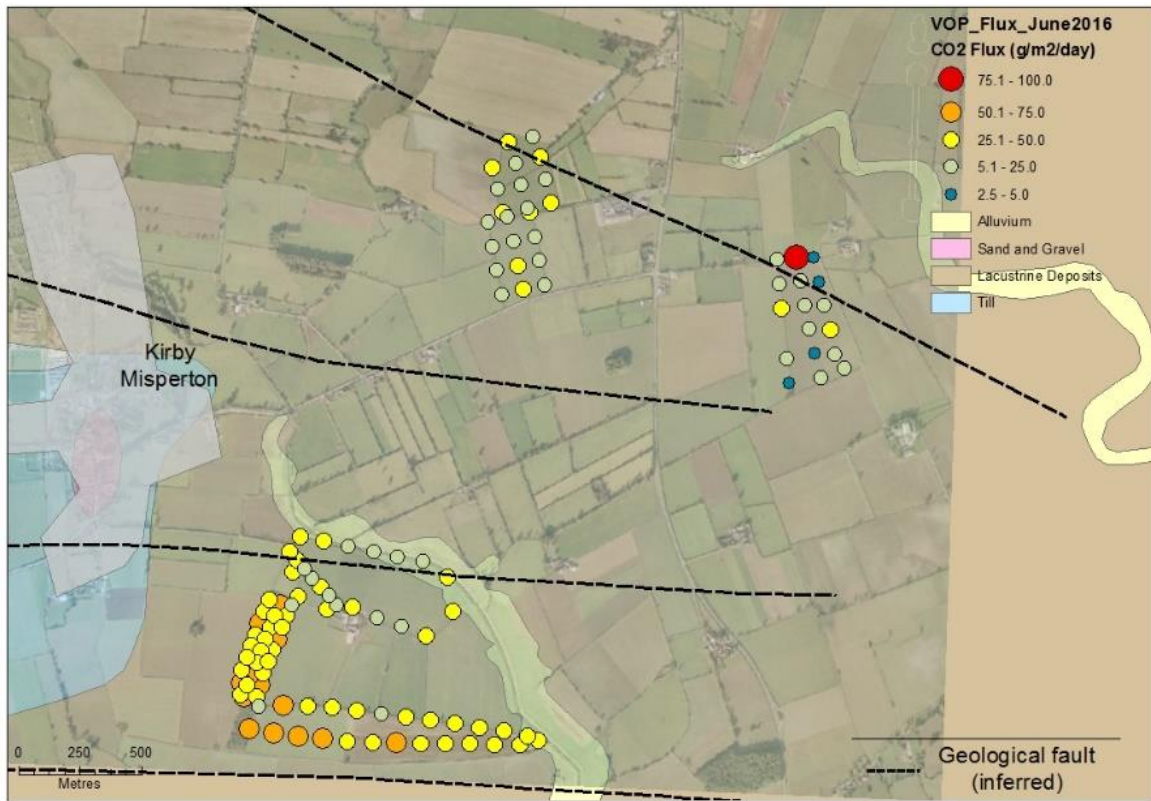


Figure 169. Example geospatial distribution of CO<sub>2</sub> flux at Kirby Misperton, from field survey June 2016.

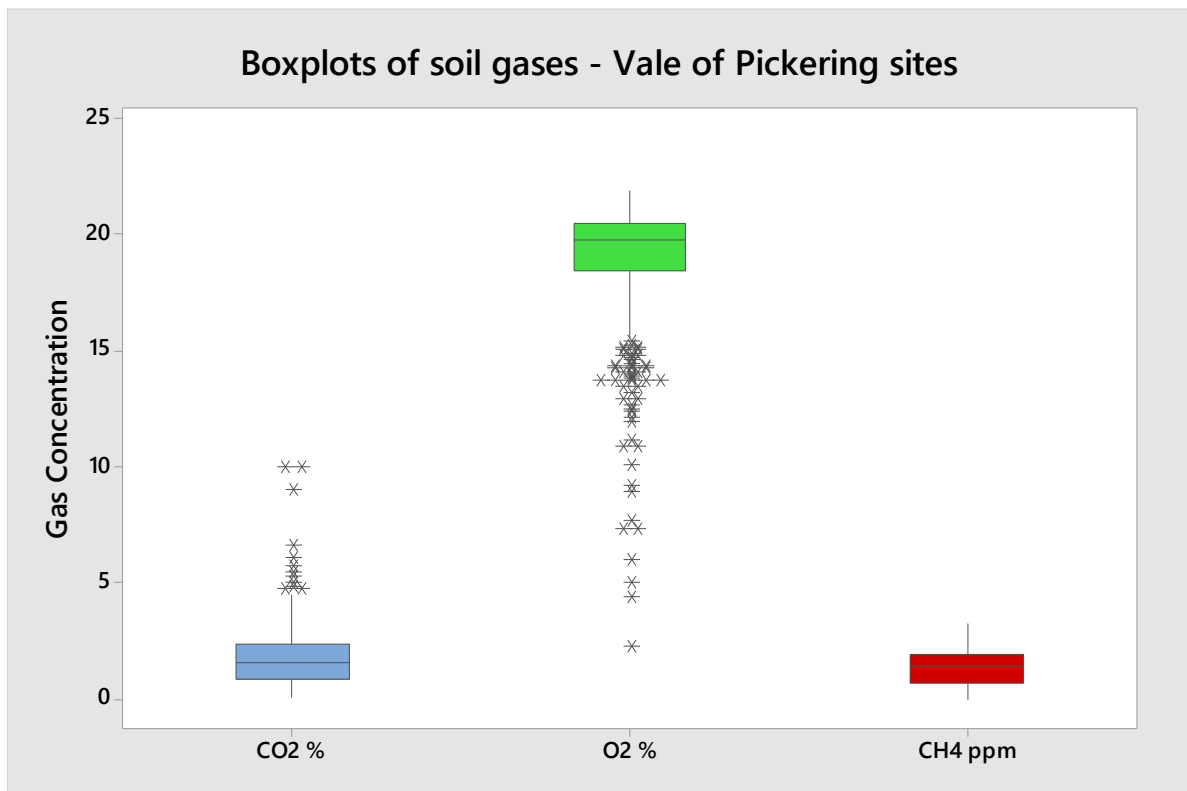


Figure 170 Compiled 2015-2018 survey soil gas data for Vale of Pickering sites

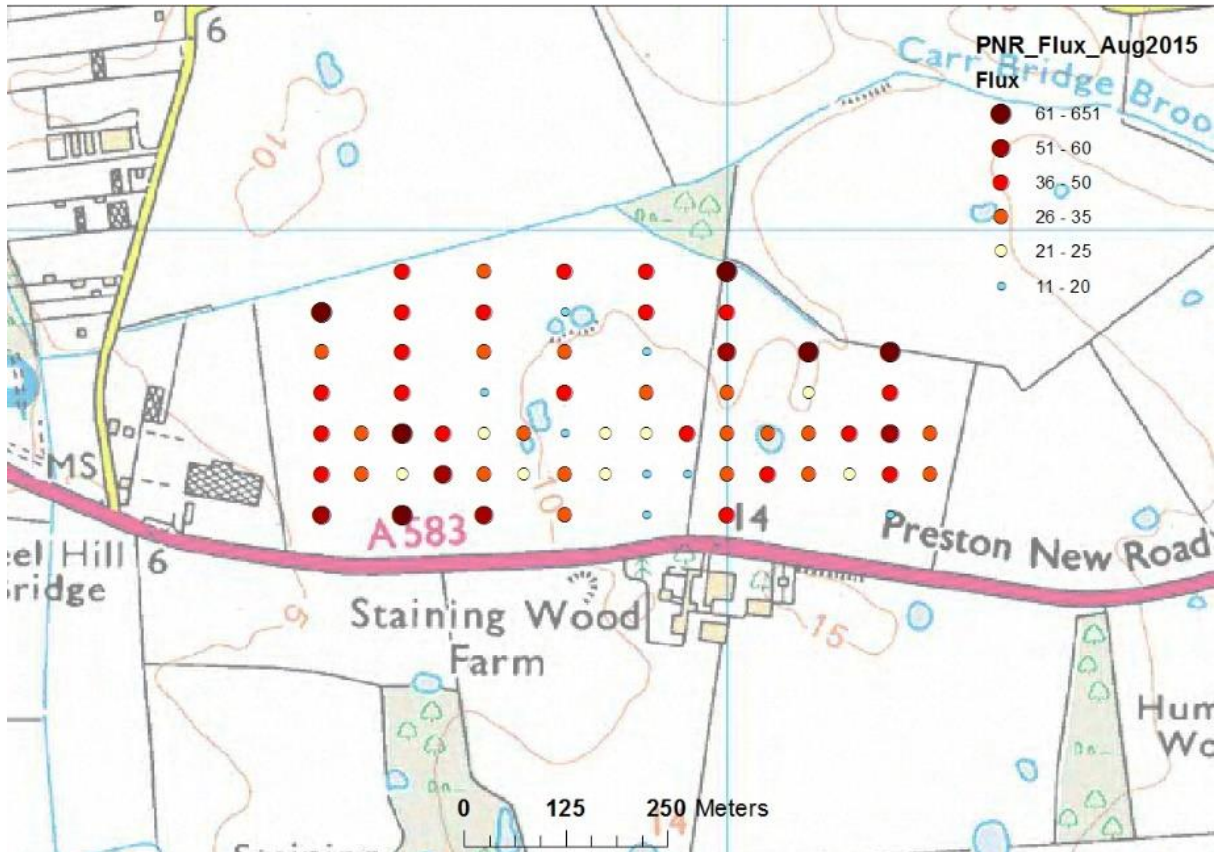


Figure 171. Example geospatial distribution of CO<sub>2</sub> flux at Preston New Road, from field survey August 2015

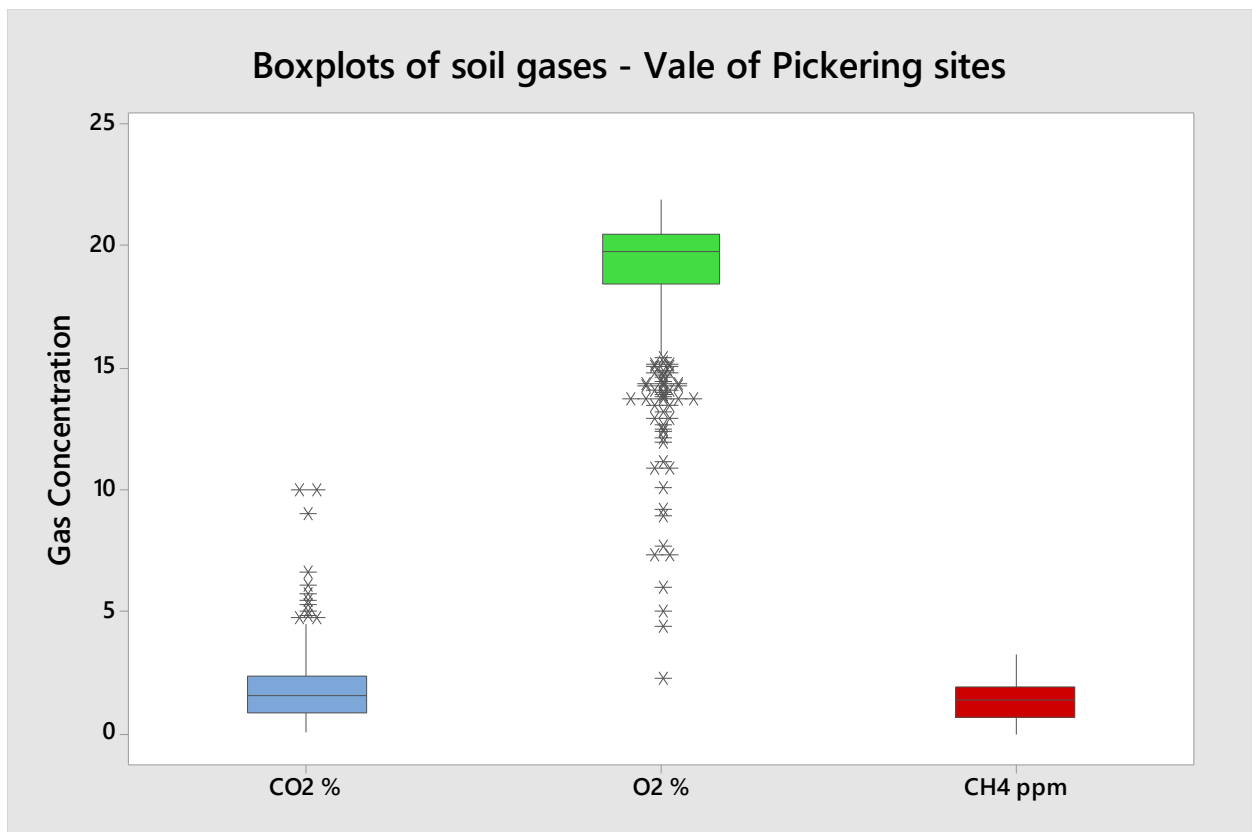
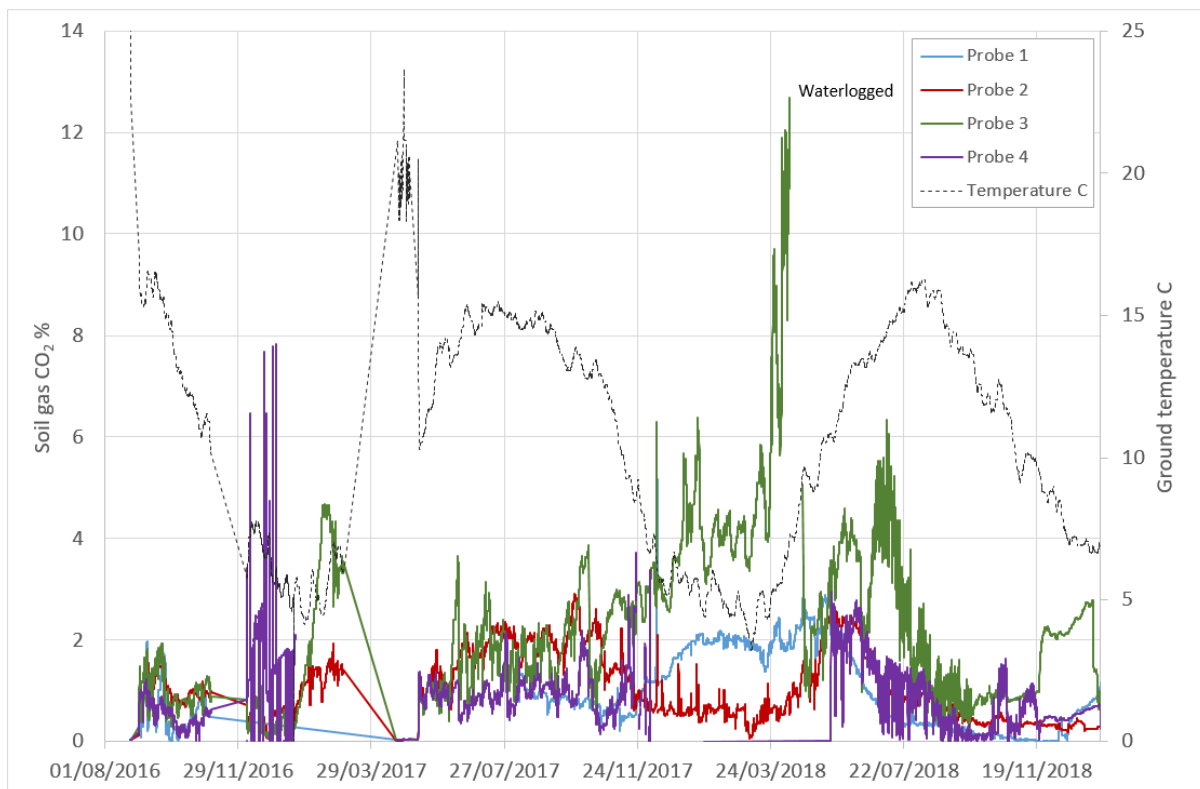
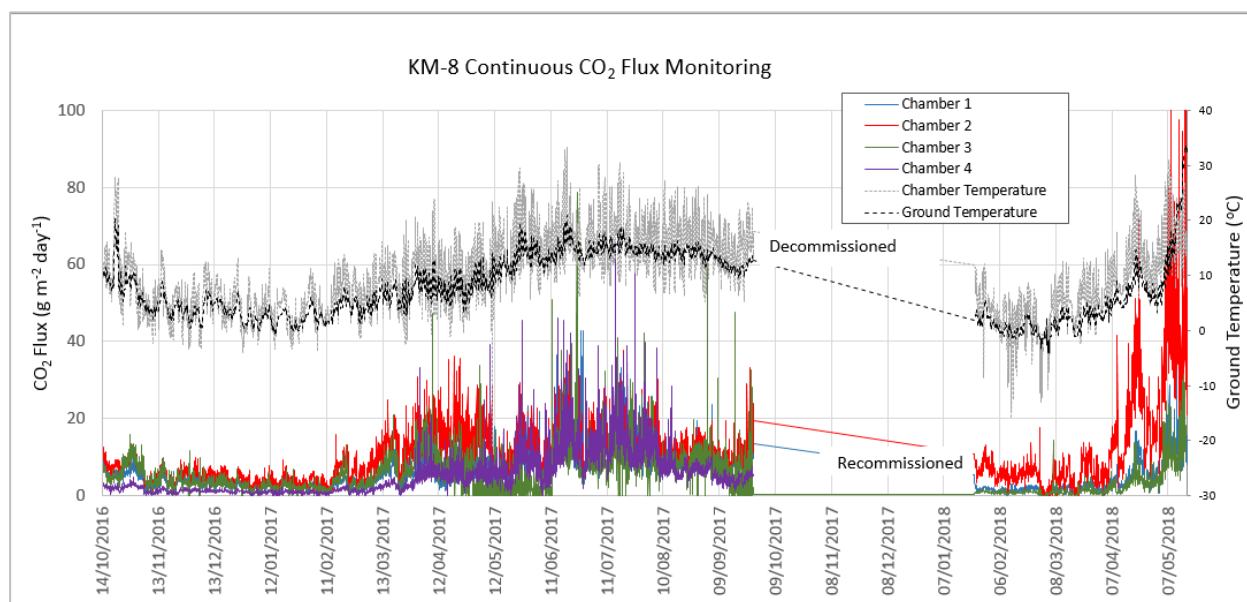


Figure 172. Compiled 2015-2018 survey soil gas data for Vale of Pickering sites



**Figure 173. Summary of all continuous soil gas data from the monitoring station east of Kirby Misperton, August 2016 to January 2019.**



**Figure 174. Continuous time series plot of CO<sub>2</sub> flux from chambers 1, 2, 3 and 4, along with ground and chamber temperature, and 10 day period in March 2017 showing flux changes in response to diurnal cycles and weather events (inset).**

The rapid response attempt to assess the impact of shale gas activities in Lancashire on soil gas using the mobile laser approach was a qualified success, given the unfavourable winter weather and challenging ground conditions. While no discrete signature was detected that might be related to the shale gas activities, the diffuse spatial distribution of CO<sub>2</sub> across the survey area was ambiguous but appeared to be constrained by field boundaries and therefore more likely to be related to surface agricultural activities than fugitive emissions from shale gas activities. Further

gas composition and isotopic analysis of CO<sub>2</sub> would provide more information and will be included in any future campaign, where conditions allow.

Fugitive emissions during shale gas operations could occur at any time of the year, and sufficient baseline soil gas monitoring data is needed as far as possible from across the seasons to allow natural/seasonal variations to be accounted for, or to enable a process-based approach (Romanak et al., 2012) to be sensibly interpreted.

We recommend baseline monitoring in survey mode be continued. The survey design is appropriate for the required level of uncertainty. We recommend spring/early summer, along with autumn, as optimum periods for conducting further surveys. Attempting baseline surveys in the UK winter is not effective and should be avoided unless it is specifically in response to shale gas activities.

### **7.6.2 Continuous monitoring**

Some continuous monitoring techniques proved more successful than others. The eddy covariance system at Little Plumpton has operated almost continuously since its installation (and continues to operate).

The soil gas monitoring station installed on land to the east of KM8 in the Vale of Pickering also performed consistently throughout most of the monitoring period, although the communications system is no longer operational and data acquisition requires a site visit and manual download (Figure 150 in Section 7.4.3, included below for convenience). Near-continuous data was also obtained from the flux system at KM8 during its deployment (Figure 143 in Section 7.4.2, and included below).

The deployment of the methane scanning laser system at KM8 suffered technical issues, exacerbated by shale gas site developments that prevented its reinstallation. Long term time series data, together with the geostatistical appraisal of selected survey data, demonstrate that emissions related to shale gas operations will be easiest to detect in the autumn when baseline biological activity is lower, and the soil remains dry.

We recommend maintaining continuous monitoring techniques where possible. Despite the technical problems, continuous monitoring is cost-effective as it provides broader temporal context and continuity, as well as supporting data from survey mode ‘snapshots’, at modest staff cost.

Finally, while not a statutory requirement for shale gas, baseline soil gas monitoring is highly visible to stakeholders and local communities, which may help with securing local cooperation and support.

## **7.7 REFERENCES**

- Beaubien, S E, Jones, D G, Gal, F, Barkwith, A K A P, Braibant, G, Baubron, J C, Ciotoli, G, Graziani, S, Lister, T R, Lombardi, S, Michel, K, Quattrocchi, F and Strutt, M H. 2013. Monitoring of near-surface gas geochemistry at the Weyburn, Canada, CO<sub>2</sub>-EOR site, 2001–2011. *International Journal of Greenhouse Gas Control*, Vol. 16, Supplement 1, S236-S262.
- Györe, D, Mckavney, R, Gilfillan, S M V and Stuart, F M. 2018. Fingerprinting coal-derived gases from the UK. *Chemical Geology*, Vol. 480, 75-85.
- Lark, R M, Cullis, B R and Welham S J. 2006. On spatial prediction of soil properties in the presence of a spatial trend: the empirical best linear unbiased predictor (E-BLUP) with REML. *European Journal of Soil Science*, Vol 57, 787–799.
- Romanak, K D, Bennett, P C, Yang, C and Hovorka, S D. 2012. Process-based approach to CO<sub>2</sub> leakage detection by vadose zone gas monitoring at geologic CO<sub>2</sub> storage sites. *Geophysical Research Letters*, Vol. 39, L15405.

- Smedley, P L, Ward, R S, Allen, G, Baptie, B, Daraktchieva, Z, Jones, D G, Jordan, C J, Purvis, R M and Cigna, F. 2015. Site selection strategy for environmental monitoring in connection with shale-gas exploration: Vale of Pickering, Yorkshire and Fylde, Lancashire. *British Geological Survey Open Report*, OR/15/067, pp. 22.
- Webster, R and Oliver, M A. 2007. *Geostatistics for Environmental Scientists*, 2nd Edition. John Wiley and Sons, Chichester.
- Allison, M L. 2001. Hutchinson, Kansas: A Geologic Detective Story. *Geotimes*, Vol. October 2001.
- Annunziatellis, A, Beaubien, S E, Bigi, S, Ciotoli, G, Coltella, M, and Lombardi, S. 2008. Gas migration along fault systems and through the vadose zone in the Latera caldera (central Italy): Implications for CO<sub>2</sub> geological storage. *International Journal of Greenhouse Gas Control*, Vol. 2, 353-372.
- Environment Agency. 2010. Guidance on monitoring landfill gas surface emissions. *Environment Agency Report*, LFTGN 07 (Bristol).
- European Union. 2009a. Directive 2009/29/EC of the European Parliament and of the Council of 23 April 2009 amending Directive 2003/87/EC so as to improve and extend the greenhouse gas emission allowance trading scheme of the Community (Text with EEA relevance).
- European Union. 2009b. Directive 2009/31/EC of the European Parliament and of the Council of 23 April 2009 on the geological storage of carbon dioxide and amending Council Directive 85/337/EEC, European Parliament and Council Directives 2000/60/EC, 2001/80/EC, 2004/35/EC, 2006/12/EC, 2008/1/EC and Regulation (EC) No 1013/2006 (Text with EEA relevance).
- Johnson, G, Hicks, N, Bond, C E, Gilfillan, S M V, Jones, D, Kremer, Y, Lister, R, Nkwane, M, Maupa, T, Munyangane, P, Robey, K, Saunders, I, Pearce, J, Shipton, Z K, and Haszeldine, R S. In press. Detection and understanding of natural CO<sub>2</sub> releases in KwaZulu-Natal, South Africa. *Energy Procedia*.
- Romanak, K D, Bennett, P C, Yang, C, and Hovorka, S D. 2012. Process-based approach to CO<sub>2</sub> leakage detection by vadose zone gas monitoring at geologic CO<sub>2</sub> storage sites. *Geophysical Research Letters*, Vol. 39, L15405.
- Ziogou, F, Gemeni, V, Koukouzas, N, de Angelis, D, Libertini, S, Beaubien, S E, Lombardi, S, West, J M, Jones, D G, Coombs, P, Barlow, T S, Gwosdz, S, and Krüger, M. 2013. Potential Environmental Impacts of CO<sub>2</sub> Leakage from the Study of Natural Analogue Sites in Europe. *Energy Procedia*, Vol. 37, 3521-3528.

# Appendix A

## **ABSTRACT TO SHAW ET AL. (2019):**

We report a 24-month statistical baseline climatology for continuously-measured atmospheric carbon dioxide (CO<sub>2</sub>) and methane (CH<sub>4</sub>) mixing ratios linked to surface meteorology as part of a wider environmental baselining project tasked with understanding pre-existing local environmental conditions prior to shale gas exploration in the United Kingdom.

The baseline was designed to statistically characterise high-precision measurements of atmospheric composition gathered over two full years (between February 1<sup>st</sup> 2016 and January 31<sup>st</sup> 2018) at fixed ground-based measurement stations on, or near to, two UK sites being developed for shale gas exploration involving hydraulic fracturing. The sites, near Blackpool (Lancashire) and Kirby Misperton (North Yorkshire), were the first sites approved in the UK for shale gas exploration since a moratorium was lifted in England. The sites are operated by Cuadrilla Resources Ltd. and Third Energy Ltd., respectively.

A statistical climatology of greenhouse gas mixing ratios linked to prevailing local surface meteorology is presented. This study diagnoses and interprets diurnal, day-of-week, and seasonal trends in measured mixing ratios and the contributory role of local, regional and long-range emission sources.

The baseline provides a set of contextual statistical quantities against which the incremental impacts of new activities (in this case, future shale gas exploration) can be quantitatively assessed. The dataset may also serve to inform the design of future case studies, as well as direct baseline monitoring design at other potential shale gas and industrial sites. In addition, it provides a quantitative reference for future analyses of the impact, and efficacy, of specific policy interventions or mitigating practices. For example, statistically significant excursions in measured concentrations from this baseline (e.g. >99<sup>th</sup> percentile) observed during phases of operational extraction may be used to trigger further examination in order to diagnose the source(s) of emission and links to on-site activities at the time, which may be of importance to regulators, site operators and public health stakeholders. A guideline algorithm for identifying these statistically significant excursions, or “baseline deviation events”, from the expected baseline conditions is presented and tested. Gaussian plume modelling is used to further these analyses, by simulating approximate upper-limits of CH<sub>4</sub> fluxes which could be expected to give observable enhancements at the monitoring stations under defined meteorological conditions.

## **ABSTRACT TO LOWRY ET AL. (2019):**

Baseline mobile surveys of methane sources have been performed in the Fylde and Ryedale regions of Northern England over the 2016-19 period, around proposed unconventional gas extraction sites. The aim was to identify and characterise nearby methane sources ahead of hydraulically fractured shale gas extraction, so that this potential additional source of emissions to atmosphere may be readily distinguished from adjacent sources for quantification, should gas production take place.

The surveys have used ethane measurement to separate combustion, thermogenic gas and biogenic sources. Sample collection of source plumes followed by high precision  $\delta^{13}\text{C}$  analysis of methane, to separate and isotopically characterise sources, adds additional distinction between active and closed landfills, and ruminant eructations from manure.

The surveys show that both drill sites and adjacent fixed monitoring sites have cow barns and gas network pipeline leaks as sources of methane within a 1 km range. Under well-mixed daytime conditions these sources are generally detectable as above baseline elevations up to 100 m downwind for the larger gas leaks and up to 500 m downwind for populated cow barns. Under night-time and cold morning inversion conditions the sphere of surface influence of these sources

is much greater. These two sources are readily separated by isotopes ( $\delta^{13}\text{C}$  of -67 to -58 ‰ for barns, compared to -43 to -39‰ for gas leaks), and ethane:methane ratios (<0.001 for barns, compared to >0.05 for gas leaks). It is considered that careful analysis of these proxies for unconventional production gas, if and when available, will allow any fugitive emissions from operations to be distinguished from surrounding sources.

#### **ABSTRACT TO ALLEN ET AL. (2019):**

Methane has been detected at the BGS-University of Manchester greenhouse gas monitoring station near Cuadrilla's shale gas operations at Preston New Road, near Little Plumpton, Lancashire.

Enhanced methane concentration in the air east of the Cuadrilla site was recorded on 7th December 2018 and again between 11th and 17th January 2019. Analysis of the monitoring data indicates that this was due to the emission of non-combusted methane from the shale gas site.

The peak concentration of methane observed, which was in the January 2019 emission, exceeded 10,000 parts per billion (ppb). To put this into context, the typical atmospheric concentration of methane in this area has been observed to be in the range 1857 to 2544 (ppb).

The monitoring being carried out is part of the BGS-led environmental monitoring project which is jointly funded the BGS's National Capability programme and a grant awarded by the Department of Business, Energy and Industrial Strategy (BEIS).

This project represents the first independent, integrated monitoring programme set up to characterise the environmental baseline and any subsequent changes in areas where shale gas development is taking place. The monitoring has continued the first hydraulic fracturing operations at the Preston New Road shale gas site.

Data analysis in the report was conducted by Dr Jacob Shaw (University of Manchester) with Dr Grant Allen (University of Manchester) who was responsible for the supervision of the greenhouse gas component of the environmental monitoring project. Professor Rob Ward (BGS) is overall project manager.

#### **ABSTRACT TO PURVIS ET AL. (2019):**

Rural observations of air quality and meteorological parameters ( $\text{NO}_x$ ,  $\text{O}_3$ , NMHCs,  $\text{SO}_2$ , PM) were made over a 2.5-year period (2016–2018) before, during and after preparations for hydraulic fracturing (fracking) at a shale gas exploration site near Kirby Misperton, North Yorkshire, England. As one of the first sites to apply for permits to carry out hydraulic fracturing, it has been subject to extensive regulatory and public scrutiny, as well as the focus for a major programme of long-term environmental monitoring. A baseline period of air quality monitoring (starting 2016) established the annual climatology of atmospheric composition against which a 20-week period of intensive activity on the site in preparation for hydraulic fracturing could be compared. During this 'pre-operational phase' of work in late 2017, the most significant effect was an increase in ambient NO (3-fold) and  $\text{NO}_x$  (2-fold), arising from a combination of increased vehicle activity and operation of equipment on site. Although ambient  $\text{NO}_x$  increased, air quality limit values for  $\text{NO}_2$  were not exceeded, even close to the well-site. Local ozone concentrations during the pre-operational period were slightly lower than the baseline phase due to titration with primary emitted NO. The activity on site did not lead to significant changes in airborne particulate matter or non-methane hydrocarbons. Hydraulic fracturing of the well did not subsequently take place and the on-site equipment was decommissioned and removed. Air quality parameters then returned to the original (baseline) climatological conditions. This work highlights the need to characterise the full annual climatology of air quality parameters against which short-term local activity changes can be compared. Based on this study, changes to ambient  $\text{NO}_x$  appear to be the most significant air quality ahead of hydraulic fracturing. However, in rural locations, concentrations at individual sites are expected to be below ambient air quality limit thresholds.

## Appendix B

### ATMOSPHERIC COMPOSITION BASELINE STATISTICS FOR PNR AND KM

**Table A1 One-minute averaged CH<sub>4</sub> mixing ratios under different wind conditions at Preston New Road and Kirby Misperton during the measurement period 01/02/2016 to 31/01/2018. The wind directions are divided evenly into the four cardinal directions i.e. south refers to wind directions of 180° ± 45°.**

Statistic	Baseline CH <sub>4</sub> mixing ratio / ppb							
	Preston New Road (PNR)				Kirby Misperton (KM)			
	North	East	South	West	North	East	South	West
Maximum	30180	70690	16170	10480	6895	5145	34180	41420
P <sub>99</sub> *	3079	6156	2779	2544	2767	2665	2632	2627
P <sub>95</sub>	2458	3998	2424	2128	2473	2360	2269	2256
P <sub>90</sub>	2274	3252	2290	2034	2336	2231	2170	2136
P <sub>75</sub>	2098	2617	2116	1973	2093	2092	2076	2029
Mean ± 1σ	2081 ± 324	2538 ± 929	2076 ± 218	1979 ± 139	2061 ± 197	2057 ± 154	2049 ± 177	2021 ± 222
Median (P <sub>50</sub> )	2000	2273	2014	1949	1977	2009	2012	1977
P <sub>25</sub>	1962	2095	1961	1935	1943	1961	1971	1950
P <sub>0.1</sub>	1906	1934	1870	1871	1897	1894	1894	1891
Minimum	1873	1871	1857	1857	1866	1879	1870	1863

\* P<sub>i</sub> refers to the *i*<sup>th</sup> percentile e.g. P<sub>90</sub> refers to the 90<sup>th</sup> percentile.

**Table A2 One-minute averaged CO<sub>2</sub> mixing ratios under different wind conditions at Preston New Road and Kirby Misperton during the measurement period 01/02/2016 to 31/01/2018. The wind directions are divided evenly into the four cardinal directions i.e. south refers to wind directions of 180° ± 45°.**

Statistic	Baseline CO <sub>2</sub> mixing ratio / ppm							
	Preston New Road (PNR)				Kirby Misperton (KM)			
	North	East	South	West	North	East	South	West
Maximum	709	719	586	886	724	661	761	738
P <sub>99</sub> *	489	493	477	442	549	508	485	478
P <sub>95</sub>	450	469	454	421	488	460	443	442
P <sub>90</sub>	436	457	443	417	462	445	434	430
P <sub>75</sub>	423	441	428	413	431	427	425	419
Mean ± 1σ	418 ± 18	430 ± 21	420 ± 17	409 ± 10	424 ± 31	420 ± 23	418 ± 18	414 ± 16
Median (P <sub>50</sub> )	413	427	416	409	413	416	416	414
P <sub>25</sub>	408	416	409	403	406	406	408	406
P <sub>0.1</sub>	388	390	391	388	389	376	378	389
Minimum	380	379	384	382	373	366	364	373

\* P<sub>i</sub> refers to the *i*<sup>th</sup> percentile e.g. P<sub>90</sub> refers to the 90<sup>th</sup> percentile.

## GHG CHANGE DETECTION ALGORITHM

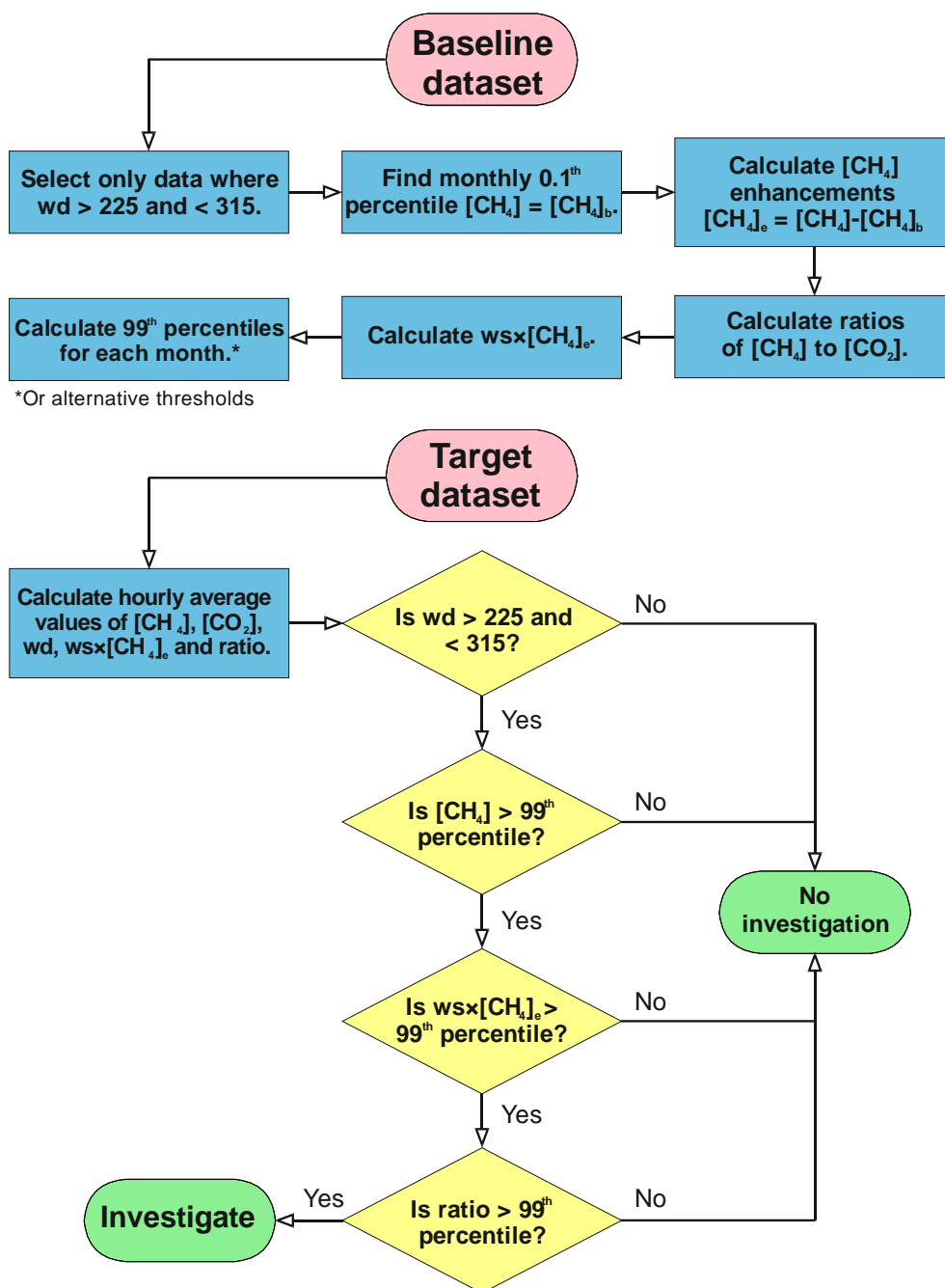


**Figure A3** Flow scheme for detecting baseline excursion events. Key to abbreviations:  $[CH_4]_b$  = 0.1<sup>th</sup> percentile  $[CH_4]$ ,  $[CH_4]_e$  =  $[CH_4]$  enhancement =  $[CH_4] - [CH_4]_b$ , wd = wind direction, ws = wind speed.

## SUMMARY OF GREENHOUSE GASES

Observations of  $CH_4$  and  $CO_2$  have continued at the fixed-site monitoring stations at PNR and KM since their inception in February 2016. Work characterising a baseline (background) of greenhouse gases ( $CH_4$  and  $CO_2$ ) over two years of observations (from February 2016 to January 2018), as a function of wind direction, time-of-day, day-of-week and month-of-year were reported in Shaw et al. (2019).  $CH_4$  and  $CO_2$  mixing ratios were shown to vary considerably depending on both wind direction (typically lower mixing ratios from the west) and season. Percentile statistics, allowing for the assessment of a “typical” range of  $CH_4$  and  $CO_2$  mixing ratios, were reported (and can be

found in Appendix B) for different wind directions. Shaw et al. (2019) also developed an algorithm which uses the baseline statistics to derive thresholds above which CH<sub>4</sub> would be enhanced beyond the typical range of baseline conditions. This algorithm allows for easy CH<sub>4</sub> change detection and was used to correctly identify venting of CH<sub>4</sub> from a conventional wellhead at the KMA site.

Multiple mobile vehicle surveys have been used to characterise a wider greenhouse gas baseline around each of the KM and PNR sites. These surveys have been used to identify local sources of CH<sub>4</sub> and CO<sub>2</sub> around each of the sites, using isotopic <sup>13</sup>C and ethane:methane ratios to apportion source type (such as biogenic, thermogenic etc.). The surveys have been conducted over a similar timeframe to the fixed-site monitoring and therefore provide further valuable insight into the local sources of greenhouse gases. Lowry et al. (2019) discusses these surveys in more detail.

Whilst baseline monitoring of greenhouse gases at KM has continued into 2019 (due to delays in commencing hydraulic fracturing), monitoring at PNR transitioned into operational monitoring when Cuadrilla began hydraulic fracturing operations in October 2018. Substantial enhancements of CH<sub>4</sub> were observed at the fixed-site monitoring station in January 2019 and were confirmed by the operators to be due to unloading of the well using a nitrogen lift. Details of this event will be the subject of a forthcoming scientific report. Measurements of greenhouse gases outside of this event at PNR, and throughout the past year at KM, have been broadly consistent with the first two years of baseline monitoring.

## BASELINE STATISTICS FOR AIR QUALITY PARAMETERS AT KM AND LP

These are the one-minute averages for the defined baseline period. However caution should be taken when using these data as air quality data has seasonal differences.

**Table A3. One minute averaged NO mixing ratios under different wind conditions at Kirby Misperton during the measurement period 1/2/16 – 18/9/17.**

\* P<sub>*i*</sub> refers to the *i*<sup>th</sup> percentile e.g. P<sub>90</sub> refers to the 90<sup>th</sup> percentile.

	Baseline NO mixing ration (ppb)							
	Kirby Misperton							
Statistic	N	NE	E	SE	S	SW	W	NW
Minimum	-0.67	-0.81	-0.87	-0.9	-1.17	-2	-2	-1.5
P <sub>1</sub>	-0.11	-0.08	-0.04	-0.1	-0.37	-0.37	-0.3	-0.15
P <sub>25</sub>	0.22	0.27	0.33	0.32	0.27	0.24	0.14	0.15
Median (P <sub>50</sub> )	0.4	0.46	0.54	0.64	0.66	0.53	0.33	0.36
P <sub>75</sub>	0.82	0.96	1.02	1.31	1.5	1.19	0.66	0.7
P <sub>90</sub>	1.49	1.55	1.89	2.36	3.09	2.62	1.32	1.26
P <sub>95</sub>	3.2	2.6	3.37	4.17	4.81	4.31	2.43	2.17
P <sub>99</sub>	13.7	11.27	12.2	12.89	10.76	11.69	10.58	11.16
Maximum	104.16	61.67	105.23	114.32	143.14	129.06	120.13	110
Mean	1.03	0.99	1.08	1.28	1.36	1.24	0.76	0.77

**Table A4. One minute averaged NO<sub>2</sub> mixing ratios under different wind conditions at Kirby Misperton during the measurement period 1/2/16 – 18/9/17.**

\* P<sub>i</sub> refers to the *i*<sup>th</sup> percentile e.g. P<sub>90</sub> refers to the 90<sup>th</sup> percentile.

	Baseline NO <sub>2</sub> mixing ration (ppb)							
	Kirby Misperton							
Statistic	N	NE	E	SE	S	SW	W	NW
Minimum	-2	-2	-1.93	-1.93	-1.57	-2	-2	-2
P <sub>1</sub>	-0.37	-0.2	0.27	0.33	0.39	-0.27	-0.23	-0.35
P <sub>25</sub>	0.49	0.81	1.36	1.62	2.08	1.1	0.53	0.54
Median (P <sub>50</sub> )	1.29	1.91	2.55	3.09	3.81	2.35	1.05	1.18
P <sub>75</sub>	2.96	3.78	4.83	6.25	7.01	4.98	2.07	2.45
P <sub>90</sub>	7.02	7.22	9.16	11.23	11.8	10.35	4.55	5.58
P <sub>95</sub>	12.99	11.45	12.12	14.14	15.81	15.6	8.77	11.35
P <sub>99</sub>	23.62	20.48	18.87	25	27.39	32.04	22.43	22.82
Maximum	70.95	81.8	251.14	276.62	167.33	153.08	120.32	118.47
Mean	2.95	3.24	3.91	4.87	5.6	4.5	2.25	2.56

**Table A5. One minute averaged NO<sub>x</sub> mixing ratios under different wind conditions at Kirby Misperton during the measurement period 1/2/16 – 18/9/17.**

\* P<sub>i</sub> refers to the *i*<sup>th</sup> percentile e.g. P<sub>90</sub> refers to the 90<sup>th</sup> percentile.

	Baseline NO <sub>x</sub> mixing ration (ppb)							
	Kirby Misperton							
Statistic	N	NE	E	SE	S	SW	W	NW
Minimum	-1.99	-1.98	-1.45	-0.62	-1.62	-2	-1.99	-2
P <sub>1</sub>	-0.09	0.1	0.49	0.57	0.51	-0.24	-0.19	-0.09
P <sub>25</sub>	0.76	1.14	1.81	2.12	2.65	1.46	0.75	0.8
Median (P <sub>50</sub> )	1.72	2.54	3.24	3.93	4.75	3.03	1.39	1.53
P <sub>75</sub>	3.79	4.69	5.86	7.71	8.66	6.38	2.67	3.17
P <sub>90</sub>	8.72	8.82	11.11	13.33	14.47	13.03	5.95	6.88
P <sub>95</sub>	16.36	14.04	15.37	18.12	19.32	19.85	11.58	13.77
P <sub>99</sub>	34.36	32.83	27.48	31.41	34.75	41.81	28.6	30.16
Maximum	127.2	126.7	260.03	313.34	292.99	251.81	234.46	167.56
Mean	3.98	4.23	4.99	6.14	6.96	5.75	3.01	3.33

**Table A6. One minute averaged O<sub>3</sub> mixing ratios under different wind conditions at Kirby Misperton during the measurement period 1/2/16 – 18/9/17.**

\* P<sub>i</sub> refers to the *i*<sup>th</sup> percentile e.g. P<sub>90</sub> refers to the 90<sup>th</sup> percentile.

	Baseline O <sub>3</sub> mixing ration (ppb)							
	Kirby Misperton							
Statistic	N	NE	E	SE	S	SW	W	NW
Minimum	-1.1	-0.72	-0.34	-1.52	-0.9	-0.71	-0.62	-1.63
P <sub>1</sub>	0.26	0.35	0.68	0.45	0.56	0.74	0.66	0.57
P <sub>25</sub>	13.44	13.13	14.68	11.07	11.31	13.98	19.07	18.28
Median (P <sub>50</sub> )	24.15	23.22	23.52	19.63	18.88	20.45	25.87	24.17
P <sub>75</sub>	31.98	30.57	30.12	27.26	24.86	26.69	31.62	29.68
P <sub>90</sub>	35.14	35.13	35.91	32.5	29.85	32.03	35.29	33.72
P <sub>95</sub>	36.79	37.27	38.82	36.26	33.32	35.08	37.36	36
P <sub>99</sub>	41.04	43.64	48.18	47.82	39.64	40.08	42.89	39.73
Maximum	56.56	61.16	66.56	68.94	71.86	69.46	87.41	52.45
Mean	22.18	21.63	22.34	19.55	18.42	20.34	24.71	23.22

**Table A7. One minute averaged PM<sub>1</sub> concentrations under different wind conditions at Kirby Misperton during the measurement period 1/2/16 – 18/9/17.**

\* P<sub>i</sub> refers to the *i*<sup>th</sup> percentile e.g. P<sub>90</sub> refers to the 90<sup>th</sup> percentile.

	Baseline PM <sub>1</sub> concentration (µm <sup>-3</sup> )							
	Kirby Misperton							
Statistic	N	NE	E	SE	S	SW	W	NW
Minimum	0.12	0.15	0.01	0.1	0.18	0.15	0.05	0.05
P <sub>1</sub>	0.37	0.49	0.84	0.93	1.03	0.61	0.31	0.29
P <sub>25</sub>	1.71	2.16	3.37	3.38	3.22	1.97	1.47	1.36
Median (P <sub>50</sub> )	3.07	4.19	7.17	6.53	5.49	3.17	2.33	2.26
P <sub>75</sub>	5.92	9.53	14.84	13.79	11.67	5.85	4.01	4.13
P <sub>90</sub>	13.75	17.52	25.98	26.93	24.83	12.78	9.02	9.46
P <sub>95</sub>	21.81	23.97	37.72	34.56	32.8	19.31	15.17	15.81
P <sub>99</sub>	41.77	44.69	51.31	45.9	49.22	36.03	30.79	33.07
Maximum	125.8	82.29	414.8	400.4	103.7	112.9	121.3	153.3
Mean	5.79	7.41	11.18	10.68	9.76	5.57	4.14	4.26

**Table A8. One minute averaged PM<sub>2.5</sub> concentrations under different wind conditions at Kirby Misperton during the measurement period 1/2/16 – 18/9/17.**

\* P<sub>i</sub> refers to the *i*<sup>th</sup> percentile e.g. P<sub>90</sub> refers to the 90<sup>th</sup> percentile.

	Baseline PM <sub>2.5</sub> concentration (µm <sup>-3</sup> )							
	Kirby Misperton							
Statistic	N	NE	E	SE	S	SW	W	NW
Minimum	0.26	0.28	0.02	0.16	0.39	0.25	0.07	0.07
P <sub>1</sub>	0.62	0.89	1.44	1.44	1.59	0.96	0.53	0.52
P <sub>25</sub>	2.87	3.53	5.18	4.89	4.68	3.09	2.35	2.24
Median (P <sub>50</sub> )	4.82	6.09	9.05	8.48	7.3	4.77	3.74	3.53
P <sub>75</sub>	8.45	11.51	17.82	15.82	13.51	7.8	6	5.93
P <sub>90</sub>	15.98	19.75	29.38	29.7	26.52	15.11	10.78	10.79
P <sub>95</sub>	23.63	26.05	41.22	37.64	35.2	21.14	16.69	17.38
P <sub>99</sub>	43.59	48.24	57.86	50.51	52.57	38.15	33.36	35.22
Maximum	132.9	89.37	451.4	436.6	112	121.5	130.2	161
Mean	7.34	9.28	13.45	12.58	11.42	7.09	5.47	5.5

**Table A9. One minute averaged PM<sub>4</sub> concentrations under different wind conditions at Kirby Misperton during the measurement period 1/2/16 – 18/9/17.**

\* P<sub>i</sub> refers to the *i*<sup>th</sup> percentile e.g. P<sub>90</sub> refers to the 90<sup>th</sup> percentile.

	Baseline PM <sub>4</sub> concentration (µm <sup>-3</sup> )							
	Kirby Misperton							
Statistic	N	NE	E	SE	S	SW	W	NW
Minimum	0.35	0.37	0.02	0.22	0.67	0.3	0.08	0.08
P <sub>1</sub>	0.84	1.21	1.73	1.78	2.02	1.24	0.69	0.74
P <sub>25</sub>	3.82	4.67	6.59	6.14	5.82	4.01	3.02	2.92
Median (P <sub>50</sub> )	6.17	7.92	10.62	9.98	8.76	6.1	4.85	4.64
P <sub>75</sub>	10.28	13.68	20.1	17.51	15.06	9.54	7.76	7.67
P <sub>90</sub>	17.93	22.07	31.84	31.6	27.84	17.05	12.4	12.57
P <sub>95</sub>	25.04	28.09	42.96	39.36	37.01	23.18	18.53	19.09
P <sub>99</sub>	44.86	50.77	62.1	53.46	53.93	40.28	35.29	36.45
Maximum	135.7	97.38	454.5	444	113.8	123.3	132	163.7
Mean	8.72	10.89	15.24	14.03	12.72	8.4	6.59	6.59

**Table A10. One minute averaged PM<sub>10</sub> concentrations under different wind conditions at Kirby Misperton during the measurement period 1/2/16 – 18/9/17.**

\* P<sub>i</sub> refers to the *i*<sup>th</sup> percentile e.g. P<sub>90</sub> refers to the 90<sup>th</sup> percentile.

Baseline PM <sub>10</sub> mixing ration (ppb)								
Kirby Misperton								
Statistic	N	NE	E	SE	S	SW	W	NW
Minimum	0.38	0.5	0.09	0.23	0.88	0.39	0.08	0.08
P <sub>1</sub>	1.21	1.56	2.27	2.29	2.63	1.66	0.9	1.04
P <sub>25</sub>	5.07	6.15	8.43	8.14	7.6	5.43	4.02	3.96
Median (P <sub>50</sub> )	7.99	10.05	12.97	12.59	10.99	8.18	6.39	6.15
P <sub>75</sub>	12.52	16.38	22.88	20.06	17.66	12.16	9.84	9.68
P <sub>90</sub>	20.81	24.86	35.12	33.56	29.75	19.69	15.02	15.14
P <sub>95</sub>	27.48	31.17	45.85	41.2	39.61	26.27	21.12	21.59
P <sub>99</sub>	47.39	55.47	66.87	57.15	58.37	47.21	37.97	38.72
Maximum	143.7	172.1	455.8	617	569.3	551.9	145.9	180.9
Mean	10.5	12.93	17.56	16.33	14.86	10.53	8.16	8.16

**Table A11. One minute averaged NO mixing ratios under different wind conditions at Little Plumpton during the measurement period 01/02/16 – 04-01/2017**

\* P<sub>i</sub> refers to the *i*<sup>th</sup> percentile e.g. P<sub>90</sub> refers to the 90<sup>th</sup> percentile.

Baseline NO mixing ration (ppb)								
Little Plumpton								
Statistic	N	NE	E	SE	S	SW	W	NW
Minimum	-1.01	-1.09	-0.47	-0.62	-2	-1.97	-2	-2
P <sub>1</sub>	-0.06	-0.06	-0.03	-0.04	-0.07	-0.09	-0.19	-1.01
P <sub>25</sub>	0.21	0.24	0.6	0.42	0.45	0.18	0.1	0.21
Median (P <sub>50</sub> )	0.84	0.86	1.1	1.43	1.17	0.48	0.4	0.66
P <sub>75</sub>	1.11	1.23	2.97	4.36	2.65	1.06	0.94	1.1
P <sub>90</sub>	1.96	3.3	8.98	14.82	7.44	1.87	1.31	1.47
P <sub>95</sub>	4.8	6.64	18.47	24.76	15.42	2.78	1.6	1.99
P <sub>99</sub>	24.97	28.91	42.12	48.55	32.03	10.2	5.46	7.64
Maximum	207.43	94.68	114.54	121.64	101.19	97.41	103.47	106.18
Mean	1.56	1.88	3.8	4.96	3.19	1	0.75	0.92

**Table A12. One minute averaged NO<sub>2</sub> mixing ratios under different wind conditions at Little Plumpton during the measurement period 01/02/16 – 04-01/2017**

\* P<sub>i</sub> refers to the *i*<sup>th</sup> percentile e.g. P<sub>90</sub> refers to the 90<sup>th</sup> percentile.

Baseline NO <sub>2</sub> mixing ration (ppb)								
Little Plumpton								
Statistic	N	NE	E	SE	S	SW	W	NW
Minimum	-0.29	-1.18	-0.88	-0.7	-0.69	-1.1	-1.21	-0.76
P <sub>1</sub>	0.34	0.43	0.78	-0.01	-0.19	-0.26	-0.3	-0.32
P <sub>25</sub>	1.55	1.77	2.8	5.05	2.76	1	0.69	0.87
Median (P <sub>50</sub> )	2.8	3.19	6.41	10.88	5.39	2.01	1.58	1.8
P <sub>75</sub>	5.29	6.58	13.1	17.7	10.47	3.28	2.79	3.62
P <sub>90</sub>	11.51	12.31	20.46	21.94	17.32	5.71	4.35	6.26
P <sub>95</sub>	15.78	17.19	23.65	24.1	20.65	9.01	6.05	9.54
P <sub>99</sub>	23.14	25.89	31.07	29.32	25.1	18.87	12.78	18.05
Maximum	71.75	44.31	61.92	88.57	61.44	128.76	83.72	41.2
Mean	4.53	5.25	8.9	11.71	7.48	2.87	2.15	2.9

**Table A13. One minute averaged NO<sub>x</sub> mixing ratios under different wind conditions at Little Plumpton during the measurement period 01/02/16 – 04-01/2017**

\* P<sub>i</sub> refers to the *i*<sup>th</sup> percentile e.g. P<sub>90</sub> refers to the 90<sup>th</sup> percentile.

Baseline NO <sub>x</sub> mixing ration (ppb)								
Little Plumpton								
Statistic	N	NE	E	SE	S	SW	W	NW
Minimum	-1.29	-1.22	-0.41	-0.78	-1.98	-1.87	-2	-2
P <sub>1</sub>	0.39	0.67	1.51	1.59	0.68	0.21	-0.2	-0.64
P <sub>25</sub>	1.99	2.34	4.01	6.13	3.81	1.67	1.43	1.75
Median (P <sub>50</sub> )	3.52	3.96	8.07	13.48	6.89	2.67	2.15	2.53
P <sub>75</sub>	6.24	7.86	16.43	23.62	13.59	4.26	3.37	4.31
P <sub>90</sub>	13.23	15.1	29.55	38.68	27.27	7.28	5.12	7.46
P <sub>95</sub>	20.65	22.39	41.3	48.77	37.77	11.39	6.96	10.72
P <sub>99</sub>	45.07	53.96	71.24	76.43	57.74	31.27	15.05	27.64
Maximum	279.18	121.01	163.57	152.16	139.03	208.14	111.38	147.38
Mean	6.13	7.12	12.98	17.72	11.27	4.03	2.92	3.93

**Table A14. One minute averaged O<sub>3</sub> mixing ratios under different wind conditions at Little Plumpton during the measurement period 01/02/16 – 04-01/2017**

\* P<sub>i</sub> refers to the *i*<sup>th</sup> percentile e.g. P<sub>90</sub> refers to the 90<sup>th</sup> percentile.

Baseline O <sub>3</sub> mixing ratio (ppb)								
Little Plumpton								
Statistic	N	NE	E	SE	S	SW	W	NW
Minimum	0.19	0.02	-0.53	-0.2	-0.14	0.07	0.03	0.11
P <sub>1</sub>	0.87	0.77	0.57	0.31	0.43	5.96	9.54	3.96
P <sub>25</sub>	14.67	12.32	8.83	5.84	10.43	17.17	18.42	18.13
Median (P <sub>50</sub> )	20.73	18.33	15.26	11.3	16.67	21.96	22.58	22.76
P <sub>75</sub>	26.77	26.18	23.19	17.53	24.23	27.82	28.8	28.39
P <sub>90</sub>	33.46	32.19	30.81	26.12	32.21	38.36	37.22	35.76
P <sub>95</sub>	36.38	36.55	35.43	30.97	36.52	41.06	39.98	39.29
P <sub>99</sub>	39.76	41.01	43.06	42.18	42.18	44.57	43.47	41.8
Maximum	48.66	50.8	57.68	57.75	54.53	51.01	117.9	48.84
Mean	20.86	19.23	16.55	12.78	17.77	23.42	24.27	23.78

**Table A15. One minute averaged PM<sub>1</sub> concentrations under different wind conditions at Little Plumpton during the measurement period 1/2/16 – 18/9/17.**

\* P<sub>i</sub> refers to the *i*<sup>th</sup> percentile e.g. P<sub>90</sub> refers to the 90<sup>th</sup> percentile.

Baseline PM <sub>1</sub> concentration (µm <sup>-3</sup> )								
Little Plumpton								
Statistic	N	NE	E	SE	S	SW	W	NW
Minimum	0	0	0.33	0	0	0.19	0	0
P <sub>1</sub>	0.14	0.25	1.23	1.17	0.62	0.49	0.51	0.4
P <sub>25</sub>	1.3	2.36	4.14	3.34	2.03	1.74	1.51	1.17
Median (P <sub>50</sub> )	2.28	3.83	7.97	7.04	3.26	2.52	2.2	1.92
P <sub>75</sub>	4.01	8.66	13.74	13.36	6.93	3.69	3.15	3.33
P <sub>90</sub>	8.97	14.58	21.04	19.91	13.55	5.29	4.39	6.28
P <sub>95</sub>	13.29	19.07	24.79	27.14	17.42	6.7	5.8	10.09
P <sub>99</sub>	22.58	26.87	34.69	37.8	27.9	15.08	16.12	19.9
Maximum	163.6	210.8	211.2	152.6	53.32	65.39	65.59	40.59
Mean	3.77	6.49	10.16	9.72	5.55	3.13	2.76	3.1

**Table A16. One minute averaged PM<sub>4</sub> concentrations under different wind conditions at Kirby Misperton during the measurement period 1/2/16 – 18/9/17.**

\* P<sub>i</sub> refers to the *i*<sup>th</sup> percentile e.g. P<sub>90</sub> refers to the 90<sup>th</sup> percentile.

	Baseline PM <sub>2.5</sub> concentration (µm <sup>-3</sup> )							
	Little Plumpton							
Statistic	N	NE	E	SE	S	SW	W	NW
Minimum	0.18	0.17	5.15	5.23	5.4	4.51	2.67	0.46
P <sub>1</sub>	0.36	0.18	5.16	5.27	6	4.56	2.87	2.35
P <sub>25</sub>	1.88	2.43	10.14	6.8	6.96	6.87	3.56	3.58
Median (P <sub>50</sub> )	2.36	6.74	11.4	7.67	7.2	7.08	3.94	3.95
P <sub>75</sub>	4.47	10.02	12.43	8.9	8.86	7.28	4.58	4.87
P <sub>90</sub>	5.66	13.57	13.22	10.94	12.25	8.75	5.34	5.19
P <sub>95</sub>	6.95	14.49	14.03	12.26	12.97	14.12	5.68	5.85
P <sub>99</sub>	14.91	16.18	14.3	12.94	14.11	15.75	7.15	11.9
Maximum	17.35	18.6	14.35	13.17	16.02	16.35	16.99	17.3
Mean	3.27	6.87	11.11	8.01	8.52	7.59	4.18	4.28

**Table A17. One minute averaged PM<sub>4</sub> concentrations under different wind conditions at Little Plumpton during the measurement period 1/2/16 – 18/9/17.**

\* P<sub>i</sub> refers to the *i*<sup>th</sup> percentile e.g. P<sub>90</sub> refers to the 90<sup>th</sup> percentile.

	Baseline PM <sub>4</sub> concentration (µm <sup>-3</sup> )							
	Little Plumpton							
Statistic	N	NE	E	SE	S	SW	W	NW
Minimum	0	0	0.58	0	0	0.5	0	0
P <sub>1</sub>	0.47	0.45	2.48	2.26	1.43	1.56	1.48	1.17
P <sub>25</sub>	2.93	4.41	7.2	6.35	4.47	4.65	4.21	3.44
Median (P <sub>50</sub> )	4.41	6.98	11.35	10.25	6.56	7.01	5.89	5.23
P <sub>75</sub>	7.02	11.93	17.7	17	10.87	9.72	8.56	7.93
P <sub>90</sub>	12.66	18.65	24.61	23.71	17.03	12.99	11.61	11.9
P <sub>95</sub>	16.98	22.61	28.59	31.36	21.06	16.06	13.83	15.1
P <sub>99</sub>	27.4	30.76	39.63	42.19	31.55	21.49	21.44	24.11
Maximum	172.3	222.7	223.2	162.3	61.91	74.35	75.13	54.51
Mean	6.01	9.28	13.51	12.85	8.53	7.71	6.83	6.46

**Table A19. One minute averaged PM<sub>10</sub> concentrations under different wind conditions at Little Plumpton during the measurement period 1/2/16 – 18/9/17.**

\* P<sub>i</sub> refers to the *i*<sup>th</sup> percentile e.g. P<sub>90</sub> refers to the 90<sup>th</sup> percentile.

	Baseline PM <sub>10</sub> concentration (µm <sup>-3</sup> )							
	Little Plumpton							
Statistic	N	NE	E	SE	S	SW	W	NW
Minimum	0	0	0.7	0	0	0.53	0	0
P <sub>1</sub>	0.63	0.62	3.4	2.89	1.92	2.31	2.01	1.55
P <sub>25</sub>	3.88	5.98	9.47	8.25	5.78	6.19	5.6	4.81
Median (P <sub>50</sub> )	5.86	9.13	14.4	12.92	8.59	9.1	7.78	7.03
P <sub>75</sub>	8.89	14.81	21.65	19.4	13.57	12.41	10.67	10.22
P <sub>90</sub>	15.49	22.06	28.58	26.77	19.75	16.16	14.49	14.88
P <sub>95</sub>	20.32	25.91	32.58	33.94	24.69	19.53	17.05	18.52
P <sub>99</sub>	31.6	36.13	47.76	46.32	34.09	26.6	25.57	30.12
Maximum	175.4	228.6	269.9	270.7	159	81.17	81.53	80.84
Mean	7.58	11.52	16.61	15.19	10.55	9.9	8.73	8.36

# Appendix C

## WATER QUALITY BASELINE STATISTICS

Site locations and further details are given in Section 2.

**Table 37. Summary statistics for groundwater chemistry from the Third Energy monitoring boreholes at KMA (SEC  $\mu\text{S}/\text{cm}$ ; Ba,Li:  $\mu\text{g}/\text{L}$ , all others:  $\text{mg}/\text{L}$ )**

Analyte	n	ncens	min	mean	max	median	95%ile	Site
SEC	26	0	1399	1560	1730	1540	1720	TE 48
Alk HCO <sub>3</sub>	26	0	496.7425	524	566	516	555	
NH <sub>4</sub>	26	0	0.084	0.134	0.321	0.103	0.298	
Ca	26	0	272.2	312	361	315	354	
Mg	26	0	6.43	7.34	8.03	7.4	7.94	
Na	26	0	30.5	34.5	40.5	34.2	40.2	
K	26	0	2.41	2.6	2.85	2.58	2.77	
Cl	26	0	96.3324	116	137	118	137	
SO <sub>4</sub>	26	0	196.8073	264	341	254	339	
Ba	26	0	68.6	91.4	146	88.1	108	
Li	26	0	44	53.3	61	53	59	
CH <sub>4</sub>	26	3	<0.0005	0.0249	0.326	0.0043	0.071	
SEC	25	0	1220	1530	1780	1530	1760	TE 49
Alk HCO <sub>3</sub>	25	0	498	523	552	523	550	
NH <sub>4</sub>	25	0	0.149	0.208	0.433	0.189	0.31	
Ca	25	0	224	314	371	318	370	
Mg	25	0	10.7	13	15.9	12.8	15.5	
Na	25	0	28.2	33.5	49.4	31.9	42	
K	25	0	2.78	3.05	3.29	3.05	3.28	
Cl	25	0	51.3	54.6	59.2	54.4	58.3	
SO <sub>4</sub>	25	0	256	377	515	369	508	
Ba	25	0	17.9	26.5	48.1	25.3	33.3	
Li	25	0	56	67.2	79	67	75	
CH <sub>4</sub>	25	6	<0.0004	0.0321	0.246	.0037	0.232	
SEC	25	0	1080	1350	1770	1320	1700	TE 50
Alk HCO <sub>3</sub>	25	0	465	503	564	504	538	
NH <sub>4</sub>	25	0	0.174	0.383	0.892	0.357	0.759	
Ca	25	0	196	266	366	264	360	
Mg	25	0	14.3	18.8	26	19.2	26	
Na	25	0	21.8	24.9	33.7	24.1	29.4	
K	25	0	2.08	2.34	2.7	2.32	2.56	
Cl	25	0	30.7	34.5	40.9	33.9	37.8	
SO <sub>4</sub>	25	0	155	313	608	273	556	
Ba	25	0	68.7	138	206	126	203	
Li	25	0	32	37.4	43	38	42.8	
CH <sub>4</sub>	25	1	<0.0005	0.0688	0.482	0.0055	0.377	
SEC	26	0	3020	3170	3220	3180	3220	TE 51
Alk HCO <sub>3</sub>	25	0	422	643	678	649	675	
NH <sub>4</sub>	26	0	0.579	0.974	1.21	0.954	1.17	
Ca	26	0	0.7	2.01	17.3	1.2	3.9	

Mg	26	0	0.3	0.737	1.34	0.64	1.14	
Na	26	0	625	690	747	693	738	
K	26	0	8.59	10.7	12	11	12	
Cl	26	0	610	669	725	670	699	
SO <sub>4</sub>	26	12	<0.5	5.86	16.4	2.65	15.7	
Ba	26	0	29.4	45.9	58.6	45.2	55.1	
Li	26	0	118	146	175	147	162	
CH <sub>4</sub>	23	0	28.4	45.0	58.6	48.2	57.7	
SEC	24	0	1650	1740	1780	1740	1780	TE 52
Alk HCO <sub>3</sub>	24	0	737	770	794	764	793	
NH <sub>4</sub>	24	0	1.3	1.81	2.08	1.76	2.06	
Ca	24	0	28	38.9	50.5	38.7	47	
Mg	24	0	4.88	6.43	8.17	6.45	7.95	
Na	24	0	351	384	416	379	409	
K	24	0	2.74	3.09	3.8	3	3.66	
Cl	24	0	39.4	46.1	64.1	42.3	61.7	
SO <sub>4</sub>	24	0	199	235	252	236	248	
Ba	24	0	12.9	17.7	23.2	17.8	23	
Li	24	0	38	46.6	57	46	56.2	
CH <sub>4</sub>	24	4	<0.0005	0.0472	0.356	0.0176	0.181	

**Table 38. Summary statistics for groundwater chemistry from the Superficial aquifer of the Vale of Pickering (n=25; units as for Table 1)**

Analyte	ncen s	min	mean	max	median	95%ile
SEC	0	690	1380	2970	1260	2390
Alk						
HCO <sub>3</sub>	0	223	583	1250	519	1240
NH <sub>4</sub>	0	0.0788	0.96	2.8	0.835	2.14
Ca	0	2.08	91.6	314	54.2	312
Mg	0	0.719	9.47	35.3	7.78	18.8
Na	0	16.1	223	613	173	609
K	0	1.16	2.7	5.9	2.34	4.62
Cl	0	24.5	101	344	72.5	287
SO <sub>4</sub>	3	<0.033	149	770	64.5	393
Ba	0	17.7	178	1200	91.4	524
Li	0	4.16	35.6	83.5	30.5	79.4
CH <sub>4</sub>	0	0.0056 5	4.01	30.4	0.24	26.4

**Table 39. Summary statistics for groundwater chemistry from the Corallian aquifer around the margins of the Vale of Pickering (n=10; units as for Table 1)**

Analyte	ncen s	min	mean	max	median	95%ile
SEC	0	377	597	746	617	746
Alk HCO <sub>3</sub>	0	159	233	309	222	303
NH <sub>4</sub>	0	0.0148	0.0592	0.328	0.0249	0.207
Ca	0	54.3	97.3	128	104	119

Mg	0	3.80	7.77	14.3	7.62	12.5
Na	0	8.96	15.1	28.9	12.1	24.9
K	0	0.969	1.59	2.43	1.33	2.35
Cl	0	15.0	31.1	58.8	29.8	49.5
SO <sub>4</sub>	0	24.5	49	75	47	74.2
Ba	0	42.8	57.9	87.8	52.5	82.8
Li	0	1.63	4.02	10.9	3	8.49
CH <sub>4</sub>	0	0.0197	0.0435	0.0665	0.0421	0.0665

**Table 40. Summary statistics for streamwater chemistry from the Vale of Pickering (n=12; units as for Table 1)**

Analyte	ncen s	min	mean	max	median	95%ile
SEC	0	340	637	1180	554	1040
Alk HCO <sub>3</sub>	0	134	230	336	231	315
NH <sub>4</sub>	0	0.0183	0.185	1.08	0.0517	0.677
Ca	0	51.9	102	165	104	154
Mg	0	2.82	6.31	10.6	5.64	9.93
Na	0	12.3	27.6	120	17.5	71
K	0	1.29	7.01	49.7	1.95	27.8
Cl	0	17.7	51.9	137	33.8	134
SO <sub>4</sub>	0	22.2	48.9	104	44.3	89.9
Ba	0	46.4	86	163	78.6	137
Li	0	1.82	4.41	14.5	3.35	9.9
CH <sub>4</sub>	-	-	-	-	-	-

**Table 41. Summary statistics for groundwater chemistry from the Cuadrilla monitoring boreholes at Preston New Road site (units as for Table 1)**

Analyte	n	ncens	min	mean	max	median	95%ile	Site	
SEC	6	0	743	919	1440	781	1330	C 55	
Alk HCO <sub>3</sub>	6	0	423	427	431	426	431		
NH <sub>4</sub>	4	1	<0.01	0.015	0.028	0.01	0.0256		
Ca	6	0	120	121	123	122	122		
Mg	6	0	34.5	37	38.3	36.8	38.2		
Na	6	0	30.4	32.2	34.9	31.9	34.4		
K	6	0	2.43	2.51	2.57	2.51	2.56		
Cl	6	0	59.8	62.3	64.8	61.9	64.5		
SO <sub>4</sub>	6	0	47.3	51.9	55.4	51	55.1		
Ba	6	0	172	188	256	174	236		
Li	6	0	8	9	10	9	9.75		
CH <sub>4</sub>	2	0	0.138	0.6	1.06	0.60	1.02		
SEC	7	0	688	768	950	771	903		C 56
Alk HCO <sub>3</sub>	7	0	442	452	466	444	465		
NH <sub>4</sub>	5	2	<0.01	0.026	0.083	0.009	0.0704		
Ca	7	0	104	108	113	108	113		
Mg	7	0	34.6	37.4	38.8	37.5	38.7		
Na	7	0	33.8	40.3	50.1	38.3	48		
K	7	0	1.81	2.06	2.3	2.1	2.27		

Cl	7	0	41.9	49.2	56.6	49.5	55.8	
SO <sub>4</sub>	7	0	52.9	62.9	70	64.6	69.2	
Ba	7	0	119	180	257	145	253	
Li	7	0	8	10.1	12	10	12	
CH <sub>4</sub>	7	0	0.607	2.57	4.81	2.08	4.45	
SEC	6	0	719	799	939	765	910	C 57
Alk HCO <sub>3</sub>	6	0	420	422	425	422	425	
NH <sub>4</sub>	5	3	<0.01	0.00774	0.018	0.005	0.0159	
Ca	6	0	118.5	122	125	122	125	
Mg	6	0	34.0	36.4	37.7	36.7	37.6	
Na	6	0	26.4	27.4	28.7	27.4	28.4	
K	6	0	2.88	3.02	3.11	3.02	3.1	
Cl	6	0	46.8	50.5	51.6	51	51.6	
SO <sub>4</sub>	6	0	53.9	60	64.3	59.8	64.2	
Ba	6	0	102	104	105	103	105	
Li	6	0	10	11.3	13	11	12.8	
CH <sub>4</sub>	6	2	<5e-04	0.178	0.735	5.00E-4	0.633	
SEC	6	0	701	786	909	758	885	C 58
Alk HCO <sub>3</sub>	6	0	417	419	423	419	422	
NH <sub>4</sub>	5	0	0.031	0.0332	0.035	0.033	0.035	
Ca	6	0	116	121	123	121	123	
Mg	6	0	32.6	35.1	37	35.4	36.7	
Na	6	0	27.6	29.1	30.9	29	30.5	
K	6	0	1.75	1.92	2.27	1.86	2.18	
Cl	6	0	43.3	48.3	50.2	48.6	50.2	
SO <sub>4</sub>	6	0	78.8	93.1	99	95.9	98.5	
Ba	6	0	68.7	71.6	77.9	70	76.8	
Li	6	0	12	13.7	15	14	14.8	
CH <sub>4</sub>	6	1	<6e-04	0.109	0.64	0.0011	0.482	
SEC	7	0	714	784	911	763	880	C 59
Alk HCO <sub>3</sub>	7	0	400	406	413	406	411	
NH <sub>4</sub>	5	2	<0.01	0.0126	0.021	0.01	0.0192	
Ca	7	0	118	120	122	119	121	
Mg	7	0	32.5	35.1	36.7	35.2	36.7	
Na	7	0	30.5	32.1	33.9	31.9	33.8	
K	7	0	1.88	1.96	2.06	1.95	2.04	
Cl	7	0	50.9	53.5	55.9	53.4	55.7	
SO <sub>4</sub>	7	0	83.9	95.5	104	95.6	103	
Ba	7	0	49.2	51.8	55.8	51	55.4	
Li	7	0	12	13.9	15	14	14.7	
CH <sub>4</sub>	7	0	5.00E-4	0.0362	0.0978	0.0322	0.0887	
SEC	7	0	637	730	865	736	838	C 60
Alk HCO <sub>3</sub>	7	0	382	388	397	386	396	
NH <sub>4</sub>	5	0	0.015	0.0614	0.237	0.018	0.194	
Ca	7	0	107	113	117	113	117	
Mg	7	0	30.86	32.8	34.3	32.7	34.1	
Na	7	0	25.6	27.1	29.5	27.3	29	
K	7	0	1.85	1.91	1.95	1.93	1.95	
Cl	7	0	42.9	46.3	47.8	47	47.6	

SO <sub>4</sub>	7	0	85.4	91.7	96.9	92.6	96.1	
Ba	7	0	56.5	61.7	66.5	61.3	65.7	
Li	7	0	12	13.9	15	14	15	
CH <sub>4</sub>	7	1	<5e-4	0.0317	0.0886	0.0282	0.0782	
SEC	7	0	752	817	1000	776	962	C61
Alk HCO <sub>3</sub>	7	0	427	433	440	433	439	
NH <sub>4</sub>	5	3	<0.01	0.0111	0.019	0.009	0.0175	
Ca	7	0	119	121	124	121	123	
Mg	7	0	33.8	36.5	39.7	36.2	39.2	
Na	7	0	38.7	41	44.2	40.1	44.2	
K	7	0	1.63	1.66	1.72	1.66	1.71	
Cl	7	0	74.3	77.8	80.7	77.8	80.4	
SO <sub>4</sub>	7	0	44.2	48.2	51.2	49.7	51.2	
Ba	7	0	137	143	149	143	148	
Li	7	0	8	9.29	10	9	10	
CH <sub>4</sub>	7	2	<5e-4	0.00925	0.0388	9.00E-4	0.0334	
SEC	6	0	573	738	906	695	881	C 62
Alk HCO <sub>3</sub>	7	0	411	418	421	419	421	
NH <sub>4</sub>	4	0	0.042	0.106	0.28	0.048	0.246	
Ca	7	0	107	119	124	120	124	
Mg	7	0	32.5	35.1	37.2	35.7	36.7	
Na	7	0	23.9	26.6	29.4	26.3	29	
K	7	0	1.59	1.8	1.9	1.82	1.89	
Cl	7	0	37.8	42.2	44.5	43.3	44.3	
SO <sub>4</sub>	7	0	87.4	99.7	107	103	106	
Ba	7	0	60.8	72.2	89.2	71	85.7	
Li	7	0	10	13.3	15	14	14.7	
CH <sub>4</sub>	7	1	<0.005	0.0413	0.26	9.00E-4	0.189	

**Table 42. Summary statistics for groundwater chemistry from the Quaternary aquifer of the Fylde, Lancashire (n=30; units as for Table 1)**

Analyte	Ncens	min	mean	max	median	95%ile
SEC	0	618	1230	8480	873	2780
Alk HCO <sub>3</sub>	0	70.0	397	588	406	571
NH <sub>4</sub>	0	0.0076	0.208	1.5	0.0657	0.566
Ca	0	74.8	147	545	119	538
Mg	0	10.2	38.7	182	32.6	111
Na	0	20.1	89.9	1360	32.4	313
K	0	1.05	3.72	18.8	2.51	7.76
Cl	0	22.0	105	1380	46.3	433
SO <sub>4</sub>	0	18.9	232	2940	75.2	1570
Ba	0	11.1	116	405	85	314
Li	0	2.65	14.6	89.5	12.3	37
CH <sub>4</sub>	0	0.0016	0.228	2.6	0.0274	2.57

**Table 43. Summary statistics for groundwater from the Sherwood Sandstone aquifer east of Woodsfold Fault (n=8; units as for Table 1)**

Analyte	ncens	min	mean	max	median	95%ile
SEC	0	690	905	1500	754	1360
Alk HCO <sub>3</sub>	0	352	455	625	413	616
NH <sub>4</sub>	0	0.008	0.632	2.57	0.405	1.94
Ca	0	46.9	104	159	101	146
Mg	0	10.7	25.4	36.1	26.8	34.2
Na	0	16.1	55.2	262	21.2	183
K	0	1.66	5.42	16.6	2.26	15.3
Cl	0	17.0	59.1	291	22.9	206
SO <sub>4</sub>	0	13.0	36.5	73.5	33.5	65.4
Ba	0	76.5	221	350	213	346
Li	0	5.00	15	40.7	11.9	31.5
CH <sub>4</sub>	0	0.00162	0.0771	0.292	0.0471	0.227

**Table 44. Summary statics for streamwater chemistry from the Fylde, Lancashire (n=14; units as for Table 1)**

Analyte	ncens	min	mean	max	median	95%ile
SEC	0	455	671	956	640	932
Alk HCO <sub>3</sub>	0	144	263	369	262	366
NH <sub>4</sub>	0	0.005	0.625	4.62	0.202	2.63
Ca	0	48.2	81	141	79.8	121
Mg	0	8.94	18.2	36.4	15.7	31.8
Na	0	15.7	35.8	97.7	26.5	88.9
K	0	2.84	10.9	53.4	8.23	29.4
Cl	0	24.1	48.7	136	41.1	98.4
SO <sub>4</sub>	0	20.9	75.9	278	49.4	230
Ba	0	20.3	61.8	105	54.9	97.9
Li	0	0.75	5.82	16	4.43	12.5
CH <sub>4</sub>	-	-	-	-	-	-